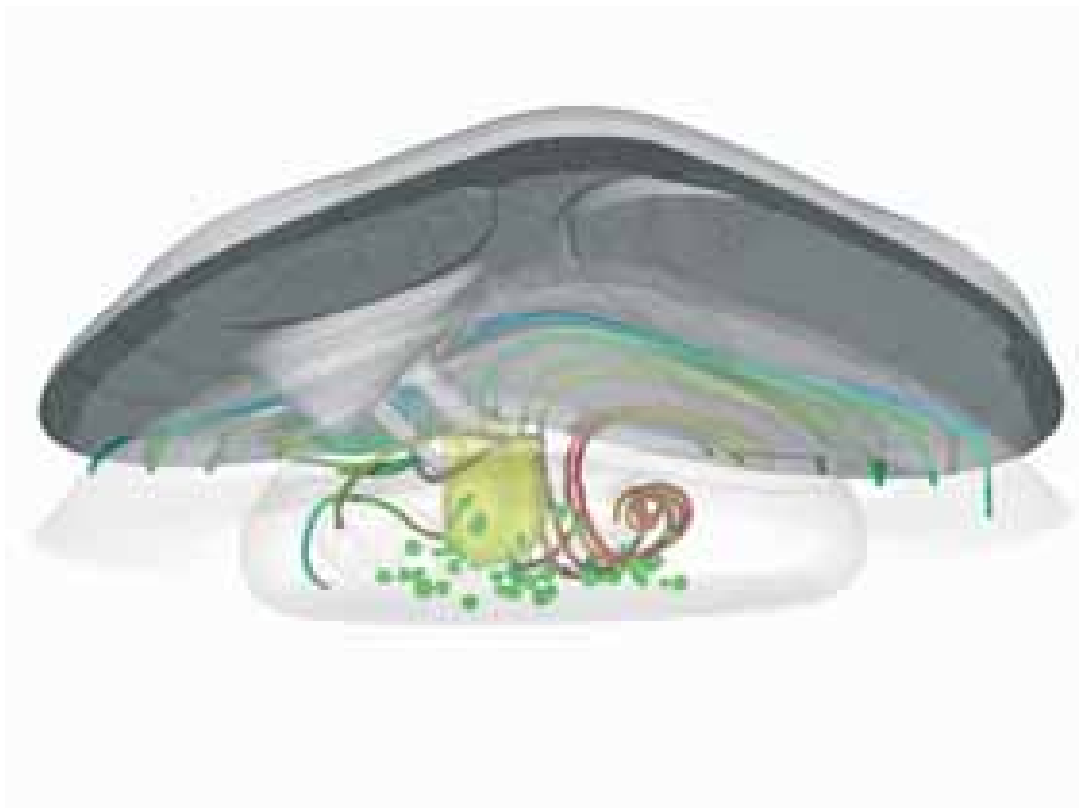


Jens Ewald

# **A Level Set Based Flamelet Model for the Prediction of Combustion in Homogeneous Charge and Direct Injection Spark Ignition Engines**



Cuvillier Verlag Göttingen



# A Level Set Based Flamelet Model for the Prediction of Combustion in Homogeneous Charge and Direct Injection Spark Ignition Engines

Der Fakultät für Maschinenwesen der Rheinisch-Westfälischen  
Technischen Hochschule Aachen zur Erlangung des akademischen  
Grades eines Doktors der Ingenieurwissenschaften genehmigte  
Dissertation

vorgelegt von

Jens Ewald

aus

Rheydt

Berichter: Univ.-Prof. Dr.-Ing. Dr. h.c. Dr.-Ing. E.h. Norbert Peters  
Univ.-Prof. Dr.-Ing. Wolfgang Schröder

Tag der mündlichen Prüfung: 20. Februar 2006

### **Bibliografische Information Der Deutschen Bibliothek**

Die Deutsche Bibliothek verzeichnet diese Publikation in der Deutschen Nationalbibliografie; detaillierte bibliografische Daten sind im Internet über <http://dnb.ddb.de> abrufbar.

1. Aufl. - Göttingen : Cuvillier, 2006  
Zugl.: (TH) Aachen, Univ., Diss., 2006  
ISBN 3-86537-800-5

© CUVILLIER VERLAG, Göttingen 2006  
Nonnenstieg 8, 37075 Göttingen  
Telefon: 0551-54724-0  
Telefax: 0551-54724-21  
[www.cuvillier.de](http://www.cuvillier.de)

Alle Rechte vorbehalten. Ohne ausdrückliche Genehmigung des Verlages ist es nicht gestattet, das Buch oder Teile daraus auf fotomechanischem Weg (Fotokopie, Mikrokopie) zu vervielfältigen.

1. Auflage, 2006  
Gedruckt auf säurefreiem Papier

ISBN 3-86537-800-5

*„Mache die Dinge so einfach wie  
möglich – aber nicht einfacher.“*

\*

*„Was wirklich zählt, ist Intuition.“*

*Albert Einstein (1879 – 1955)*



# Zusammenfassung

Numerische Strömungs- und Verbrennungssimulationen von ottomotorischen Brennverfahren mit geeigneten Turbulenz- und Verbrennungsmodellen bieten die Möglichkeit, Design- und Parameterstudien zu unterstützen. Gegenstand dieser Arbeit ist die Weiterentwicklung von dazu geeigneten Verbrennungsmodellen.

Der in ottomotorischen Brennverfahren umgesetzte Kraftstoff wird sowohl in Homogen- als auch in Schichtladebetrieb überwiegend durch vorgemischte Verbrennung umgesetzt. Zur Modellierung der turbulenten vorgemischten Verbrennung wird ein Modell auf Basis des sog. Level Set Konzeptes diskutiert. Durch das Level Set Konzept wird die mittlere turbulente Flammenfront mit Hilfe einer Oberfläche dargestellt, und die Brennrate wird durch eine turbulente Brenngeschwindigkeit modelliert.

Die Arbeit ist wie folgt gegliedert: Zunächst werden nach der Einleitung im zweiten Kapitel notwendige Grundlagen der Strömungsmechanik und der verwendeten Turbulenzmodellierung dargestellt. Danach wird im dritten Kapitel das Verbrennungsmodell auf Basis des Level Set Konzeptes hergeleitet. Hierbei wird im Besonderen auf die Modellierung von instationärer Flammenausbreitung eingegangen und ein Modell zur Beschreibung der Entwicklung von laminaren Flammenkernen entwickelt, wie sie auch bei der elektrischen Zündung entstehen. Im vierten Kapitel wird das vorgestellte Verbrennungsmodell durch ausgewählte Testfälle evaluiert. Dazu wird zur Vorhersage der turbulenten Strömung ein Reynoldsgemittelttes Turbulenzmodell auf Basis der turbulenten kinetischen Energie  $k$  und der turbulenten Dissipation  $\varepsilon$  verwendet. Die Testfälle bestehen aus Verbrennungssimulationen in einem Zylindergeometrie mit konstantem Volumen einerseits und Simulationen in einer realistischen Motorengeometrie andererseits. Dabei wurden für die Testfälle Vergleiche mit Experimenten in der Motorengeometrie für sowohl Homogenbetrieb als auch im strahlgeführten direkteinspritzenden Schichtladebetrieb durchgeführt. Die Arbeit schließt mit einer Diskussion der Ergebnisse und einem Ausblick ab.





# Preface

This work was conducted during my position as research assistant at the Institute of Combustion Technology (German *Institut für Technische Verbrennung*; until August 1st, 2005 named *Institut für Technische Mechanik*) at RWTH Aachen University, Germany.

First of all, I am indebted to University-Professor Dr.-Ing. Dr. h.c. Dr. E.h. Norbert Peters for his supervision, fruitful discussions and invaluable advice. Additionally I would like to thank University-Professor Dr.-Ing. Wolfgang Schröder for being the co-examiner of this work and University-Professor Dr.-Ing. (U.S.A.) Stefan Pischinger for serving as chair of my doctoral examination.

Also, I would like to thank my colleagues at the institute for the collaboration, especially those who also work with the CFD software AC-FluX.

Furthermore, I am greatly indebted to Dr. Andreas Lippert, Dr. Todd Fansler, Dr. Michael Drake and Dr. Hardo Barths from the General Motors Research, Development and Planning division in Warren, Michigan, U.S.A., for the supply of experimental engine data and their hospitality during my stays at their research facility. From the same group, Dr. Sherif El Tahry sat me thinking about important theory aspects that are discussed in this work.

Last but not least, I would like to thank my parents for the steady support over the whole time. And I will not forget to mention Caroline's advice in non-technical issues and her enduring motivation.



# Contents

|          |   |           |
|----------|---|-----------|
| <b>1</b> | <b>Introduction</b>   | <b>1</b>  |
| <b>2</b> | <b>Physics of Fluid Dynamics</b>                                | <b>5</b>  |
| 2.1      | Fundamental Equations of Fluid Dynamics . . . . .               | 5         |
| 2.1.1    | Equation of state . . . . .                                     | 8         |
| 2.1.2    | Fuel/Oxidizer Mixtures . . . . .                                | 9         |
| 2.2      | Statistics of turbulent flows . . . . .                         | 10        |
| 2.2.1    | Conventional and Favre averaging . . . . .                      | 10        |
| 2.2.2    | The scales of turbulent motion . . . . .                        | 11        |
| 2.3      | Mean principal conservation equations . . . . .                 | 14        |
| 2.4      | RANS turbulence model equations . . . . .                       | 15        |
| <b>3</b> | <b>Premixed Combustion</b>                                      | <b>19</b> |
| 3.1      | Physics of laminar flame propagation . . . . .                  | 20        |
| 3.1.1    | The laminar Flamelet Equations . . . . .                        | 21        |
| 3.1.2    | The Structure of Premixed Flames . . . . .                      | 24        |
| 3.1.3    | Influences of strain and curvature . . . . .                    | 27        |
| 3.2      | A Model for laminar flame propagation . . . . .                 | 30        |
| 3.3      | Physics of turbulent flame propagation . . . . .                | 32        |
| 3.3.1    | The turbulent burning velocity . . . . .                        | 32        |
| 3.3.2    | Regimes in premixed combustion . . . . .                        | 33        |
| 3.3.3    | Approaches to modeling the turbulent burning velocity . . . . . | 35        |
| 3.4      | Progress variable approaches . . . . .                          | 37        |
| 3.4.1    | The Eddy-Breakup-Model . . . . .                                | 38        |
| 3.4.2    | The Bray-Moss-Libby Model . . . . .                             | 39        |
| 3.4.3    | Flame Surface Models . . . . .                                  | 40        |
| 3.5      | The Level Set approach . . . . .                                | 41        |
| 3.5.1    | Unclosed mean flame front position equation . . . . .           | 42        |
| 3.5.2    | Unclosed equation for the flame brush thickness . . . . .       | 45        |
| 3.5.3    | Modeling closure . . . . .                                      | 47        |
| 3.5.4    | A dynamical equation for the flame surface area ratio . . . . . | 52        |

|          |  |            |
|----------|--|------------|
| 3.5.5    | Behavior close to the wall . . . . .   | 54         |
| 3.5.6    | Combining the presumed pdf shape approach with the flamelet equations . . . . .                        | 57         |
| 3.5.7    | Stratified mixtures . . . . .  | 58         |
| 3.6      | Spark Ignition Modeling . . . . .  | 61         |
| 3.6.1    | A Brief Literature Review . . . . .  | 61         |
| 3.6.2    | A Spark Ignition Model Derived from the $\tilde{G}$ -equation . . . . .                                | 62         |
| <b>4</b> | <b>Numerical Implementation</b>  | <b>67</b>  |
| 4.1      | General integration of the model into the CFD code . . . . .   | 67         |
| 4.2      | Solving of model equations . . . . .   | 69         |
| 4.2.1    | $\tilde{G}$ equation . . . . .   | 69         |
| 4.2.2    | $\widetilde{G''^2}$ equation . . . . .   | 72         |
| 4.2.3    | $\tilde{\sigma}_t$ equation . . . . .  | 72         |
| 4.3      | Coupling of $G$ -equation and heat release . . . . .   | 72         |
| 4.3.1    | Determination of $\tilde{P}_b$ . . . . .   | 73         |
| 4.3.2    | Determination of a premixed volumetric reaction rate . . . . .   | 74         |
| 4.3.3    | Model for thermodynamical states . . . . .   | 75         |
| <b>5</b> | <b>Validations</b>   | <b>79</b>  |
| 5.1      | Cylindrical Vessel experiment . . . . .  | 79         |
| 5.1.1    | Experimental setup . . . . .   | 79         |
| 5.1.2    | Cold Swirl Flow . . . . .  | 82         |
| 5.1.3    | Validity of Flamelet/Heat release coupling . . . . .   | 83         |
| 5.1.4    | Evaluation of different approaches for turbulent flame surface and turbulent curvature terms . . . . . | 84         |
| 5.1.5    | Discussion of results with swirl variation . . . . .   | 88         |
| 5.2      | Homogeneous charge SI engine . . . . .   | 91         |
| 5.2.1    | Setup for homogeneous charge . . . . .   | 91         |
| 5.2.2    | Setup of numerical calculation . . . . .   | 92         |
| 5.2.3    | Results . . . . .  | 92         |
| 5.3      | Stratified charge SIDI engine . . . . .  | 100        |
| 5.3.1    | Fuel injection . . . . .   | 102        |
| 5.3.2    | Optically accessible engine . . . . .  | 102        |
| 5.3.3    | Variation of engine speed and injected fuel mass . . . . .   | 108        |
| 5.4      | Discussion . . . . .   | 115        |
| <b>6</b> | <b>Conclusions</b>   | <b>119</b> |
| <b>A</b> | <b>The premixed turbulent reaction rate</b>  | <b>121</b> |

|          |   |            |
|----------|---|------------|
| <b>B</b> | <b>Level Sets methods on unstructured grids</b>   | <b>123</b> |
| B.1      | Level Set Numerics . . . . .                      | 123        |
| B.1.1    | Introduction . . . . .                            | 123        |
| B.1.2    | Characteristics of the $G$ -equation . . . . .    | 124        |
| B.2      | Defining an Extension Velocity . . . . .          | 125        |
| B.3      | The Fast Marching Method . . . . .                | 127        |
| B.4      | Discretisation on an unstructured grid . . . . .  | 128        |
| B.5      | Temporal integration . . . . .                    | 129        |
| <b>C</b> | <b>Laminar Burning Velocity approximation</b>     | <b>133</b> |
| <b>D</b> | <b>Turbulence prediction in the engine squish</b> | <b>141</b> |
|          | <b>Bibliography</b>                               | <b>147</b> |
|          | <b>Author's Index</b>                             | <b>157</b> |
|          | <b>Nomenclature</b>                               | <b>161</b> |



# Chapter 1

## Introduction

Combustion has been one of mankind's oldest technologies to convert chemical energy into heat or mechanical energy. Although there have been many attempts to supersede that technology, for example by fuel cells, photovoltaics, not to mention nuclear technology, it seems likely that in the near and intermediate future combustion will still play an important role for the exploitation of energy sources, provided either by means of fossil fuels or by other, renewable energy sources. Today, growing global demand for individual means of transportation, increasing implications on environmental issues, and future possible penury of fossil fuels make it even more important to intensify the efforts in improving existing energy conversion technologies. With respect to passenger cars, for example, internal combustion engines will still play a viable role in those efforts. Here, two major important research directions can be identified; these are High-Pressure Direct Injection Diesel engines (f. ex. Common-Rail based systems) and Direct Injection Spark Ignition (DISI) gasoline engines.

Unfortunately, the development of new strategies for internal combustion engines today is increasingly costly for additional gain in fuel efficiency and further reduction of pollutant emissions. In order to reduce development costs and enhance the number of parameters studied to optimize, the concept of Computational Fluid Dynamics (CFD) is becoming more and more important. Internal Combustion engines are subjected to the combined physics of chemistry, fluid mechanics and turbulence theory. Even though the microscopic interaction between these three topics is probably sufficiently understood, prediction of problems pertinent to industrial scale applications using Direct Numerical Simulation (DNS) of these mechanisms is not possible at present and will remain impracticable in the foreseeable future.

This dilemma necessitates the development of physical sub-models for turbulent flows and combustion on a macroscopic scale. These models do not only enable the numerical simulation of engineering applications with combustion. Also the macroscopic physical mechanisms of flow, turbulence, and combustion can be understood by researchers and engineers and thus may lead to additional approaches for technology

improvement.

This work focuses on the further development of turbulent premixed combustion modeling which is the main mechanism of combustion in DISI gasoline engines. The goal of this model is to understand the influence parameters on turbulent flame propagation in the engine and finally the kinematics of the turbulent flame front. Employing this information, global data as the heat release and the pressure trace can be predicted. It is possible to visualize where and when combustion in the chamber occurs. Coupled with a corresponding prediction model, eventually pollutant production could be calculated.

For most of (DI)SI engine operation modes it can be assumed that turbulent premixed combustion takes place in the so-called *flamelet regime*. This regime is furnished with a complex fractal-like distribution of laminar premixed flame structures that are surrounded by turbulent eddies of an otherwise non-reacting flow. The microscopic complexity of the combined physics addressed above can in this case be simplified by model assumptions since the time and length scales of the turbulent flow on the one hand and the chemistry of the laminar flame on the other hand are decoupled up to a certain order of magnitude.

With regards to premixed turbulent combustion modeling two major approaches exist which describe the structure of the turbulent premixed flame front. The first approach is called *progress variable approach* in which modeling is based on the local mean premixed reaction rate formulation for a burnt gas mass fraction transport equation. While models based on this equation type can easily be implemented into existing CFD computer programs since the methodology essentially follows the one for reactive species, difficulties arise in regions where the premixed flame front is very thin compared to the numerical grid used for the computation. This is also an attribute for the transition from laminar to turbulent flames.

The other approach is based on *Level Sets* which was first derived for laminar flame configuration initially by *Williams* [110]. Those Level Sets describe the flame front as a surface for which a kinematic equation can be postulated. This approach was extended by *Peters* [69, 68] into the turbulent regime by introducing a second model equation for the turbulent flame brush thickness. Due to the kinematic approach, the modeling is based on the formulation of a turbulent burning velocity instead of a local reaction rate. This model is able to give a consistent representation of a premixed flame in the laminar as well as in the turbulent regime. It was chosen to be the basis in this work although the implementation into a CFD code requires additional efforts. Due to the nature of the equation to be solved a different numerical solver other than one for conserved and reactive scalars needs to be employed. In most CFD codes, also initially in the code AC-FluX used in this work, an appropriate solver is not per se implemented.

In this work, a further development of the original combustion model by *Peters* [70, 71] is presented. The original model was developed and validated on averaged stationary turbulent flames, that is fully premixed [42] and partially premixed flames [13]. This model then was extended by the author in order to also consistently predict premixed flame propagation during the stage of turbulent flame development in which



the original model still is a sub-set of the new model. In order to predict the dynamics of spark ignition the new model was then formulated for a spherical flame kernel. In contrast to other approaches [99] the model developed in this work employs the same model for the phase of the spark ignition as well as for the later stages of turbulent flame development and flame propagation. Additionally, flame-wall interactions and effects of mean flame front curvature are studied.

This work is structured as follows: In chapter 2 the basic physical principles of fluid dynamics and turbulent flows are discussed. With respect to the turbulence modeling, a statistical approach towards Reynolds Averaged Navier-Stokes equations (RANS) is presented. Starting from this review, in the following chapter 3 the theory of turbulent premixed flow is derived. This chapter is subdivided into a discussion of the physics of turbulent flows, and modeling of turbulent flame propagation based on progress variable and Level Set approaches. Chapter 4 presents the numerical implementation of the  $G$ -equation model into the research code that was used for the validations in chapter 5. The validation is performed at first on a simple combustion setup in a cylindrical vessel carried out by *Hamamoto et al.* [36]. Following from there, numerical results employing the  $G$ -equation model are compared against experimental results obtained from a DISI spray guided gasoline engine. This engine was operated for this comparison in homogeneous charge as well as in stratified charge mode. This work closes with conclusions and an outlook to future research in chapter 6. In the appendix, also the numerical method in order to solve numerically for the Level Set transport equation is explained and an approximative expression for the determination of the laminar burning velocity of rich and lean iso-octane/air mixtures including Exhaust Gas Recirculation (EGR) is presented.



## Chapter 2

# Physics of Fluid Dynamics

In this chapter we will discuss the fundamental principles of Fluid Dynamics and turbulent flows as they are needed in this work. The first section deals with the fundamental equations as they can directly be derived from kinetic gas theory. This appears as overly extensive to be presented in this framework because the equations will not be used in that form. However, the simplifications that already on this level of modeling are applied need to be pointed out. This presentation includes basic principles of elementary reaction kinetics and the introduction of mixture states descriptors such as the mixture fraction  $Z$ . Continuing from there, basic principles of turbulent flows are briefly discussed. This includes an introduction of statistical principles as well as the description of conventional and Favre averaging. At last, the Reynolds Averaged Navier Stokes turbulence modeling approach is presented.

### 2.1 Fundamental Equations of Fluid Dynamics

The fundamental transport equations of Fluid Dynamics are based on the so-called Navier-Stokes equations. The Navier-Stokes equations can be derived by a heuristic approach, that is, the governing differential equations are in this case derived by assuming space continuity and applying macroscopically observable quantities like pressure, density, tension, mass flux, etc. to infinitesimally small control volumes.

Based on kinetic gas theory, a mathematically more rigorous ansatz (i.e. an ad-hoc assumption) can be followed as well. This mathematical approach is based on statistical mechanics and the kinetic theory of gas dynamics. A comprehensive treatment of this topic can be found in pertinent monographs, f. ex. *Ferziger et al.* [27], *Chapman and Cowling* [12], and *Giovangigli* [31]. While the first two references focus on the physics of kinetic transport by gas diffusion, the last reference emphasizes the numerical issues of solving the equations for determining the diffusion velocities and coefficients. In the following, the fundamentals of this theory will only briefly be discussed and finally the resulting Navier-Stokes equations will be given.

The kinetic theory parametrizes the gas molecules as particles propagating in a multi-dimensional parameter space. For monoatomic molecules, only six dimensions are necessary, these are the molecule position  $\vec{r}$  and the molecule velocity  $\vec{c}$ . For polyatomic molecules, additional dimensions are required which describe the rotational state of the molecules.

The further derivations are based on mainly two assumptions:

- The gas density is low. As a consequence only pairs of particles do interact with each other. This requirement is fulfilled for the problems treated in this work.
- The validity of the so-called ‘‘Stoßzahlansatz’’ as postulated by Boltzmann [6]. This approach assumes non-deterministic particle propagation and molecular chaos thus leading to an irreversibility of particle interaction events.

As a result the so-called Boltzmann-equations can be derived. Core of these equations is the velocity distribution function  $f$ . The macroscopic quantities density  $\rho$ , velocity  $\vec{u}$ , and pressure  $p$  can be expressed as different integral moments of  $f$ .

In order to yield the macroscopic conservation equations, the so called Chapman-Enskog method asymptotically expands the differential equation  $f$  into a series of powers of a small expansion parameter. Based on the assumption of a state near to thermodynamical equilibrium, the Boltzmann equations are thus linearized. Using such an expansion approach for  $f$ , the transport equations can be derived employing the linearized Boltzmann equations. An approximation of zero order yields the Euler equations of gas dynamics. Using a first order approximation of  $f$ , the Navier-Stokes equations are obtained. Those comprise the Euler equations extended by transport terms due to molecular viscosity and diffusivity. Then, the resulting transport equations for the velocity, the enthalpy  $h$ , and the species mass fractions  $Y_\alpha$  for species  $\alpha$  read:

$$\frac{\partial \rho \vec{u}}{\partial t} + \nabla \cdot (\rho \vec{u} \circ \vec{u} + p \bar{I}) = -\nabla \cdot \bar{\Pi} + \sum_{\alpha} \rho b_{\alpha}^{\vec{}} \quad (2.1)$$

$$\frac{\partial \rho h}{\partial t} + \nabla \cdot (\rho h \vec{u}) = -\nabla \cdot \vec{Q} - \bar{\Pi} : \nabla \circ \vec{u} + \sum_{\alpha} \vec{F}_{\alpha} \cdot b_{\alpha}^{\vec{}} + \frac{\partial p}{\partial t} + \vec{u} \cdot \nabla p \quad (2.2)$$

$$\frac{\partial \rho Y_{\alpha}}{\partial t} + \nabla \cdot (\rho Y_{\alpha} \vec{u}) = -\nabla \cdot \vec{F}_{\alpha} + W_{\alpha} \dot{\omega}_{\alpha} . \quad (2.3)$$

Before we focus on the definition of the the viscous tensor  $\bar{\Pi}$  we will introduce the rate-of-strain tensor  $\bar{S}^*$

$$\bar{S}^* = S_{ij}^* = \frac{1}{2} \left( \frac{\partial u_i}{\partial x_j} + \frac{\partial u_j}{\partial x_i} \right) \quad (2.4)$$

and the rate-of-rotation tensor

$$\bar{\Omega} = \Omega_{ij} = \frac{1}{2} \left( \frac{\partial u_i}{\partial x_j} - \frac{\partial u_j}{\partial x_i} \right) , \quad (2.5)$$

decomposing the velocity gradient tensor  $\partial u_i / \partial x_j$  into a symmetric and an anti-symmetric component. Here, however, we will employ a modified definition for the rate-of-strain tensor eqn. (2.4),

$$\bar{\bar{S}} = S_{ij} = \frac{1}{2} \left( \frac{\partial u_i}{\partial x_j} + \frac{\partial u_j}{\partial x_i} \right) - \frac{1}{3} \frac{\partial u_l}{\partial x_l} \delta_{ij} , \quad (2.6)$$

in which for compressible flows the strain tensor is made traceless. Then, the viscous tensor  $\bar{\bar{\Pi}}$  is defined using the volume viscosity  $\kappa$  and the shear viscosity  $\eta$  as

$$\bar{\bar{\Pi}} = -\kappa(\nabla \cdot \vec{u})\bar{\bar{I}} - \eta 2\bar{\bar{S}} . \quad (2.7)$$

The equation for the enthalpy (2.2) does not contain a source term due to chemical reactions since  $h$  is the total enthalpy which includes the chemical heat of formation. The acceleration vector  $\vec{b}_\alpha$  indicates external forces (e.g. gravity).

For the conservation equations of enthalpy and species  $\alpha$ , an expression for the species mass fluxes

$$\vec{F}_\alpha = -\rho Y_\alpha \vec{V}_\alpha \quad (2.8)$$

is needed, which is based on the species diffusion velocities

$$\vec{V}_\alpha = - \sum_{\beta} D_{\alpha\beta} (\vec{d}_\beta + \chi_\beta \nabla \log T) \quad (2.9)$$

with the multicomponent diffusion coefficients  $D_{\alpha\beta}$  of species  $\alpha$  into species  $\beta$  and the thermal diffusion ratio  $\chi_\beta$ . The diffusion driving forces  $\vec{d}_\alpha$  do not only comprise the effects of species concentration gradients and external forces but also the pressure gradient:

$$\vec{d}_\alpha = \nabla \left( \frac{p_\alpha}{p} \right) + \left( \frac{p_\alpha}{p} - \frac{\rho_\alpha}{\rho} \right) \nabla \log p + \frac{\rho_\alpha}{p} \left( \frac{\sum_{\beta} \rho_\beta \vec{b}_\beta}{\rho} - \vec{b}_\alpha \right) . \quad (2.10)$$

The species concentrations are expressed in this equation as the ratios of the density  $\rho_\alpha$  and partial pressure  $p_\alpha$  to the total density  $\rho$  and pressure  $p$ , respectively. The heat flux vector  $\vec{Q}$  is based on the expressions given above and the thermal conductivity  $\lambda$ ,

$$\vec{Q} = \sum_{\alpha} h_\alpha \vec{F}_\alpha - \lambda \nabla T + p \sum_{\alpha} \chi_\alpha \vec{V}_\alpha . \quad (2.11)$$

In many problems, these fundamental equations are simplified for analysis. This applies mainly to the determination of the diffusion fluxes. Here, we will neglect effects of thermal diffusion  $\chi_\beta D_{\alpha\beta}$  and diffusion due to pressure gradients. Additionally, instead of multicomponent diffusion coefficients, mean diffusivities  $D_{\alpha\beta} \approx D_\alpha$  for each species are assumed.

Summing up eqns. (2.3) over all species  $k$ ,

$$\rho = \sum_{\alpha} \rho_{\alpha} = \sum_{\alpha} \rho Y_{\alpha} \quad (2.12)$$

the continuity equation is obtained.

$$\frac{\partial \rho}{\partial t} + \nabla \cdot (\rho \vec{u}) = 0 \quad (2.13)$$

The only terms of the eqns. (2.3) that still need to be closed are the chemical reaction rates  $\omega_{\alpha}$ . Each of the reaction rates contains the rates of progress  $\tau_t$  of any elementary reactions  $r$  multiplied by the stoichiometric coefficients  $\nu$  of species  $\alpha$  in reaction  $r$

$$\dot{\omega}_{\alpha} = \sum_r \nu_{\alpha r} \tau_r = \sum_r (\nu_{\alpha r}^b - \nu_{\alpha r}^f) \tau_r . \quad (2.14)$$

The rate of progress is given by the forward (index f) and backward (index b) rate constants  $K_r$  and the product of the molar concentrations  $[X]_{\beta}$  of the educt species:

$$\tau_r = K_r^f \prod_{\beta} [X]_{\beta}^{\nu_{\alpha\beta}^f} - K_r^b \prod_{\beta} [X]_{\beta}^{\nu_{\alpha\beta}^b} . \quad (2.15)$$

For the forward rate constants usually an approach similar to the generalized Arrhenius empirical relation

$$K_r^f = A_r T^{n_r} \exp\left(-\frac{E_r}{R_m T}\right) \quad (2.16)$$

is employed. Here  $A_r$  is the frequency factor of the reaction,  $R_m$  the gas constant,  $E_r$  the activation energy of the reaction, and  $n_r$  a non-dimensional exponent. The relation (2.16) can then also be employed for the backward rate constant, but in most cases  $K_r^b$  is linked with  $K_r^f$  by an equilibrium constant  $K_{c,r}$  (for further information one may refer to standard literature, e.g. [29]):

$$K_{c,r} = \frac{K_r^f}{K_r^b} . \quad (2.17)$$

### 2.1.1 Equation of state

For the link between temperature, species distribution, density, and pressure, the ideal gas law is employed. With the ideal gas constant  $\mathcal{R}$  the relationship reads:

$$\frac{p}{\rho} = \sum_{\alpha} \frac{Y_{\alpha}}{W_{\alpha}} \mathcal{R} T . \quad (2.18)$$

Using the definition for the mean molecular weight  $W$ ,

$$W = \left( \sum_{\alpha} \frac{Y_{\alpha}}{W_{\alpha}} \right)^{-1}, \quad (2.19)$$

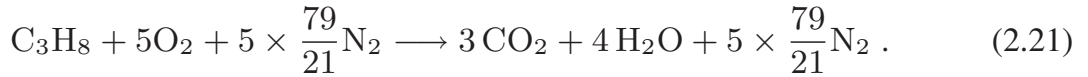
this equation solved for the pressure reduces to  $p = \frac{\rho}{W} \mathcal{R}T$ .

### 2.1.2 Fuel/Oxidizer Mixtures

The composition of fuel and the oxidizer – commonly air – may consist of a large number of different species. In order to describe the state of mixture between fuel and oxidizer by means of a small number of parameters, the *mixture fraction*  $Z$  will be introduced. One possibility is to define it as the mass fraction of the chemical elements in the gas that belong to or originate<sup>1</sup> from the educt fuel:

$$Z = \frac{\dot{m}_{\text{fuel}}}{\dot{m}_{\text{fuel}} + \dot{m}_{\text{air}} + \dot{m}_{\text{inert}}}. \quad (2.20)$$

Here  $Z$  is defined in terms of fractions of mass streams  $\dot{m}_i$ . Inert mass streams, as for example Exhaust Gas Recirculation (EGR), can be considered in the determination of  $Z$ . The *stoichiometric* mass fraction  $Z_{\text{st}}$  is constant for a given fuel and oxidizer definition. For example, the global reaction step for a propane and air mixture reads



For this setup, the stoichiometric mixture fraction is  $Z_{\text{st}} \approx 0.0601$ .

In engine combustion, instead of  $Z$  the air fuel ratio  $a_{\text{fr}}$  and the equivalence ratio  $\phi$  are used. They are defined as

$$a_{\text{fr}} \equiv \frac{\dot{m}_{\text{Air}}}{\dot{m}_{\text{Fuel}}} \quad (2.22)$$

$$\phi \equiv \frac{1}{\lambda} \equiv \frac{a_{\text{fr, st}}}{a_{\text{fr}}} \quad (2.23)$$

Here, also the definition of the normalized air/fuel ratio  $\lambda$  is shown. Neglecting inert gas as separate streams, the relationship between  $\phi$ ,  $a_{\text{fr}}$ , and  $Z$  can be derived to

$$a_{\text{fr}} = \frac{1 - Z}{Z}, \text{ and} \quad (2.24)$$

$$\phi = \frac{Z}{1 - Z} \frac{1 - Z_{\text{st}}}{Z_{\text{st}}}. \quad (2.25)$$

---

<sup>1</sup>In case that chemical reactions already occurred

## 2.2 Statistics of turbulent flows

In a turbulent flow, the velocity field  $\vec{u}$  and the other describing field quantities are subjected to random fluctuations. Therefore, the statistical distribution of all flow quantities needs to be described. Be  $U$  and  $V$  two instantaneous realizations of a flow quantity. The probability  $p$  that  $U$  is smaller than  $V$  defines the cumulative distribution function

$$F_U(V) \equiv p\{U < V\}. \quad (2.26)$$

The probability density function (pdf) of  $U$  being  $V$  can then be obtained by deriving  $F$  with respect to  $V$

$$P_U(V) \equiv \frac{dF_U(V)}{dV} \quad (2.27)$$

satisfying the normalization condition

$$\int_{-\infty}^{+\infty} P_U(V) dV = 1. \quad (2.28)$$

The mean (or expectation) of the random variable  $U$  is defined by

$$\bar{U} \equiv \langle U \rangle \equiv \int_{-\infty}^{+\infty} V f(V) dV \quad (2.29)$$

which also can be referred to as the first moment of  $U$ . The overline and the brackets operator are two different conventions to specify the averaging procedure. The second moment of  $U$ ,

$$\langle u^2 \rangle \equiv \langle (U - \langle U \rangle)^2 \rangle = \int_{-\infty}^{+\infty} (U - \langle U \rangle)^2 f(V) dV, \quad (2.30)$$

is called the variance of  $U$ . The square root of the variance,  $\sqrt{\langle u^2 \rangle}$  is defined as the standard deviation.

### 2.2.1 Conventional and Favre averaging

A classical approach in Fluid Dynamics is to decompose the equations (2.1–2.2) into a mean component and a fluctuation for all quantities. In terms of the velocity, the decomposition reads

$$\vec{u}(\vec{x}, t) = \langle \vec{u}(\vec{x}, t) \rangle + \vec{u}'(\vec{x}, t) \text{ with } \langle \vec{u}'(\vec{x}, t) \rangle = \vec{0}. \quad (2.31)$$

This approach is called ‘‘Reynolds decomposition’’.



For flows with large variations in density as in problems involving combustion processes, the averaging is carried out by density weighting. This approach is called ‘‘Favre averaging’’ and is defined by

$$\widetilde{\vec{u}(\vec{x}, t)} = \frac{\langle \rho(\vec{x}, t) \vec{u}(\vec{x}, t) \rangle}{\langle \rho(\vec{x}, t) \rangle}. \quad (2.32)$$

The decomposition – the Favre decomposition indicated by double primes – reads then:

$$\rho(\vec{x}, t) \vec{u}(\vec{x}, t) = \langle \rho(\vec{x}, t) \vec{u}(\vec{x}, t) \rangle + \rho(\vec{x}, t) \vec{u}''(\vec{x}, t) \text{ with } \langle \rho(\vec{x}, t) \vec{u}''(\vec{x}, t) \rangle = \vec{0}. \quad (2.33)$$

While simultaneous measurements of density and velocity are often difficult to obtain, Favre averaging has considerable advantages for the mathematical development. As an example, the averaging of the second (convective) term in eq. (2.1) either with the conventional or with the Favre method will be considered. The average of the product of the density  $\rho$  with the velocity components  $u_i$  and  $u_j$  would lead with conventional averaging of  $\langle \rho u_i u_j \rangle$  to an expanded expression having five terms with the density fluctuations  $\rho'$  included. On the other hand Favre averaging leads to

$$\langle \rho u_i u_j \rangle = \langle \rho \rangle \widetilde{u_i u_j} = \langle \rho \rangle \widetilde{u_i} \widetilde{u_j} + \langle \rho \rangle \widetilde{u_i'' u_j''} \quad (2.34)$$

with only two terms after expanding and the density fluctuations dropped.

## 2.2.2 The scales of turbulent motion

The first two statistical moments presented in section 2.2 only give one-point (i.e. non-spatial) information about the turbulent flow. This information does not suffice in order to completely describe the structure of three dimensional turbulence. Turbulent flows are featured with a multitude of eddy motions that can be characterized by different length scales and turnover times. If the energy contained by those eddies is plotted in terms of their wave number, we obtain *turbulent energy spectra*.

In this section we will discuss several length scale definitions that give additional information about the state of the turbulent flow. Here, for brevity, we will confine ourselves to homogeneous turbulence. Using spatial Fourier analysis on the velocity fluctuations  $u'_j$ , we can obtain the turbulent kinetic energy  $E(\kappa)$  in wave number space  $\kappa$  (see f.ex. [81]). With the turbulent kinetic energy  $k$  of eddy motion, which is defined by the trace of the Reynolds stress tensor

$$k \equiv \frac{1}{2} \langle u'_k u'_k \rangle, \quad (2.35)$$

the following relationship exists, integrating over the entire wave number range:

$$k = \int_0^{\infty} E(\kappa) d\kappa. \quad (2.36)$$

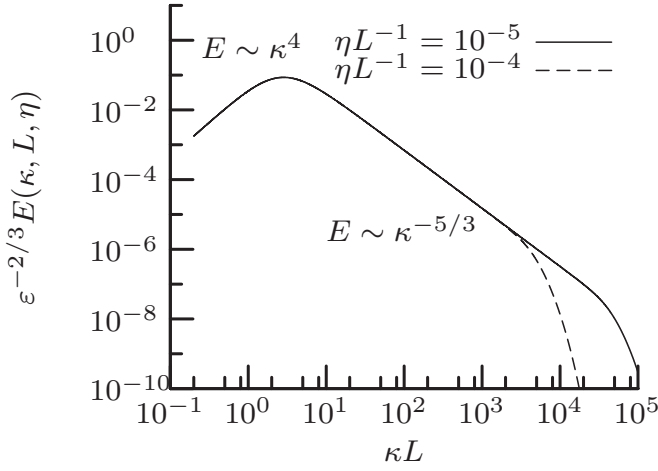


**Figure 2.1:** Two realizations of the Kármán-Pao spectrum for the turbulent energy cascade normalized by the turbulent length  $L$  and the dissipation  $\varepsilon$ . Both curves vary in terms of the dissipative length scale  $\eta$ . The spectrum is plotted using functional expressions which will not be given here for brevity. Those can be found in [81].

The turbulent dissipation  $\varepsilon$ , which can be described as the conversion of turbulent energy due to molecular viscous forces into thermal energy, is defined as

$$\varepsilon \equiv 2\nu \langle S_{ij}^* S_{ij}^* \rangle, \quad (2.37)$$

where  $\nu = \mu/\rho$  is the kinematic molecular viscosity. Using that definition we can also write in relation to  $E(\kappa)$ :

$$\varepsilon = \int_0^{\infty} 2\nu\kappa^2 E(\kappa) d\kappa. \quad (2.38)$$

For a special but frequently used case, namely *free shear flow*, model spectra exist. One of those is the so-called *Kármán-Pao spectrum* [64, 81], which is depicted in fig. 2.1. The spectrum can be approximately divided into four ranges. The first range contains the large scales, which are of the size of the mean flow scales. They are larger than the the energy containing eddies, therefore the turbulent energy increases towards smaller scales:  $E \propto \kappa^4$ . In the second range around the turbulent scale

$$L \equiv \frac{k^{\frac{3}{2}}}{\varepsilon} \quad (2.39)$$

most of the turbulent energy containing eddies are found. In this range it is assumed that turbulence is produced by mean velocity gradients.

In the third range, the so-called *inertial range*, it is assumed that larger turbulent eddies break up into subsequently smaller ones, thus transferring turbulent kinetic energy to the small scales. Since in this region the turbulent production is zero and the turbulent dissipation – as in the larger ranges – is negligibly small, the transfer rate in the state of equilibrium must be constant. This rate must be  $\varepsilon$ . From there, we conclude  $E = f(\kappa, \varepsilon)$  and assume energy conservation. Then, dimensional analysis yields

$$E(\kappa) \propto \varepsilon^{2/3} \kappa^{-5/3}, \quad (2.40)$$

which is also referred to as the “minus-five-thirds-law”. Deducing from this expression we can also formulate a turnover velocity  $v_n$  for eddies of different sizes  $l_n$  in relation to an energy containing eddy of size  $l_0$  as

$$v_n \approx (\varepsilon l_n)^{\frac{1}{3}} = v_0 \left( \frac{l}{l_0} \right)^{\frac{1}{3}} . \quad (2.41)$$

The fourth range eventually is called the *dissipative scale*. As the name already indicates, due to the small scales in this range, the molecular forces are effective for the actual turbulent dissipation to take place, thus the conversion rate must be  $\varepsilon$ . Dimensional analysis here leads us to an appropriate length scale definition

$$\eta = \left( \frac{\nu^3}{\varepsilon} \right)^{\frac{1}{4}} , \quad (2.42)$$

which yields the *Kolmogorov scale*.

In this context we also need to define further expressions for the integral length scale. All definitions are proportional to  $L$ , that is, to  $k^{3/2}/\varepsilon$ , but differ from each other by fixed constants. Using

$$v' \equiv \sqrt{\frac{2}{3}k} , \quad (2.43)$$

Bray [9] defines an integral length scale as

$$\ell = a_1 \frac{v'^3}{\varepsilon} , \text{ where } a_1 = 0.37 . \quad (2.44)$$

This expression is frequently employed in chapter 3 where different regimes of turbulent premixed combustion are discussed.

Another turbulent length scale originates from the law of the wall. Here, the mixing length  $\ell_m$  is defined in order to determine the turbulent viscosity  $\mu_t$  in  $k, \varepsilon$  turbulence models (which will be discussed below, in section 2.4). A consequence of this approach is that in the logarithmic law region,  $\ell_m$  is linearly dependent on the wall distance  $y$ ,

$$\ell_m = \kappa y , \quad (2.45)$$

with  $\kappa \approx 0.419$  being the von-Kármán constant. On the other hand,  $k \approx \text{const}$ . Then it can be shown – which will not be exercised here – that in the context of the  $k, \varepsilon$  model as discussed below, the mixing length can also be expressed as

$$\ell_m = c_D \frac{k^{3/2}}{\varepsilon} , \quad (2.46)$$

with the constant  $c_D = c_\mu^{3/4}$  in which  $c_\mu^{3/4}$  is the turbulent viscosity constant given in section 2.4. Both length scales,  $\ell_m$  and  $\ell$ , differ in magnitude by about 20%.

## 2.3 Mean principal conservation equations

A statistical formulation of the conservation equations to be solved for requires simplification and Favre averaging of the eqns. presented in section 2.1. In this section the principal conservation equations are presented in accordance with their implementation in the CFD code AC-FluX.

The principal, coupled PDEs solved in AC-FluX express conservation of mass, linear momentum, energy, and chemical species [24]. Favre averaging has been applied in order to account for density variations in the flow. The averaged momentum equation reads

$$\frac{\partial \langle \rho \rangle \tilde{\mathbf{u}}}{\partial t} + \nabla \cdot \left( \langle \rho \rangle \tilde{\mathbf{u}} \circ \tilde{\mathbf{u}} \right) = \nabla \cdot \overline{\overline{\boldsymbol{\tau}}}^t + \nabla \cdot \overline{\overline{\boldsymbol{\tau}}} + \nabla \langle p \rangle + \langle \rho \rangle \vec{g}. \quad (2.47)$$

$\vec{g}$  denotes the acceleration due to gravity.  $\overline{\overline{\boldsymbol{\tau}}}^t$  and  $\overline{\overline{\boldsymbol{\tau}}}$  denote the laminar viscous and turbulent shear stresses, respectively. They are defined as

$$\overline{\overline{\boldsymbol{\tau}}} = \nabla \cdot 2\mu \overline{\overline{\mathbf{S}}} \quad (2.48)$$

and

$$\overline{\overline{\boldsymbol{\tau}}}^t = \tau_{ij}^t = - \langle \rho u_i'' u_j'' \rangle. \quad (2.49)$$

In order to ensure mass conservation, a pressure-based formulation is used. It is based on a Poisson equation for pressure by taking the divergence of the momentum equation (2.47) and inserting the result into the Favre averaged continuity equation  $\partial \langle \rho \rangle / \partial t + \partial (\langle \rho \rangle \tilde{u}_i) / \partial x_i = 0$ . The resulting equation is

$$\nabla^2 \langle p \rangle = \frac{\partial^2 \langle \rho \rangle}{\partial t^2} - \nabla^2 \cdot [\langle \rho \rangle \tilde{\mathbf{u}} \circ \tilde{\mathbf{u}}] + \nabla^2 (\overline{\overline{\boldsymbol{\tau}}} + \overline{\overline{\boldsymbol{\tau}}}^t) + \vec{g} \cdot \nabla \langle \rho \rangle. \quad (2.50)$$

This formulation of the conservation equations enables the principal quantities to be calculated implicitly by means of linearized discretized equations. Appropriate numerical methods are for example the SIMPLE [28, 45] or the PISO [65] methods.

The PDEs for the averaged enthalpy  $\tilde{h}$  and the species mass fractions  $\tilde{Y}_\alpha$  read:

$$\frac{\partial \langle \rho \rangle \tilde{h}}{\partial t} + \nabla \cdot \langle \rho \rangle \tilde{\mathbf{u}} \tilde{h} = \nabla \cdot \left[ \left( \frac{\lambda}{c_p} + \frac{\mu_t}{\text{Pr}_t} \right) \nabla \tilde{h} \right] + \frac{\partial \langle p \rangle}{\partial t} + \tilde{\mathbf{u}} \cdot \nabla \langle p \rangle \quad (2.51)$$

$$\frac{\partial \langle \rho \rangle \tilde{Y}_\alpha}{\partial t} + \nabla \cdot \langle \rho \rangle \tilde{\mathbf{u}} \tilde{Y}_\alpha = \nabla \cdot \left[ \left( \frac{\mu}{\text{Sc}_\alpha} + \frac{\mu_t}{\text{Sc}_{t,\alpha}} \right) \nabla \tilde{Y}_\alpha \right] + \langle \rho \rangle \tilde{S}_\alpha \quad (\alpha = 1, \dots, N_S). \quad (2.52)$$

Here  $\tilde{S}_\alpha$  denotes the species source and dissipation terms. Again, the averaged enthalpy equation (2.51) is source term free with respect to chemical reactions. The laminar species diffusivities are approximated by assuming a constant laminar Schmidt

number  $Sc_\alpha$  in relation to the laminar viscosity  $\mu$ . Turbulent diffusivities are related to a turbulent eddy viscosity  $\mu_t$  (see the following section) by means of turbulent Prandtl  $Pr_t$  and Schmidt  $Sc_{t,\alpha}$  numbers. For ideal gas flows, the average density  $\langle \rho \rangle$  is obtained by the equation of state (see section 2.1.1).

## 2.4 RANS turbulence model equations

Reynolds Averaged Navier Stokes (RANS) turbulence model equations belong to the class of statistical turbulence models. The core of these models is to describe turbulent effects in analogy to laminar physical parameters. The main assumption of these models is the *turbulent viscosity hypothesis*, by means of which the effect of turbulent eddy motion is expressed as a turbulent viscosity  $\mu_t$ , a quantity used – in analogy to molecular diffusivity – for description of turbulent transport. In the following we will introduce additional quantities that are required to estimate  $\mu_t$ .

The first turbulent transport equation describes the transport of the turbulent kinetic energy  $k$ , eqn. (2.35). The conservation equation for  $k$  can be derived by subtracting the averaged momentum equations (2.47) from the instantaneous ones, followed by multiplication with  $u_j$  and Favre averaging. Thus, we obtain a set of equations for the Reynolds stresses, the trace of which yields the equation for  $k$ . Written in a form as it is used in standard CFD codes it reads:

$$\frac{\partial \langle \rho \rangle k}{\partial t} + \nabla \cdot \langle \rho \rangle \tilde{u} k = \nabla \cdot \left[ \left( \mu + \frac{\mu_t}{Pr_{t,k}} \right) \nabla k \right] + \mathcal{P} - \langle \rho \rangle \varepsilon . \quad (2.53)$$

The three terms on the r.h.s. describe turbulent transport, turbulent production, and turbulent dissipation of kinetic energy (2.38), respectively. All of these terms require modeling assumptions. To the first term assumptions have already been applied: Turbulent transport is described as turbulent diffusion, its coefficient determined by the turbulent Prandtl number  $Pr_{t,k}$ . The turbulent production

$$\mathcal{P} = - \langle \rho u_i'' u_j'' \rangle \frac{\partial \tilde{u}_j}{\partial x_i} \quad (2.54)$$

still requires modeling of the turbulent Reynolds stresses as well as the turbulent dissipation  $\varepsilon$ . For the latter quantity, a transport equation can be derived, see f. ex. Wilcox [107], but that equation defies modeling closure.

With the equation for  $k$ , the turbulence model is not complete yet, that is, another quantity is necessary. One possibility would be the mixing length  $\ell_m$ . In that case, the turbulent viscosity could be expressed as

$$\mu_t = \langle \rho \rangle \ell_m u^* , \quad (2.55)$$

where  $u^*$  is a characteristic velocity scale. In simple shear flow we can assume that  $u^*$  is locally determined by the mean velocity gradient, therefore obtaining

$$u^* = \ell_m \left| \frac{\partial \langle u \rangle}{\partial y} \right| . \quad (2.56)$$

| $C_\mu$ | $\text{Pr}_{t,k}$ | $\text{Pr}_{t,\varepsilon}$ | $C_{\varepsilon 1}$ | $C_{\varepsilon 2}$ | $C_{\varepsilon 3}$ |
|---------|-------------------|-----------------------------|---------------------|---------------------|---------------------|
| 0.09    | 1.0               | 1.22                        | 1.44                | 1.92                | -0.33               |

**Table 2.1:** Model constants of the linear  $k,\varepsilon$  model.

A more general approach, proposed by *Prandtl* [82] and *Kolmogorov* [49], relates  $u^*$  to  $k^{1/2}$ , thus giving

$$\mu_t = \text{const.} \langle \rho \rangle k^{1/2} \ell_m . \quad (2.57)$$

This approach is known as the *mixing length hypothesis*.

It is possible to incorporate  $k$  and  $\ell_m$  as base for a second model equation. An equation for  $k\ell_m$  can be found in [83]. Today, however, commonly the turbulent dissipation  $\varepsilon$  is chosen. Due to the difficulties with closing the exact transport equation for  $\varepsilon$ , another one was postulated by *Launder* and *Spalding* [50] in analogy to the equation for  $k$ , eqn. (2.53). This equation reads

$$\frac{\partial \langle \rho \rangle \varepsilon}{\partial t} + \nabla \cdot \langle \rho \rangle \tilde{u} \varepsilon = \nabla \cdot \left[ \left( \mu + \frac{\mu_t}{\text{Pr}_{t,\varepsilon}} \right) \nabla \varepsilon \right] + C_{\varepsilon 1} \mathcal{P} \frac{\varepsilon}{k} - C_{\varepsilon 2} \langle \rho \rangle \frac{\varepsilon^2}{k} + C_{\varepsilon 3} \langle \rho \rangle \varepsilon \nabla \cdot \tilde{u} , \quad (2.58)$$

thus forming along with (2.53) the so-called “ $k,\varepsilon$ -model”. The first three terms on the r.h.s. in (2.58) correspond to the analogous terms of the  $k$  equation, but with respect to  $\varepsilon$  instead of  $k$ . The third term, the dissipation rate of turbulent dissipation, is closed by assuming the eddy turnover time  $k/\varepsilon$  to be the crucial parameter, avoiding the necessity to derive a third model equation for this term. The last term on the r.h.s. in (2.58) has no counterpart in (2.53). It describes influence of global fluid compression and expansion on the dissipation rate and hence on the turbulent length scale, as these effects are present in reciprocating engines, e.g. by piston motion, see *El Tahry* [23]. However, one should note that global compression and expansion is only one phenomenon of compressible fluids. For example, gas expansion caused by (premixed) combustion acts locally, thereby resulting in steep velocity gradients.

The model constants of the  $k,\varepsilon$  model, except for  $C_{\varepsilon 3}$ , are tuned for simple incompressible flow configurations, namely for decaying homogeneous turbulence, homogeneous shear flow, and the logarithmic law region of wall-bounded flows.

In addition, a suitable expression for the Reynolds stress tensor needs to be found. From the arguments mentioned above it can be estimated that  $\langle u'_i u'_j \rangle$  is a function of  $k$ ,  $\varepsilon$ , the velocity gradients, and its products. Using (2.6) and (2.5), a general approach reads, here for the incompressible case,

$$\frac{\langle u'_i u'_j \rangle}{k} - \frac{2}{3} \delta_{ij} = a_{ij}(k, \varepsilon, \tilde{S}, \tilde{\Omega}) , \quad (2.59)$$

in which the normalized anisotropic tensor  $a_{ij}$  is symmetric and traceless. Furthermore,  $a_{ij}$  can be an arbitrary function that satisfies the rules of dimensional analysis.

It is possible to expand  $a_{ij}$  into powers of the strain and rotation tensors  $\underline{\underline{S}} \underline{\underline{\Omega}}$ , leading to linear, quadratic, cubic, etc. [80] terms. While there exist quadratic and cubic variants of the  $k, \varepsilon$ -model, f. ex. the quadratic models of *Rubinstein* and *Barton* [84], *Shih, Zhu, and Lumley* [91], and the cubic models of *Craft, Launder, and Suga* [15], and *Wallin and Johansson* [104], only to mention a few, we will confine ourselves to the linear  $k, \varepsilon$  model.

In the linear approach, the anisotropic components of the Reynolds stress tensor are linearly determined by means of the strain tensor in analogy to the molecular viscous stresses. It is also called the *Boussinesq approach* [8]

$$-\langle \rho u_i'' u_j'' \rangle = \mu_t \left( \frac{\partial \tilde{u}_i}{\partial x_j} + \frac{\partial \tilde{u}_j}{\partial x_i} \right) - \frac{2}{3} \mu_t \frac{\partial \tilde{u}_l}{\partial x_l} \delta_{ij} - \frac{2}{3} \langle \rho \rangle k \delta_{ij} . \quad (2.60)$$

Assuming high Reynolds numbers, the expression for the turbulent viscosity reads:

$$\mu_t = C_\mu \langle \rho \rangle \frac{k^2}{\varepsilon} . \quad (2.61)$$

For this linear ansatz, appropriate model constants can be found in table 2.1.





## Chapter 3

# Premixed Combustion

In this chapter we will discuss physics and modeling of premixed combustion. Ideally, in premixed combustion, fuel and oxidizer are completely mixed to an unburnt mixture first before combustion takes place. In this case, the mixing process of fuel and oxidizer is not the reaction rate dominating influence factor. The conversion of mixture to its products can then be initiated by two different mechanisms. Depending on the ambient conditions of pressure and temperature radicals may be formed and the fuel thermally cracked into smaller intermediates which eventually leads to a thermal runaway. This process is called auto-ignition. This may be unwanted in Spark Ignition engines since it can lead to engine knock. On the other hand, for other combustion modes, for example in diesel and Homogeneous Charge Compression Ignition (HCCI) engines, auto-ignition is the desired initiation of the combustion process.

The second possibility for initiation is either a spark discharge or a propagating flame front. While the auto-ignition delay time of the unburnt fuel/air mixture is very large, diffusion of radicals and heat from the spark plasma or burnt hot gas into the unburnt mixture cause the initiation of chemical reactions in the unburnt zone ahead of the plasma or flame front.

In this work we will mainly focus on the second process. It contributes mainly to the combustion mode in Spark Ignition engines and involves more complex influences than the auto-ignition process. While auto-ignition phenomena in some cases can be reduced to a zero-dimensional Perfectly Stirred Reactor (PSR) assumption, this is not feasible for premixed flame propagation. In premixed flame propagation, diffusion processes introduce a spatial influence that cannot be neglected.

Since this chapter is very substantial, its basic outline is sketched in figure 3.1. It roots in Fluid Mechanics, Reaction Kinetics, and Turbulence Theory drafted in the previous chapter. In the first section, laminar flamelet equations will be presented and the physics of laminar flame propagation will be discussed. Based on that, concepts as the laminar burning velocity, flame thickness and diffusivity are introduced and effects of strain and curvature are discussed. A model for laminar flame propagation

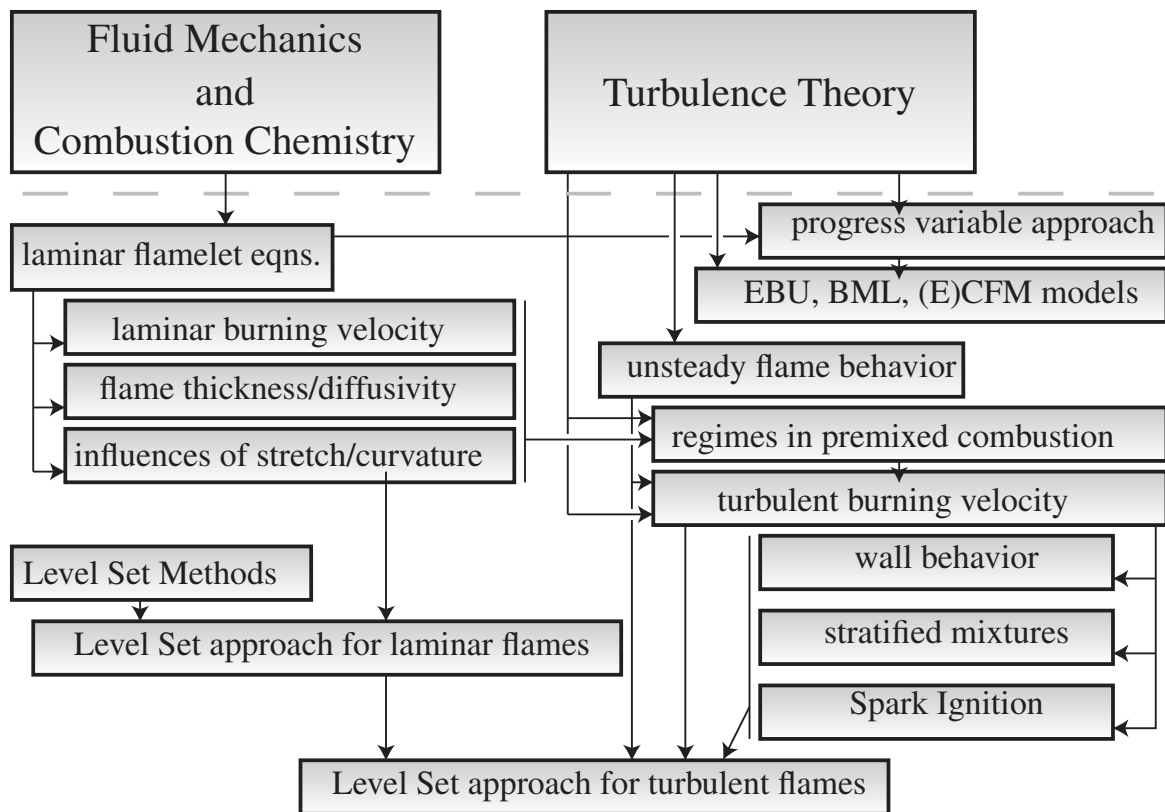


**Figure 3.1:** Structure of this chapter

modeling based on the Level Set approach is then presented in section 3.2. Next, the concept of the turbulent burning velocity is introduced in section 3.3.1 and a premixed turbulent combustion regime diagram according to Peters [70] is shown in section 3.3.2 which helps us to identify different turbulent combustion regimes for which different expressions of the turbulent burning velocity are assumed. This leads to the discussion of different aspects of the turbulent burning velocity modeling, which are: unsteady flame behavior, model behavior close to the wall, spark ignition modeling and the consideration of fuel/oxidizer mixture stratification.

Very briefly, also the progress variable approach for premixed combustion is presented and different models based on that approach are given. However, the main intention of this work is not to give an introduction to this approach, only common properties and differences to the Level Set approach are discussed.

### 3.1 Physics of laminar flame propagation

The models for turbulent flame propagation presented in this work are attributed to the *flamelet* regime. We will define a flamelet as a thin, low-dimensional, reactive-diffusive layer where the influence of the surrounding non-reacting flow on that layer can be expressed by simple scalar parameters. These parameters can for example be

the scalar dissipation rate  $\chi$  and turbulent length scales.

In many types of combustion devices the turbulent time and length scales of the chemistry are much smaller than the smallest scales of the surrounding turbulent flow. By a first-order approximation, the combustion process – viewed microscopically – can then be regarded as not influenced by the turbulence. This allows for decoupling of the chemistry calculation from the prediction of the turbulent flame propagation.

When the smallest scales of the turbulence begin to interfere with the largest scales of the premixed flame, turbulent straining effects begin to interact with the chemistry. However, it can be shown that up to a certain magnitude of influence, the ongoing processes can still be attributed to the flamelet regime by introducing asymptotic second-order expansions that take into account curvature effects on the laminar flame structure.

### 3.1.1 The laminar Flamelet Equations

The simplest premixed flame which is not influenced by a surrounding turbulent flow field is a laminar unstretched planar stationary flame. For this flame, only one-dimensional equations normal to the front are employed. In the following, the normal coordinate is referred to as the flamelet coordinate  $x_n$ .

The equation of continuity reduces for the case of a planar flame to a constant expression for the mass flow rate. In most cases, the unstretched laminar burning velocity is related to the state of the unburnt. In the following, if not stated otherwise,  $s_L^0$  always refers to the unburnt.

$$\rho u = \text{const.} = (\rho s_L^0) = \rho_u s_{L,u}^0 \quad (3.1)$$

Here, the expression  $(\rho s_L^0)$  is also referred to as the *mass burning rate*. For the species diffusivity, mean diffusion coefficients  $D_\alpha$  for each species  $\alpha$  are assumed. Furthermore, influences of pressure gradients on the diffusion velocities are neglected as well as thermal diffusion. Then, the equations (2.3) read:

$$(\rho s_L^0) \frac{\partial Y_\alpha}{\partial x_n} = \frac{\partial}{\partial x_n} \left( \rho D_\alpha \frac{\partial Y_\alpha}{\partial x_n} \right) + W_\alpha \dot{\omega}_\alpha . \quad (3.2)$$

The enthalpy equation (2.2) is modified according to the same assumptions. Additionally, by assuming zero Mach number flow, the pressure derivative is neglected.

$$(\rho s_L^0) \frac{\partial h}{\partial x_n} = \frac{\partial}{\partial x_n} \left( \lambda \frac{\partial T}{\partial x_n} \right) - \sum_\alpha h_\alpha \frac{\partial}{\partial x_n} \left( \rho D_\alpha \frac{\partial Y_\alpha}{\partial x_n} \right) \quad (3.3)$$

Since  $h$  contains the chemical heat of formation, no source terms due to chemical reactions occur. However, the heat release  $\dot{h}_{\text{hr}}$  due to reactions reads:

$$\rho \dot{h}_{\text{hr}} = - \sum_\alpha h_\alpha W_\alpha \dot{\omega}_\alpha . \quad (3.4)$$

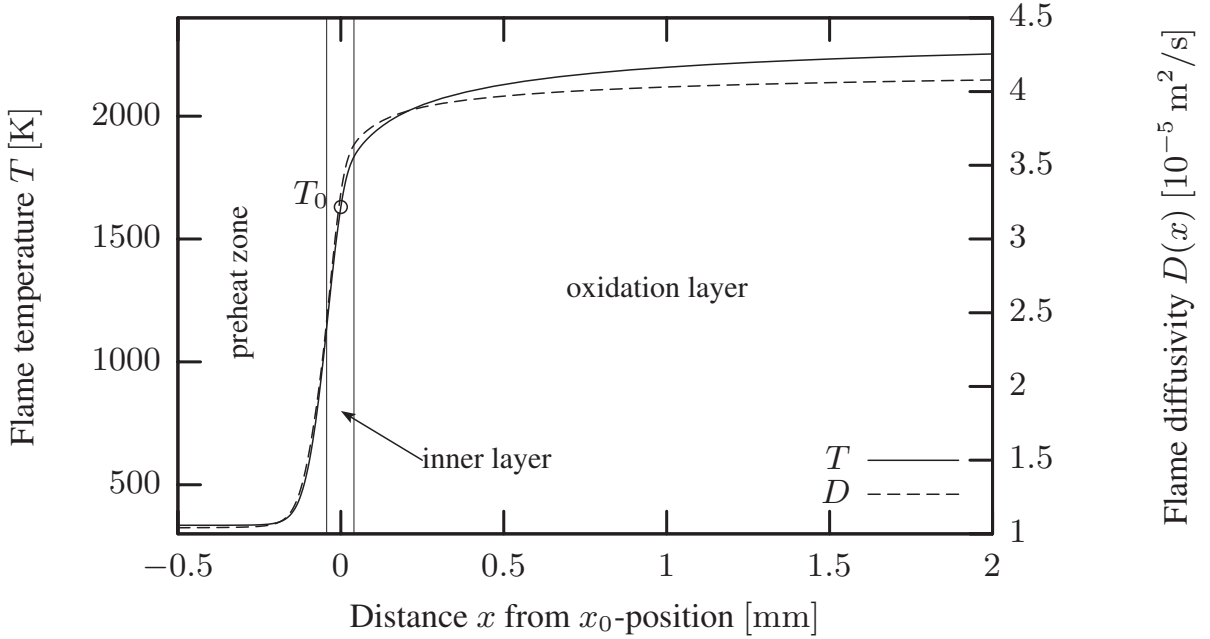


**Figure 3.2:** Structure of a stoichiometric premixed  $\text{C}_3\text{H}_8/\text{air}$  flame for  $T_u = 335 \text{ K}$  and  $p = 2.43 \times 10^5 \text{ Pa}$ , divided into three domains: the preheat zone, the inner layer, and the oxidation layer. The flame temperature and the flame diffusivity  $D(x)$  evaluated at every position of the laminar flame are plotted with respect to the perpendicular distance coordinate  $x$ .

The one-dimensional equations have two boundaries with respect to large and small  $x_n$ . For  $x_n \rightarrow -\infty$ , inlet boundary conditions reflecting the unburnt gas species composition and the unburnt gas temperature  $T_u$  are applied.  $x_n \rightarrow +\infty$  refers to the burnt gas composition. This burnt gas composition can be assumed to be in chemical equilibrium subjected to constant pressure, because the residence times in the burnt are very large and spatial gradients of enthalpy and species concentrations can be neglected there. In practice, however, instead of domain boundaries at  $\pm\infty$ , finite boundaries are applied provided that give the 1D-flamelet sufficient spatial extension. The location of the  $x_n = x_0 \equiv 0$  position is for the time being arbitrary. However, as it becomes clear in the following sections, we will define  $x_0$  as the position of maximum heat release  $\dot{h}_{\text{hr}}$ .

For a laminar premixed flame the flamelet coordinate  $x_n$  is equivalent to the physical normal coordinate  $x$ , which is used for the following plots of a premixed propane/air flame. This is not the case in general. For small scale turbulence, interactions between the flow and the flamelet may lead to non-identical coordinate transformation between  $x$  and  $x_n$ .

In fig. 3.2, the temperature  $T(x)$  and the thermal conductivity  $D(x)$  of a stoichiometric propane-air flame is plotted over  $x$ .  $D(x)$  has the unit of a species diffusivity and is defined by

$$D(x) = \frac{\lambda}{\rho_u c_p} \Big|_x. \quad (3.5)$$

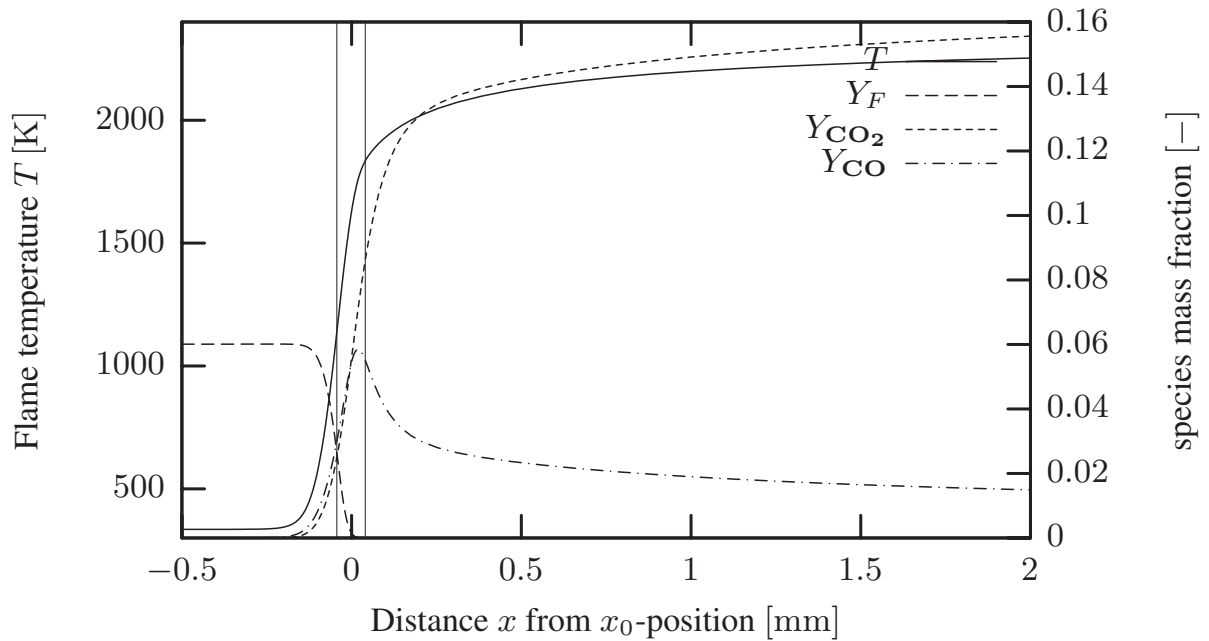


**Figure 3.3:** Plot of flame temperature against product species concentrations for the same flame as in fig. 3.2.

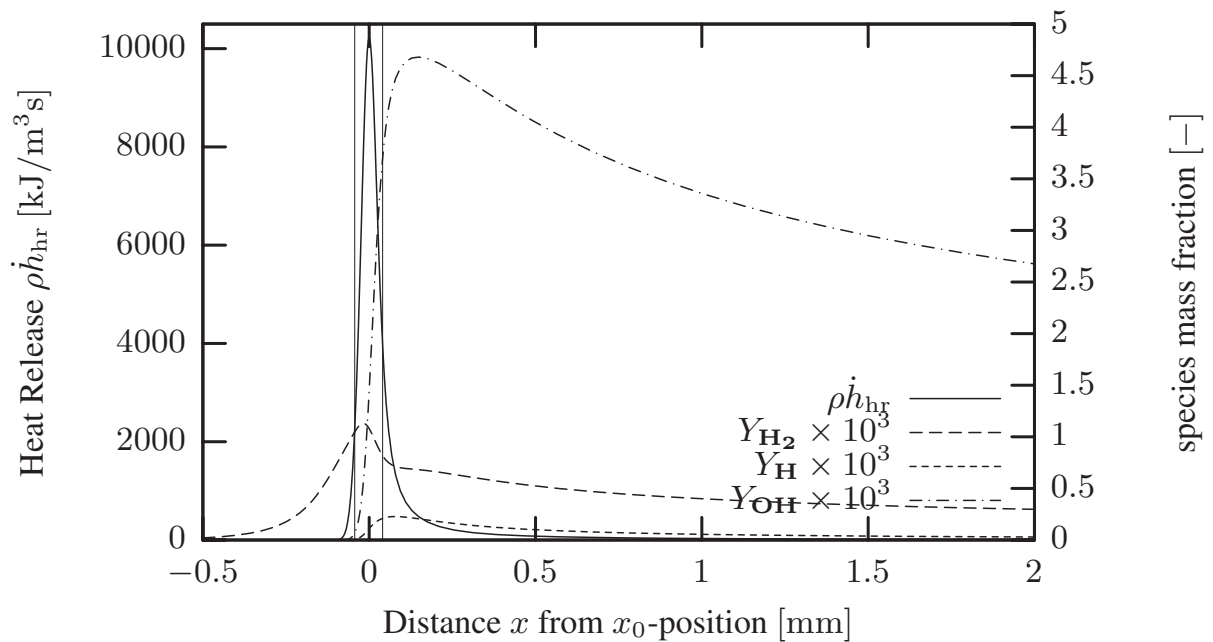


**Figure 3.4:** Plot of heat release  $\rho \dot{h}_{hr}$  on the left ordinate and intermediate species concentrations on the right ordinate, respectively, in respect to  $x$ . The domain separators from fig. 3.2 have been retained.

In figs. 3.3 and 3.4, plots of heat release, fuel and major product species concentrations are plotted as well as concentrations for major intermediate species. These plots have been obtained using the 1D flame code `FlameMaster` [76]. The premixed flame in all of these three plots is divided into three regions which are the preheat zone, the inner layer, and the oxidation layer. The physical understanding of these sub-ranges is explained in the following section.

### 3.1.2 The Structure of Premixed Flames

In 1938, *Zeldovich* and *Frank-Kamenetzki* [112] investigated the structure of a premixed flame subjected to global one-step kinetics. Even although the assumption of one-step kinetics is overly simplifying for realistic premixed flames, main conclusions from that simplified analysis can be drawn and used in turbulent combustion modeling.

In one-step kinetics, direct conversion of fuel and oxidizer into the product is assumed. Therefore, intermediate species are not considered. The flame propagation is induced by the transport of thermal energy from the region where the heat release occurs into the unburnt gas mixture. Thus, at the head of the premixed flame front the so-called preheat zone is formed. The mixture temperature in the unburnt gas rises exponentially towards the reaction zone until the thermal energy reaches the activation energy threshold of the global reaction step. This point separates the preheat zone from the reaction zone.

In [68], *Peters* discusses an asymptotic analysis of the problem posed. Herein, the laminar burning velocity is obtained as an eigenvalue. An expression for the mass burning rate primarily depends on the ratio of the thermal conductivity  $\lambda_b$ , the heat capacity  $c_p$ , and the combustion time scale  $t_c$ :

$$(\rho_u s_L)^2 = \frac{\lambda_b \rho_u}{c_p t_c} . \quad (3.6)$$

The square on the l.h.s. of the equation originates from the second derivative of the heat conduction term of eqn. (3.3). The combustion time scale  $t_c$  can be understood as the time required for a premixed mixture to be consumed by a propagating flame front. In the equation above, it is defined as

$$t_c = \frac{\rho_u c_p (T_b - T_u)^2 E^2}{2B \rho_b \mathcal{R}^2 T_b^4 A} \exp\left(\frac{E}{\mathcal{R} T_b}\right) . \quad (3.7)$$

The meaning of each quantity will not be elaborated on in this work. They are defined and explained in [68]. The implication of (3.7) is that  $t_c$  is primarily dependent on the ratio of burnt ( $T_b$ ) and unburnt ( $T_u$ ) temperatures, and the rate coefficient  $B$  as well as the activation energy  $E$  of the underlying reaction mechanism. Effects of diffusion do not influence the chemical time scale.

As we see from these expressions, two physical processes are mainly responsible for the flame propagation: The first process is the chemical reaction that imposes a

chemical time scale. The second process is the transport of thermal energy – and radicals as they occur in multi-step mechanisms – into the preheat zone. Hence an increase of burning velocity can be achieved by either decreasing  $t_c$  or increasing  $\lambda_b/c_p$ .

This main observation also applies to multi-step reaction mechanisms. For lean and stoichiometric Methane/Air flames, a reduced four step mechanism was derived by Peters [67]. This mechanism was subsequently used in order to derive an asymptotic analysis of a stoichiometric flame [73]. As a result of this analysis, the structure of the flame was subdivided into three regions:

- the chemically inert *preheat zone* as it was also found for one-step asymptotics
- the so called *inner layer* in which the hydrocarbon fuel is completely consumed and intermediate species such as  $H_2$  and  $CO$  are formed, and
- the *oxidation layer*, where the intermediates are oxidized.

The resulting equation of the mass burning rate is of the same form as eqn. (3.6), although the expression for the chemical time scale  $t_c$  is more complex than eqn. (3.7). The ratio  $\lambda_b/c_p$  has to be evaluated at the temperature  $T_0$ , which is a characteristic temperature for the inner-layer. At the same location, the *flame diffusivity*  $D_0$  will be defined, and along with the laminar burning velocity  $s_{L,u}$  we also obtain an expression for the laminar flame thickness  $\ell_f$ :

$$D_0 = s_{L,u} \ell_f = \frac{1}{\rho_u} \left. \frac{\lambda}{c_p} \right|_{x_0}. \quad (3.8)$$

The exact position of the inner layer temperature  $T_0$  is assumed to be where the maximum heat release occurs, and this is at the position  $x = x_0$  as defined in the previous subsection. The thickness of the inner layer  $\ell_\delta$  is approximately one order of magnitude smaller than the flame thickness  $\ell_f$ .

One statement that we can deduce from the eqns. 3.6 and 3.8 is that the dependency of  $s_L^2$  from  $D_0$  or  $\lambda/c_p|_{x_0}$ , respectively, is linear. It was justified by asymptotic theory for lean and stoichiometric methane/air mixtures [68, 73], moderately rich and

|           |  |
|-----------|--|
| $s_{L,u}$ | 0.439 m/s                                    |
| $T_{x_0}$ | 1139 K                                       |
| $T_0$     | 1630 K                                       |
| $T_{ei}$  | 1834 K                                       |
| $D$       | $3.31 \times 10^{-5} \text{ m}^2/\text{s}$   |
| $\ell_f$  | $0.286 \times 10^{-3} \text{ m, eqn. (3.8)}$ |

**Table 3.1:** Properties computed for the stoichiometric premixed  $C_3H_8$ /air flame depicted in fig. 3.2 as calculated with the methods presented in this section.

rich methane/air mixtures [86, 85], and lean heptane flames [87]. Henceforth we will assume that it is also valid for higher hydrocarbon flames.

For complex reaction mechanisms involving dozens of species and hundreds of elementary reactions, an asymptotic analysis is not feasible. However, a structural subdivision into domains is still desirable. In figs. 3.2–3.4 such a subdivision for a stoichiometric propane/air flame is carried out by evaluating the slope of the heat release. The ambient condition for that flame is chosen to be the same as for the gas mixture used in the cylindrical vessel validation case presented in chapter 5.1.

The location of  $x_0$  was defined in section 3.1.1 as the position of maximum heat release in the inner layer. However, a constraint for finding the beginning and the end of the inner layer was not found. In this work, the second derivative of the heat release  $\rho \dot{h}_{hr}$  was evaluated for this purpose. Its maximum ahead of  $x_0$  was taken as the beginning of the inner layer (index “x0”) and the other maximum after  $x_0$  was taken for the end of the inner layer (index “ei”). These subdivisions are employed in figures 3.2–3.4. As can be seen, it is of the same order of magnitude as  $\ell_f$ . This is due to the fact that in this definition of the inner layer also regions are included in which the heat release is much lower than the maximum heat release at  $x_0$ .

In table 3.1 the properties for that flame obtained by this approach are listed. The temperature  $T_{x_0}$  therefore corresponds to the beginning of the inner layer, and  $T_{ei}$  to its end. It is clearly seen that the temperature range of the heat release defined by these borders is relatively large and varies about 700 K, the flame diffusivity, cf. fig. 3.2, about 50 %.

It needs to be noted that other different definitions of the flame thickness [32] are also common. The definition according to eqn. (3.8) is difficult to handle because besides the temperature profile, also the species concentrations need to be given at the inner layer temperature in order to compute the flame diffusivity  $D_0$ . A more convenient way would be to define the flame thickness based on the temperature profile only. This definition of flame thickness  $\ell_{f,grmax}$  is only dependent on the maximum and minimum temperatures  $T_{ad}$  and  $T_u$ , and the largest temperature gradient that usually coincides with the location of the maximum heat release:

$$\ell_{f,grmax} = \frac{T_{ad} - T_u}{\left(\frac{dT}{dx}\right)\bigg|_{x_0}} . \quad (3.9)$$

This definition gives larger results than eqn. (3.8) for the thickness. However, both definitions are approximately related to each other as

$$\ell_f \approx \ell_{f,grmax} \frac{T_0 - T_u}{T_{ad} - T_u} . \quad (3.10)$$

In figure 3.5, the three temperatures  $T_{x_0}$ ,  $T_0$ , and  $T_{ei}$  that indicate the range of the inner layer are plotted together with corresponding values of the flame diffusivity over the equivalence ratio  $\phi$ . Within the plotted equivalence ratio range the inner layer temperature varies about 450 K which results in a variation for the diffusivity  $D_0$  of



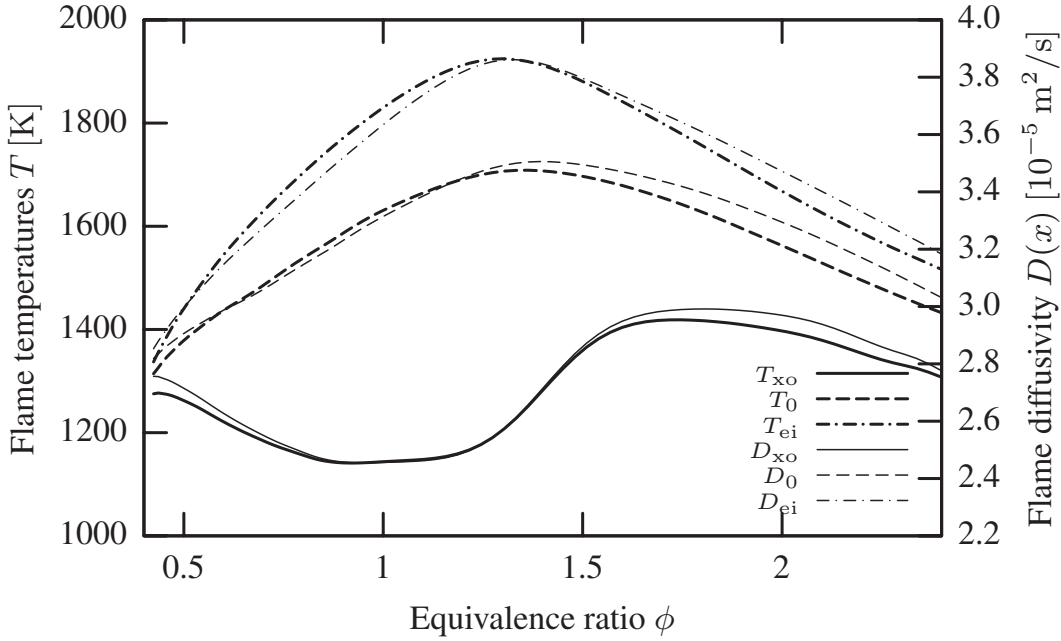


**Figure 3.5:** Plot of cross-over temperature  $T_{xo}$ , inner layer temperature  $T_0$ , and the region separating temperature  $T_{ei}$  (thick lines, left ordinate) between inner layer and oxidation layer for propane/air mixtures at  $T_u = 300$  K,  $p = 2.43$  bar, and different equivalence ratios. On the right ordinate, corresponding flame diffusivities  $D$  are plotted using thin lines.

15%. This variation is often neglected and the flame diffusivity is assumed to be approximately constant over equivalence ratio range:

$$D_0(\phi) = s_L(\phi) \ell_f(\phi) \approx \text{const.} \quad (3.11)$$

In order to approximate the flame diffusivity by means of (3.8) a commonly used relationship for hydrocarbon fuels is according to *Smooke et al.* [93]

$$\frac{\lambda}{c_p} = 2.58 \times 10^{-5} \frac{\text{kg}}{\text{m s}} \left( \frac{T_0}{298 \text{ K}} \right)^{0.7}. \quad (3.12)$$

### 3.1.3 Influences of strain and curvature

In the previous section, the premixed flame was considered as a one-dimensional structure. However, in 3D-space, the flame front can be curved and subjected to strain caused by the fluid flow, thus influencing the structure of the flame and modifying the laminar burning velocity  $s_L$ . In order to define and identify curvature and strain, a reference surface for the flame front must be introduced. We will employ the position of the inner layer  $x_0$  for the definition of this surface. In fig. 3.6, a curved surface of the inner layer of a flame front is depicted. The  $x_n$  coordinate points perpendicular to the flame surface into the burnt gas in direction  $\vec{n}_\perp$ . The coordinates  $\xi_1$  and  $\xi_2$  point parallel to the flame surface in directions  $\vec{n}_{\parallel,1}$  and  $\vec{n}_{\parallel,2}$ , respectively. The flame normal

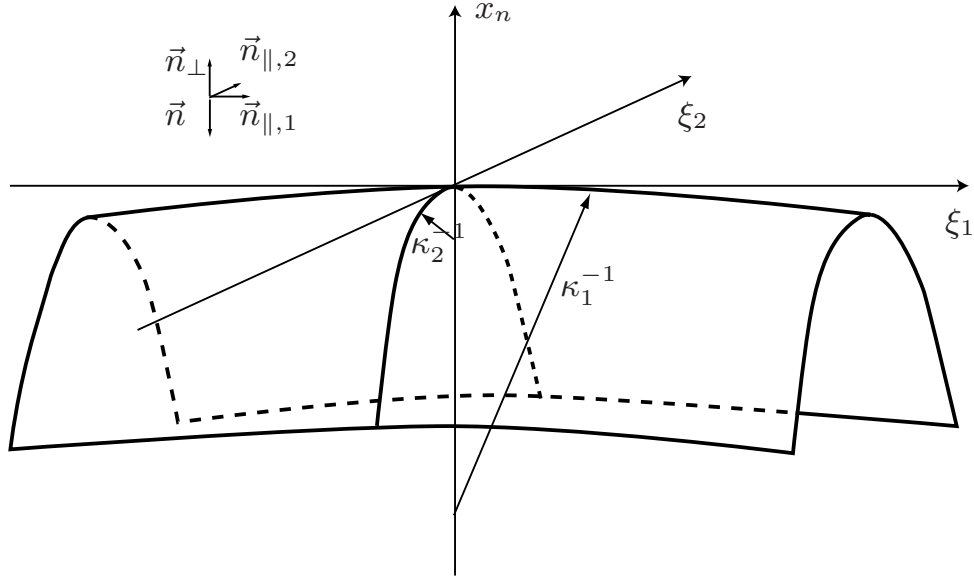


**Figure 3.6:** Schematic of a curved flame front surface.

$\vec{n}$  is defined such that it points perpendicular to the flame front into the unburnt gas,  $\vec{n} = -\vec{n}_\perp$ .

By virtue of these definitions, the strain of the flame is determined by

$$S = - (\vec{n} \cdot \nabla \vec{u} \cdot \vec{n})|_{x_n=x_0} . \quad (3.13)$$

The curvature is then defined by evaluating

$$\kappa = \nabla \cdot \vec{n} = -\nabla \cdot \vec{n}_\perp . \quad (3.14)$$

Since the flame curvature can be different in  $\xi_1$  and  $\xi_2$  direction,  $\kappa$  is the gaussian mean curvature  $\kappa = \kappa_1 + \kappa_2$ .

It can be shown (cf. [14, 59]) that for a one-step large activation energy reaction and with the assumption of constant properties the burning velocity  $s_L$  subjected to strain and curvature can be approximated by first order to

$$s_L = s_L^0 - D_{\mathcal{L}} \kappa - \mathcal{L} S , \quad (3.15)$$

where  $s_L^0$  is the velocity of a planar unstrained flame,  $\mathcal{L}$  the *Markstein length*, and

$$D_{\mathcal{L}} = s_L^0 \mathcal{L} \quad (3.16)$$

the *Markstein diffusivity*. By relating  $\mathcal{L}$  to the flame thickness  $\ell_f$ , the *Markstein number* is introduced:

$$\mathcal{M} = \frac{\mathcal{L}}{\ell_f} . \quad (3.17)$$

Effects of strain and curvature can be combined to the *flame stretch*  $K$ . Different definitions of flame stretch are possible. The first definition of flame stretch was suggested by *Williams* [109]. It represents the fractional area change of a small surface element  $A$  which is transported with the flame:

$$K_A = \frac{1}{A} \frac{dA}{dt}. \quad (3.18)$$

A recent definition traces back to *De Goey* and *ten Tije Boonkkamp* [17]. Here  $K$  is defined by the fractional change of the mass burning rate  $\rho_{SL}$ :

$$K_M = \frac{1}{(\rho_{SL})} \frac{d(\rho_{SL})}{dt}. \quad (3.19)$$

A comprehensive discussion of the two definitions can be found in [32]. What is left to be noted here is that by introducing  $K$ , eqn. (3.15) gives

$$\frac{s_L}{s_L^0} = 1 - \mathcal{M} \text{Ka}_l \quad (3.20)$$

with the Karlovitz number

$$\text{Ka}_l = \frac{\rho \ell_f}{(\rho_{SL})} \Big|_{x_n=x_0} K. \quad (3.21)$$

*Groot* and *De Goey* [33] have investigated the burning velocity and mass burning rates of spherical and cylindrical premixed flames. They discuss the influence of the various flame configurations on the Markstein number for large ratios of the flame radius to its thickness. For example, they found that if the mass burning rate of a stationary premixed cylindrical or spherical flame was evaluated at the inner layer, it would be almost independent of the flame radius. According to their explanation, in this configuration at the inner layer the reaction influence would be of greater order than that of diffusion and convection, and secondly, effects of strain and curvature would be in balance, thus leading to zero stretch. However, they point out that it is impossible to define unique Markstein numbers for both strain and curvature independent of the flame configuration [34]. This finding especially holds for the influence of strain. As a suggestion to resolve this difficulty, they propose to give a combined Markstein number for flame stretch.

For flames subjected to strong curvature – that is, when the curvature radius is of the order of the laminar flame thickness – *Peters et al.* [72] have performed 2D DNS calculations of methane/air mixtures. The curvature effects on the net burning velocity were investigated. Strong curvature can occur in turbulent premixed combustion when the small eddies are able to enter the premixed zone and increase the diffusive transport of heat and radicals in the preheat zone. The laminar burning velocity then can be decomposed into contributions due to reaction, normal diffusion, and curvature. As an

example, the influence of curvature on the diffusion term of the temperature equation is shown. The same investigation can be done for the species equations. The temperature gradient in 3D space can be expressed by the normal derivative as

$$\nabla T = \vec{n}_\perp (\vec{n}_\perp \cdot \nabla T) + \sum_{j=1,2} \vec{n}_{\parallel,j} \overbrace{(\vec{n}_{\parallel,j} \cdot \nabla T)}^{=0} = \vec{n}_\perp \frac{\partial T}{\partial x_n}. \quad (3.22)$$

Here we also have assumed that iso-temperature surfaces locally align with iso- $G$  surfaces, that is, locally there are homogeneous mixture conditions. Inserting this result into the diffusion term gives:

$$\begin{aligned} \nabla \cdot (\rho D \nabla T) &= \nabla \cdot \left( \rho D \vec{n}_\perp \frac{\partial T}{\partial x_n} \right) = \vec{n}_\perp \cdot \nabla \left( \rho D \frac{\partial T}{\partial x_n} \right) + \rho D \frac{\partial T}{\partial x_n} \nabla \cdot \vec{n}_\perp \\ &= \frac{\partial}{\partial x_n} \left( \rho D \frac{\partial T}{\partial x_n} \right) - \rho D \kappa \frac{\partial T}{\partial x_n} \end{aligned} \quad (3.23)$$

If this derivation is appropriately carried out for the enthalpy and the species equations, the term proportional to the curvature can be combined with the convective term on the l.h.s. of eqns. (3.2) and (3.3), respectively. By comparing the results obtained with the flamelet equations for a planar flame, the following expression for the flame speed can be deduced:

$$s_L(\kappa) = s_L^0 - D\kappa, \quad (3.24)$$

with the assumption that the influence of the flame stretch is of a smaller order in comparison to curvature, viz.  $s_L(S) \approx s_L^0$ .

If we compare eqns. (3.15), (3.16), and (3.17), a similar expression for the flame speed can be derived:

$$s_L(\kappa) = s_L^0 - \mathcal{M}D \left( \kappa + \frac{S}{s_L^0} \right) \quad (3.25)$$

With the strain term neglected and the Markstein number  $\mathcal{M} = 1$ , this gives equation (3.24).

The result of this simple thermal flame propagation theory is that the burning velocity increases for a concave the flame front (viz.  $\kappa < 0$ ) and decreases for a convex (viz.  $\kappa > 0$ ) front towards the unburnt gas. Therefore perturbations of the front are smoothed out by diffusive effects towards a flattened flame. Effects of Markstein numbers different from unity are not considered because they are not identified as a leading order influence in this limit of flame curvature and stretch.

## 3.2 A Model for laminar flame propagation

In this section we will discuss model equations for the description of laminar flame propagation. These kinematic model equations are based on the Level Set approach as

introduced at first by *Williams* [110]. The starting point is the kinematic equation of a flame front “particle”. This “particle” is advected by the local fluid flow velocity  $\vec{u}$  and the local laminar burning velocity normal to the front. The differential equation for the particle position  $\vec{x}_f(t)$  therefore reads:

$$\frac{d\vec{x}_f}{dt} = \vec{u} + s_L \vec{n} . \quad (3.26)$$

However, we do not want to model the flame front as a set of particles. Instead, we employ a scalar field that defines the flame front surface as the position of one of its iso-surface values. We will call the scalar  $G$  and the position of the flame front *the  $G_0$  iso-surface of  $G$* . As reference position of the flame surface, the inner layer position is employed, where  $x_n = x_0$ . The kinematic relationship between  $G$  and  $\vec{x}(t)$  then reads:

$$\left. \frac{\partial G}{\partial t} + \nabla G \cdot \frac{d\vec{x}_f}{dt} \right|_{x_0} = 0 . \quad (3.27)$$

In order to close eqn. (3.27), an expression for the flame normal  $\vec{n}$  in terms of  $G$  must be found. With the assumption that  $G$  is strictly monotonic and continuous

$$\vec{n} = - \frac{\nabla G}{|\nabla G|} \quad (3.28)$$

is the flame front normal for  $G = G_0$ . The following transport equation

$$\frac{\partial G}{\partial t} + \vec{u} \cdot \nabla G = s_L |\nabla G| \quad (3.29)$$

is valid only where  $G = G_0$  and effects of non-uniform flow density due to combustion are not yet accounted for.

With the new definition of  $\vec{n}$ , the curvature still can be evaluated by means of eqn. (3.14) using  $\kappa = \nabla \cdot \vec{n}$  and the expression for the modified burning velocity (3.24) can be inserted into (3.27). Multiplying the result with the local density we obtain

$$\rho \frac{\partial G}{\partial t} + \rho \vec{u} \cdot \nabla G = (\rho s_{L,s})_u |\nabla G| - \rho D \kappa |\nabla G| , \quad (3.30)$$

where  $s_{L,s} \approx s_L^0$ . The local mass burning rate has also been replaced here by the mass burning rate of an unstretched flame with respect to the unburnt.

For  $G \neq G_0$ , a suitable definition and equation for  $G$  still needs to be found. The condition that  $G$  be strictly monotonic, will be extended into the region  $G \neq G_0$ . This can be fulfilled by demanding

$$|\nabla G| = 1 . \quad (3.31)$$

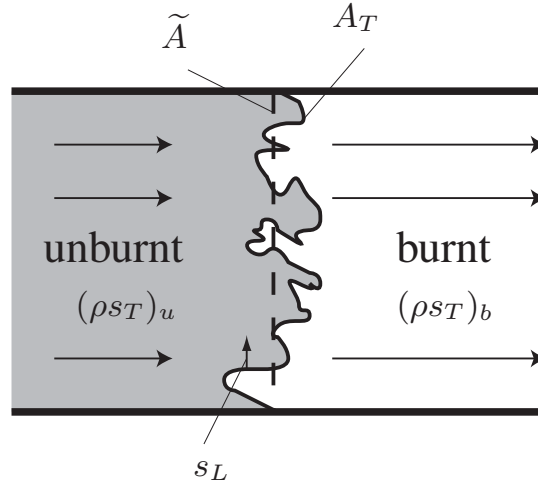


**Figure 3.7:** The turbulent burning velocity  $s_T$  and the turbulent flame surface  $A_T$ .

### 3.3 Physics of turbulent flame propagation

In the following, modeling of turbulent premixed flame propagation in the flamelet regime will be discussed. As already noted at the beginning of this chapter, in the flamelet regime a laminar-like flame front is embedded into an otherwise turbulent flow.

#### 3.3.1 The turbulent burning velocity

At first the concept of the turbulent burning velocity and turbulent flame surface area needs to be introduced. In figure 3.7, a turbulent flame front in a stationary duct configuration is depicted. Due to the stationarity, the turbulent mass burning rate  $(\rho s_T)$  is equal not only to the mass flow in the unburnt but also to the burnt region. The cross-sectional area  $A$  of the duct describes the area that can be observed from a viewpoint perpendicular to the turbulent flame front. In fact, this front is constantly perturbed and convoluted by the turbulence, thus enhanced to a total surface area  $A_T$ . The ratio between the instantaneous area of the turbulent flame front  $A_T$  and the area of the so-called mean flame front  $\tilde{A}$  is called the *flame surface area ratio*  $\sigma$ :

$$\sigma = \frac{A_T}{\tilde{A}} = \sigma_t + 1 \quad (3.32)$$

For a laminar flame  $\sigma = 1$  or the *turbulent* flame surface area ratio  $\sigma_t = 0$ . After averaging  $\sigma$  (or  $\sigma_t$ , respectively) we obtain the turbulent burning velocity as:

$$s_T = \tilde{\sigma} s_L = (1 + \tilde{\sigma}_t) s_L. \quad (3.33)$$

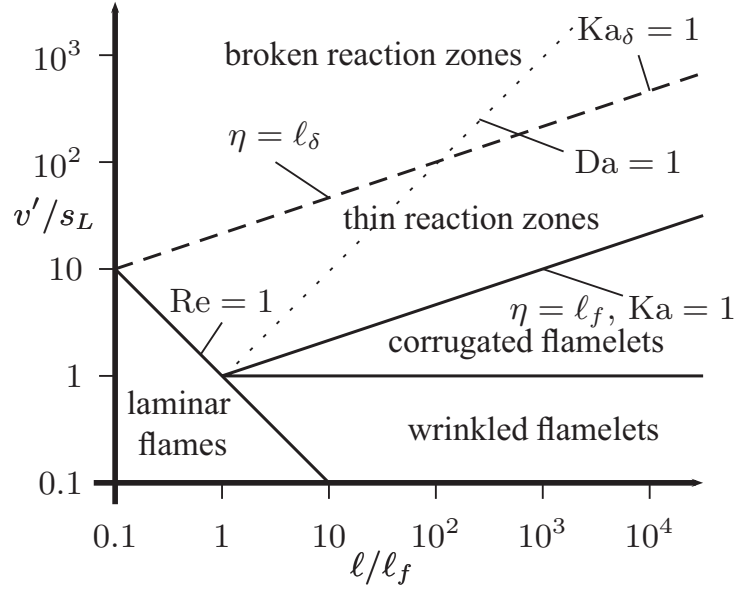


**Figure 3.8:** The combustion regime diagram according to Peters [70].

This approach of describing the propagation is required for models based on kinematic equations, for example when the Level Set approach based upon the scalar  $G$  is employed. However, there exist models where a turbulent volumetric reaction rate is sought. For these models the *flame surface density*  $\Sigma$  is an important quantity.  $\Sigma$  can be viewed as the ratio between the instantaneous flame front surface  $A_T$  and the volume containing it. Expressed in differential form it may be written as:

$$\Sigma = \frac{dA_T}{dV} \quad (3.34)$$

The volumetric reaction rate  $\dot{\omega}$  is then obtained with the mass flow rate as

$$\dot{\omega} = \rho s_L \Sigma . \quad (3.35)$$

Its unit is mass per unit volume and time.

### 3.3.2 Regimes in premixed combustion

Figure 3.8 depicts different premixed combustion regimes for fully developed turbulent flames in terms of the normalized turbulence intensity  $v'/s_L$  and the normalized turbulent length scale  $l/l_f$ . The laminar flames regime is separated from the other regimes by the turbulent Reynolds number

$$\text{Re} \equiv \frac{v'}{s_L} \frac{l}{l_f} = 1 . \quad (3.36)$$

The boundary  $v'/s_L = 1$  identifies the regime where the largest turbulent eddies with turnover velocity  $v'$  are able to interact with the advancing flame front propagating with the velocity  $s_L$ . This regime is called the *corrugated flamelets regime*. Eddies down to a size  $\ell_n$  with a turnover velocity  $v_n$  that is larger equal to  $s_L$  are active in that regime. Those eddies push the flame front around; the kinematic advance of the flame is unable to completely smooth out the corrugations that have been produced. The corresponding scale of these turbulent eddies is called the *Gibson scale*  $\ell_G$ . It may be obtained by integral quantities as (see also eqn. (2.41))

$$\frac{\ell_G}{\ell} = \left( \frac{s_L}{v'} \right)^3. \quad (3.37)$$

In the *wrinkled flamelets regime* where  $v'/s_L < 1$ , the same mechanisms are active. However here, the strongest turbulent eddies are not able to produce substantial corrugation but only minor wrinkling. In these two regimes the thickness of the flame can be regarded as small in comparison to the size of the turbulent eddies that can interact with the flame. Therefore we will assume that – viewed microscopically – the flame structure is not internally influenced by the turbulence. In this case, equation (3.30) can be used for the modeling of laminar flame propagation while it is possible to omit the curvature term on the right hand side. In comparison with the flamelet structure we will call the turbulence in these two regimes as *large scale turbulence*.

In case that the smallest turbulent eddies of the Kolmogorov size  $\eta$  become so small that they start to interact with the laminar flame structure, the *thin reaction zones regime* is reached. The boundary that separates this regime from the corrugated flamelets regime is determined by the turbulent Karlovitz number

$$\text{Ka} \equiv \frac{\ell_f^2}{\eta^2} = 1. \quad (3.38)$$

By assuming equal diffusivities  $\nu = D$  and replacing  $\eta$  in the equation above by eqn. (2.42) we can express Ka in terms of  $\ell_f$ ,  $s_L$ , and the turbulent dissipation  $\varepsilon$ . With  $\varepsilon \propto v'^3/\ell$  for constant values of Ka the following relationship is obtained:

$$\left( \frac{s_L}{v'} \right)^3 \propto \frac{\ell_f}{\ell}. \quad (3.39)$$

In this regime we will assume that the equation (3.30) is valid including the curvature term on the right hand side. The turbulence in this regime will henceforth be characterized as *small scale turbulence*. The correct position of the line for  $\text{Ka} = 1$  in the combustion diagram can be obtained by the general equation for Ka:

$$\text{Ka} = \left( \frac{v'}{s_L} \right)^{\frac{3}{2}} \left( \frac{\ell}{\ell_f} \right)^{-\frac{1}{2}}. \quad (3.40)$$

The range of the thin reaction zones regime extends up to the region where the smallest turbulent eddies are of comparable size to the thickness of the inner layer  $\ell_\delta$ .



This boundary then corresponds to a Karlovitz number  $Ka_\delta \equiv Ka (\ell_\delta/\ell)^2 = 1$ . With the approximation  $\ell_\delta/\ell_f \approx 0.1$  taken from the combustion diagram of *Poinsot et al.* [79] this gives  $Ka \approx 100$ .

Above that boundary the turbulent eddies can perturb the reaction zone to such an extent that it is torn apart and partially quenched. At such turbulence intensities there is no premixed flamelet structure. This regime is called *broken reaction zones*. Depending on the boundary conditions, the premixed mixture is either stochastically quenched or behaves like a perfectly stirred reactor.

Another important quantity is the Damköhler number  $Da$  which is defined as the ratio of the integral turbulent eddy turnover time to the chemical flame time. Based on quantities of the combustion diagram, it reads:

$$Da = \frac{s_L}{v'} \frac{\ell}{\ell_f} = \frac{Re^{\frac{1}{2}}}{Ka} . \quad (3.41)$$

This quantity is no regime separator in the combustion diagram. However, it is a very important quantity in turbulent burning velocity modeling. It will be discussed in the following sections.

### 3.3.3 Approaches to modeling the turbulent burning velocity

In this section, we will discuss asymptotic limits of possible turbulent burning velocity approximations. In the limit  $Re \rightarrow \infty$ , *Damköhler* [16] distinguished two limits between which premixed turbulent flame propagation takes place: The limit of large and small scale turbulence. With regards to the combustion regimes discussed in the previous section, large scale turbulence would correspond to a limit in the wrinkled and corrugated flamelets regime on the one hand, and small scale turbulence to a limit in the thin reaction zones regime.

In the limit of large scale turbulence, *Damköhler* postulated the turbulent burning velocity to be proportional to the turbulence intensity,

$$s_T \propto v' . \quad (3.42)$$

In this case, the turbulence intensity would be the turbulent flame surface area producing effect. The surface reducing effect which has to balance production is assumed to be kinematically driven by the spatial propagation of the laminar flamelet and therefore called *kinematic restoration*.

On the other hand, in the limit of small scale turbulence, the ratio between the turbulent burning velocity and the laminar flame speed is assumed to be proportional to the square root of the ratio between turbulent diffusivity and laminar heat conductivity (or flame diffusivity):

$$\frac{s_T}{s_L} \propto \sqrt{\frac{D_t}{D_0}} . \quad (3.43)$$

The latter relationship takes into account that there is an interaction of turbulent eddies with the preheat zone of the flamelet structure which in turn enhances mixing for heat and radicals and transport into the unburnt. The relationship is postulated in analogy to the expression (3.6) for laminar flames. As becomes clear below, also the turbulence intensity is the flame front producing effect in this limit, but here the flame front is reduced by *scalar dissipation*. It needs to be noted that with  $D_t \propto v' \ell$  eqn. (3.43) gives  $s_T \propto v'^{1/2}$ . Therefore, in small scale turbulence, the increase in burning velocity with respect to turbulence intensity is attenuated as in comparison to the large scale turbulence expression (3.42). This behavior is called *bending effect*.

Examination of the compilation of experimental results by *Abdel-Gayed et al.* [1] for large scale turbulence ( $Re \rightarrow \infty$  and  $v'/s_L \rightarrow \infty$ ) indicates the following relationship:

$$s_T - s_L = b_1 v' \quad \text{with} \quad b_1 = 2.0 . \quad (3.44)$$

For small scale turbulence, we postulate

$$\frac{s_T - s_L}{s_L} = b_3 \left( \frac{D_t}{D_0} \right)^{1/2} . \quad (3.45)$$

Both expressions are defined in such a way to yield consistent expressions for  $s_T$  in the limit of vanishing turbulence  $v' \rightarrow 0$ .

The constant  $b_3$ , however, still needs to be determined. DNS simulations by *Wenzel* [105, 106] indicate a variation of  $b_3$  from 0.95 to approx. 1.2 depending on Reynolds and Damköhler number with a mean of  $b_3 = 1.07$ . The predictions tend to 1.0 for large Reynolds numbers what is also Damköhler's assumption. From this point,  $b_3 = 1.0$  appears to be a good choice. Using

$$D_t = a_4 v' \ell , \quad (3.46)$$

eqn. (3.8), and introducing the turbulent flame surface area ratio by means of (3.33) we can rearrange (3.44) and (3.45):

$$\tilde{\sigma}_t = b_1 \frac{v'}{s_L} \quad \text{and} \quad \tilde{\sigma}_t^2 = a_4 b_3^2 \frac{\ell}{\ell_f} \frac{v'}{s_L} . \quad (3.47)$$

In both equations the effect of kinematic restoration is expressed as  $s_L \tilde{\sigma}_t$  and scalar dissipation as  $D \tilde{\sigma}_t^2$ , respectively.

Since these two expressions only give expressions for the (normalized) turbulent burning velocity in two limits, a combined expression is sought that yields a continuous transition from the one limit to the other. Following the arguments above, the turbulence intensity is identified as the driving force of flame surface production for both limits. On the other hand, the destruction term of flame surface area can be decomposed into a contribution due to kinematic restoration and another one to scalar dissipation. Combining both equations leads to the quadratic equation

$$\frac{\tilde{\sigma}_t^2}{a_4 b_3^2} \frac{\ell_f}{\ell} + \frac{\tilde{\sigma}_t}{b_1} = \frac{v'}{s_L} . \quad (3.48)$$

The physically only possible solution of this equation – expressed in terms of the turbulent burning velocity normalized against the turbulence intensity and the Damköhler number  $Da$  (3.41) – is:

$$\frac{\Delta s}{v'} \equiv \frac{s_T - s_L}{v'} = \tilde{\sigma}_t \frac{s_L}{v'} = -\frac{a_4 b_3^2}{2b_1} Da + \sqrt{\left(\frac{a_4 b_3^2}{2b_1} Da\right)^2 + a_4 b_3^2 Da} . \quad (3.49)$$

This relationship was found by *Peters* [71]. All constants are summarized in table 3.2 on page 53.

The expression (3.49) for the normalized turbulent burning velocity is a function of  $Da$  and not of the Karlovitz number  $Ka$ . If one took the remarks in section 3.3.2 into account, a function in terms of  $Ka$  instead of  $Da$  would be more appropriate. In view of eqn. (3.41) this would require introducing the Reynolds number  $Re$ . However, we want to employ a turbulent combustion model here that is compatible to a turbulence model which is based on integral scales, and which is independent of the Reynolds number. Additionally, a set of model coefficients for such a Reynolds-dependent approach would require a database of DNS results over a wide range of Reynolds numbers that are not available at present. The Damköhler number is based on integral scales, hence independent from the Reynolds number.

At last, it needs to be noted that the expression (3.49) is only valid for fully developed flames. For developing or instationary flames, a modified expression needs to be found. For example, in spark ignition problems, the flame is initiated as a small laminar-like kernel that at first propagates with a velocity close to the laminar flame speed. In equation (3.49), however, no measure for the development of the flame is included and thus with this expression a too high flame speed is predicted for the early spark kernel. As a consequence, in the following sections this expression will be modified in order to account for the magnitude of flame development.

### 3.4 Progress variable approaches

It is very appealing to formulate a model for the description of turbulent flame propagation that is based on a progress variable approach, because the fractions of burnt and unburnt gases in the flow problems can be calculated very easily, and the source term in the transport equation for the progress variable can also very easily be linked to the heat release.

In terms of the laminar flamelet structures, the flamelet progress parameter  $c$  can be defined as a nondimensional temperature

$$c \equiv \frac{T - T_u}{T_b - T_u} , \quad (3.50)$$

or as the mass fraction of the product species  $Y_p$  over the possible maximum mass fraction in the burnt  $Y_{p,b}$ :

$$c \equiv \frac{Y_p}{Y_{p,b}} . \quad (3.51)$$

Other definitions of  $c$  slightly differ from these two approaches presented, f. ex. by additionally taking into account equilibrium chemistry.

$c$  represents a nondimensional coordinate for a premixed flamelet. It may therefore replace the normal coordinate  $x_n$  in the flamelet equations (3.2-3.3) as introduced in section 3.1.2.  $c$  must be monotonic, that is, in the reference frame of the flamelet

$$\frac{\partial c}{\partial x_n} \geq 0 . \quad (3.52)$$

In analogy to (2.3) the conservation equation for the flamelet progress variable reads

$$\frac{\partial \rho c}{\partial t} + \nabla \cdot (\rho \vec{u} c) = \nabla \cdot (\rho D \nabla c) + \dot{\omega}_c , \quad (3.53)$$

where  $\dot{\omega}_c$  is the reaction rate of the premixed flamelet for a given  $c$ . We will derive in the following a conservation equation for the Favre average  $\tilde{c}$ . This equation will also need an average for the reaction rate.

Favre averaging leads to a transport equation for the mean progress variable

$$\tilde{c} = \frac{\tilde{Y}_p}{\tilde{Y}_{p,b}} \quad (3.54)$$

that reads

$$\langle \rho \rangle \frac{\partial \tilde{c}}{\partial t} + \langle \rho \rangle \tilde{\vec{u}} \cdot \nabla \tilde{c} = \nabla \cdot \left( \frac{\mu_t}{Pr_t} \nabla \tilde{c} \right) + \langle \dot{\omega}_c \rangle . \quad (3.55)$$

For the mean reaction rate  $\langle \dot{\omega}_c \rangle$ , a model closure is required.

### 3.4.1 The Eddy-Breakup-Model

A possible closure for  $\langle \dot{\omega}_c \rangle$  is the Eddy-Breakup-Model (EBU model) [94, 95]. It relates the average reaction rate to the inverse of the integral turbulent time scale  $\tau_t \equiv k/\varepsilon$ ,

$$\langle \dot{\omega}_c \rangle = C_{\text{EBU}} \langle \rho \rangle \frac{\varepsilon}{k} \tilde{c}(1 - \tilde{c}) . \quad (3.56)$$

The maximum of the reaction rate occurs therefore at  $\tilde{c} = 1/2$ .  $C_{\text{EBU}}$  is a modeling constant.

The EBU model estimates the mean reaction rates without the inclusion of chemical kinetics and the laminar burning velocity. Since the influence of turbulence is only considered by using integral time scales and not by ratios of turbulent to chemical time and length scales, this model is unable to capture the interaction of the flow with chemistry.

Close to a wall, the turbulent time scale  $\tau_t$  will tend to zero because  $k \rightarrow 0$  for the wall distance  $y \rightarrow 0$  [81]. In that limit  $\langle \dot{\omega}_c \rangle$  predicted by the EBU tends to infinity which means that the turbulent flame is accelerated close to walls. Therefore without appropriate wall modeling, the EBU gives inconsistent predictions in near wall regions.

Despite these defects, this model is widely used, especially in industrial design processes because of its attractive simplicity. In these cases the model factor  $C_{\text{EBU}}$  is varied in order to obtain acceptable numerical predictions.

### 3.4.2 The Bray-Moss-Libby Model

While the EBU model is independent of chemistry, the Bray-Moss-Libby (BML) [10] model belongs to the class of flamelet models. It assumes an inner structure of the underlying laminar flamelet. Next to the reaction rate  $\langle \dot{\omega}_C \rangle$  the probability function  $p(c, \vec{x})$  of finding an instantaneous flamelet progress is employed. This pdf consists essentially of two delta peaks for finding the unburnt and burnt state, and of a functional expression  $f$  for finding the reacting flamelet:

$$p(c, \vec{x}) = \begin{cases} \alpha(\vec{x}) & \text{for } c = 0 \\ \beta(\vec{x}) & \text{for } c = 1 \\ (1 - \alpha(\vec{x}) - \beta(\vec{x}))f(c, \vec{x}) & \text{for } 0 < c < 1 . \end{cases} \quad (3.57)$$

Starting from there, two different formulations for the mean reaction have been established in literature. The first one is based on postulating an expression for the scalar dissipation, the other one employs flame crossing frequencies.

#### Scalar dissipation formulation

By means of the pdf approach (3.57), a reaction rate balanced progress variable

$$c_m \equiv \frac{\int_0^1 c \dot{\omega}_c(c) f(c) dc}{\int_0^1 \dot{\omega}_c(c) f(c) dc} \quad (3.58)$$

represents one input of the flamelet chemistry into the turbulent reaction rate model. For the simple BML model, we get:

$$\langle \dot{\omega}_c \rangle = \frac{\langle \rho \rangle \tilde{\chi}_c}{2c_m - 1} . \quad (3.59)$$

Here  $\tilde{\chi}_c$  is the scalar dissipation of  $c$ , which is commonly modeled as

$$\tilde{\chi}_c = \frac{\varepsilon}{k} \tilde{c}'^2 . \quad (3.60)$$

If no equation for the variance of  $c$ , that is  $\tilde{c}'^2$ , is solved for, this quantity is also modeled:

$$\tilde{c}'^2 = \tilde{c}(1 - \tilde{c}) . \quad (3.61)$$

In this form the BML model is – apart from the constant  $C_{\text{EBU}}$  – equal to the EBU model.

### Flame crossing frequency formulation

This formulation is based on the assumption that for developed turbulent flames the mean reaction rate is more dependent on the frequency of passing the instantaneous flame front at a given point within the turbulent fluctuating flame than the chemistry of the laminar flamelet. Then the mean reaction rate is determined to

$$\langle \dot{\omega}_c \rangle = \dot{\omega}_c f_c , \quad (3.62)$$

where  $f_c$  is an expression for the flame crossing frequency times the probability to be within the the reacting flame and  $\dot{\omega}_c$  the reaction rate per flame crossing

$$\dot{\omega}_c = \frac{\rho_0 s_L^0}{\ell_f / t_t} \quad (3.63)$$

with  $t_t$  being the time to cross the flame.

With a suitable assumption for  $f_c$  [78] the mean reaction rate finally is given by:

$$\langle \dot{\omega}_c \rangle = 2 \frac{\rho_0 s_L^0}{\ell_f / t_t} \frac{\varepsilon}{k} \tilde{c}(1 - \tilde{c}) . \quad (3.64)$$

In practice it is difficult to determine  $f_c$  or  $t_t$  appropriately [78]. If one assumes for the transit time  $t_t$  the relationship  $t_t = \ell_f / s_L^0$  again an EBU type of reaction rate is recovered.

### 3.4.3 Flame Surface Models

The request to determine the mean reaction rate without tuning the model constant(s) and expressions in the EBU or BML models led to the class of the so-called flame surface models. Here the mean reaction rate is determined by the laminar mass burning rate ( $\rho s_L^0$ ), a stretch factor  $I_0$  [9], and the flame surface density  $\Sigma$  as defined in (3.34):

$$\langle \dot{\omega}_C \rangle = (\rho s_L^0) I_0 \Sigma . \quad (3.65)$$

For the flame surface area, a conservation equation is being solved for:

$$\langle \rho \rangle \frac{\partial \Sigma}{\partial t} + \langle \rho \rangle \tilde{u} \cdot \nabla \Sigma = \nabla \cdot \left( \left[ \frac{\mu_t}{Sc_t} + \frac{\mu}{Sc} \right] \nabla \Sigma \right) + \alpha_0 \frac{\varepsilon}{k} \langle \rho \rangle \Sigma - \langle \rho \rangle D \quad (3.66)$$

The convective and diffusive terms can be identified in analogy to regular transported scalars. The second term on the r.h.s. models production, with  $\alpha_0$  being a model parameter, and is given in a form here in common with most flame surface models [78]. The last term on the right hand side describes dissipation of flame surface density in which the destruction  $D$  varies for different model variants. In many of these models,

$$D \propto \Sigma^2 . \quad (3.67)$$

As can be seen in this model example, only local flamelet parameters are used in order to close the reaction term. That means that no spatial gradients of the mean progress variable are employed. In this model, the thickness of the turbulent flame is not used. It could be evaluated, however, for example by  $|\nabla c|^{-1}$ .

For an infinitely thin flame, the gradient  $|\nabla c|$  tends to infinity. On a numerical grid with a finite resolution, such a gradient cannot correctly be evaluated. Additionally the source term  $\langle \dot{\omega}_c \rangle$  becomes a delta peak, which can cause numerical inaccuracies in predicting the correct flame propagation. This also holds for thin flames if those thicknesses are smaller than the computational grid size, with the implication that the model in this limit is not grid independent. Either artificial thickening of the flame or grid refinement is required.

We conclude therefore that a combustion model, based on a turbulent burning velocity approach as discussed in section 3.3.3 is not recommended to be used in conjunction with a progress approach based flamelet model, because a consistent flame propagation prediction in the regime of laminar flames is not feasible. Additionally, we will see in the following sections that another important parameter for the turbulent burning velocity is the thickness of the turbulent flame brush. This quantity cannot correctly be evaluated in all possible cases by means of a progress variable approach.

As a consequence, a turbulent flamelet approach is required that can return reliable information on flame thicknesses not only for fully turbulent flames, but also in the limit of laminar structures. Such requirements can be met by employing Level Sets.

### 3.5 The Level Set approach

In the following, we will derive kinematic equations for both the position of the mean flame front and the thickness of the flame brush. First an appropriate averaging procedure has to be defined for this. A suitable averaging procedure has already been introduced by *Oberlack et al.* [63] for incompressible fluids. In this averaging procedure the probability of finding the flame surface of the underlying flamelet structure is required. Any reference position  $x_n$  of the premixed flamelet could be used, but it is particularly useful to employ the  $x_n = x_0$  surface. The reaction zone in premixed flamelets with a finite thickness represents then the reference.

For the coupling of the premixed combustion modeling equations with the equations of the mean flow, the mean species distribution is needed. Since these equations are formulated for a compressible flow and therefore Favre averaged (see also sections 2.2.1 and 2.3) the averaging procedure mentioned above needs to be suitably extended for compressibility.

As a clarifying example, an infinitely thin flame sheet may be discussed. In this case, only the thermodynamical states of the burnt and the unburnt gas composition are relevant. Here,  $f_b$  be the *volumetric* probability of finding burnt gas. In order to obtain the mean species distribution  $\tilde{Y}_i$ ,  $f_b$  must be mass weighted by

$$\langle \rho \rangle \tilde{Y}_i = \rho_u Y_{i,u} (1 - f_b) + \rho_b Y_{i,b} f_b . \quad (3.68)$$

For the mean density we obtain

$$\langle \rho \rangle = \rho_u(1 - f_b) + \rho_b f_b . \quad (3.69)$$

From a numerical point of view the *mass averaged* probability  $\tilde{P}_b$  is an important quantity. It can be determined to

$$\tilde{P}_b = \frac{\rho_b f_b}{\rho_b f_b + \rho_u(1 - f_b)} \quad (3.70)$$

as the mass fraction of burnt gases to the total sum of combustible gases. It is therefore equal to the progress variable  $\tilde{c}$  defined in section 3.4.

As for CFD, it has been found desirable to define the mean flame front position where  $\tilde{P}_b = 1/2$  and not where  $f_b = 1/2$  which is also possible.

The volumetric averaging as conducted in [63] reads:

$$\langle\langle \vec{x}_f \rangle\rangle \equiv \iiint_{-\infty}^{+\infty} \vec{x}_f P(\vec{x}_f) d\vec{x}_f . \quad (3.71)$$

Here  $\langle\langle \vec{x}_f \rangle\rangle^1$  denotes the position of the volumetrically averaged flame front,  $\vec{x}_f$  an instantaneous realization of the flame front position, and  $P(\vec{x}_f)$  the probability of finding the instantaneous position in 3D-space of the  $x_n = x_0$  position in flamelet space. As we can see from that definition the mean flame front position would be with this kind of averaging at the volumetric probability  $f_b = 1/2$ . This is also a formally correct approach of postulating model equations, but in numerical simulations with a CFD code using compressible equations of fluid dynamics, it has proven to be less accurate. This can be attributed to the fact that with volumetric averaging, a broadening of the turbulent flame brush causes the mass of the gases to move towards the burnt gas composition since the unburnt gas has a higher density than the burnt. This again causes finally a movement of the mean flame front position.

With mass weighted averaging, on the other hand, this movement is avoided because at the mean flame front the averaged masses of burnt and unburnt gas are equal. Therefore, the masses of burnt and unburnt gases are balanced on both sides of the mean flame front by means of this approach and a mean flame front movement due to flame brush broadening is avoided.

### 3.5.1 Unclosed mean flame front position equation

The goal in this section is to derive a kinematic equation for the mean flame front position. As in laminar combustion, we will employ an equation of level set type that

---

<sup>1</sup>For better typesetting and understanding of wide expressions, here the symbol “ $\langle\langle \rangle\rangle$ ” is used instead of the symbol “ $\hat{\phantom{x}}$ ” as introduced in [63] for the averaging operation of level set related expressions.



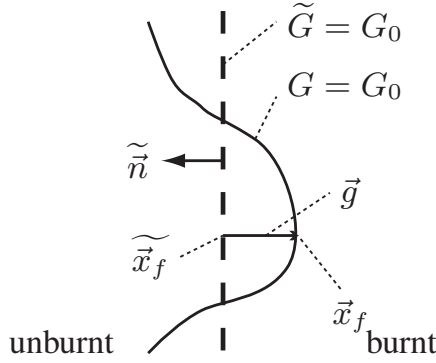


**Figure 3.9:** Fluctuating and mean flame front position.

will have a similar form as equation (3.30). In contrast to the laminar field  $G$  we will introduce the field  $\tilde{G}$  and define the mean flame front position where

$$\tilde{G} = G_0 . \quad (3.72)$$

Then we will introduce mass weighted averaging by an averaging procedure in the spirit of eqn. (3.71):

$$\langle \rho \rangle \tilde{x}_f \equiv \langle \langle \rho \vec{x}_f \rangle \rangle \equiv \iiint_{-\infty}^{+\infty} \rho(\tilde{x}_f | \vec{x}_f) \vec{x}_f P(\vec{x}_f) d\vec{x}_f . \quad (3.73)$$

That means that eqn. (3.72) is valid exactly where  $\vec{x} = \tilde{x}_f$ . Here for both the mass weighted flame front position  $\tilde{x}_f$  and the level set field (3.72) the symbol “ $\sim$ ” as for Favre averaging is employed in order to indicate an averaging procedure. This should not be mistaken as Favre averaging as it was presented in section 2.2.1. As Oberlack [63] has pointed out, an averaging procedure in the form  $G = \tilde{G} + G'$  is not possible because  $\tilde{G}$  is not *per se* defined outside of  $G_0$ . In (3.73), the density  $\rho(\tilde{x}_f | \vec{x}_f)$  denotes the instantaneous density at the mean flame front position  $\tilde{x}_f$  conditioned on the position of the fluctuating flame front  $\vec{x}_f$ . Therefore, except for  $\vec{x}_f$ , only quantities on the  $\tilde{G} = G_0$  iso-surface are employed.

This averaging procedure appears to contradictory since in order to determine the density  $\rho(\tilde{x}_f | \vec{x}_f)$ , already the averaged position of  $\tilde{x}_f$  is needed. However, this approach allows for a density weighted averaging procedure while at the same time the averaging constraints [63] are met. Secondly, with eqn. (3.73),  $\tilde{P}_b = 1/2$  for thin flames exactly where  $\tilde{G} = G_0$ .

It is apparent that there exist global curvature effects in turbulent flames that need to be modeled. Shepherd and Cheng [90], in order to consider these effects, distinguished between the turbulent consumption speed  $S_C$  – as a correspondence to the turbulent

burning velocity – and a displacement speed  $S_D$  that accounts for a net flux of burnt gases into the unburnt or vice versa for spherical flame shapes. Lee and Lee [52] employed a correction method in their experimental data processing in order to render the results for turbulent flame speed independent from the globally curved flame produced in the experimental burner. Even though the qualitative phenomenon is reported in the literature, quantitative estimations are not found.

In terms of the implications for the equation of the mean flame front positions, these curvature effects were first introduced into the equation for  $\tilde{G}$  in [69], but they were not considered in [63]. In order to derive a kinematic equation of  $\tilde{G}$  on the mean flame front position that also accounts for these mean turbulent curvature effects, the correlation of velocity and flame front fluctuations needs again to be accounted for.

In fig. 3.9, the vector  $\vec{g}$  is introduced as the distance between  $\vec{x}_f$  and  $\widetilde{\vec{x}}_f$ . With

$$\vec{g} \equiv \vec{x}_f - \widetilde{\vec{x}}_f \quad (3.74)$$

and the euclidean norm of  $\vec{g}$

$$g \equiv -\text{sign}(G) |\vec{g}| \quad (3.75)$$

we can define a Level Set  $G^*$  on the mean flame front  $\tilde{G} = G_0$  accounting for the front fluctuations:

$$G^* \equiv \tilde{G} + g . \quad (3.76)$$

This Level Set  $G^*$  is independent of the definition for  $\tilde{G}$  and  $G$  outside of the mean flame front. However, we impose that  $G^*$  satisfies the distance constraint  $|\nabla G^*| = 1$  outside of  $\tilde{G} = G_0$ . The starting point then is the substantial derivative of  $G^*$ :

$$\frac{DG^*}{Dt} = 0 \quad \Rightarrow \quad \frac{\partial G^*}{\partial t} + \nabla G^* \cdot \frac{d\vec{x}_f}{dt} = 0 . \quad (3.77)$$

Inserting (3.26) into the latter and using a suitable velocity decomposition

$$\frac{d\vec{x}_f}{dt} = \tilde{\vec{u}} + \widetilde{\vec{u}''} + s_L(\kappa) \vec{n} \quad (3.78)$$

yields after a multiplication with the density and after averaging:

$$\langle \rho \rangle \frac{\partial \tilde{G}}{\partial t} + \langle \rho \rangle \nabla \tilde{G} \cdot \tilde{\vec{u}} + \langle \rho \rangle \widetilde{\nabla g \cdot \vec{u}''} + \nabla \tilde{G} \cdot \langle \langle \rho(s_L(\kappa) \vec{n}) \rangle \rangle = 0 . \quad (3.79)$$

The last two terms on the left hand side of this equation still remain unclosed. The third term on the left hand side appears as a common turbulent transport term that is modeled with a turbulent diffusion type of approach for conventional scalars. Such a modeling is not feasible here since this would imply an information transport from the  $\tilde{G}$  field outside of  $G_0$  that violates the generalized scaling symmetry of the  $G$ -equation as discussed in [63]. Only information transport tangential to the mean flame front surface is allowed for. On the other hand, this term can only be oriented normal to the

flame surface. Modeling approaches that take this constraint into account are discussed in section 3.5.3.

The last term on the l.h.s. is the turbulent flame propagation term expressing the flame propagation by the turbulent burning velocity:

$$\langle\langle \rho s_L(\kappa) \vec{n} \rangle\rangle = (\rho s_T) \tilde{\vec{n}} . \quad (3.80)$$

In this context  $\tilde{\vec{n}}$  is the normal of the mean flame front as shown in fig. 3.9. It is defined in analogy to (3.28) as

$$\tilde{\vec{n}} = - \frac{\nabla \tilde{G}}{|\nabla \tilde{G}|} . \quad (3.81)$$

This definition is feasible since it does not violate the symmetries of the  $G$ -equation. Provided that  $\tilde{G}$  is continuous and monotonic in that region  $\tilde{\vec{n}}$  does not change its direction on the mean flame front surface independent from the definition of  $\tilde{G}$  outside of the flame front.

The numerical procedure, as will be outlined in the following chapter and in appendix B, ensures that  $|\nabla \tilde{G}| = 1$ , which will therefore vanish, if that procedure is applied. However, for consistency, this gradient is still taken account of where required in case that a different numerical procedure is employed that does not strictly guarantee  $|\nabla \tilde{G}| = 1$ .

In view of

$$\frac{\partial \tilde{G}}{\partial t} + \nabla \tilde{G} \cdot \frac{d\tilde{\vec{x}}_f}{dt} = 0 , \quad (3.82)$$

the kinematic equation for  $\tilde{\vec{x}}_f$  is finally determined by comparison with (3.79) as

$$\frac{d\tilde{\vec{x}}_f}{dt} = \tilde{\vec{u}} + (\nabla \tilde{g} \cdot \tilde{\vec{u}}'') \cdot \tilde{\vec{n}} + \frac{(\rho s_T)}{\langle \rho \rangle} \tilde{\vec{n}} . \quad (3.83)$$

### 3.5.2 Unclosed equation for the flame brush thickness

The turbulent flame brush thickness  $\ell_{f,t}$  is defined as the square root of the variance  $\widetilde{G''^2}$  of the  $G$ -equation:

$$\ell_{f,t} \equiv \frac{\sqrt{\widetilde{G''^2}}}{|\nabla \tilde{G}|} . \quad (3.84)$$

The averaging operator that yields the variance is valid on the mean flame front position only. It can be defined in analogy to (3.73) as:

$$\langle \rho \rangle \widetilde{G''^2} \equiv \langle\langle \rho g^2 \rangle\rangle = \int_{-\infty}^{+\infty} \int \int \rho(\tilde{\vec{x}}_f | \bar{\vec{x}}_f) \bar{g}^2 P(\bar{\vec{x}}_f) d\bar{\vec{x}}_f . \quad (3.85)$$

In order to derive an average of the substantial derivative of  $\bar{g}^2$  at first the following decomposition is applied:

$$\bar{g}^2 = \widetilde{G''^2} + g'' . \quad (3.86)$$

On the one hand, the substantial derivative is given as

$$\frac{D\bar{g}^2}{Dt} = \frac{\partial(\widetilde{G''^2} + g'')}{\partial t} + \nabla(\widetilde{G''^2} + g'') \cdot \frac{d(\vec{x}_f + \vec{g})}{dt} \quad (3.87)$$

After multiplying with the density and after the averaging operator we obtain

$$\langle \rho \rangle \frac{D\bar{g}^2}{Dt} = \langle \rho \rangle \frac{\partial \widetilde{G''^2}}{\partial t} + \langle \rho \rangle \nabla \widetilde{G''^2} \cdot \frac{d\vec{x}_f}{dt} + \langle \rho \rangle \nabla \widetilde{g''} \cdot \vec{u}'' + \langle \langle \rho \nabla g'' \cdot (s_L \vec{n}) \rangle \rangle . \quad (3.88)$$

On the other hand, after exercising the chain rule of differentiation, the substantial derivative gives

$$\frac{D\bar{g}^2}{Dt} = 2\bar{g} \cdot \frac{d\bar{g}}{dt} \quad (3.89)$$

and with (3.74), (3.78), and (3.83) the following relationship

$$\frac{D\bar{g}}{Dt} = \vec{u}'' + s_L \vec{n} - \left[ \frac{(\rho s_T)}{\langle \rho \rangle} + \nabla \widetilde{g} \cdot \vec{u}'' \right] \vec{n} \quad (3.90)$$

can be inserted into (3.89). Multiplying the latter equation with the density and applying the averaging operator yields

$$\langle \rho \rangle \frac{d\bar{g}^2}{dt} = \langle \langle 2\rho \bar{g} \cdot \vec{u}'' \rangle \rangle + \langle \langle 2\rho \bar{g} \cdot (s_L \vec{n}) \rangle \rangle . \quad (3.91)$$

Combining equations (3.88) and (3.91) then yields:

$$\langle \rho \rangle \frac{\partial \widetilde{G''^2}}{\partial t} + \langle \rho \rangle \nabla \widetilde{G''^2} \cdot \frac{d\vec{x}_f}{dt} + \langle \rho \rangle \nabla \widetilde{g''} \cdot \vec{u}'' + \rho \nabla \widetilde{g''} \cdot (s_L \vec{n}) = 2\rho \bar{g} \cdot \vec{u}'' + 2\rho \bar{g} \cdot (s_L \vec{n}) \quad (3.92)$$

The second term on the l.h.s. on eqn. (3.92) shows that the scalar  $\widetilde{G''^2}$  is advected not by the mean flow velocity  $\vec{u}$  but by the propagation of the mean flame front position. The last two terms on the left hand side describe turbulent transport effects that with the arguments given in the previous section can be modeled using a diffusion type approach acting tangential to the mean flame front. The first term on the right hand side describes turbulent production of  $\widetilde{G''^2}$ . Since the laminar burning velocity  $s_L$  of the second term on the right hand side is dependent on laminar flamelet curvature, this term describes the destruction of variance either due to kinematic restoration or due to scalar dissipation, depending on the magnitude of the local flamelet curvature.

It needs to be kept in mind that (3.92) is only defined at  $\vec{G} = G_0$  and an extension into the whole computational domain is required. Such an extension is discussed in the next section.

### 3.5.3 Modeling closure

In the preceding section, the kinematic equations for  $\widetilde{G}$  and  $\widetilde{G''^2}$  have been left unclosed concerning the diffusion terms, the production, and the dissipation term. In this section possible closures of these terms will be presented. At first, the kinematic equation for  $\widetilde{G''^2}$  will be closed. Then, the kinematic equation for  $\widetilde{G}$  will be closed with respect to the turbulent transport term and several possible closure approaches will be presented. Those are partially based on  $\widetilde{G''^2}$ . Finally,  $\widetilde{G''^2}$  will also be introduced into the equation for  $\widetilde{\sigma}_t$ , thereby adopting the unsteady behavior of the  $\widetilde{G''^2}$  for modeling the turbulent burning rate.

#### $\widetilde{G''^2}$ - closure

The turbulent production term in the  $\widetilde{G''^2}$ -equation will be closed assuming a classical gradient transport hypothesis by

$$\langle\langle 2\rho\vec{g} \cdot \vec{u}'' \rangle\rangle = 2 \langle\rho\rangle D_t (\nabla\widetilde{G})^2, \quad (3.93)$$

where the turbulent diffusivity  $D_t$  is related to the turbulent viscosity as

$$D_t \equiv \frac{\mu_t}{\langle\rho\rangle Sc_t}. \quad (3.94)$$

The flame brush thickness reducing term  $\langle\langle 2\rho\vec{g} \cdot (s_L\vec{n}) \rangle\rangle$  is either dominated by kinematic restoration in the corrugated flamelets regime, or by scalar dissipation in the thin reaction zones regime. In the latter case the curvature term in eqn. (3.24) becomes dominant so that

$$\langle\langle 2\rho\vec{g} \cdot (s_L\vec{n}) \rangle\rangle \approx \langle\langle 2\rho\vec{g} \cdot (-D\vec{n} \nabla \cdot \vec{n}) \rangle\rangle = \chi_G \quad (3.95)$$

showing the scalar dissipative nature of the term in this limit. Here, we will follow the unified approach by *Peters* [70] for both regimes. There, a classical approach is used, assuming a constant ratio between the turbulent mechanical and scalar time scales and thereby relating the scalar dissipation  $\chi_G$  to the turbulent dissipation  $\varepsilon$  [102, 46]. Then, this reads

$$\langle\langle 2\rho\vec{g} \cdot (s_L\vec{n}) \rangle\rangle = -c_s \langle\rho\rangle \widetilde{G''^2} \frac{\varepsilon}{k} \quad (3.96)$$

in which by calculating the turbulent and scalar spectra the constant  $c_s = 2.0$  [70] for both combustion regimes is used.

The turbulent transport terms on the l.h.s. of eqn. (3.92) are modeled by a mean gradient transport hypothesis type of approach:

$$-\langle\rho\rangle \nabla \widetilde{g'' \cdot u''} - \langle\langle \rho \nabla g'' \cdot (s_L\vec{n}) \rangle\rangle = \nabla_{||} \cdot \left( \langle\rho\rangle D_t \nabla_{||} \widetilde{G''^2} \right) \quad (3.97)$$

The  $\parallel$  subscripts on the  $\nabla$  operators indicate that spatial gradients only tangential to the mean flame front positions are considered.

Compiling all modeling closures into (3.92), we obtain:

$$\langle \rho \rangle \frac{\partial \widetilde{G''^2}}{\partial t} + \langle \rho \rangle \frac{d\widetilde{x}_f}{dt} \cdot \nabla \widetilde{G''^2} = \nabla_{\parallel} \cdot \left( \langle \rho \rangle D_t \nabla_{\parallel} \widetilde{G''^2} \right) + 2 \langle \rho \rangle D_t (\nabla \widetilde{G})^2 - c_s \langle \rho \rangle \widetilde{G''^2} \frac{\varepsilon}{k} \quad (3.98)$$

Neglecting the temporal and spatial derivatives we can derive a steady state, *algebraic* solution for  $\widetilde{G''^2}$ ,

$$2D_t (\nabla \widetilde{G})^2 = c_s \widetilde{G''^2}_{\text{alg}} \frac{\varepsilon}{k} . \quad (3.99)$$

If we solve this equation for  $\widetilde{G''^2}_{\text{alg}}$ , keeping in mind that  $D_t \propto k^2/\varepsilon$  and  $\ell_t \propto k^{3/2}/\varepsilon$ , it becomes evident that  $\widetilde{G''^2}_{\text{alg}} \propto \ell_t^2$  if  $|\nabla \widetilde{G}| = 1$ . In analogy to eqn. (3.84) we define the *algebraic flame brush thickness*

$$\ell_{f,t,\text{alg}} \equiv \frac{\sqrt{\widetilde{G''^2}_{\text{alg}}}}{|\nabla \widetilde{G}|} \quad (3.100)$$

which is as well as  $\ell_t$  a turbulent length scale, however with a different constant factor. We can conclude that for a fully developed turbulent flame in steady state, the flame brush thickness  $\ell_{f,t}$  must be proportional to the turbulent length scale  $\ell_t$ .

For unsteady turbulent flames subjected to constant turbulent intensity and length scales a flame response equation can be derived. From (3.98), only assuming spatial homogeneity, we can obtain an ordinary differential equation in time. The solution of that is:

$$\widetilde{G''^2}(t) = \widetilde{G''^2}(t=0) \exp\left(-c_s \frac{\varepsilon}{k} t\right) + \widetilde{G''^2}_{\text{alg}} \left[1 - \exp\left(-c_s \frac{\varepsilon}{k} t\right)\right] . \quad (3.101)$$

The response of  $\widetilde{G''^2}$  to changes in the turbulent length scale is therefore of the order of the turbulent eddy turnover time  $\tau_t = k/\varepsilon$ .

Outside of  $\widetilde{G} = G_0$ , it is very appealing also to employ the equation (3.98). However, it needs to be ensured that information of the flame front propagates into the domain and not vice versa, see also [63]. *Herrmann* [42], for example, has applied a so-called “redistribution” step, by which  $\widetilde{G''^2}$  is imposed to be constant normal to the flame outside of the mean flame front,

$$\nabla \widetilde{G} \cdot \nabla \widetilde{G''^2} = 0 . \quad (3.102)$$

If the latter constraint is strictly imposed, two different types of PDEs have to be simultaneously solved in the domain.

Here, we will focus on an appropriate definition of the advective term  $d\widetilde{x}_f/dt$ . If the gradients of  $\widetilde{G''^2}$  normal to the flame front are negligibly small, the only significant

component will be the mean velocity tangential to the mean flame front. In order to ensure the propagation of information normal from the mean flame front surface into the burnt and unburnt domain we will use the maximum turbulent burning velocity approximation as the transport speed of that information. In view of eqn. (3.44) we will adopt (3.78) especially for the  $\widetilde{G}''^2$  equation (3.98) such that

$$\frac{d\vec{x}_f}{dt} = \widetilde{\vec{u}} - b_1 v' \text{sign}(\widetilde{G}) \vec{n} \quad (3.103)$$

with  $\text{sign}(\widetilde{G}) = 1$  if  $\widetilde{G} > G_0$  and  $\text{sign}(\widetilde{G}) = -1$  otherwise. With this approximation of the turbulent burning velocity and curvature terms, this setting is on the mean flame front position in line with (3.78) and ensures consistent advective propagation of information. Additionally, the closed equation for  $\widetilde{G}''^2$  is independent of the laminar flamelet properties and only one type of PDE is employed inside and outside of the mean flame front.

### $\widetilde{G}$ - closure

With regards to the  $\widetilde{G}$ -equation, a closure for the turbulent transport term  $\widetilde{\nabla g \cdot u''}$  must be found. Since  $\widetilde{G}$  is a level set field variable information from outside of the mean flame front position must not be taken. Usually, the turbulent transport term will be closed using a diffusion type approach. Here, in analogy to eqn. (3.23) for laminar flames, this term will be closed as

$$\widetilde{\nabla g \cdot u''} = D'_t \widetilde{\kappa} |\nabla \widetilde{G}|, \quad (3.104)$$

where

$$\widetilde{\kappa} = \nabla \cdot \widetilde{\vec{n}} \quad (3.105)$$

is the curvature of the turbulent mean flame front. The closed transport equation therefore reads:

$$\langle \rho \rangle \frac{\partial \widetilde{G}}{\partial t} + \langle \rho \rangle \nabla \widetilde{G} \cdot \widetilde{\vec{u}} = - \langle \rho \rangle D'_t \widetilde{\kappa} |\nabla \widetilde{G}| + \widetilde{(\rho s_T)} |\nabla \widetilde{G}|. \quad (3.106)$$

Here  $D'_t$  is the effective turbulent diffusivity of the curvature term for which an appropriate closure needs to be found. In [69] and [70], the equality

$$D'_t = D_t \quad (3.107)$$

was used. From the unclosed term (3.97), a mixing length approach reads

$$D'_t = \sqrt{\frac{c_\mu c_s}{2S c_t}} \ell_{f,t} k^{1/2}. \quad (3.108)$$

Here  $\ell_{f,t}$  acts as a mixing length for the turbulent flame. The constants on the r.h.s. of eqn. (3.108) have been chosen such that the equality (3.107) is again obtained if  $\widetilde{G}''^2$

is in steady state, that is, if (3.99) is valid. Eqn. (3.106) could be defined in the whole domain. However, in order to maintain smooth gradients and a continuous  $\tilde{G}$  field everywhere, (3.106) is restricted to the mean flame front surface  $\tilde{G} = G_0$ . Everywhere else, a signed distance constraint is applied, expressed as

$$|\nabla \tilde{G}| = 1 . \quad (3.109)$$

### Turbulent Flame Surface Area Ratio

Now, for the  $\tilde{\sigma}_t$ -equation, an unsteady but algebraic expression will be introduced. The expression for  $\tilde{\sigma}_t$  (3.49) does not account for unsteady flame development effects. The development of the turbulent flame can be measured by the relationship between the turbulent flame brush thickness and the turbulent length scale, for example by the ratio

$$\ell^* \equiv \frac{\ell_{f,t}}{\ell_{f,t,\text{alg}}} . \quad (3.110)$$

The condition  $\ell^* = 0$  then refers to a laminar flame configuration,  $\ell^* = 1$  to a fully developed one. The ratio now can be appropriately accounted for by introducing  $\ell_{f,t}$  into the expressions for the turbulent burning velocity used in the equations for large and small scale turbulence, (3.44) and (3.45), respectively. For a fully developed turbulent flame, the expressions discussed in section 3.3.3 need to be recovered.

In large scale – we recall the relationship  $\tilde{\sigma}_t = b_1 v' / s_L$  for full development – two possibilities are investigated:

1. Employing dimensional analysis, *Peters* [70] suggests the scaling  $s_L \sigma \propto \ell_{f,t} \varepsilon / k$  in large scale turbulence. In there,  $\ell_{f,t}$  can be viewed as a mixing length. In order to follow that approach and determine the correct proportionality constants, we replace  $v'$  in (3.44) with aid of (3.94) and (3.108) such that

$$s_L \tilde{\sigma}_t = b_1 \left( \frac{Sc_t c_s}{3c_\mu} \right)^{\frac{1}{2}} \ell_{f,t} \frac{\varepsilon}{k} . \quad (3.111)$$

2. The other approach is again based on (3.44). In contrast to the previous approach, we employ for the turbulence intensity  $v'$  only turbulent eddies that can enter the developing turbulent flame brush. Those turbulent eddies must be equal to the thickness of the turbulent flame brush or smaller. Fundamental turbulence theory therefore suggests the scaling  $\ell^{*1/3}$ . We obtain:

$$s_L \tilde{\sigma}_t = b_1 v' \ell^{*1/3} . \quad (3.112)$$

The fundamental difference between both approaches is the exponent on  $\ell_{f,t}$ . For a fully developed flame, i.e.  $\ell^* = 1$  both approaches give the same result.



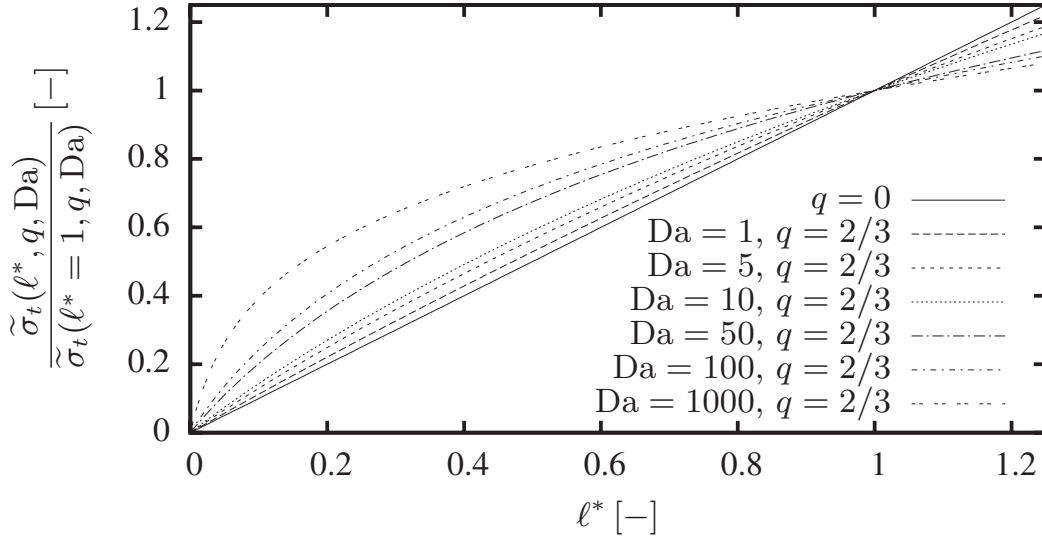


**Figure 3.10:** Plot of normalized  $\tilde{\sigma}_t$  over  $\ell^*$  for the two different values of the model parameter  $q$  as given by eqn. (3.115).

For small scale turbulence,  $D_t$  in eqn. (3.45) is replaced by using (3.99), that is, by assuming that production equals dissipation for  $\widetilde{G''^2}/(\nabla\widetilde{G})^2$ . Thus we obtain

$$D_0 \tilde{\sigma}_t^2 = b_3^2 \frac{c_s}{2} \ell_{f,t}^2 \frac{\varepsilon}{k}. \quad (3.113)$$

This equation underlines the assumption that in the small scale turbulence regime the total average flame surface area balance is controlled by scalar dissipation.

If we carry out the same algebra as in section 3.3.3 using any of the two approaches in the large scale turbulence limit, a modified expression for  $\tilde{\sigma}_t$  is obtained:

$$\tilde{\sigma}_t = -\frac{b_3^2}{4b_1} \sqrt{\frac{3c_\mu c_s}{Sc_t} \frac{\ell_{f,t}}{\ell_f} \ell^{*q}} + \sqrt{\frac{b_3^4}{16b_1^2} \frac{3c_\mu c_s}{Sc_t} \frac{\ell_{f,t}^2}{\ell_f^2} \ell^{*2q} + \frac{c_s b_3^2}{2s_L \ell_f} \ell_{f,t}^2 \frac{\varepsilon}{k}}. \quad (3.114)$$

With the Damköhler number reintroduced, this equation can also be expressed in an analogous form to eqn. 3.49 as

$$\frac{\Delta s}{v'} = -\frac{a_4 b_3^2}{2b_1} Da \ell^{*q+1} + \sqrt{\left(\frac{a_4 b_3^2}{2b_1} Da \ell^{*q+1}\right)^2 + a_4 b_3^2 Da \ell^{*2}}. \quad (3.115)$$

Unsteady effects are accounted for by introducing  $\ell_{f,t}$ . For  $\ell_{f,t} = 0$ ,  $s_T = s_L$  is obtained. If eqn. (3.111) is used, this results in  $q = 0$  with the implication that the turbulent flame surface area as determined by (3.114) is linearly proportional to the flame brush thickness, regardless of Damköhler number. On the other hand, with (3.112),  $q = 2/3$ , and the bending over  $\ell_{f,t}$  is hyperbolic and dependent on Da. The relationship of  $\tilde{\sigma}_t$  on  $\ell^*$  is plotted normalized in figure 3.10 for both model parameters

$q = 0$  and  $q = 2/3$ . It can be seen that for  $q = 2/3$ , it is predicted that a higher increase in turbulent flame surface area is achieved already for small thicknesses of the turbulent flame than for an almost fully developed flame where  $\ell^* \approx 1$ , especially for large Damköhler numbers. However, the linear proportionality between the turbulent flame surface area ratio and the turbulent flame brush thickness is also obtained for  $q = 2/3$  if  $\text{Da} \rightarrow 0$ .

### 3.5.4 A dynamical equation for the flame surface area ratio

In the previous sections, algebraic expressions for the flame surface area ratio were derived. In previous works (see eg. [71]) the algebraic expression (3.49) was obtained as the steady-state result of a transport equation with partial derivatives in space and time.

That exact dynamical transport equation for the – however, unclosed – flame surface area ratio can be derived [48],

$$\frac{\partial \langle \sigma \rangle}{\partial t} + \langle \vec{v} \cdot \nabla \sigma \rangle = - \underbrace{\langle \vec{n} \cdot \nabla \vec{v} \cdot \vec{n} \sigma \rangle}_{\langle \Pi \rangle} + s_L \underbrace{\langle (\kappa \sigma + \nabla^2 G) \rangle}_{-\langle \Omega \rangle} - D \underbrace{\langle (\nabla \cdot (\kappa \nabla G) + \kappa^2 \sigma) \rangle}_{\langle X \rangle}, \quad (3.116)$$

where  $\langle \Pi \rangle$  is the mean turbulent production term,  $\langle \Omega \rangle$  the mean influence of kinematic restoration, and  $\langle X \rangle$  the mean scalar dissipation of flame surface area. This equation defies direct closure of the production and dissipation terms. In order to overcome this difficulty *Peters* [70] derived a transport equation for  $\tilde{\sigma}_t$  by means of partial differential equation expressions. These have been obtained in the corrugated flamelets regime from the steady state expression (3.111) to

$$\frac{d\tilde{\sigma}_t}{\tilde{\sigma}_t} = \frac{d\varepsilon}{\varepsilon} - \frac{dk}{k} + \frac{1}{2} \frac{d\widetilde{G''^2}}{\widetilde{G''^2}} \quad (3.117)$$

and in the thin reaction zones regime by means of (3.113) to

$$2 \frac{d\tilde{\sigma}_t}{\tilde{\sigma}_t} = \frac{d\varepsilon}{\varepsilon} - \frac{dk}{k} + \frac{d\widetilde{G''^2}}{\widetilde{G''^2}}. \quad (3.118)$$

With the transport equations for  $k$ ,  $\varepsilon$ ,  $\widetilde{G''^2}$ , and eqn. (3.84) a dynamical equation for  $\tilde{\sigma}_t$  for both combustion regimes reads

$$\begin{aligned} \langle \rho \rangle \frac{\partial \tilde{\sigma}_t}{\partial t} + \langle \rho \rangle \tilde{\vec{u}} \cdot \nabla \tilde{\sigma}_t &= \nabla_{||} \cdot (\langle \rho \rangle D_t \nabla_{||} \tilde{\sigma}_t) + c_0 \mathcal{P} \frac{\tilde{\sigma}_t}{k} \\ &+ c_1 \langle \rho \rangle \frac{D_t \tilde{\sigma}_t}{\ell_{f,t}^2} - c_2 \langle \rho \rangle \frac{s_L^0 \tilde{\sigma}_t^2}{\ell_{f,t}} - c_3 \langle \rho \rangle \frac{D \tilde{\sigma}_t^3}{\ell_{f,t}^2} \end{aligned} \quad (3.119)$$

| Symbol | Value | definition/origin   |
|--------|-------|---|
| $a_1$  | 0.37  | $\varepsilon = a_1 v'^3 / \ell$ , Bray [9]                |
| $a_4$  | 0.78  | $= 9c_\mu / (4Sc_t a_1)$ since $D_t = a_4 v' \ell$        |
| $b_1$  | 2.0   | experimental data [1]                                     |
| $b_3$  | 1.0   | experimental data [16]                                    |
| $c_0$  | 0.44  | $= C_{\varepsilon_1} - 1$ , [70]                          |
| $c_1$  | 4.63  | DNS, [106]  |
| $c_2$  | 1.01  | $= \sqrt{\frac{3c_\mu c_s}{4Sc_t} \frac{c_1 b_3^2}{b_1}}$ |
| $c_3$  | 4.63  | $= c_1 / b_3^2$   |
| $c_s$  | 2.0   | [69, 70]  |
| $Sc_t$ | 0.70  | analog to $Pr_t$ for the enthalpy equation                |

**Table 3.2:** Constants for the level set based turbulent premixed combustion model used in this work.

with  $\mathcal{P}$  being the turbulent production (2.54) due to mean velocity gradients. The model constants  $c_0$ ,  $c_1$ ,  $c_2$ , and  $c_3$  are listed in table 3.2. These model constants have to be chosen carefully. Results obtained by means of differential equation expressions such as (3.117) and (3.118) give the leading terms of the transport terms sought for but require readjustment of the model constants. One touchstone – in order to accomplish that – is DNS data [106], from which the constant  $c_1$  has been determined. The other constants can be obtained by assuming steady state for the  $\tilde{\sigma}_t$ -equation and neglecting spatial influences. The steady state algebraic equation thus obtained is the solution of a quadratic form exactly as (3.49). Comparison of these two equations for a fully developed flame gives the values for the missing coefficients.

Equation (3.119) bears some difficulties for practical application. The solution  $\tilde{\sigma}_t = 0$  is trivial since all terms in (3.119) are proportional to  $\tilde{\sigma}_t$  itself. Therefore, an initial value of  $\tilde{\sigma}_t > 0$  is required in order to model the transition from a laminar to a turbulent flame. On the one hand, this initial value can be arbitrarily small, but on the other hand, the temporal evolution of flame surface area is in general different for different initial values. Furthermore, a value of  $\widetilde{G''^2} = 0$  also causes a singularity due to the denominators in the production and destruction terms.

In order to overcome these two problems, it is now proposed to modify the transport equation (3.119). The  $\widetilde{G''^2}$  expression in the denominator of the turbulent production term may be substituted by the expression for  $\widetilde{G''^2}_{\text{alg}}$  (3.99). Secondly, for removing the singular solution  $\tilde{\sigma}_t = 0$ , one factor of  $\tilde{\sigma}_t$  in the turbulent production and destruc-

tion terms is replaced by  $\tilde{\sigma}_t + 1$ , thus giving the following dynamical equation:

$$\begin{aligned}
 \langle \rho \rangle \frac{\partial \tilde{\sigma}_t}{\partial t} + \langle \rho \rangle \tilde{\vec{u}} \cdot \nabla \tilde{\sigma}_t &= \nabla_{||} \cdot (\langle \rho \rangle D_t \nabla_{||} \tilde{\sigma}_t) + c_0 \mathcal{P} \frac{\tilde{\sigma}_t}{k} \\
 &+ c_1 \langle \rho \rangle \frac{c_s}{2} \frac{\varepsilon}{k} (\tilde{\sigma}_t + 1) \\
 &- c_2 \langle \rho \rangle \frac{s_L^0 \tilde{\sigma}_t}{\ell_{f,t}} (\tilde{\sigma}_t + 1) - c_3 \langle \rho \rangle \frac{D \tilde{\sigma}_t^2}{\ell_{f,t}^2} (\tilde{\sigma}_t + 1) .
 \end{aligned} \tag{3.120}$$

These modifications have been chosen in such a way that the homogeneous steady state solution of (3.120) is (3.114), with identical modeling constants as in (3.119).

An approach according (3.119) or (3.120) is not further pursued in this work and the algebraic form is employed instead. Due to the third order dissipation term in  $\tilde{\sigma}_t$  for both transport equation, it is expected that in most cases, the response of  $\tilde{\sigma}_t$  to changes in the turbulence condition will be faster than for the  $\widetilde{G''^2}$ -equation and therefore it is concluded that the unsteady flame effects can sufficiently be covered by the transport equation for  $\widetilde{G''^2}$  only.

### 3.5.5 Behavior close to the wall

In many practical applications, interactions between flame and walls occur. This is especially true in internal combustion engines where the turbulent flame finally reaches the cylinder wall, head or piston surfaces and burns out there.

Flame/wall interactions can basically be attributed to two categories: The influence of the wall to the chemistry of the flame, either by heat loss or by chemical inhibition, or the influence of a wall boundary layer on the turbulent flow and subsequently the turbulent flame brush. In both respects, the rate of flame propagation is reduced for a turbulent flame originating from the inner cylinder region when the flame approaches the wall region.

#### Influence of chemistry

*Hasse et al.* [40] have investigated the influence of cold walls to laminar premixed iso-octane/air flames. It was shown that the temperature of the preheat and the reaction zone is reduced by thermal diffusion, and when the temperature in the burnt zone falls below the inner layer temperature due to that process – usually at about 1400 K – the flame is quenched. The quenching distance to the wall determined for this configuration is of the order of the laminar flame thickness.

Concerning the modeling one can conclude from these observations that a correct measure for the temperature of the burnt gas close to the wall is required. This involves that the correct enthalpy and the species composition for the burnt state are correctly determined. With respect to the enthalpy, this is guaranteed if the enthalpy formulation

with inclusion of the chemical heat of formation is employed as it was used throughout this work.

The burnt gas temperature  $T_b$  can be used to determine the laminar burning velocity (see also the laminar burning velocity approximation presented in appendix C). In this work  $T_b$  is determined by the unburnt gas temperature  $T_u$ . An unburnt temperature close to the wall is calculated based on the averaged mean enthalpy of the flow and the unburnt species composition.

### Influence of wall bounded turbulence

Independently from chemistry aspects of flame/wall interactions we will discuss effects of wall bounded turbulence on the turbulent flame in this subsection. Wall bounded turbulence reduces to zero at the wall in the viscous sub-layer with the result that flame propagation is dominated by laminar processes only. In the logarithmic law region, where  $k \approx \text{const.}$  and the mixing length  $\ell_m = \kappa y$ , eqn. (2.45), the algebraic flame brush thickness  $\ell_{f,t,\text{alg}}$  is also proportional to the wall distance  $y$ . The result for  $\tilde{\sigma}_t$  in the log-law region is dependent on the behavior of the  $\widetilde{G''^2}$ -equation (3.98) in this region. Effects of instationarity are not considered in the log-law region. Therefore only stationary solutions of the equation for  $\widetilde{G''^2}$  will be discussed.

We assume the flame to be perpendicular to the wall and the density at the mean flame front to be constant. Then  $\widetilde{G''^2} = \widetilde{G''^2}(y)$  and (3.98) reduces to an ordinary differential equation (ODE) of second order:

$$0 = \frac{d}{dy} \left( D_{t,d} \frac{d\widetilde{G''^2}}{dy} \right) + 2D_{t,\mathcal{P}} \overbrace{(\nabla \widetilde{G})^2}^{=1} - c_s \widetilde{G''^2} \frac{\varepsilon}{k}. \quad (3.121)$$

For generality, we introduce two different turbulent diffusion coefficients for turbulent transport and production. They are both defined according to eqn. (3.94). Thereby, we allow for two different turbulent Schmidt numbers  $\text{Sc}_{t,d}$ , and  $\text{Sc}_{t,\mathcal{P}}$ . We apply the scaling relationships for the mixing length  $\ell_m$ , eqns. (2.45) and (2.46) in order to eliminate the turbulent dissipation  $\varepsilon$  and the turbulent diffusivity  $D_t$ , eqn. (3.94). For example, the inverse turbulent time scale reads in the log-law region

$$\frac{\varepsilon}{k} = \frac{c_\mu^{3/4} k^{1/2}}{\kappa y}. \quad (3.122)$$

After some transformations we obtain

$$0 = C_1 k^{1/2} y^2 \frac{d^2 \widetilde{G''^2}}{dy^2} + C_1 k^{1/2} y \frac{d\widetilde{G''^2}}{dy} + 2C_2 k^{1/2} y - C_3 k^{1/2} \widetilde{G''^2}, \text{ where } (3.123)$$

$$C_1 \equiv \frac{c_\mu^{1/4} \kappa}{\text{Sc}_{t,d}}, \quad C_2 \equiv \frac{c_\mu^{1/4} \kappa}{\text{Sc}_{t,\mathcal{P}}}, \text{ and } C_3 \equiv \frac{c_s c_\mu}{\kappa}.$$

As can be seen, the ODE is independent from  $k$ , since its root can be canceled out. Depending on the values for the constants  $\mathcal{C}_1$  and  $\mathcal{C}_3$ , we obtain two sets of solutions.

$$\widetilde{G}''^2(y) = \begin{cases} \frac{2\mathcal{C}_2}{3\mathcal{C}_1}y + \mathcal{C}_4y^2 + \mathcal{C}_5y^{-2} & \text{if } \mathcal{C}_3 = 4\mathcal{C}_1, \\ \frac{2\mathcal{C}_2}{\mathcal{C}_3 - 4\mathcal{C}_1}y^2 + \mathcal{C}_4y^{\sqrt{\mathcal{C}_3/\mathcal{C}_1}} + \mathcal{C}_5y^{-\sqrt{\mathcal{C}_3/\mathcal{C}_1}} & \text{otherwise.} \end{cases} \quad (3.124)$$

$\mathcal{C}_4$  and  $\mathcal{C}_5$  are two constants that solely depend on the boundary conditions. On the left hand boundary it is reasonable to assume that  $\widetilde{G}''^2(y=0) = 0$  which gives  $\mathcal{C}_5 = 0$ . Therefore, the constant  $\mathcal{C}_4$  must be determined by the conditions on the right hand boundary, that is, the outer layer.

Due to the large gradients close to the wall that can be expected for  $\widetilde{G}''^2$  the influence of the diffusion term and hence the influence of  $\text{Sc}_{t,d}$  needs to be studied. For  $\text{Sc}_{t,d} \rightarrow \infty$  we obtain  $\widetilde{G}''^2 \propto y^2$  because  $\ell_m \propto y^2$ . Otherwise, for other values of  $\text{Sc}_{t,d}$ , the leading order exponent in the polynomial solution (3.124) is variable and depends on  $\text{Sc}_{t,d}$ .

Now, the response of the algebraic  $\widetilde{\sigma}_t$ -equation (3.114) to solutions for  $\widetilde{G}''^2$  in the log-law region according to eqn. (3.124) will be investigated with regards to variations of  $\text{Sc}_{t,d}$ . After substituting  $\ell^*$  and  $\varepsilon/k$  for expressions valid in the log-law region the algebraic  $\widetilde{\sigma}_t$ -equation can be written as

$$\widetilde{\sigma}_t(y) = -\frac{\mathcal{C}_6(q)}{\ell_f} \frac{\widetilde{G}''^2^{\frac{q+1}{2}}}{y^q} + \sqrt{\frac{\mathcal{C}_6(q)^2}{\ell_f^2} \frac{\widetilde{G}''^2^{q+1}}{y^{2q}} + \frac{\mathcal{C}_7}{\ell_f} \frac{\widetilde{G}''^2}{y} \frac{k^{1/2}}{s_L}}. \quad (3.125)$$

All model constants are combined in  $\mathcal{C}_6(q)$  and  $\mathcal{C}_7$ .

It is required that  $\widetilde{\sigma}_t(y) \rightarrow 0$  for  $y \rightarrow 0$  using the expressions for the log-law region. This is achieved if all three terms in (3.125) vanish for  $y \rightarrow 0$ . Then, the lowest polynomial order of (3.124) must be larger than one. This condition is satisfied if  $\mathcal{C}_3 > \mathcal{C}_1$ , in other words if

$$\text{Sc}_{t,d} > \frac{\kappa^2}{c_s c_\mu^{1/2}} \approx 0.29. \quad (3.126)$$

Then, the first and the second term (i.e. the first under the square root) additionally require that  $(q+1)/2 > q$ , which is fulfilled if  $q < 1$ . With that condition,  $\widetilde{\sigma}_t(y=0) = 0$ . Furthermore,  $\widetilde{\sigma}_t$  remains bounded in this case for  $y \rightarrow 0$ . Recall the model constants used in this work,  $\text{Sc}_{t,d} = \text{Sc}_{t,\mathcal{P}} = \text{Sc}_t = 0.7$ ; therefore the choice of constants appears to be suited for the log-law region.

One exception should be noted: The condition  $\mathcal{C}_3 = 4\mathcal{C}_1$  leads to

$$\text{Sc}_{t,d} = \frac{4\kappa^2}{c_s c_\mu^{1/2}} \approx 1.17. \quad (3.127)$$

For this value of  $Sc_{t,d}$  the leading order term in eqn. (3.124) is only linear and therefore inappropriate.

It is noted the two Schmidt numbers are independent of each other from the point of view discussed here. However, an independent consideration of both numbers is only carried out in this section.

### 3.5.6 Combining the presumed pdf shape approach with the flamelet equations

In this section we discuss the approach to couple the flamelet parameters  $\tilde{G}$  and  $\widetilde{G''^2}$  with the species distribution of the 1D flamelet in order to approximate the species distribution in CFD space. For this, the distribution of the instantaneous flame front realizations needs to be taken into account. This is accomplished by applying a presumed probability density function (pdf). The Favre average of the mass fraction of a species  $k$  can be calculated by

$$\tilde{Y}_k(\vec{x}) = \int_{-\infty}^{+\infty} Y_k(x_n) P_{x_n}(\tilde{G}(\vec{x}), \widetilde{G''^2}(\vec{x})) dx_n . \quad (3.128)$$

Here  $P_{x_n}$  is the probability of finding the instantaneous position  $x_n$  of the one dimensional flamelet in the 3D flow, for which usually a Gaussian presumed pdf is assumed:

$$P_{x_n}(\tilde{G}, \widetilde{G''^2}) = \frac{1}{\sqrt{2\pi\widetilde{G''^2}}} \exp\left(-\frac{(x_n - \tilde{G})^2}{2\widetilde{G''^2}}\right) . \quad (3.129)$$

For the corrugated flamelets the species distribution is obtained using eqn. (3.2).

In the thin reaction zones regime turbulent eddies enter and therefore thicken the preheat zone. They also interact dynamically with the reaction zone. In order to employ the approach (3.128) averaged flamelet profiles in the thin reaction zones are needed. This is accomplished by introducing the turbulent diffusivity into the flamelet equation (3.2) which is active in the preheat and in the post-reactive zone only, but not in the inner layer. That is possible because in the preheat and in the post-reactive zone, time scales of reaction and diffusion can be decoupled. In view of eqn. (3.45), we obtain  $D_t = \sigma^2 D$  and (3.2) modifies [71] to

$$\overline{\rho\sigma s_L} \frac{\partial \hat{Y}_k}{\partial x_n} = \frac{\partial}{\partial x_n} \left( \rho [(\sigma - 1)^2 D + D_k] \frac{\partial \hat{Y}_k}{\partial x_n} \right) + W_k \hat{\omega}_k \quad (3.130)$$

where the filtering operator “ $\overline{\quad}$ ” indicates that averaged profiles are obtained in this case [42]. A transformation of the normal coordinate  $x_n$  into a ‘stretched’ coordinate

$$x'_n = \frac{x_n}{\sigma} \quad (3.131)$$

leads to

$$\widehat{\rho s_L} \frac{\partial \hat{Y}_k}{\partial x'_n} = \frac{\partial}{\partial x'_n} \left( \frac{\rho D}{\widehat{Le}_k} \frac{\partial \hat{Y}_k}{\partial x'_n} \right) + W_k \dot{\omega}_k . \quad (3.132)$$

Here the Lewis number  $\widehat{Le}_k$  is a function of the normal coordinate  $x'_n$ . In the thin reaction zone laminar diffusion is dominant, and therefore  $\widehat{Le}_k = D/D_k$ . Outside of this zone, turbulent mixing is predominant and  $\widehat{Le}_k \rightarrow Le_t = 1$ .

As we see, the flamelet equations for the corrugated and thin reaction zones combustion regimes differ merely in the assumption of Lewis numbers outside of the reaction zone. By assuming unity laminar Lewis numbers, especially with regards to the reaction zone, the laminar species profiles for the two regimes would be self similar, that is

$$\hat{Y}_k(x'_n) \approx Y_k(x_n) . \quad (3.133)$$

If one is only interested in the kinematics of the turbulent flame propagation and the influence of the combustion process on the flow due to heat release, averaged species distributions of the flamelets within the reaction zone are not strictly required in an approach like (3.128). In that case, the species composition in the unburnt and the burnt gas are sufficient for satisfying results. Eqn. (3.128) can then be reduced to

$$\widetilde{Y}_k(\vec{x}) = Y_{k,u} [1 - \widetilde{P}_b(\widetilde{G}(\vec{x}), \widetilde{G''^2}(\vec{x}))] + Y_{k,b} \widetilde{P}_b(\widetilde{G}(\vec{x}), \widetilde{G''^2}(\vec{x})) , \quad (3.134)$$

with  $\widetilde{P}_b$  from (3.70) determined to

$$\widetilde{P}_b(\widetilde{G}, \widetilde{G''^2}) = \frac{1}{2} + \frac{1}{2} \operatorname{erf} \left( \frac{\widetilde{G} - G_0}{\sqrt{2\widetilde{G''^2}}} \right) . \quad (3.135)$$

This relationship can be used in purely premixed configuration as well as in partially premixed, i.e. stratified mixtures which will be discussed in the following section. However, it needs to be pointed out that *unburnt* and *burnt* in the context of this section here refer to the positions ahead and behind the premixed flame front, which means for example that fuel residing in a rich mixture and crossing the premixed flame front is considered here as *premixed burnt*. However, with respect to a diffusion flame behind the premixed front, this fuel can still be subjected to non-premixed combustion.

### 3.5.7 Stratified mixtures

In practical applications, in addition to premixed combustion also non-premixed combustion or a combination of the two, namely *partially premixed* combustion can occur. Examples of such configurations are lifted diffusion flames. Prior to combustion, fuel and oxidizer require time for diffusion. After that, a so called ‘triple flame structure’ is observed, exhibiting three wings in which reactions occur [18, 19]. Two wings correspond to the lean and rich limit of premixed propagation while the third is due to diffusive combustion.



In this work, we will primarily focus on the premixed wings, for which a corresponding expression of the turbulent burning velocity is sought. For the diffusion controlled burning behind the premixed front, a simplified infinitely fast chemistry assumption is made. It is possible to use a more elaborated model for non-premixed combustion in combination with the Level Set concept, however, this is beyond the scope of this work.

Apart from the premixed flamelet parameters  $\widetilde{G}$  and  $\widetilde{G}''^2$ , a coordinate for the non-premixed mode, the mixture fraction  $Z$ , eqn. (2.20) needs to be introduced. The instantaneous transport equation for the mixture fraction is similar to the laminar species equations (2.3) except for the absence of a chemical source term. *Pitsch et al.* [77] propose to base the definition of  $Z$  on such a transport equation, employing a diffusion coefficient related to the thermal conductivity by a unity Lewis number. By means of the decomposition

$$Z = \widetilde{Z} + Z'' \quad (3.136)$$

it is straightforward to derive a Favre averaged transport equation for the mean mixture fraction  $\widetilde{Z}$  similar to the mean species mass fraction equation:

$$\frac{\partial \langle \rho \rangle \widetilde{Z}}{\partial t} + \langle \rho \rangle \nabla \widetilde{Z} \cdot \widetilde{\mathbf{u}} = \nabla \cdot \left( \langle \rho \rangle D_t \nabla \widetilde{Z} \right). \quad (3.137)$$

In order to describe the statistics of the instantaneous mixture fraction fluctuations, the mixture fraction variance  $\widetilde{Z}''^2$  is an important measure. It is straight forward to derive an equation for this second moment [68],

$$\frac{\partial \langle \rho \rangle \widetilde{Z}''^2}{\partial t} + \langle \rho \rangle \nabla \widetilde{Z}''^2 \cdot \widetilde{\mathbf{u}} = \nabla \cdot \left( \langle \rho \rangle D_t \nabla \widetilde{Z}''^2 \right) + 2 \langle \rho \rangle D_t (\nabla \widetilde{Z})^2 - \langle \rho \rangle \chi_Z. \quad (3.138)$$

For the scalar dissipation  $\chi_Z$  a spectral closure similar to (3.95) is commonly used:

$$\chi_Z = c_\chi \widetilde{Z}''^2 \frac{\varepsilon}{k} \quad \text{with} \quad c_\chi = 2.0. \quad (3.139)$$

The mean turbulent mass burning rate is obtained by integrating the instantaneous turbulent mass burning rate which depends on the instantaneous mixture fraction  $Z$  and the pdf of finding  $Z$  [13]. The instantaneous turbulent burning velocity again is dependent on the laminar burning velocity and on the mixture fraction conditioned flame surface area  $\widetilde{\sigma}_t(Z)$ :

$$\langle \rho s_T \rangle = \int_0^1 \rho(Z) s_L(Z) (1 + \widetilde{\sigma}_t(Z)) \widetilde{P}(Z) dZ. \quad (3.140)$$

For the pdf  $\widetilde{P}(Z)$  of finding the instantaneous mixture fraction  $Z$  commonly the beta probability function [68] is employed.

$$\widetilde{P}(Z) = P_\beta(Z, \widetilde{Z}, \widetilde{Z}''^2) \quad (3.141)$$

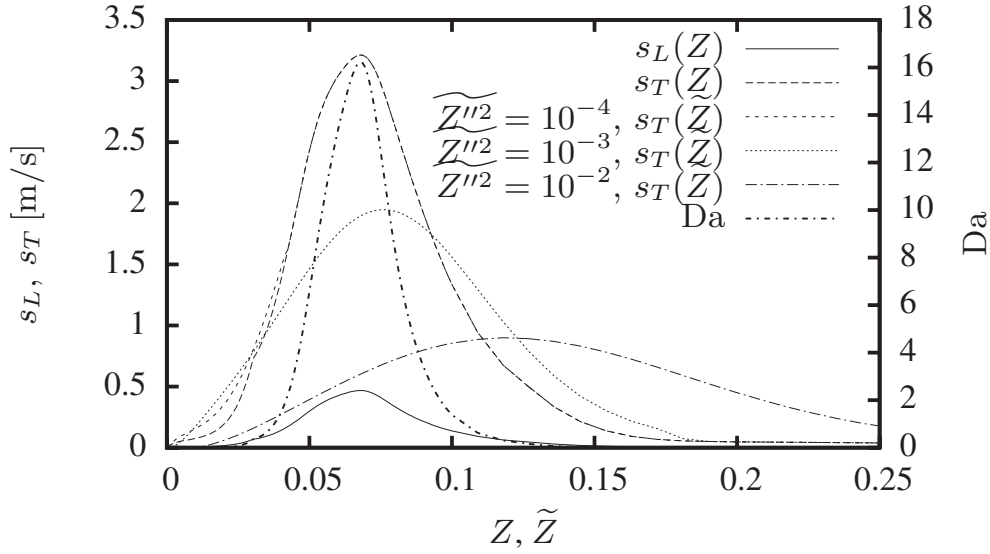


**Figure 3.11:** Plot of laminar burning velocity  $s_L(Z)$  for a premixed iso-octane/air flame at  $T_u = 350$  K,  $p = 1$  bar,  $v' = 2$  m/s,  $\ell = 10^{-2}$  m, corresponding Damköhler number  $\text{Da}(Z)$  and turbulent burning velocity  $s_T(\tilde{Z})$  according to eqn. (3.49) over mixture fraction space.  $s_T(\tilde{Z})$  is determined according to eqn. (3.140) and the variation of mixture fraction variance  $\tilde{Z}''^2$  is studied.

The expression (3.140) is a consistent extension of (3.33) for fluctuating mixture fractions. Since  $s_L$  is strongly dependent on the mixture fraction, the Damköhler number can significantly vary over the mixture fraction as well. This also causes large variations for  $\tilde{\sigma}_t$  over  $Z$ .

The effect of considering the mixture fraction pdf is shown in figure 3.11 for an arbitrary mixture fraction example. The comparison of the result for the turbulent burning velocity  $s_T(Z)$  in homogeneous mixtures on the one hand and stratified mixtures according to the expression (3.140) for different mixture fraction variances  $\tilde{Z}''^2$  on the other yields different results for  $s_T(\tilde{Z})$  with increasing  $\tilde{Z}''^2$ . For small values of  $\tilde{Z}''^2$ , only minor differences between turbulent burning velocity over mean mixture fraction  $\tilde{Z}$  and the corresponding homogeneous results are observed. With increasing  $\tilde{Z}''^2$ , the maximum of turbulent burning velocity according to this model assumption is shifted towards rich mixtures and at the same time this maximum is decreased. On the other hand, the turbulent burning velocity increases for lean mixtures. This can be attributed to the fact that for average lean and very rich mixtures, intermittency effects increasingly become important, that is, for those mixtures the probability of finding mixtures with a high combustion propensity increases while for mean mixtures close to stoichiometry, the possibility increases to find very lean and very rich mixtures.

It is required to consider  $\tilde{\sigma}_t$  as a function of  $Z$  for each mixture fraction realization. It is an additional argument for using the algebraic expression (3.114) instead of the one discussed in section 3.5.4. A consistent application of the transport equation

would require the use of a set of transport equations (3.120) for a set of representative mixture fractions  $Z$ , each with different values for the laminar burning velocity and flame diffusivity.

## 3.6 Spark Ignition Modeling

The initiation of combustion is realized in most gasoline engines by an electrical spark that is formed between the two electrodes of a spark plug. This process can be subdivided into different phases [44]. The first phase, at which an ionized plasma between the electrodes is established, is called the *breakdown phase*. This phase is followed by the *arc phase* which is characterized by an expansion of the plasma due to diffusive effects and by chemical reactions leading to a propagating flame. It is required that the mixture at the spark plug gap is ignitable. In the final *glow discharge phase*, more energy of the electrical circuit may be released into the spark plasma. The overall duration time of the spark including all phases is assessed to be of the order of several milliseconds, whereas the breakdown and the arc phase last for nano- and microseconds, respectively.

The subdivision of the spark ignition process was at first developed by *Maly and Vogel* [58] who also reported the voltage and current dependency of the spark phases. *Ballal et al.* [4] pointed out that the ignition energy can be minimized in a slightly rich mixture at  $\phi \approx 1.1$  for a successful ignition event to occur. At this equivalence ratio, for hydrocarbon mixtures, the laminar burning velocity reaches its maximum. The influence of turbulence was recognized as a twofold process: Under some conditions, turbulence promotes flame propagation, whereas it can cause quenching of the flame kernel due to heat losses under other conditions.

### 3.6.1 A Brief Literature Review

As *Pischinger and Heywood* [74] have pointed out, the effect of the electrical energy source is limited to the breakdown phase and difficult to be measured quantitatively. Immediately after the breakdown, the laminar flame chemistry is the dominating physical process. However, the balance of heat loss to the spark plug electrodes and the electrical energy source during the glow discharge influences the expansion of the flame kernel. Further studies by the same authors [75] presented thermodynamic models of the spark physics among other results. Deformation of the arc due to convective gas effects was found to cause increased electrical energy deposited into the spark and therefore improved inflammability.

*Herweg and Maly* [43] presented a further refined model which assumes the spark kernel to be approximately spherical while it is convected by the mean flow. During breakdown and glow discharge the expansion speed was assumed to be determined by the plasma velocity caused by a sum of laminar and turbulent flame propagation and by plasma expansion due to the spark energy deposition. The influence of the first

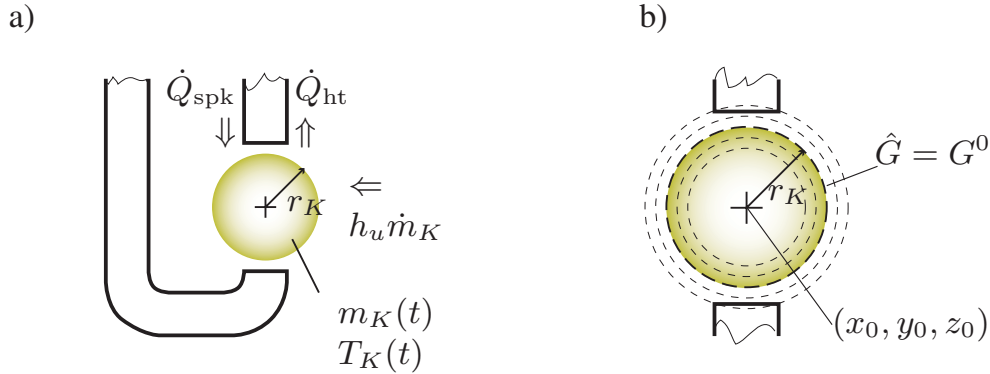


**Figure 3.12:** a) Energy balance between the spark plug electrodes and the spark kernel. b) Relation between spark kernel radius  $r_K$  and filtered  $\hat{G}$ -field.

two effects was assumed to increase with time while the last effect was estimated to decrease down to zero for increasing time.

As for the influence of turbulence on the spark the spark size is taken into account in [7], where an expression for the turbulent spark expansion velocity was derived. In that work, it is assumed that the spark kernel only is affected by turbulent eddies of smaller or equal size.

Other contributions discuss spark ignition models that are implemented into 3D CFD codes. One of these model is the Discrete Particle Ignition Kernel (DPIK) model [25, 26, 101, 99]. In order to achieve a certain level of grid independency, a set of marker particles was employed and advected in order to specify the size and the spatial extension of the spark kernel. Applying a criterion to be specified (e.g. size of the spark) the DPIK model was switched to a different 3D combustion model, for example, a characteristic time scale combustion model or the  $G$ -equation model. For the turbulent flame propagation in some of those publications, it was reported that for the DPIK phase and the 3D equation combustion phase two different combustion models were used.

Another recent development is the Arc Kernel Tracking Ignition Model (AKTIM) [21]. This model does not only take the physics of the spark plasma and laminar to turbulent flame propagation into account, but it also includes an electrical circuit model in order to estimate the amount of electrical energy deposition into the spark kernel. A certain mesh independency is achieved by representing spherical flame kernels by marker particles. In [21] the AKTIM model was coupled together with an Extended Coherent Flamelet Model (ECFM). The authors reported weak dependency of simulation results on the switching criteria between the AKTIM and the ECFM model.

### 3.6.2 A Spark Ignition Model Derived from the $\tilde{G}$ -equation

In the following a new spark ignition model based on the  $G$ -equation methodology is presented. In contrast to the other models discussed in above, the same physical mod-

eling assumptions will be used here as for turbulent premixed flame propagation which especially hold for the expression of the turbulent burning velocity and the variance (3.85). Additionally, kernel expansion effects due to electrical spark energy and kernel curvature will be accounted for. The thermodynamical analysis is carried out similar to *Tan* [100]. As a first approximation we assume that the initial spark kernel is spherical with a given initial position and radius. During the growth of the kernel towards a fully turbulent flame the kernel will be assumed to be spherical on average as well. It is also subjected to the convection of the background flow.

In figure 3.12a, the energy balance between the spark and the spark plug electrodes is depicted. According to the first law of thermodynamics, the energy budget of the spark reads

$$\dot{Q}_{\text{spk}} + \dot{Q}_{\text{chem}} - \dot{Q}_{\text{ht}} = \frac{dH}{dt} - h_u \dot{m}_K - V \frac{dp}{dt}, \quad (3.142)$$

where  $H$  represents the thermal spark and plasma enthalpy.  $\dot{Q}_{\text{spk}}$  denotes the gross electrical energy transfer from the electrodes and  $\dot{Q}_{\text{ht}}$  the heat loss to the electrodes. Since  $H$  does not include the heat of formation here,  $\dot{Q}_{\text{chem}}$  accounts for the heat release caused by combustion.  $h_u$  denotes the specific enthalpy of the unburnt gas mixture which is transported into the spark by (laminar or turbulent) flame propagation through the mass stream  $\dot{m}_K$ . In this equation the effect of global pressure rise is still accounted for in the last term on the r.h.s.; however, this term will be neglected in the application of the model due to the relatively low pressure rise.

The effect of spark energy and heat losses commonly are [43] related to each other by forming an effectivity coefficient  $\eta_{\text{eff}}$ , in the following assumed to be approximately 0.3:

$$\dot{Q}_{\text{ht}} \approx (1 - \eta_{\text{eff}}) \dot{Q}_{\text{spk}}. \quad (3.143)$$

The continuity equation gives the following ordinary differential equation for the increase of spark kernel mass:

$$\frac{dm_K}{dt} = \dot{m}_K = 4\pi r_K^2 \rho_u s_{T,\kappa}. \quad (3.144)$$

Here,  $r_K$  is the radius of the kernel and  $s_{T,\kappa}$  an expression for the flame propagation which takes into account the turbulent burning velocity and the effect of laminar and turbulent kernel curvature, cf. (3.106). The radius is readily obtained by

$$r_K = \sqrt[3]{\frac{3m_K}{4\pi\rho_b}}. \quad (3.145)$$

The density of the gas in the spark  $\rho_b$  needs to be known which is – depending on ignition conditions – lower than the density of adiabatically burned gas due to plasma effects caused by the electrical energy which results in an increased kernel temperature  $T_K$ . In order to approximate  $T_K$  eqn. (3.142) needs to be further modified.

The derivative of the kernel enthalpy gives

$$\frac{dH}{dt} = \dot{m}_K h_K + \dot{h}_K m_K \quad (3.146)$$

and the heat release due to premixed combustion can be expressed as

$$\dot{Q}_{\text{chem}} = \dot{m}_K (h_{\text{ad}} - h_u) . \quad (3.147)$$

Substituting these equations into each other and assuming constant heat capacities,  $c_p \approx \text{const.}$ , we eventually obtain

$$\frac{dT_K}{dt} = -\frac{\dot{m}_K}{m_K} (T_K - T_{\text{ad}}) + \frac{\dot{Q}_{\text{spk}} \eta_{\text{eff}}}{m_K c_p} + \frac{1}{\rho_b c_p} \frac{dp}{dt} \quad (3.148)$$

as the second ordinary differential equation for the kernel temperature  $T_K$ . Therefore eqns. (3.144) and (3.148) form a set of coupled ordinary differential equations. For  $T_K$ , appropriate initial conditions need to be specified. The initial value could be in the range of the kernel plasma temperature which is in the range of approx. 60,000 K [44] or alternatively the adiabatic flame temperature  $T_{\text{ad}}$ . According to the numerical investigation by *Andreassi et al.* [3], this temperature drops rapidly within the range of tenths microseconds to about 10,000 K. Additionally, this temperature only prevails within a kernel radius of 100  $\mu\text{m}$ . Therefore, in this work here, as an ad-hoc assumption, the initial value of  $T_K$  was assumed to be 1000 K higher than  $T_{\text{ad}}$ .

The burning velocity  $s_{T,\kappa}$ , including curvature effects can be deduced from (3.106), where the curvature of the spherical kernel amounts to  $\kappa = 2/r_K$ .

$$s_{T,\kappa} = s_T - \frac{2}{r_K} (D_0 + D'_t) \quad (3.149)$$

Here  $D'_t$  can be expressed by one of the two possibilities as presented in section 3.5.3. An equation describing the thickness of the flame brush can be deduced from (3.98) by assuming uniform turbulent profiles and thereby neglecting the diffusion term while the convection term is incorporated in the substantial derivative:

$$\frac{d\widetilde{G}_{\text{spk}}''/2}{dt} = 2\hat{D}_{t,\text{spk}} - c_s \frac{\varepsilon}{\hat{k}_{\text{spk}}} \widetilde{G}_{\text{spk}}''/2 \quad (3.150)$$

The development of the initially laminar spark kernel into a fully turbulent flame will therefore be modeled by 0D-reduced equations based on the  $G$ -equation for turbulent premixed combustion. However, as it was already pointed out in [7] the spark is affected only by turbulent structures that are smaller or equal in size as the spark. In this work this is accomplished by re-scaling the turbulent kinetic energy  $k$  to a value  $\hat{k}_{\text{spk}}$  corresponding to the size of the spark according to an relationship found by *Willems*

[108]. This is also done for the turbulent diffusivity  $\hat{D}_{t, \text{spk}}$  which is proportional to  $\hat{k}_{\text{spk}}^2$ . Following that approach,  $\hat{k}_{\text{spk}}$  can be determined to

$$\hat{k}_{\text{spk}} = k \left( \frac{2r_K}{l_t} \right)^{\frac{2}{3}}, \quad (3.151)$$

if  $2r_K < l_t$ , where the turbulent length scale  $l_t$  is determined to be

$$l_t = \ell_{f,t,\text{alg}}. \quad (3.152)$$

Note that here the choice of  $\ell_{f,t,\text{alg}}$  as turbulent length scale is ad-hoc for the purpose of downscaling the effective turbulent kinetic energy. Other choices for the turbulent length scale also would be appropriate.

When the flame kernel reaches a specified size  $r_{K,\text{end}}$ , the model is switched to the 3D equations. This is feasible because a scalar field for  $\tilde{G}$  can easily be determined by the center of the spark location and the spark radius.





## Chapter 4

# Numerical Implementation

In this chapter the integration of the model equations into the CFD code, the solving procedure, and the coupling of the model with the underlying flow structure are presented. The model was implemented into AC-FluX (formerly known as GMTEC) [24], a flow solver based on Finite Volume methods [28] that employs unstructured, mostly hexahedral meshes. AC-FluX is mainly used for internal combustion engine simulations, for gasoline as well as for diesel engines. This code is able to treat moving meshes and non-conforming internal mesh motion boundaries that facilitate generating a realistic geometric model of the intakes and the in-cylinder in combination with valve motion. In order to provide high spatial accuracy, adaptive run-time controlled mesh refinement can be used optionally. The basic version of this solver already is able to predict chemically reacting flows and fuel spray interaction employing a Lagrangian particle tracking algorithm.

The basic structure of this CFD code will not be elaborated on here, but it is described in detail in [24]. Only modifications of the code that are required for the Level Set based turbulent premixed combustion model are discussed. The general integration is given in the following section. Then, in section 4.2, the numerical implementation of the equations for  $\tilde{G}$ ,  $\tilde{G}''^2$ , and  $\tilde{\sigma}_t$  is explained. The numerical strategy behind the application of the Level Set Method for  $\tilde{G}$  needs to be explained in detail and is therefore not given in this chapter. It can be found in appendix B. A significant section is devoted to the coupling of the  $\tilde{G}$ -equation to the fluid flow, since the effect of combustion on the flow becomes apparent as heat release. However, heat release is not directly given by the  $\tilde{G}$ -equation model and needs to be deduced instead.

### 4.1 General integration of the model into the CFD code

In figure 4.1 the interaction between the Level Set module, the required flamelet libraries, and the CFD code is depicted. However, one should note that this diagram

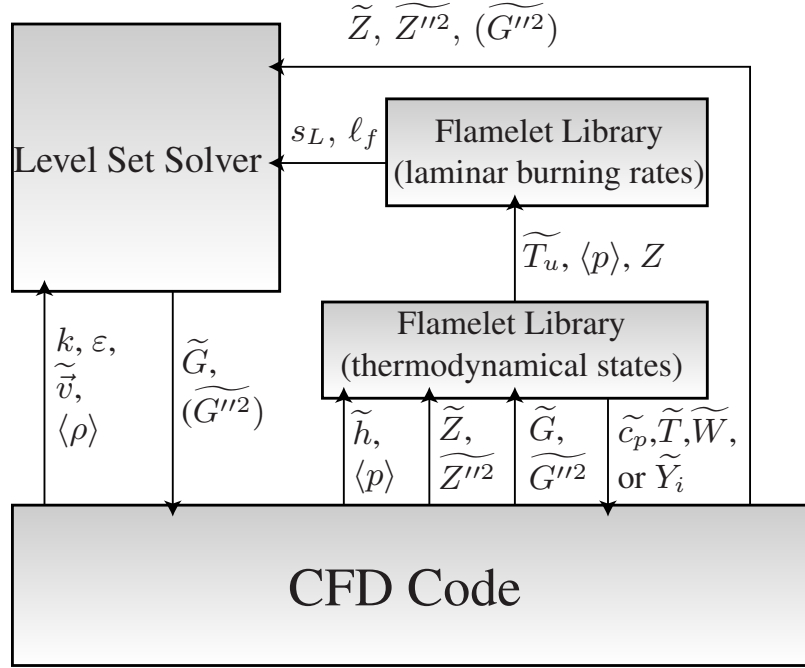


**Figure 4.1:** Level Set module and flamelet library interaction with the CFD-Code

confines itself only to the main principles. In reality, the Level Set Solver needs to be highly adopted to the internal data structure of the host CFD code. This issue will be dealt with below in detail.

In AC-FluX the enthalpy already includes the heat of formation per default. Therefore, no source terms due to chemical reactions appear in the  $\tilde{h}$ -equation. The state of the flow, that is, the mean temperature  $\tilde{T}$ , the averaged heat capacity  $\tilde{c}_p$ , and the molecular weight  $\tilde{W}$  need to be determined using the flamelet parameters  $\tilde{G}$ ,  $\tilde{G}''^2$ , optionally (in stratified configurations)  $\tilde{Z}$ , and  $\tilde{Z}''^2$ . The state variables are listed in a flamelet table and transferred back to the CFD code.

In this work, the aforementioned flamelet parameters return *active stream concentrations*  $\tilde{Y}_i$  such as fuel, air and burnt gas streams stored in the flamelet table. These streams are converted by the CFD code internally into thermodynamical states. By means of the source term free enthalpy equation, the completely burnt and unburnt states of the flow at every location can be determined independently of the actual thermodynamical state of the mean flow. The unburnt state serves as an input into the flamelet library for the laminar burning velocity  $s_L$  and the laminar flame thickness  $\ell_f$ , which are needed for the determination of the turbulent flame surface area ratio  $\tilde{\sigma}_t$ .

The transport equations  $\tilde{Z}$  and  $\tilde{Z}''^2$  are solved in the CFD code by an implicit finite volume method. The equation for  $\tilde{G}''^2$  is *per se* defined only on the mean flame front and requires an appropriate definition outside of that front. Depending on the corresponding outside definition,  $\tilde{G}''^2$  can be solved either within the Level Set solver

along with  $\tilde{G}$  or by an implicit finite volume method using the same principle as for the non-premixed flamelet parameters.

The  $\tilde{G}$ -equation, however, is not solved by an implicit finite volume equation since the definition of  $\tilde{G}$  requires a distance constraint outside of the mean flame front position. This distance constraint would require additional numerical treatment if a conventional implicit method was employed in order to solve for  $\tilde{G}$  on  $G_0$ . Such numerical treatments are called “reinitialization”. In order to avoid the numerical overhead involved by this procedure, an entirely new solver based on the so-called *Fast Marching Methods* has been used. Numerical details on Fast Marching Methods are given in appendix B.

## 4.2 Solving of model equations

In order to solve the coupled time-dependent conservation equations within AC-FluX, a combination of the PISO (Pressure-Implicit Split Operator, [65]) and SIMPLE (Semi-Implicit Method for Pressure Linked Equations, [45]) algorithm is employed. The general structure of the solving procedure within one time step is depicted in figure 4.2. In that flow chart those steps that are due to the  $G$ -equation model are marked. The basic solving algorithm is obtained by excluding these steps.

The time integration consists of two steps. The first steps performs preparatory steps for the  $G$ -equation model and solves for  $\tilde{G}$  which will be discussed below. The second step solves iteratively for the other conservation equations by the pressure correction method.

This basic pressure correction can be subdivided into three major iteration loops which are denoted as *outer iteration* loop, *inner iteration* loop (index *ccp*), and *turbulence iteration* loop here. The latter two loops are encompassed by the first, which is initiated by the velocity predictor. The inner iteration loop iteratively calculates the pressure and momentum correction combined with the update of the (re-)active species and the flamelet parameters that need to be in balance with the enthalpy equation. The other loop, the turbulence iteration loop is carried out separately from the inner iteration for improved numerical stability.

In the first preparatory step, the  $\tilde{G}$ -equation is solved. This solving procedure could be integrated into the pressure correction step, however, due to its different numerical treatment, this step is separated from the other steps. Prior to the equation for  $\tilde{G}$ ,  $\overline{G''^2}$  is updated to the new time level by a predictor step. After solving for  $\tilde{G}$ , optionally the reaction rate  $\dot{\omega}_G$  due to the turbulent premixed reaction can be estimated.

### 4.2.1 $\tilde{G}$ equation

Due to the Level Set nature of the  $\tilde{G}$ -equation, equation (3.106) at  $G_0$  needs to be fitted into the general Level Set form as given by (B.1). This is trivial for the term containing the turbulent burning velocity, but also needs to be done for the convection

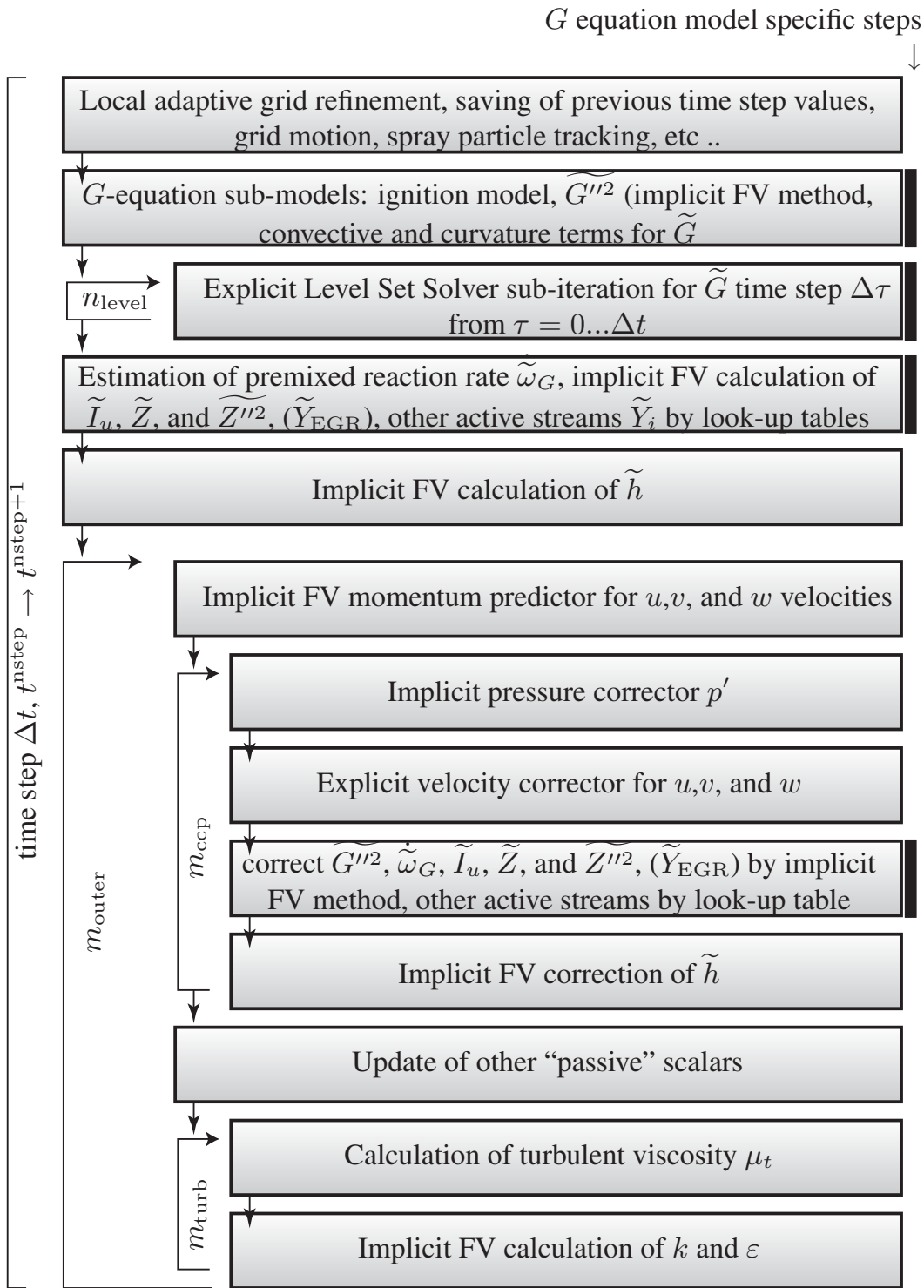


**Figure 4.2:** Integration of the  $G$ -equation model into the algorithm for the time dependent solution of the conservation equations. The steps pertinent to the  $G$ -equation are marked with a black line at the right side. Several iterative loops are depicted which are named according to their strict number of loop counts ( $n_{\text{level}}$  for the Level Set Solver) or their maximum iteration count depending on convergence criteria ( $m_{\text{outer}}$ ,  $m_{\text{ccp}}$ , and  $m_{\text{turb}}$ ).

and turbulent transport terms. The term  $\tilde{\mathbf{u}} \cdot \nabla \tilde{G}$ , for instance, can be transformed with eqn. (3.81) into a suitable form. Then (3.106) transforms to

$$\frac{\partial \tilde{G}}{\partial t} + \overbrace{(F_{\text{cd}} + F_{\text{prop}})}^{=F} |\nabla \tilde{G}| = 0, \quad (4.1)$$

where the convective and diffusive term read

$$F_{\text{cd}} = -\tilde{\mathbf{u}} \cdot \tilde{\mathbf{n}} + \kappa D'_t, \quad (4.2)$$

and the propagation term

$$F_{\text{prop}} = -\frac{\widetilde{\rho s_T}}{\langle \rho \rangle}. \quad (4.3)$$

The convective-diffusive term involves spatial gradients. In order to evaluate them, one can make use of the fact that the curvature term transforms to a diffusion term if the distance constraint outside of the mean flame front is fulfilled, in other words, for a given time  $t^{\text{nstep}}$ , there is a  $\tilde{G}$ -field where  $|\nabla \tilde{G}^{\text{nstep}}| = 1$ . Therefore, the numerical procedure is required to ensure this constraint in the vicinity of the  $G_0$ -surface.

In this case,  $F_{\text{cd}}$  is evaluated by solving for  $\tilde{G}$  in an operator-splitting manner by implicitly solving the field equation

$$\left. \frac{\partial \langle \rho \rangle \tilde{G}}{\partial t} \right|_{\text{cd}} + \nabla \cdot \langle \rho \rangle \tilde{\mathbf{u}} \tilde{G} = \nabla \cdot \left( \langle \rho \rangle (D + D'_t) \nabla \tilde{G} \right). \quad (4.4)$$

The effects of laminar flame curvature by the flame diffusivity  $D$  may also be accounted for in this context.

Obtaining a predicted field  $\tilde{G}_{\text{cd}}^{\text{nstep}+1}$  due to convection and diffusion at the new time level, the normal velocities can be approximated to

$$F_{\text{cd}} \approx -\frac{\tilde{G}_{\text{cd}}^{\text{nstep}+1} - \tilde{G}_{\text{cd}}^{\text{nstep}}}{\Delta t}. \quad (4.5)$$

Prior to advecting the  $\tilde{G}$  field to the new time level  $t^{\text{nstep}+1}$ ,  $F_{\text{cd}}$  will be evaluated as depicted in fig. 4.2. The propagation  $F_{\text{prop}}$ , on the other hand, is evaluated during the iterative update of the  $\tilde{G}$  field. Since the  $G_0$  front is mostly located between two computational cell centers, either two evaluations of the turbulent mass burning rate  $\widetilde{\rho s_T}$  or the geometrical weight of the two could be taken. In this implementation, the turbulent mass burning rate is evaluated in the cell immediately ahead of the mean flame front.

For the explicit Fast Marching Method by which  $\tilde{G}$  is updated to the new time level, a restriction on the time step  $\Delta\tau$  according to the CFL condition is required for numerical stability reasons. A temporal sub-cycling may be required, here indicated by the iteration count  $n_{\text{level}}$ . However, it is favorable to ensure that the overall time step  $\Delta t$  does not exceed the Level Set imposed time step  $\Delta\tau$ , otherwise the flame front may move too far within one computational time step. The consequence would be too much heat release induced into the flow field, thereby causing instability in the turbulent flow equations which in turn cause increased flame propagation.

### 4.2.2 $\widetilde{G''^2}$ equation

In this implementation the equation for  $\widetilde{G''^2}$ , eqn. (3.98), is solved in the whole computational domain employing an implicit Finite Volume method. Assuming that the gradients of  $\widetilde{G''^2}$  normal to the mean flame front surface are negligibly small, the parallel diffusion term (3.98) can be approximated as a regular diffusion term.

As a further simplification, one can approximate (3.103) with the flow velocity only, that is

$$\frac{d\vec{x}_f}{dt} \approx \vec{u}. \quad (4.6)$$

In that case, (3.98) would be calculated as a regular transport equation with source and dissipation terms only.

### 4.2.3 $\widetilde{\sigma}_t$ equation

As mentioned in the previous sections, the algebraic form of the equation for the turbulent flame surface area ratio is primarily used in this work. Besides the one form derived in here, two other versions of the quadratic  $\widetilde{\sigma}_t$ -equation published in literature were evaluated. These three forms can be cast into the general form

$$\widetilde{\sigma}_t = -\frac{b_3^2}{4b_1} \sqrt{\frac{3c_\mu c_s}{Sc_t} \frac{l_1}{\ell_f}} + \sqrt{\frac{b_3^4}{16b_1^2} \frac{3c_\mu c_s}{Sc_t} \frac{l_1^2}{\ell_f^2} + b_3^2 \frac{D_t}{D} \frac{l_1^2}{l_2^2}} \quad (4.7)$$

with  $l_1$  and  $l_2$  being different between different versions. The setting

$$l_1 = \ell_{f,t} \quad \text{and} \quad l_2 = \ell_{f,t} \quad (4.8)$$

corresponds to the solution of the expression (2.186) in [71], while with

$$l_1 = \ell_{f,t,\text{alg}} \quad \text{and} \quad l_2 = \ell_{f,t,\text{alg}} \quad (4.9)$$

and (3.84) as well as (3.99) the expression (2.187) in [71] is recovered.

The configuration

$$l_1 = \ell_{f,t} \ell^{*q} \quad \text{and} \quad l_2 = \ell_{f,t,\text{alg}} \quad (4.10)$$

again yields the algebraic expression (3.114) derived in this work. All three settings of  $l_1$  and  $l_2$  will be investigated in chapter 5.

## 4.3 Coupling of $G$ -equation and heat release

Since the flamelet parameters  $\widetilde{G}$ ,  $\widetilde{G''^2}$ , and optionally  $\widetilde{Z}$  and  $\widetilde{Z''^2}$  prescribe the chemical composition of the mean flow, information about the heat release due to premixed

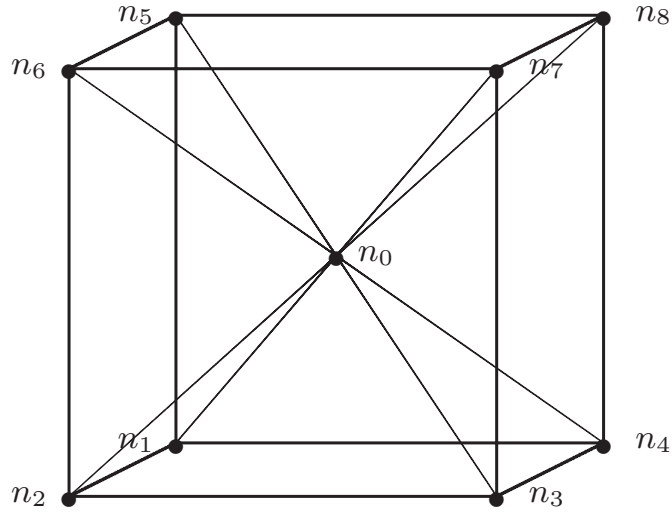


**Figure 4.3:** A regular Finite Volume cell with the cell nodes  $n_1 \dots n_8$  and the cell center  $n_0$ . The cell is subdivided into 6 pyramids.

and non-premixed reaction is not available *per se*. The source term free equation for total enthalpy is employed for this reason and heat release information is not required.

In this section the focus lies on the coupling between the premixed flamelet parameters and the fluid flow. This involves the determination of the specific probability of finding burnt gas  $\tilde{P}_b$ , which will be described below. On the other hand, there exists a numerical technique to deduce the premixed reaction rate  $\tilde{\omega}_G$ . This issue is presented in section 4.3.2. At last, the mixed-equal burnt approach is given in section 4.3.3.

#### 4.3.1 Determination of $\tilde{P}_b$

The link between the premixed flamelet parameters and the specific probability of finding burnt gas has already been given by eqn. (3.134), where a discontinuous step profile between the burnt and unburnt state of the laminar flamelet was assumed. This equation could very easily be evaluated at the center of each computational cell, assuming that this cell centered result represents the whole cell. However, since  $\tilde{G}$  is a Level Set field variable, it varies within one computational cell. The simple approach therefore may lead to oscillating results for  $\tilde{P}_b$ , especially for cell center positions close to the mean flame front position for a very small flame brush thickness. Then, the state of the whole cell depends on whether the cell center is immediately ahead or behind the mean flame front. As a consequence, a refined numerical approach was followed in which  $\tilde{P}_b$  is integrated and averaged over all locations within the cell. As stated in equation (3.134),  $\tilde{P}_b$  is a function of  $\tilde{G}$  and  $\tilde{G}''^2$ . By replacing the fractional expression in that equation by

$$\tilde{\xi} = \frac{\tilde{G}}{\sqrt{2\tilde{G}''^2}}, \quad (4.11)$$

$\tilde{P}_b$  can be expressed as function of  $\tilde{\xi}$  only.

The cell averaged result is then the averaged probability  $\tilde{P}_{b,ic}$  of the cell ic:

$$\tilde{P}_{b,ic} = \frac{1}{m_{ic}} \int_{V_{ic}} \bar{\rho}(\tilde{\xi}_{\vec{x}}) \tilde{P}_b(\tilde{\xi}_{\vec{x}}) dV, \quad (4.12)$$

where

$$m_{ic} = \int_{V_{ic}} \bar{\rho}(\tilde{\xi}_{\vec{x}}) dV \quad (4.13)$$

is the mass contained in the cell. The mean density  $\bar{\rho}(\tilde{\xi}_{\vec{x}})$  is determined from the burnt and unburnt states to

$$\bar{\rho}(\tilde{\xi}_{\vec{x}}) = \frac{\rho_u \rho_b}{\rho_u \tilde{P}_b(\tilde{\xi}_{\vec{x}}) + \rho_b (1 - \tilde{P}_b(\tilde{\xi}_{\vec{x}}))}. \quad (4.14)$$

Here the differences between this expression for the density and the expression (3.69) should be noted, in which the volumetric probability  $f_b$  of finding burnt gas is employed.

In order to perform the integration, the computational hexahedral cell is decomposed into 6 pyramids as depicted in figure 4.3 which will then be decomposed into a total of 12 tetrahedra. The integration finally is carried out by a Finite-Element like method [5]. The values of  $\tilde{\xi}$  required at the nodes of the cell are determined by a weighted average of the cell centered values  $\tilde{\xi}_{icn}$  of all neighboring cells icn of the considered node. Special boundary treatment is applied to all nodes which belong to a boundary cell face.

### 4.3.2 Determination of a premixed volumetric reaction rate

The determination of the premixed volumetric reaction rate  $\dot{\tilde{\omega}}_G$  can be helpful both for model analysis and for numerical reasons. In model analysis, a comparison with progress variable based combustion models could be performed. But it is also possible to carry out global analysis in terms of the burning rate which is an important measure, for example in internal combustion diagnostics. In terms of the numerics, it is evident that the equation for  $\tilde{G}$  is solved by a different numerical procedure than the equations for the other quantities, which also has different numerical discretization errors. This can be especially important for thin turbulent flames, in which effects of unphysical reverse combustion may be predicted due to these numerical discretization differences. By determining a premixed reaction rate such numerical phenomena may be detected and eliminated.



The approach for determining  $\dot{\tilde{\omega}}_G$  is conceived around a conservation equation for the specific probability of finding *unburnt* gas  $\tilde{I}_u$ . The relationship to  $\tilde{P}_b$  is simply

$$\tilde{I}_u = 1 - \tilde{P}_b .^1 \quad (4.15)$$

In appendix A a transport equation is derived. Using  $\partial\tilde{I}_u/\partial\tilde{G} < 0$ , eqn. (A.8) reads:

$$\langle\rho\rangle\frac{\partial\tilde{I}_u}{\partial t} + \langle\rho\rangle\tilde{u}\cdot\nabla\tilde{I}_u = \langle\rho\rangle D_t'\tilde{\kappa}|\nabla\tilde{I}_u| - \langle\rho\rangle\dot{\tilde{\omega}}_G . \quad (4.16)$$

In order to calculate  $\dot{\tilde{\omega}}_G$ , eqn. (4.16) can simply be rearranged, obtaining the numerical reaction rate  $\dot{\tilde{\omega}}_G^{\text{num}}$ . The temporal derivative is simply discretized as

$$\langle\rho\rangle\frac{\partial\tilde{I}_u}{\partial t} \approx \frac{\langle\rho\rangle^{\text{nstep}+1}\tilde{I}_u^{\text{nstep}+1} - \langle\rho\rangle^{\text{nstep}}\tilde{I}_u^{\text{nstep}}}{\Delta t} , \quad (4.17)$$

in which the  $\text{nstep} + 1$  is the index for the new time level  $t^{\text{nstep}+1}$  and  $\text{nstep}$  for the corresponding old one. For  $t^{\text{nstep}}$  a field distribution of  $\tilde{I}_u$  is available. In order to obtain  $\dot{\tilde{\omega}}_G^{\text{num}}$  at the time level  $t^{\text{nstep}+1}$  the field of  $\tilde{I}_u$  is determined by  $\tilde{P}_b$  and therefore by the flamelet parameters  $\tilde{G}^{\text{nstep}+1}$ ,  $\tilde{G}''2^{\text{nstep}+1}$ , and the presumed pdf.

Alternatively, the premixed reaction rate could be determined using eqn. (A.9). Here, however, only the leading order influences of premixed reaction are included. Another problem arises if the turbulent flame brush becomes very small compared to the numerical grid resolution and thus spatial gradients of  $\tilde{I}_u$  become difficult to evaluate numerically. Furthermore, the calculation employing the transport eqn. (4.16) is the only possibility to detect unphysical reverse reaction due to different discretization errors of the numerical schemes employed.

After obtaining  $\dot{\tilde{\omega}}_G^{\text{num}}$ , equation (4.16) is solved again, applying a reaction rate according to

$$\dot{\tilde{\omega}}_G = \max\left(0, \dot{\tilde{\omega}}_G^{\text{num}}\right) , \quad (4.18)$$

clipping unphysical reverse reaction rates to zero.

The application of the transport equation for  $\tilde{I}_u$  in the framework of the  $G$ -equation concept is optional.

### 4.3.3 Model for thermodynamical states

In AC-FluX, as it was mentioned already in chapter 2.3, an enthalpy equation without source term due to combustion is solved. Therefore, a consistent determination of the

<sup>1</sup>The reason for introducing another probability  $\tilde{I}_u$  instead of  $\tilde{P}_b$  is merely of numerical nature. In AC-FluX, sink (i. e. negative source) terms in conservation equations for a general scalar  $\phi$  are linearized with respect to the scalar itself and treated implicitly. By deriving a conservation equation for  $\tilde{I}_u$ , the premixed reaction rate becomes a sink term in this equation. The resulting numerical linearization avoids negative numerical results for  $\tilde{I}_u$ , which would correspond to  $\tilde{P}_b > 1$ .

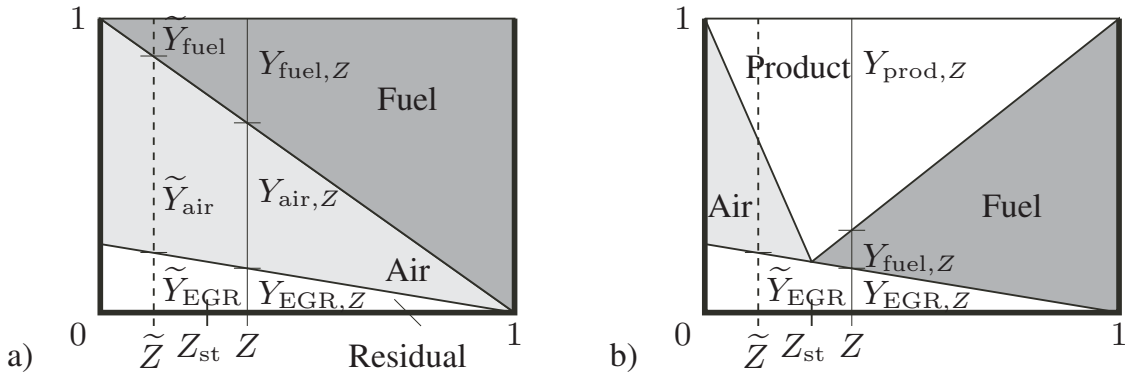


**Figure 4.4:** Presumed active streams distribution in the unburnt (a) and burnt (b) gas including residual (i. e. external and/or internal EGR) gas.

gas mixture properties, namely the chemical heat of formation, its heat capacity, and its molecular weight in each computational cell in the burnt and unburnt gas is required in order to obtain a correct heat release and flow coupling. Since the number of molecular species can be quite large and therefore can pose numerical efficiency and memory limitations, and additionally the combustion model only requires a few flamelet parameters, in the computations a small number of pseudo species are used instead of a large number of physical ones. Those pseudo species in the context of AC-FluX are denoted as “active streams”. The current implementation distinguishes between four active streams. These streams represent a pre-defined species composition, one each for air, fuel, burnt gas and inert residual gas, respectively. The inert residual gas – indexed by “EGR” (Exhaust Gas Recirculation) here – must be understood as a non-reacting component. However, it has an influence on the burning velocity  $s_L$  (see also appendix C) as bath gas. Here, the residual gas is defined as the mixed-equal burnt product of a stoichiometric fuel/air mixture. By means of this definition, the EGR stream can be used in order to represent parts of the residual burnt gas in an internal combustion engine from the previous cycle as well as external EGR. Compositions of lean or rich residual gas need to be accounted for by adjusting the (unburnt) air and fuel streams, respectively.

In fig. 4.4 the presumed active streams distribution over mixture fraction  $Z$  in case of stratified operation is depicted. Pure mixing is assumed for the unburnt condition, whereas infinitely fast chemistry is assumed for the burnt condition. Correctly, in order to account for fluctuations of residual gas, similar to the mixture fraction variance  $\widetilde{Z''^2}$ , a flamelet parameter equation for  $\widetilde{Y_{EGR}''^2}$  would strictly speaking be required. EGR is mixed with fresh air at early times. Therefore the magnitude of  $\widetilde{Y_{EGR}''^2}$  can be expected to be much smaller than that of  $\widetilde{Z''^2}$ , which is mainly due to fuel injection, and the variance of EGR can be neglected in order to reduce flamelet parameter space. If we assume that residual gas and air are locally perfectly mixed prior to fuel injection, a linear dependency between the instantaneous species distribution over mixture fraction space is obtained (see fig. 4.4a) for the unburnt. In the burnt gas (fig. 4.4b), the same

relationship is retained only between the stream mass fraction EGR and instantaneous mass fraction  $Z$ . The fuel stream mass fraction  $Y_{\text{fuel}}$  is assumed to be completely depleted in lean mixture ( $Z < Z_{\text{st}}$ ), and air is assumed to be consumed in rich mixture ( $Z > Z_{\text{st}}$ ). The consumed masses of air and fuel are then collected in the product stream mass fraction  $Y_{\text{prod}}$ .

Due to its inert nature a conservation equation is solved for the Favre averaged mass fraction of residual gas  $\tilde{Y}_{\text{EGR}}$ . The other averaged mass fraction streams are determined by the relationships as depicted in figure 4.4 using the flamelet parameters and  $\tilde{Y}_{\text{EGR}}$ .

In order to obtain Favre averaged mass fractions of these streams, integration over the instantaneous realizations in mixture fraction space using a presumed pdf (see section 3.5.7) is only required for the burnt state. Due to the linear dependencies in the unburnt, presumed pdf integration can here be omitted.



## Chapter 5

# Validations

In this chapter, the physical models developed for turbulent premixed combustion presented in the previous chapters are applied and validated against combustion cases that were experimentally investigated. At first, a combustion case in a non-moving cylindrical vessel is presented. Here, different approaches for the global flame front curvature and the expression of  $\tilde{\sigma}_t$  are compared to experimental results. Then, in the following two sections, the model will be tested in a realistic engine environment, first in homogeneous charge operation (section 5.2 and then in stratified charge mode 5.3 of a direct fuel injection engine.

### 5.1 Cylindrical Vessel experiment

In this section, the ignition and 3D combustion model based on the turbulent  $G$ -equation is initially validated against combustion experiments in a cylindrical vessel which were carried out by *Hamamoto et al.* [36, 35]. A homogeneous stoichiometric propane/air mixture is subjected to an axi-symmetric swirling flow, in which by varying the ignition timing during the swirl decay the effect of different swirl intensities are studied. Several model alternatives discussed in the chapters 3 and 4 are calculated and compared against the experimental results.

#### 5.1.1 Experimental setup

The experimental setup (see also fig. 5.1) is documented in various publications [35, 36, 37, 38, 39, 47]. The cylindrical vessel has a diameter of  $d = 125$  mm and an axial length of  $l = 35$  mm. It is charged through a swirl valve by means of a pressurized mixture tank, creating the swirling flow. At the end of charging, the valve is moved out of the vessel, thus closing it. Different swirl intensities are realized by igniting the mixture at different times after intake valve closure. Therefore this test case investi-

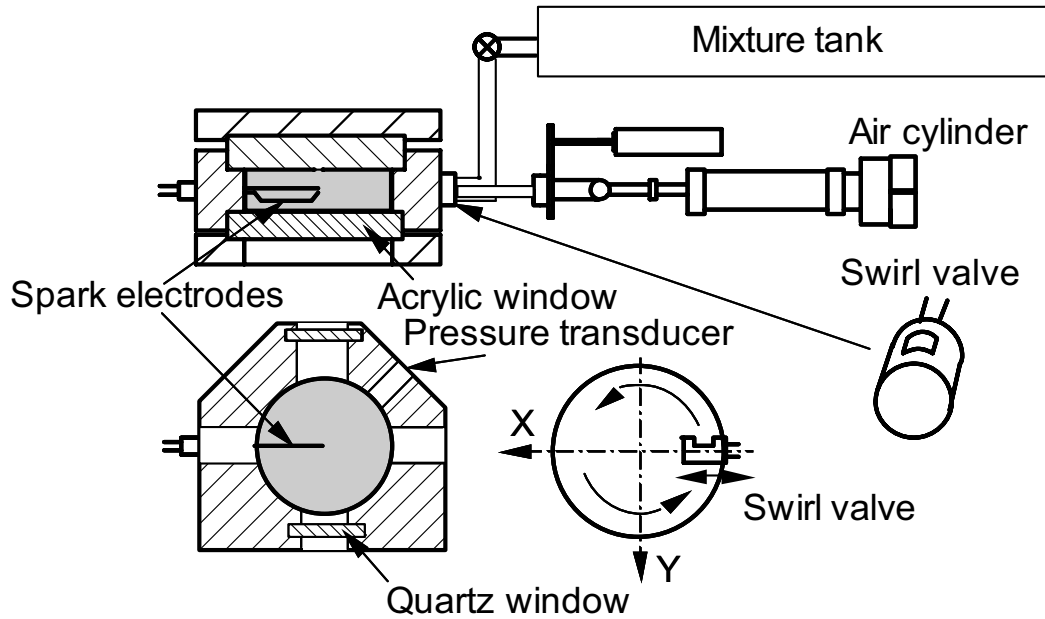


**Figure 5.1:** Sketch of the experimental setup for the cylindrical vessel as published by [47]

gates the behavior of the combustion model at the time of ignition, the development of the turbulent flame, and the flame quenching at the wall.

From the experimental investigations, pressure traces and, deduced from these, normalized heat release rates are reported. In addition, for each variation of ignition timing, averaged flame front contours obtained from schlieren measurements are recorded for different times of flame propagation.

The computational domain is initialized at  $t = 0$  (which corresponds to the time of valve closure) with a flow and turbulence field as given in table 5.1. This field is not uniform over the domain, the magnitude of the axial rotational frequency  $\omega$  is dependent on the radial distance  $r$  as well as to the distance from the upper and lower wall  $y_{w1}$  at  $z = \pm 17.5$  mm. The turbulent mixing length  $\ell_m$  is attenuated towards the walls to zero. The swirling flow is initialized such that the mean tangential velocities in the radial radial coordinate at  $z = 0$  match the experimental observations for different times after charging valve closure. The comparison in fig. 5.3 reveals good agreement between experiment and simulation.

The initial flame kernel volume is set to  $V_{\text{ign}} = 6.545 \times 10^{-11} \text{ m}^3$ , which corresponds to a kernel radius of  $r_{K,0} = 0.25$  mm. For simplicity, the spark energy release  $\dot{Q}_{\text{spk}}$  is assumed to be negligibly small. The ignition duration is assumed to be 2 ms. For the laminar burning velocity, a correlation for propane/air mixtures by Müller *et al.* [62] is employed as well as for the inner layer temperature  $T_0$ , which is used to determine the flame diffusivity  $D_0$  according to eqn. (3.12). In this case, best agreement to the experimental results is achieved by modifying the expression for the flame diffusivity by a constant factor of  $f_D = 1.76$  such that the effective diffusivity used in

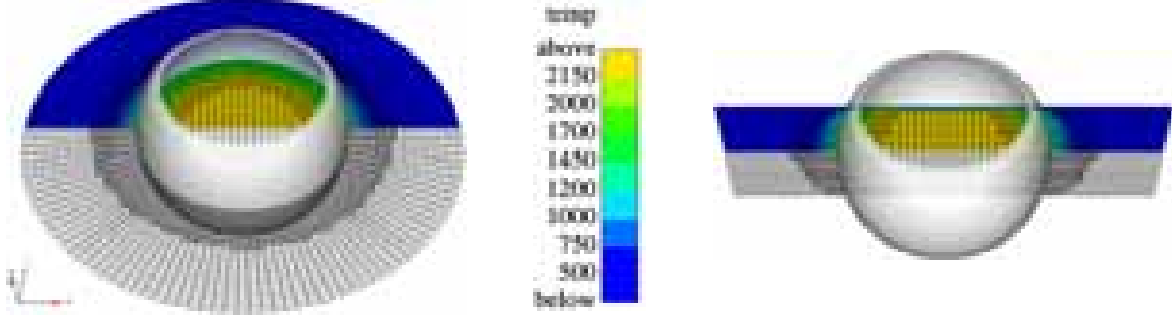


**Figure 5.2:** Horizontal (left) and vertical (right) cut through the computational mesh during combustion calculation using local grid refinement within the flame brush. On the right and left image the mean flame front surface is depicted. On the upper half of each image the temperature is depicted in false colors. Additionally, the mean flame front surface is shown as white translucent surface.

|               |  |
|---------------|--|
| $p$           | 243 kPa  |
| $T$           | 335 K  |
| $\omega$      | $\frac{5.05 \text{ m/s}}{r} \tanh \frac{r}{0.013 \text{ m}}, r = \sqrt{x^2 + y^2}$ |
| $\vec{u}$     | $\omega (\vec{e}_z \times \vec{x}), \vec{e}_z = (0, 0, 1)^T$                       |
| $k$           | $5.0 \frac{\text{m}^2}{\text{s}^2}$  |
| $\ell_m$      | $\min(8 \cdot 10^{-3} \text{ m}, \kappa y_{\text{wall}}), \kappa = 0.419$          |
| $\varepsilon$ | according to eqn. (2.46)   |
| $\phi$        | 1.0  |
| $\vec{G}$     | $\ll 0 \text{ m}$  |
| $\vec{G}''^2$ | $0 \text{ m}^2$  |

**Table 5.1:** Initialization of the cylindrical disk test case.

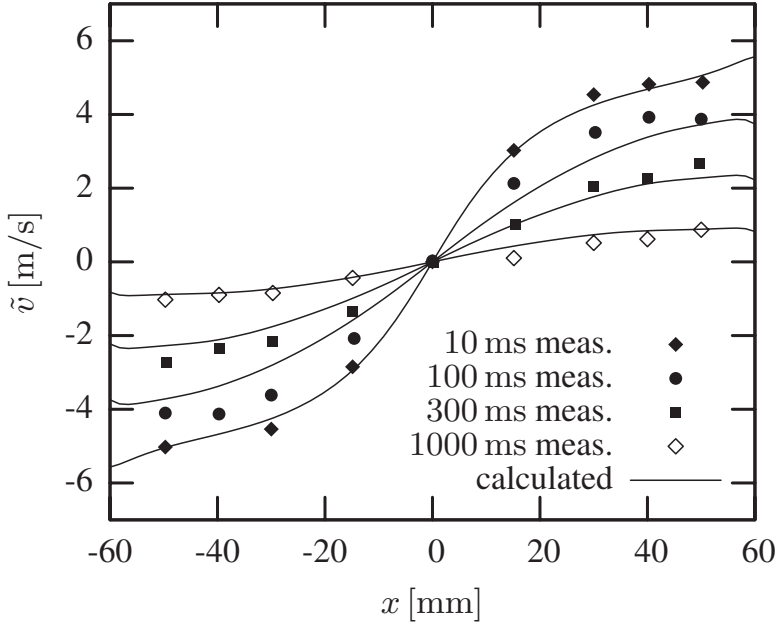


**Figure 5.3:** Radial velocity for the swirl decay of the non-reacting flow on the  $x$ -axis. The measured mean velocities immediately before ignition are compared to the computed mean velocities. The times given in the plots are related to the ignition times after charging valve closure.

the CFD calculation is

$$D_{\text{eff,CFD}} = f_D D_0|_{\text{approx. [62]}} \cdot \quad (5.1)$$

The inner layer temperature estimated according to [62] is  $T_0 = 1253$  K for this case of a stoichiometric propane/air premixed flame subjected to the initial conditions as given in table 5.1. Using eqn. (3.12) and (3.8) the corresponding flame diffusivity is  $D_0 = 2.74 \times 10^{-5} \text{ m}^2/\text{s}$ . On the other hand, the results presented in chapter 3.1.1 predict  $D_0$  to be approximately 20% larger, which is still smaller than the effective value that was finally taken.

The computational grid as depicted in figure 5.2 consists of 58311 base cells. During the combustion calculation, the mesh is refined by one refinement level in the region of the turbulent flame brush, where high spatial gradients of  $\tilde{I}_u$  exist, replacing the master cell by eight child cells in three dimensions. Due to the grid refinement, the boundary layer at the wall is assumed to be resolved and therefore the wall boundary condition for  $\widetilde{G}''^2$  is set to be zero.

### 5.1.2 Cold Swirl Flow

In figure 5.3 computed and experimentally measured radial mean velocities are compared for different computational times during swirl decay. The agreement of both flow patterns shows the validity of the chosen initial conditions.



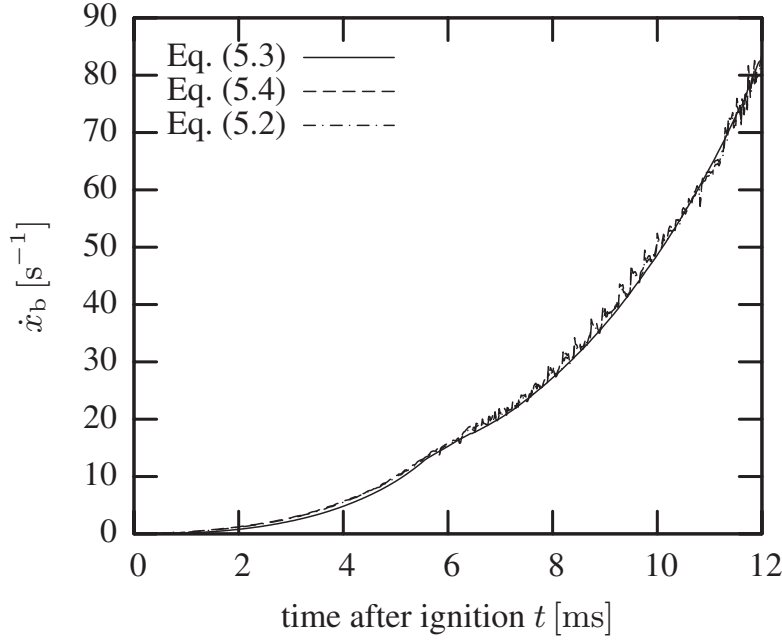


**Figure 5.4:** Comparison of normalized mass burning rates determined by three different approaches for the 10 ms ignition case. Hardly any difference can be seen between the results for eqn. (5.2) and eqn. (5.4).

### 5.1.3 Validity of Flamelet/Heat release coupling

At first we need to discuss the accuracy of the Level Set implementation with regards to the flow and heat release coupling. Prior to discussing the validity of the physical model for the turbulent mass burning rate it needs to be assessed whether the mass burning rate ( $\widetilde{\rho_u s_T}$ ) over the mean flame front surface is correctly expressed by the temporal mass balance change of burnt and unburnt gases.

With  $m_u$  and  $m_b$  being the global burnt and unburnt masses, respectively, one can formulate the temporal derivative of the normalized burnt gas mass fraction

$$\dot{x}_b|_1 = \frac{1}{\langle m_u \rangle + \langle m_b \rangle} \frac{d \langle m_b \rangle}{dt} \quad (5.2)$$

which is identical here to the normalized heat release rate.  $x_b$  is determined in 3D-space by the unburnt gas probability  $\tilde{I}_u$  (see section 4.3.2). It does not directly represent the predicted global heat release by the model, but rather the effective heat release that is practically applied to the flow by means of the numerical procedures described in section 4.3. On the other hand, the heat release is directly determined by the model by integrating the mass burning rate over the mean flame front surface:

$$\dot{x}_b|_2 = \frac{1}{\langle m_u \rangle + \langle m_b \rangle} \int_{\tilde{G}=G_0} \widetilde{\rho_u s_T} dA. \quad (5.3)$$

This is numerically determined in the CFD code by determining the  $G_0$  surface segment  $\delta A$  of each cell containing a part of the mean flame front, followed by a multiplication with the mass burning rate predicted by the thermodynamical and turbulent states of each cell.

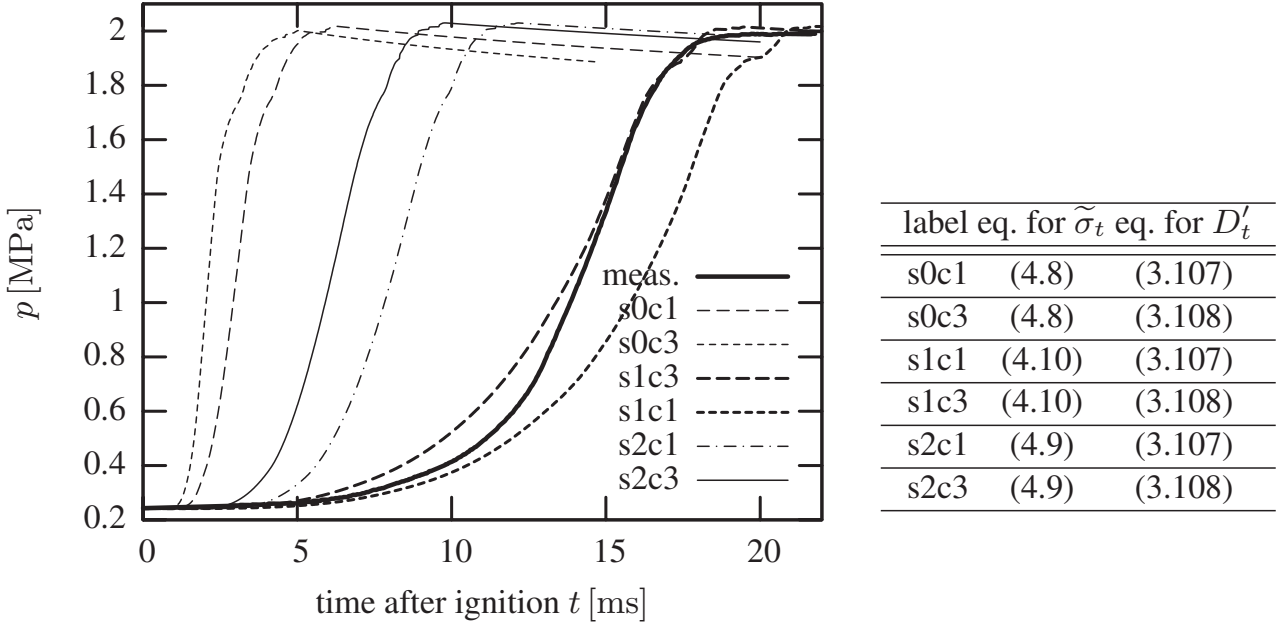


**Figure 5.5:** Comparison of different approaches for  $\tilde{\sigma}_t$  (4.7) and  $D'_t$  in the term for the mean curvature in equation (3.106).

The third approach is to spatially integrate the premixed reaction rate  $\tilde{\omega}_G$  obtained from eqn. (4.18):

$$\dot{x}_b|_3 = \frac{1}{\langle m_u \rangle + \langle m_b \rangle} \int_V \langle \rho \rangle \tilde{\omega}_G dV. \quad (5.4)$$

These three computed heat release rates can be compared without the need to discuss the correctness of the physical model for the turbulent mass burning rate. However, the physical model chosen in this work is already anticipated from the following section.

Figure 5.4 compares results for these three approaches with each other. The results for  $\dot{x}_b|_2$  and  $\dot{x}_b|_3$  are in very good agreement. This assesses the accuracy of the Finite Volume implementation only. However, oscillations can be observed for times  $t > 6$  ms, which can be traced back to two reasons: Firstly, the computational grid around the mean flame front surface for these times is coarser than before because local adaptive refinement is turned off. Secondly, flame/wall interactions take place. However, the results for  $\dot{x}_b$  are still in good agreement with the rate determined by means of eqn. (5.3).

#### 5.1.4 Evaluation of different approaches for turbulent flame surface and turbulent curvature terms

In section 3.5.3 a new expression for  $\tilde{\sigma}_t$ , eqn. (3.114), and different expressions for the effective turbulent diffusivity  $D'_t$  appearing in the curvature term of the closed equation for  $\tilde{G}$ , eqn. (3.106) were presented. Along with other modeling options using

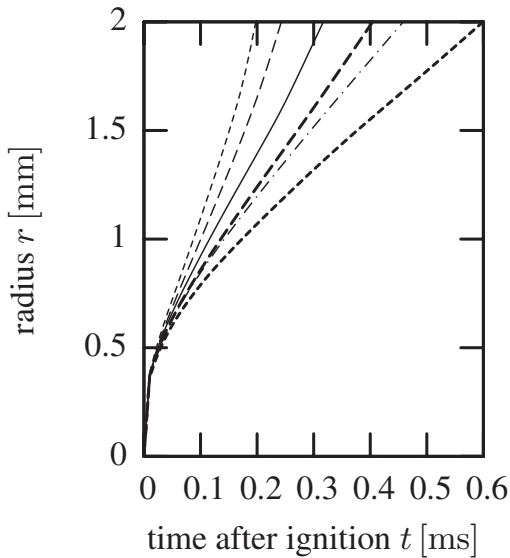


**Figure 5.6:** Spark kernel radius plotted over time for the 10 ms ignition case computed by different approaches for the  $\tilde{\sigma}_t$  equation and the diffusivity in the curvature term. The line styles in this plot correspond to those in figure 5.5. Immediately after ignition,  $r(t)$  shows concave behavior for all models. This is due to the electrical spark energy released into the hot gas which results in higher kernel temperatures and increased kernel expansion. This effect is attenuated with increasing kernel size.

an algebraic  $\tilde{\sigma}_t$ -equation as presented by *Peters* [71], two possible expressions for  $D'_t$  are combined with three possible algebraic expressions for the turbulent flame surface area ratio. From the CFD calculations for the 10 ms ignition test case, pressure curves are compared against the experimental measurement in figure 5.5 .

It can be clearly seen that the predicted increase of pressure for each of the three investigated versions of the algebraic  $\tilde{\sigma}_t$ -expression is lower with the “conventional” turbulent curvature approach (3.107) than with the mixing length type of approach (3.108). This can be explained by the fact that the turbulent diffusivity according to the conventional approach is non-zero already immediately after ignition. Curvature effects play an important role due to the small size of the ignition kernel. These curvature effects lead to a decreased kernel expansion velocity and possibly even to a quenched flame kernel [54]. With the mixing length approach based on the flame brush thickness on the other hand, turbulent curvature effects immediately after combustion are not predicted due to the zero initial condition of  $\widetilde{G}''^2$ .

Best agreement in terms of the pressure history is achieved with the  $\tilde{\sigma}_t$  equation according to (3.114) (with  $q = 0$ ) which is equal to (4.7) with (4.10). The other two approaches for  $\tilde{\sigma}_t$  predict flame propagation to be turbulent already immediately after ignition since they are not proportional to the laminar flame brush thickness  $\ell_{f,t}$ . The prediction of increased flame propagation for small kernels cannot be compensated by the conventional diffusivity approach in the turbulent curvature term such that agreement between experimental and modeled pressure history can be achieved. Finally, it is important to remark that the difference in results for all of these three models is only due to the different behavior immediately after ignition where the turbulent flame brush is not fully developed, that is,  $\ell_{f,t} < \ell_{f,t,alg}$  .

In figure 5.6 the radius of the flame kernel is plotted over time when the spark ignition model is in use. The final calculations employed the  $r_K \geq 2$  mm criterion to switch from the ignition model to the 3D-equations. It can be clearly seen that already

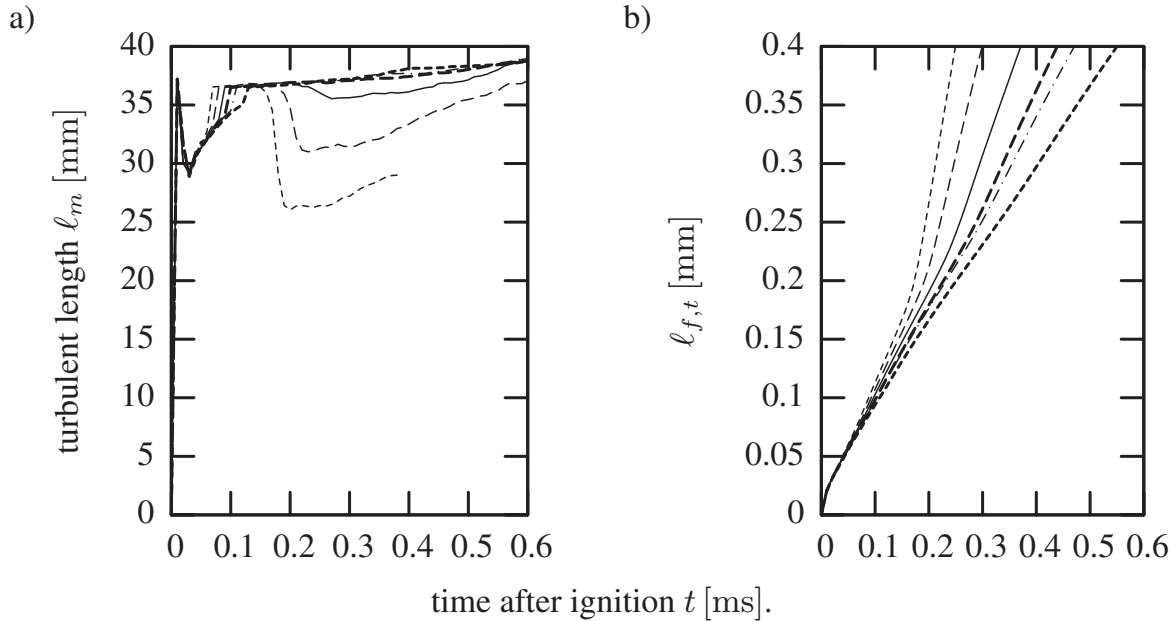


**Figure 5.7:** a) Turbulent mixing length  $\ell_m$ . b) Development of the flame brush thickness of the spark kernel over time. Again, the line styles correspond to those in figure 5.5. For this plot and the following one, the spark ignition model was continued beyond the switch criterion  $r_K \geq 2$  mm.

at very early stages of flame expansion, the chosen model for  $\tilde{\sigma}_t$  and the curvature contribution have a significant influence on the expansion rate, while the scale of the turbulent flow essentially remains constant, as long as the expansion speed is moderate. This is depicted in figure 5.7a, where the turbulent length is plotted for all model configurations. Therefore, at the initial stage of kernel expansion, the flow around the kernel remains almost undisturbed by the kernel expansion, because the size of the kernel is much smaller than the largest turbulent eddies. However, this is not the case for the flame brush thickness; figure 5.7b shows that the larger the flame kernel, the larger  $\ell_{f,t}$ , which can be explained by the fact that only turbulent eddies equal or smaller than the size of the flame kernel can interact with the kernel (see also section 3.6.2).

However, the variation of the turbulent flame brush thickness evolution at very early times ( $< 0.2$  ms), can be neglected in comparison to the differences in modeling of  $\tilde{\sigma}_t$  and the turbulent curvature term  $-\kappa D'_t$ . This is shown in figure 5.8. Although the influence of laminar flame curvature (fig. 5.8c) is large, especially for small kernels, this effect is more and more attenuated when the flame kernel expands. On the other hand, the influence of turbulent mean curvature still increases for the time period shown because the decrease in mean flame kernel curvature is compensated by the increase in kernel size and therefore by the ability to interact with larger turbulent structures.

In terms of spark ignition, it was assumed that the initial flame propagation is driven by laminar effects. The laminar burning velocity with respect to the unburnt gas  $s_{L,u}$  was obtained from burning velocity approximations as 42.9 cm/s. This seems to be most accurately recovered for the expansion velocity  $s_{T,\kappa}$  as shown in fig. 5.8b by the

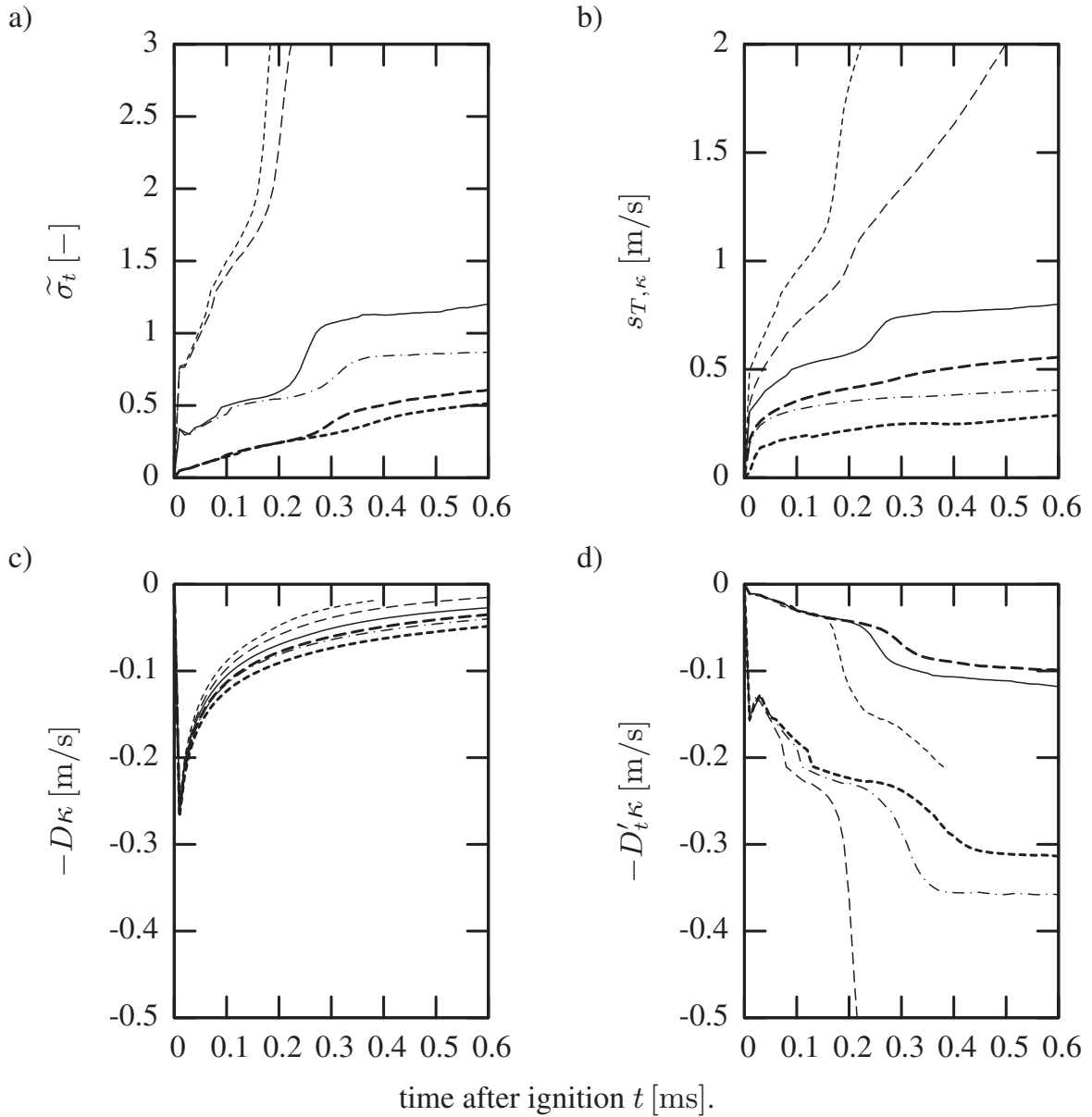


**Figure 5.8:** a) Turbulent flame surface area ratio of the spark kernel for different modeling options b) Modified turbulent burning velocity of the spark  $s_{T,\kappa}$  according to eqn. (3.149). c) Contribution of laminar kernel curvature to  $s_{T,\kappa}$ . d) Contribution of turbulent mean curvature to  $s_{T,\kappa}$ . For all plots the time after ignition for the 10 ms case is shown on the abscissa. Again, the line styles correspond to those in figure 5.5.

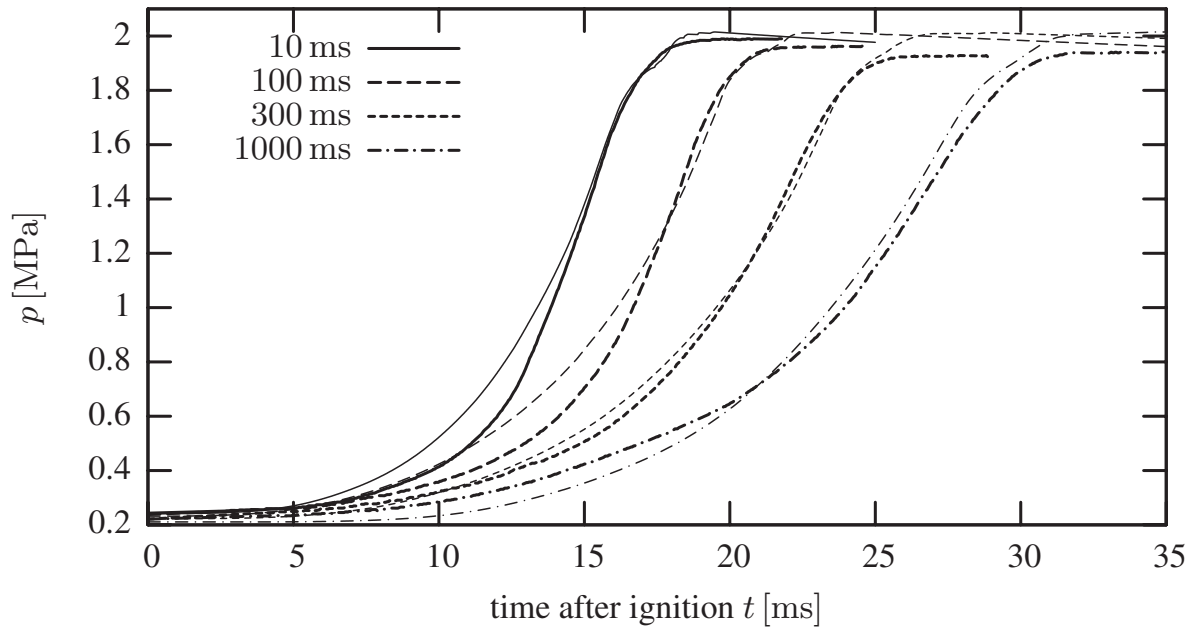


**Figure 5.9:** Comparison between experimentally observed (thick lines) and numerically predicted pressure histories (thin lines) for different ignition timings. Eqn. (3.114) was employed in order to determine  $\tilde{\sigma}_t$ . The turbulent diffusivity in the curvature term of the  $\tilde{G}$ -equation was determined according to eqn. (3.108).

model choice ‘s2c1’. However, the resulting expansion velocity from this model is a superposition of turbulent flame speed and the influence of mean curvature.

As a conclusion from this investigation, the algebraic  $\tilde{\sigma}_t$ -expression according to (3.114) with the turbulent diffusivity (3.108) for the curvature term in the  $\tilde{G}$  equation was chosen for all combustion calculations.

### 5.1.5 Discussion of results with swirl variation

In figure 5.9, the measured and calculated pressure histories are depicted for different ignition timings, employing model chosen in the previous section. Experimentally measured pressure traces are only available for the time during pressure rise. Unfortunately, experimental data are not available thereafter [103], for example in order to study heat losses to the walls after combustion. The over-all agreement between experiment and simulation is good, however, for the 10 ms case the predicted pressure is initially higher than in the corresponding experiment, but eventually both traces are in good agreement again.

In figure 5.10, the total mass burning rate  $\dot{x}_b$  normalized by the total cylinder mass is displayed. The experimental and numerical results were obtained by means of different approaches. The experimental results were determined by evaluating the pressure trace using an assumption for the heat capacity ratios in the burnt and unburnt gas according to Lavoie [51]. The numerical results, on the other hand, were determined

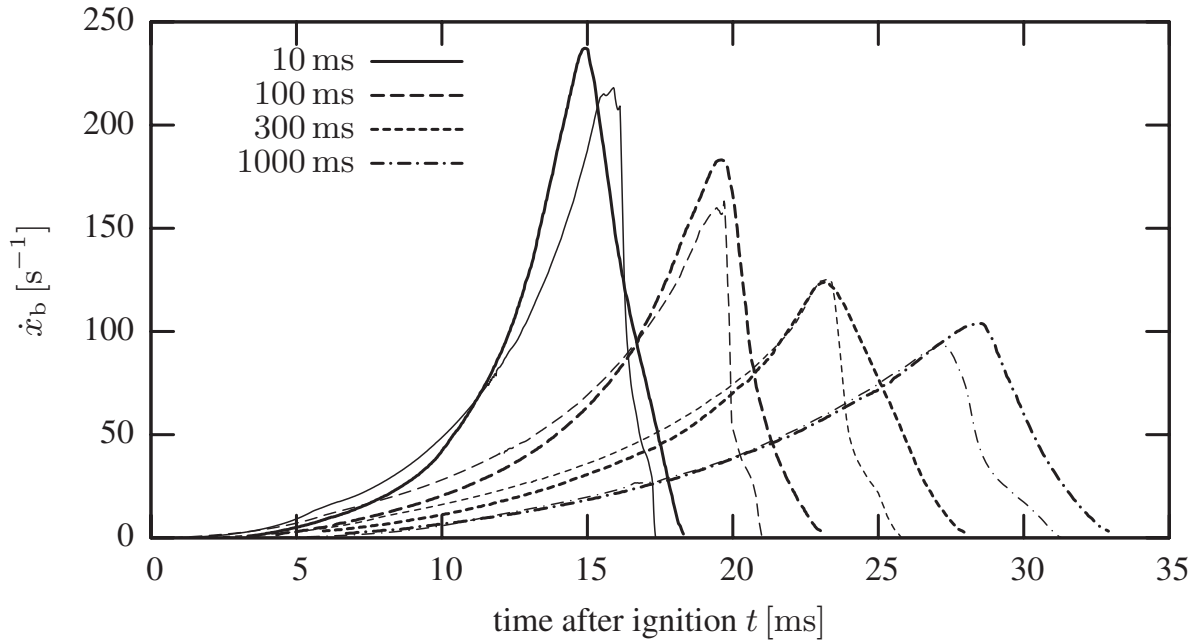


**Figure 5.10:** Comparison between the normalized mass burning rate obtained from the experimentally measured pressure history (thick lines) and the normalized first temporal derivative of the numerically predicted burned mixture mass (thin lines).

from the integrated turbulent mass burning rate over the mean flame front area, taking the temporal derivative, eqn. (5.2). Both approaches do not necessarily lead to the same results because the heat losses to the walls need to be sufficiently accurately quantified for an accurate determination of the burnt gas fraction from the pressure curves. Here, the agreement between experiment and simulation is acceptable, and the shapes of the normalized mass burning rates are similar. This applies to the increase phase before reaching the maximum burning rate as well as to the phase hereafter. Furthermore, the better the agreement in terms of pressure, also the better in terms of mass burning rate.

In figure 5.11, flame shapes obtained from experiment and simulation are compared. The flame contours obtained from the experiment do not represent the mean flame front position but a front of the turbulent flame brush ahead of the mean flame front. The visualization of the numerical results accounts for this by plotting both the mean flame front position  $\tilde{G} = G_0$  and the position  $\tilde{I}_u = 0.75$  ahead of it. Therefore the distance between these two lines represents half of the flame brush thickness.

Good agreement of turbulent flame contours is achieved for with ignition timings 300 ms and 1000 ms and for 100 ms the agreement is still acceptable. For the 10 ms case, the experimentally observed contours are more ellipsoidal than those numerically predicted. This is argued to be due to the assumed initial condition of the turbulent flow at charge valve closing and the initial values of the turbulent quantities  $k$  and  $\varepsilon$ . For all cases, the cold flow simulation started at intake valve closure,  $t = 0$ . Therefore, the flow, the turbulent fields of  $k$  and  $\varepsilon$ , and the boundary layers at start of combustion had more time to develop for the cases with later ignition timings.

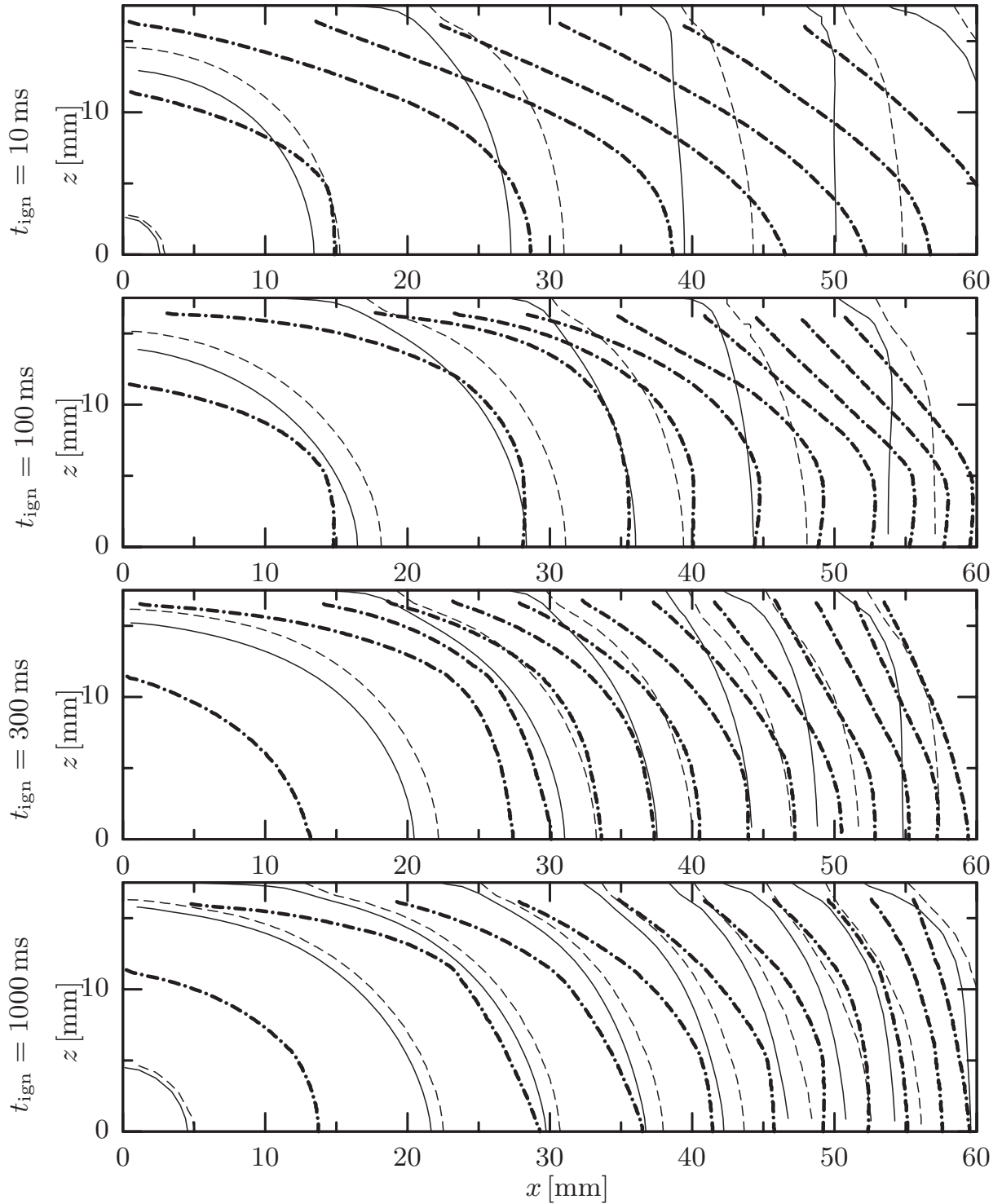


**Figure 5.11:** Comparison of measured flame fronts (thick dot-dashed lines) with calculated  $\tilde{G} = G_0$  positions (thin solid lines) and  $\tilde{I}_u = 0.75$  (thin dashed lines) for different ignition timings and different times after ignition, respectively. For  $t_{\text{ign}} = 10$  ms, fronts 4.2, 6.4, 8, 9, 10, 11, and 12 ms after ignition are depicted, for  $t_{\text{ign}} = 100$  ms, fronts 4.3, 8.15, 10, 11, 12, 13, 14, 15, 16, and 17 ms after ignition, with  $t_{\text{ign}} = 300$  ms, 13 different fronts for 4.8, 9.3, and 10 to 20 ms with an interval of 1 ms are plotted, while for  $t_{\text{ign}} = 1000$  ms 10 fronts at 4.9, 9.7, and 12 to 26 ms with an interval of 2 ms are depicted.



|                                  |              |
|----------------------------------|--------------|
| Bore                             | 86 mm        |
| Stroke                           | 86 mm        |
| Displacement                     | 0.5 L        |
| Compression ratio                | 10.3         |
| Manifold Absolute Pressure (MAP) | 95 kPa       |
| Intake air temperature           | 95°C         |
| Coolant and oil temperature      | 90°C         |
| Intake valve closing             | -119°CA aTDC |

**Table 5.2:** Engine specifications for both the homogeneous as well as the stratified charge operation mode as published in [20].

| case | $\phi$ | N <sub>2</sub> [%] |
|------|--------|--------------------|
| I    | 0.6    | 0                  |
| II   | 0.6    | 15                 |
| III  | 0.6    | 30                 |
| IV   | 0.8    | 30                 |

**Table 5.3:** Specifications of homogeneous charge operation points studied

|                      |            |
|----------------------|------------|
| Engine speed         | 2000 r/min |
| Ignition advance     | 40°bTDC    |
| Spark duration       | 2 ms       |
| Spark energy         | 60 J/s     |
| Initial Spark radius | 1.00 mm    |
| $r_{K,0}$            |            |

**Table 5.4:** Engine specifications for the homogeneous charge operation mode, used in the computation.

## 5.2 Homogeneous charge SI engine

In the two following sections, experimental investigations and numerical results obtained from a Spray Guided Spark-Ignition Direct-Injection (SG-SIDI) engine setup are compared with each other. The engine was operated [55] both in a direct-injected as well as in a homogeneous charge mode, whereas the latter modes is presented in this section. The stratified mode follows in section 5.3. The four-valve single cylinder engine has a pentroof-head. In table 5.2 engine operating conditions for both homogeneous and stratified charge operation are given. For all cases studied, identical valve timings were employed.

### 5.2.1 Setup for homogeneous charge

The fuel used in homogeneous charge operation mode is propane. The fuel/air mixture is provided at two different equivalence ratios  $\phi$ , and the corresponding mixtures are also diluted with different amounts of nitrogen addition, serving as a substitute for EGR. The engine speed is constant.

The spark timings for the different dilution cases are the same. This allows for the study of effects of varying laminar burning velocities and laminar flame thicknesses on combustion. The width of the spark plug electrodes was 2.8 mm and the spark electrode gap 2.2 mm. However, the amount of heat released is significantly different for all of these cases.

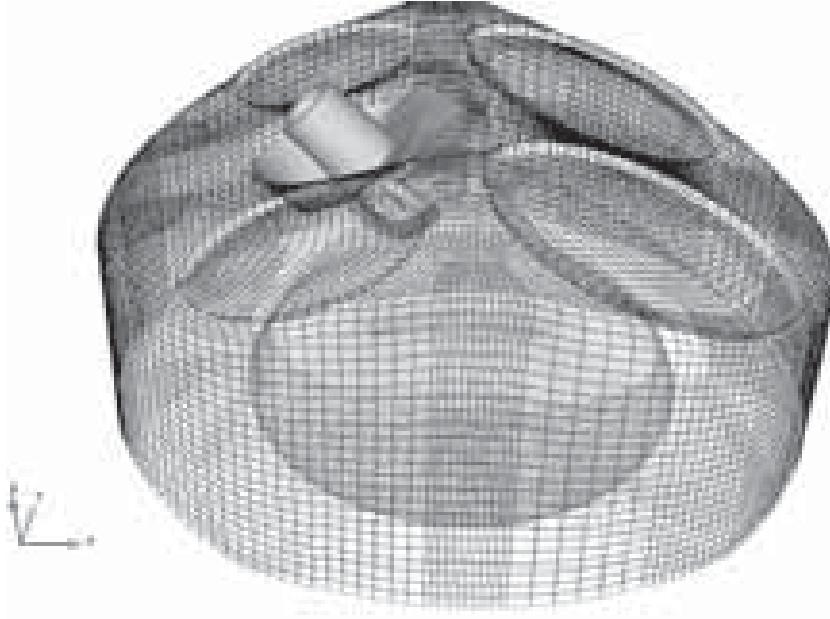


**Figure 5.12:** Unstructured computational grid of the closed engine geometry highlighting the modeled spark plug. This mesh comprises 302,000 grid cells.

## 5.2.2 Setup of numerical calculation

Two meshes are employed for the numerical computation, one with the intake manifold starting shortly after  $366^\circ\text{CA}$  aTDC until  $630^\circ\text{CA}$  aTDC at which an interpolation of the numerical results (“remap”) to the closed geometry is carried out.

The initial spark kernel radius is assumed to be  $r_{K,0} = 1$  mm. Therefore, the initial spark plasma size is of the order of the spark gap size in the model. The spark ignition model is switched to the 3D equations at approximately 2.5 mm spark kernel radius.

The laminar burning velocities are calculated by the approximative relationships already discussed in the previous section [62]. However, the nitrogen dilution requires further assumptions. This is realized by adjusting the burnt gas temperature  $T_b$  in the approximations in accordance with the same approach as for the iso-octane laminar burning velocity approximation in appendix C. The results of the laminar burning velocities thus obtained at the spark location for the time of ignition are compared to 1D DNS code results from FlameMaster and henceforth accordingly adjusted.

The value of the flame diffusivity  $D_0$ , however, was scaled using the adjustable parameter  $f_D$ , see eqn. (5.1). The adjustment factor  $f_D$  was varied for the computations between 0.1 and 0.16.

## 5.2.3 Results

At first, we will discuss results for case I in order to find an appropriate choice for the model parameter  $q$  in eqn. (3.114). In figures 5.13 and 5.14 the shapes of the mean flame front and the turbulent flame brush are depicted for different two crank angles and the two chosen values of the model parameter  $q$ , respectively. In both cases it can

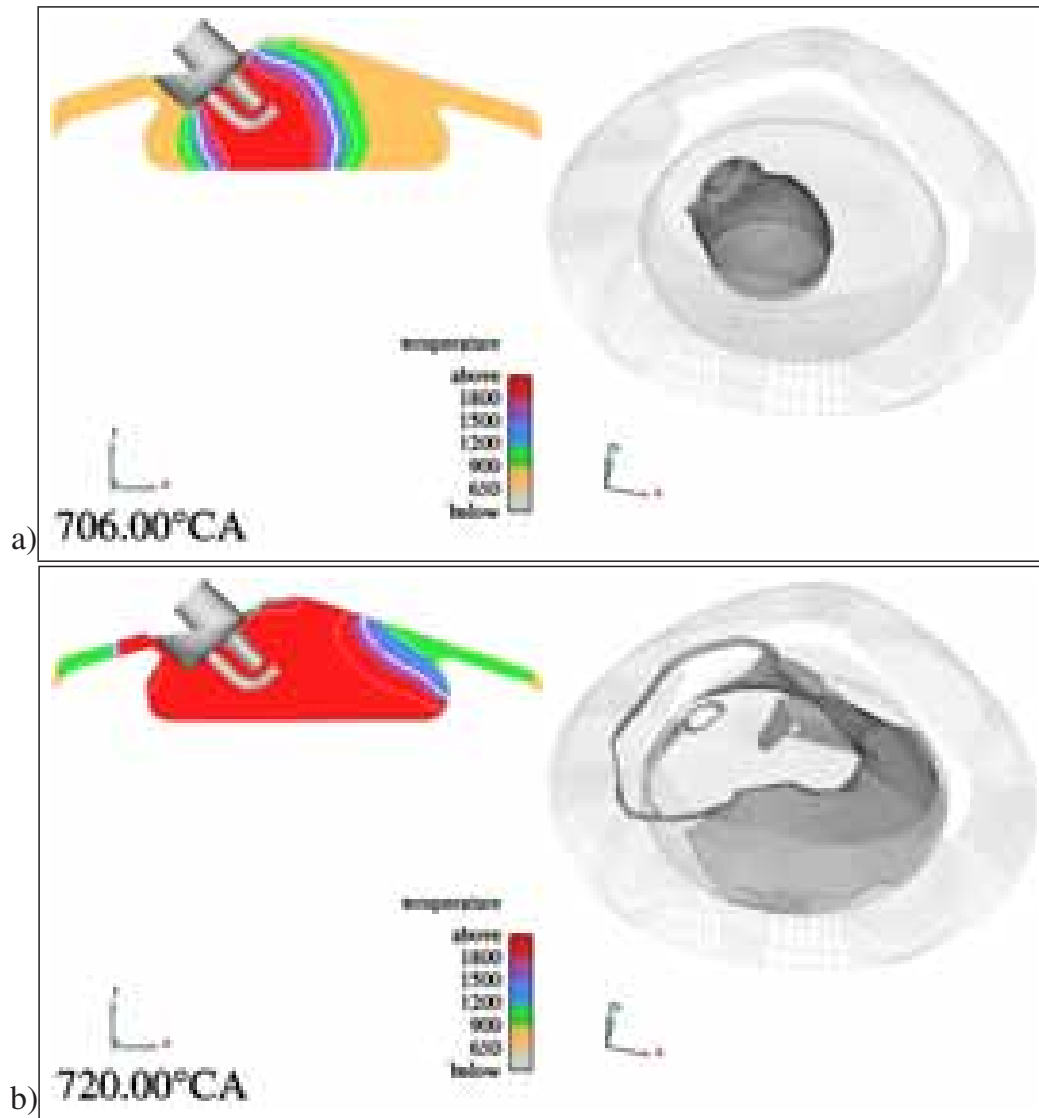


**Figure 5.13:** Plot of color coded averaged temperature and mean flame front position including the turbulent flame brush on a vertical cross-section through the cylinder (left images) and mean flame front surface in 3D space (right images) for two crank angle positions. Both plots are depicted for case I and parameter  $q = 0$  in eqn. (3.114).

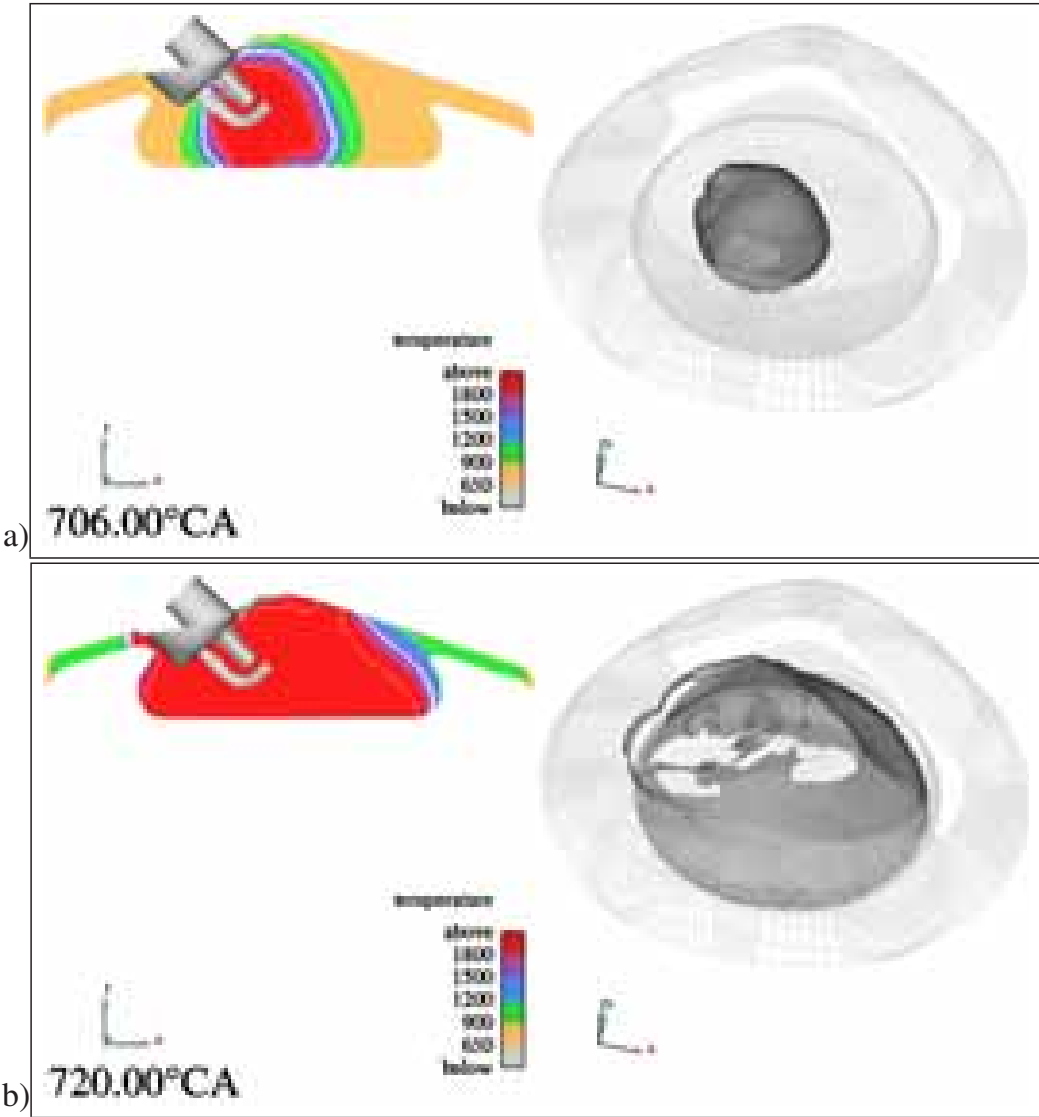
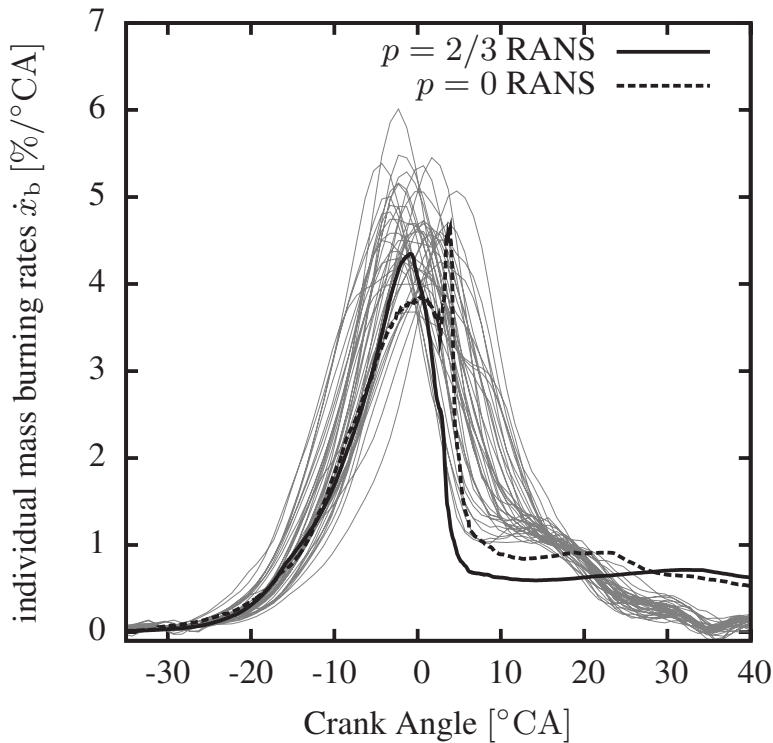


Figure 5.14: Same plots as in figure 5.13, but with  $q = 2/3$ .



**Figure 5.15:** Comparison of experimentally cycle-to-cycle resolved mass burning rates (gray) to RANS CFD obtained results (black) for both the modeling parameter  $q = 2/3$  used throughout this section and  $q = 0$  as defined in equation (3.114). The results for operating case I are shown.

be seen that at about  $720^\circ\text{CA}$  the flame enters the squish region. For  $q = 0$  the flame has a concave curvature towards the unburnt gas directly at the wall which indicates that there is an increase of predicted burning velocity. For  $q = 2/3$ , this behavior is not observed and the flame at the wall is convex towards the unburnt which seems to be more plausible.

In figure 5.15, a comparison of cycle-to-cycle resolved experimentally indicated mass burning rates and the RANS calculations with different values for  $q$  is depicted in order to assess an appropriate choice for  $q$ . It can be seen that the calculated mass burning rates are in the range of the different cyclic resolved realizations for both parameter values, except for the phase after Top Dead Center (TDC), in which lower mass burning rates are predicted. However, it can be seen that the predicted mass burning rate curves for both values of  $q$  exhibit the same slope as several individual cycles of the experiment shown in the figure. For  $q = 0$ , a sharp peak at about  $5^\circ\text{CA}$  after TDC is observed. For a short time period, when the turbulent flame approaches the wall, the ratio  $\ell_{f,t}/\ell_{f,t,\text{alg}}$  is greater than unity which results for  $q = 0$  in a significant increase in turbulent burning velocity. This behavior is not observed for  $q = 2/3$ .

The observations made here and the variations in computed mean heat release rate lead to the conclusion that the parameter  $q = 2/3$  is more plausible than  $q = 0$  for the engine case. Therefore  $q = 2/3$  was chosen for all engine calculations.

The experiments revealed that for three operating points the engine ran stable and with a low Coefficient Of Variability (COV) of Inner Mean Effective Pressure (IMEP), that is,  $\text{COV} < 3\%$  for the cases I, II, and IV. In these cases no misfires were encoun-

| case | $^{\circ}\text{CA}$                                      | $T_u$ [K]                     | $s_L^0$ [m/s]                 | $\ell_f$ [mm]              | $\ell_{f,t}$ [mm]    | $r_K$ [mm] |
|------|--|-------------------------------|-------------------------------|----------------------------|----------------------|------------|
| I    | 680.25   | 631                           | 0.28                          | 0.01                       | 0.12                 | 1.03       |
| II   | 680.25   | 629                           | 0.12                          | 0.02                       | 0.12                 | 1.02       |
| III  | 680.25   | 615                           | 0.01                          | 0.18                       | 0.12                 | 1.00       |
| IV   | 680.25   | 635                           | 0.20                          | 0.01                       | 0.12                 | 1.02       |
| case | $\tilde{\sigma}_t$                                       | $\ell_{f,t,\text{alg}}$ [mm]  | $\kappa D$ [m/s]              | $\kappa D'_t$ [m/s]        | $s_{T,\kappa}$ [m/s] |            |
| I    | 1.99   | 4.09                          | $6.04 \times 10^{-3}$         | 0.15                       | 0.68                 |            |
| II   | 2.52   | 5.03                          | $3.84 \times 10^{-3}$         | 0.17                       | 0.26                 |            |
| III  | 2.78   | 4.82                          | $3.83 \times 10^{-3}$         | 0.17                       | -0.13                |            |
| IV   | 2.22   | 4.78                          | $4.26 \times 10^{-3}$         | 0.16                       | 0.49                 |            |
| case | $\hat{k}_{\text{spk}}$ [m <sup>2</sup> /s <sup>2</sup> ] | $\tau_t = k/\varepsilon$ [ms] | $\widetilde{\Sigma}_t$ [1/mm] | $r_{k,t,\text{crit}}$ [mm] |                      |            |
| I    | 4.52   | 1.41                          | 13.65                         | 1.20                       |                      |            |
| II   | 3.91   | 1.73                          | 18.50                         | 0.90                       |                      |            |
| III  | 3.94   | 1.67                          | 24.43                         | 15.58                      |                      |            |
| IV   | 3.89   | 1.68                          | 15.34                         | 0.65                       |                      |            |

**Table 5.5:** Thermodynamical and turbulent flow conditions at the spark location at the time of ignition.

tered. For case III, however, 86% of the cycles were identified as misfires. Therefore we will discuss ignition simulation results for all four cases first and then only focus on cases I, II, and IV for discussion of the combustion in 3D space.

In order to predict successful and unsuccessful ignition strategies, we will at first discuss the results from the ignition model. In view of eqn. (3.149)

$$s_{T,\kappa} = s_T - \kappa(D_0 + D'_t),$$

the criterion for successful ignition would be  $s_{T,\kappa} > 0$ . We can now insert eqns. (3.8), (3.33), and (3.108) into (3.149). By linearizing the equation (3.114)  $\tilde{\sigma}_t$  using the turbulent flame brush thickness such that

$$\tilde{\sigma}_t = \ell_{f,t} \widetilde{\Sigma}_t \quad (5.5)$$

and decoupling laminar from turbulent effects, we obtain two constraints. Concerning laminar effects it is required that

$$1 - 2 \frac{\ell_f}{r_k} > 0 \quad \Rightarrow \quad r_K > 2\ell_f, \quad (5.6)$$

while the turbulent condition for successful ignition reads

$$s_L \widetilde{\Sigma}_t - \frac{2c_\kappa}{r_K} \hat{k}_{\text{spk}} > 0 \quad \Rightarrow \quad r_K > \frac{2c_\kappa \hat{k}_{\text{spk}}^{1/2}}{s_L \widetilde{\Sigma}_t} \equiv r_{k,t,\text{crit}}, \quad \text{where } c_\kappa \equiv \sqrt{\frac{c_\mu c_s}{\text{Sc}_t}}. \quad (5.7)$$

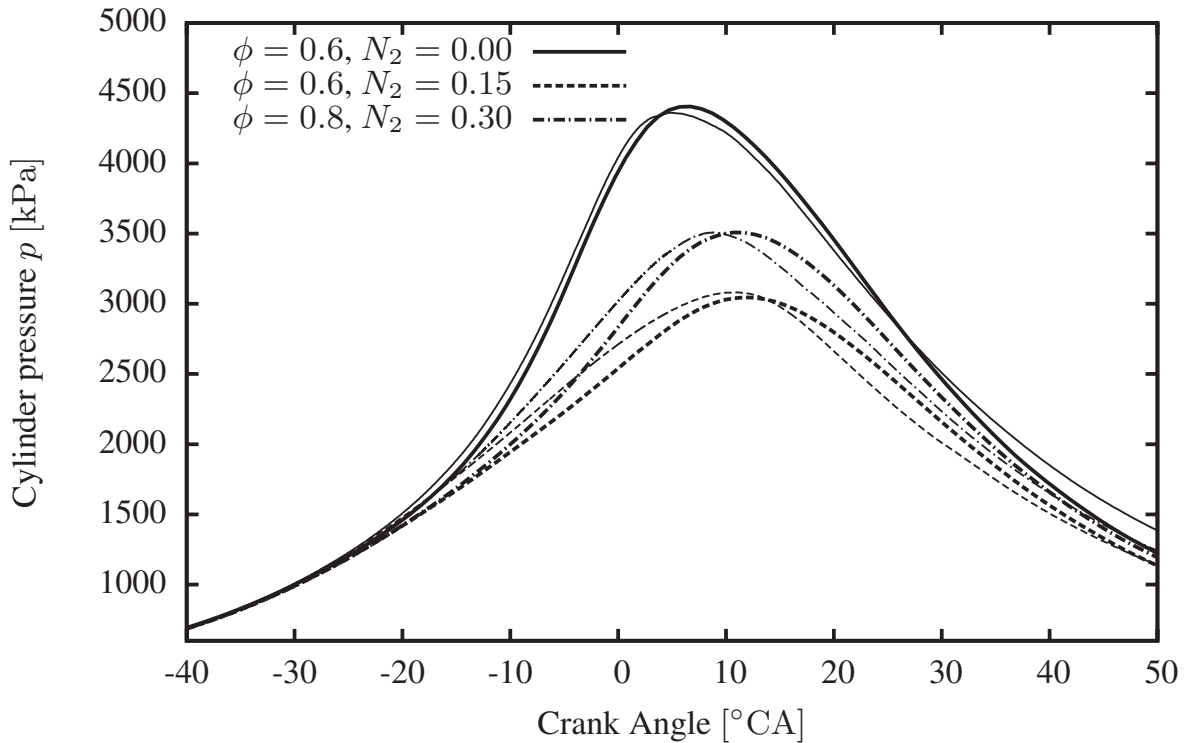


**Figure 5.16:** Cylinder pressure comparisons between experiments (thick lines) and simulations (thin lines) for those operating points for which no misfires were encountered.

In table 5.5 conditions immediately after ignition were determined for all four cases. It is evident that  $s_{T,\kappa}$  is negative for case III, one indicator for unsuccessful ignition. Because  $s_{T,\kappa}$  is based on the  $\tilde{\sigma}_t$  expression with  $q = 2/3$ , it tends to predict higher turbulent burning velocities during the evolution of the turbulent flame brush thickness  $\ell_{f,t}$  than with  $q = 0$ . This is depicted in figure 3.10. The quantity  $\tilde{\Sigma}_t$ , eqn. (5.5) is based on (3.114) with  $q = 0$  and therefore independent of  $\ell_{f,t}$ . In fig. 3.10 it can be seen that  $\tilde{\sigma}_t$  determined with  $q = 0$  is smaller for developing flames than with  $q = 2/3$ . Therefore,  $\tilde{\Sigma}_t$  is a safe estimation with respect to a successful ignition criterion based on a curvature and flame propagation balance.

In figure 5.16-5.18 the results from simulations are compared to cycle averaged results from the experimental measurements. As can be seen, all pressure traces are in reasonable to good agreement. However, the calculated maximum pressure for all cases is reached few degrees crank angle prior to the averaged measured maximum pressure. The cylinder pressure is slightly overpredicted for the cases with nitrogen dilution during the pressure rise phase, while during the pressure decrease it is slightly underpredicted. In terms of the averaged burnt fuel mass fractions, it can be seen that until approximately 50% fuel is burnt, the agreement between RANS-CFD and the experimental average is good, for the 0%  $N_2$  and 15%  $N_2$  nitrogen dilution cases even is very good. This indicates that early combustion after spark ignition is well predicted. Above 50% burnt, heat release rate is underpredicted. Analysis of the spatial CFD

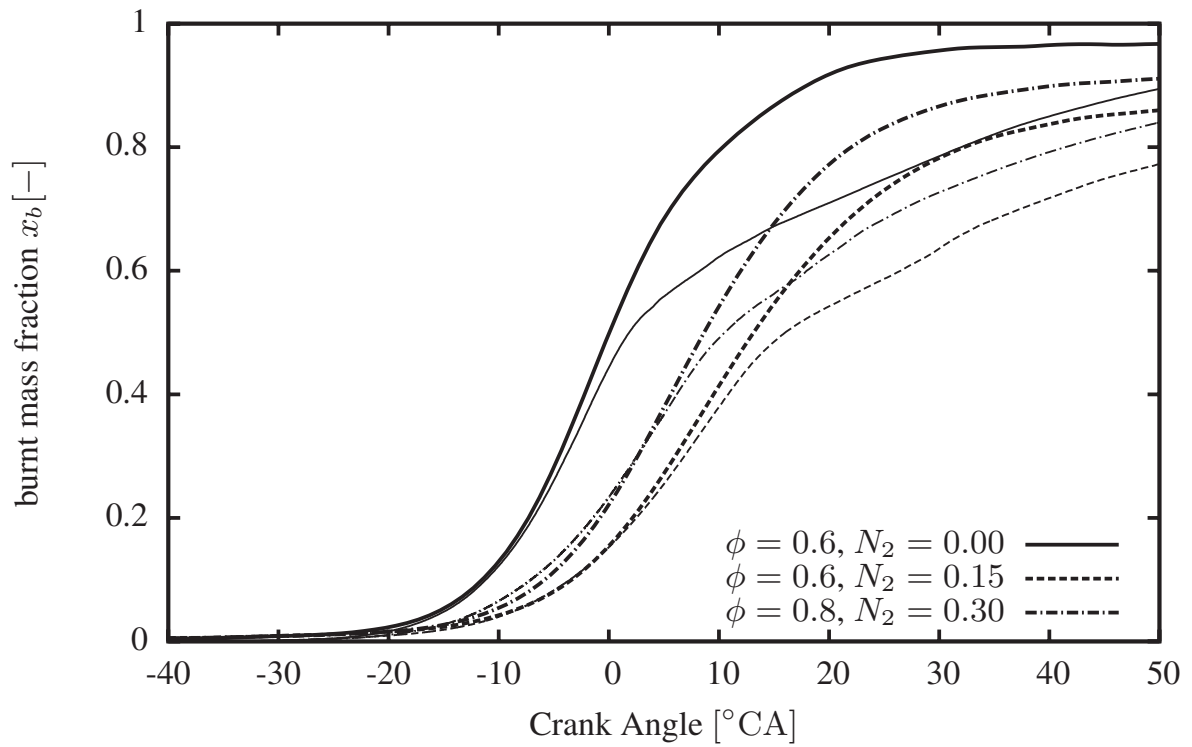


**Figure 5.17:** Comparison between numerically and experimentally obtained burnt fuel mass fractions. The line styles correspond to those in figure 5.16.

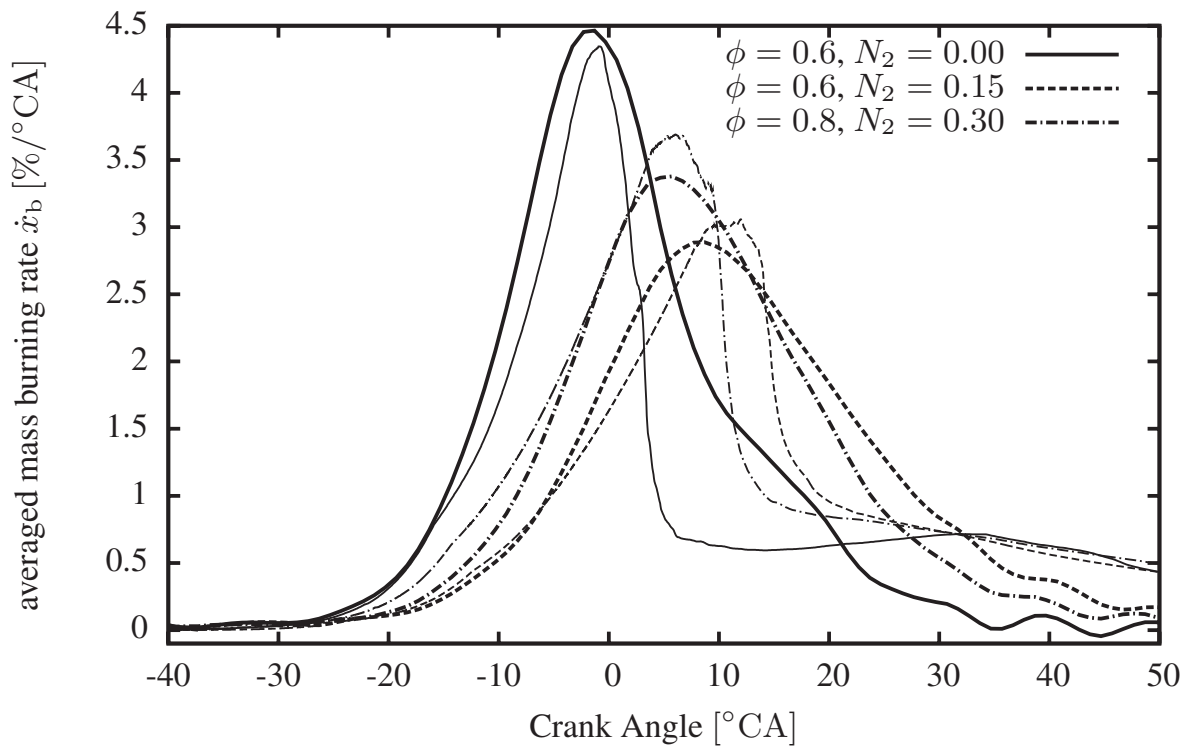


**Figure 5.18:** Comparison between numerically and experimentally obtained fuel mass burning rate. The line styles correspond to those in figure 5.16.



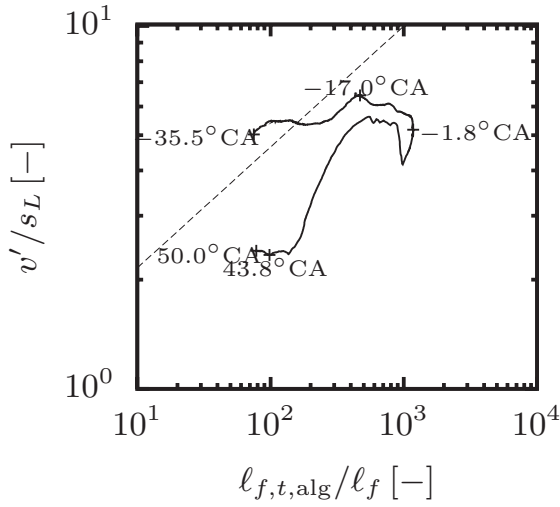


**Figure 5.19:** Phase diagram for case I of the non-dimensional turbulence intensity  $v'/s_L$  over the non-dimensional turbulent length scale  $\ell_{f,t,alg}/\ell_f$ . In correspondence to the logarithmic scaling of the plot on both axes, the logarithms of both ratios are averaged over the mean flame front surface for the corresponding crank angle position. The dashed line indicates the regime boundary between the corrugated flamelets and the thin reaction zones regime (see figure 3.8).

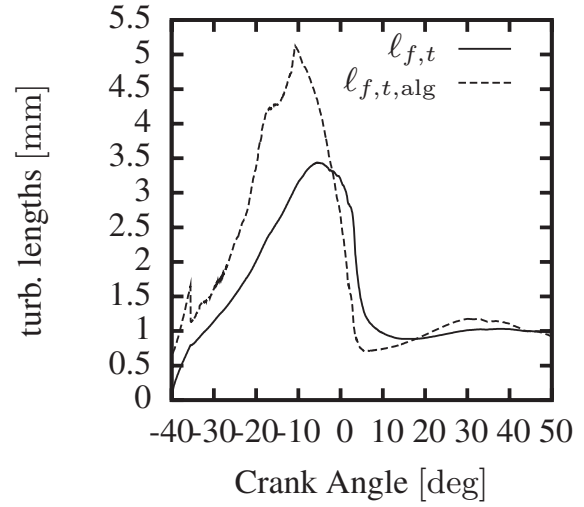


**Figure 5.20:** Comparison of turbulent flame brush thickness  $\ell_{f,t}$  to the corresponding turbulent length scale  $\ell_{f,t,alg}$ . Both quantities are averaged over the values on the mean flame front surface.

results indicates that the flame enters the squish region when approximately 50% of the fuel is consumed.

The following discussion is confined to case I only. In figure 5.19 an averaged phase diagram of the combustion regimes occurring during the combustion phase is depicted. The first point after switching from the spark ignition model to the fully spatial equations is located in the thin reaction zones regime. For increasing crank angles until about TDC, a significant increase in non-dimensional turbulent length scale can be observed. Not only the flame expands from the spark plug into the inner cylinder region in which larger turbulent structures exist (see fig. 5.20). Furthermore, the laminar flame thickness  $\ell_f$  is decreased due to the pressure increase. The non-dimensional turbulence intensity, however, only exhibits a minor increase. Therefore, shortly after TDC, a transition into the corrugated flamelets regime is observed. This is also the time at which the turbulent flame enters the squish region (see figure 5.14b). The turbulent length scales as well the turbulence intensity interacting with the flame decrease from this time on again.

The comparison of the turbulent flame brush thickness  $\ell_{f,t}$  to its corresponding turbulent length scale  $\ell_{f,t,alg}$  in figure 5.20 underlines the previously made statement that the flame sees increasingly larger turbulent structures later during the combustion

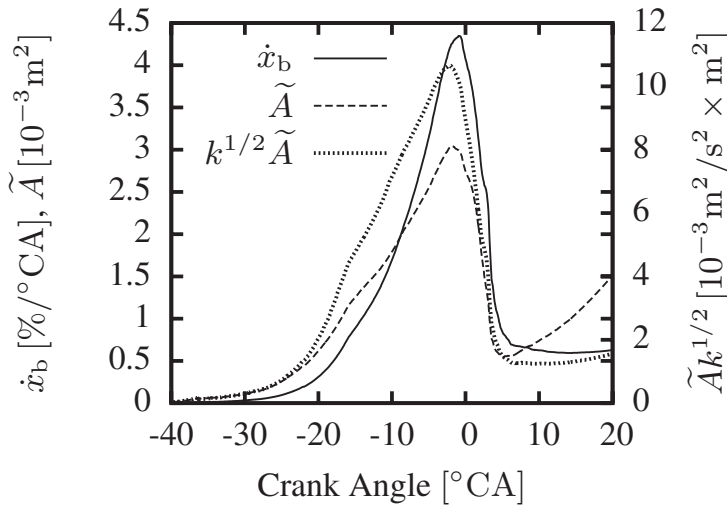


**Figure 5.21:** Qualitative comparison of normalized mass burning rate  $\dot{x}_b$  and turbulent mean flame surface area  $\tilde{A}$  (both on the left ordinate, thin lines) and  $\tilde{A}k^{1/2}$  (right ordinate, thick dotted line).  $\tilde{A}k^{1/2}$  serves as a measure for the highest possible burning rate.

phase. As soon as the flame enters the squish region, the turbulent length scales interacting with the flame are significantly smaller. The turbulent flame brush thickness follows this development with a delay of approximately  $10^\circ\text{CA}$ . Hence, according to this model the turbulent flame is in continuous development until shortly before TDC.

Now, the results for flame propagation in the squish will be discussed. As was stated above, global mass burning for the late stages of the cycle after TDC is underpredicted. Two possible reasons for this behavior need to be investigated: Either the approximation for the turbulent burning velocity underpredicts combustion in the squish region while the turbulent flow is correctly predicted or the turbulence model underpredicts the turbulence intensity which leads to the underpredicted turbulent mass burning rate. In figure 5.21 the mass burning rate is qualitatively compared with the maximum possible rate effective at large Damköhler numbers. In view of eqn. (3.42) the maximal rate is approximated by  $\tilde{A}k^{1/2}$  as  $\dot{x}_b$ . This quantity is independent from the flamelet based premixed combustion model that is subject of this work. It can be seen that  $\tilde{A}k^{1/2}$  follows the same qualitative decrease after TDC. Therefore the decrease in turbulent mass burning rate is due to the decrease in turbulence intensity.

In appendix D the behavior of the turbulent kinetic energy and turbulent dissipation fields in the squish for this specific engine are discussed. For the  $k$ -equation, the influence of the different terms contributing to turbulent production are investigated. There, it is concluded that the reason for this underprediction is likely due to the turbulence model employed.

### 5.3 Stratified charge SIDI engine

Spark-Ignition Direct-Injection (SIDI) engines are presently subject to extensive research. It is expected that SIDI engines provide a future concept of engine design on the market. This is due to the fact that SIDI concepts promise to yield better fuel

economy and performance due to charge cooling by direct injection [113], especially at full load. Additionally at part load conditions, mixture stratification enables further thermodynamic improvements because – in contrast to homogeneous charge concepts – throttling of a SIDI engine can be reduced. For mixture stratification, an ignitable and combustible fuel/air mixture needs to be convected to the plug at the time of spark ignition. First generation SIDI engines realize the mixture formation and transport by means of Wall-Guided (WG) or Air-Guided (AG) concepts. However, the gain in fuel economy was not as significant as expected, and only low market acceptance was achieved [96]. Several reasons for this behavior can be identified. The stratified mode is only limited to a small operation window because mixture formation is difficult to realize and requires a very defined flow pattern. This flow pattern must be controlled by swirl control valves which reduce the volumetric efficiency and hence the maximal achievable power output. The injection timing is therefore constrained by the flow pattern, and since the ignition timing is constrained by the injection timing, a thermodynamic optimization of the combustion process is difficult to realize. This results in the possibility of incomplete combustion and an increase in pollutant emissions. Especially in Wall-Guided concepts, deposits of unburnt hydrocarbons on the wall and piston surfaces lead to an increase of such unburnt hydrocarbons and soot emissions.

The SIDI engine that is investigated in this section is pertinent to so-called 2nd generation DI engines. Its design follows the Spray-Guided (SG) engine concept [20, 55]. According to this concept, spray injection and ignition are tightly constrained but allow for thermodynamic optimization of the combustion process. Usually, a centrally placed fuel injector sprays towards the spark plug such that the spray cloud rim is established at the plug. Problems may arise by spray impingement on the electrodes that leads to spark plug fouling. The characteristics of spray formation and fuel evaporation is crucial for the ignition and combustion process. Suitable injector types are multi-hole injectors or outwardly-opening piezo-injectors [30].

In this section, CFD results using the  $G$ -equation concept for stratified mixtures and the ignition model are compared to experimental investigations of a SG-SIDI engine. One question is whether the model is able to successfully predict time frames of ignitable conditions at the spark plug. It is evident that the fuel/air mixture must be in an equivalence ratio in the ignitable range. In order to identify an ignitable mixture at spark location in stratified configurations, not only the turbulent conditions and the mean mixture conditions as discussed in the previous section but also the inhomogeneity of the mixture in the vicinity of the spark plug need to be taken into account. Within a suitable control volume, a fraction of the total mixture fraction fluctuations are resolved by the  $\tilde{Z}$ -distribution, the other fraction is modeled the equation for  $\widetilde{Z''^2}$ . The differences of model results with and without the information from the  $\widetilde{Z''^2}$ -equation are compared with each other.

The ignition criterion applied in this work is entirely based on the  $G$ -equation concept and therefore follows a different approach than existing concepts. In this context, the criteria by *Maab et al.* [57] are worth mentioning. They have developed criteria for

successful ignition based on flow and mixture distribution analysis in the vicinity of the spark plug. There, the average normalized air-fuel ratio  $\lambda \equiv \phi^{-1}$  in a control volume around the spark plug should be in the range  $0.85 \leq \lambda \leq 1.15$  and the standard deviation of  $\lambda$  should be lower equal 0.15 which applies to spatial inhomogeneity as well as to cyclic variability. Additionally, criteria for the mean spray vapor concentrations are taken into account.

### 5.3.1 Fuel injection

In all cases presented here, indolene III was used as fuel. The fuel was injected by a Bosch 60 degree eight-hole circular injector with an injection pressure of 11 MPa. The injector axis is oriented towards the spark plug such that the plug is encompassed by two single sprays on each side (see figure 5.22).

The spray is modeled employing a Lagrangian approach based on *spray parcels* in which each parcel is representative for a class of droplets with a given position, velocity, temperature, and diameter. In order to describe injection, 6000 spray parcels for each injector nozzle are introduced in a state after primary and secondary breakup into the computational domain. Therefore, no physical models for neither of the two breakup phases were applied to the spray computation. A Generalized Rosin-Rammler droplet size distribution [53] of the spray cloud with a Sauter Mean Radius (SMR) of  $\text{smr} = 7.5 \mu\text{m}$  is assumed at the time of injection.

The fuel evaporation is modeled using a multicomponent fuel assumption by applying a continuous thermodynamics approach according to *Lippert et al.* [56]. A dense-spray correction [92] is applied for both droplet drag and vaporization.

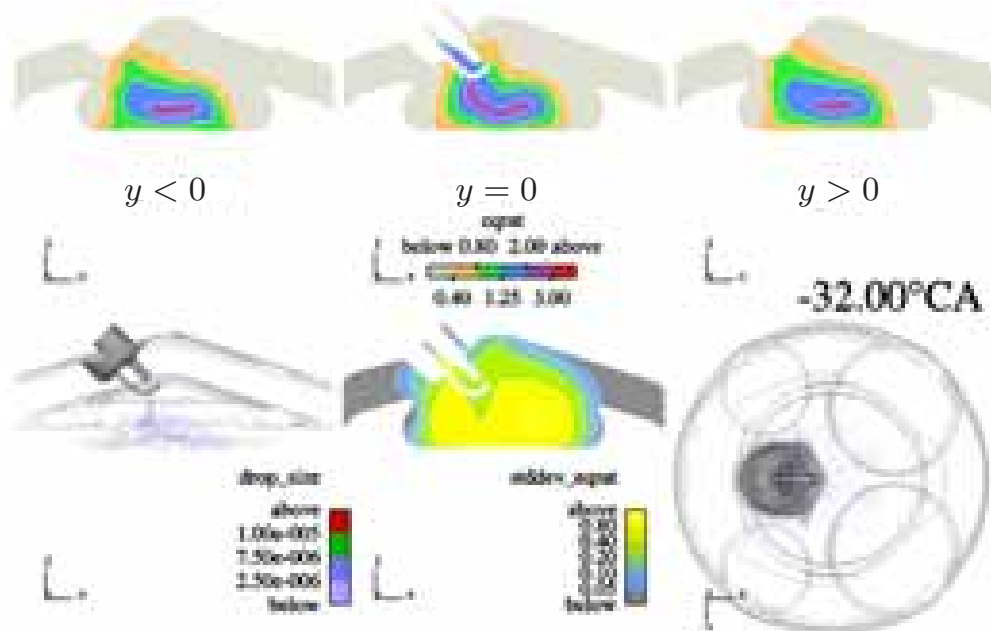
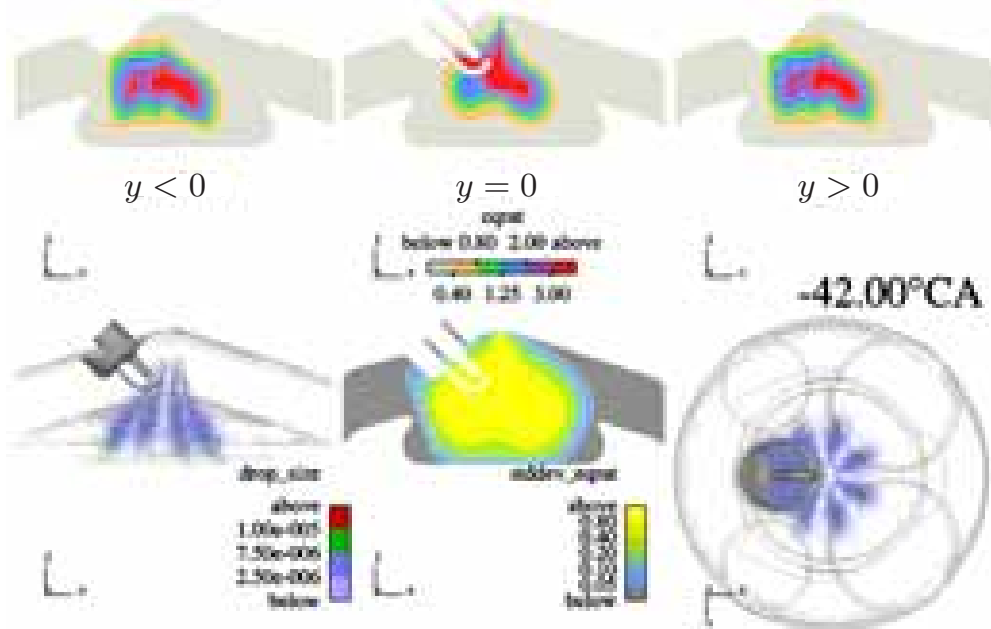
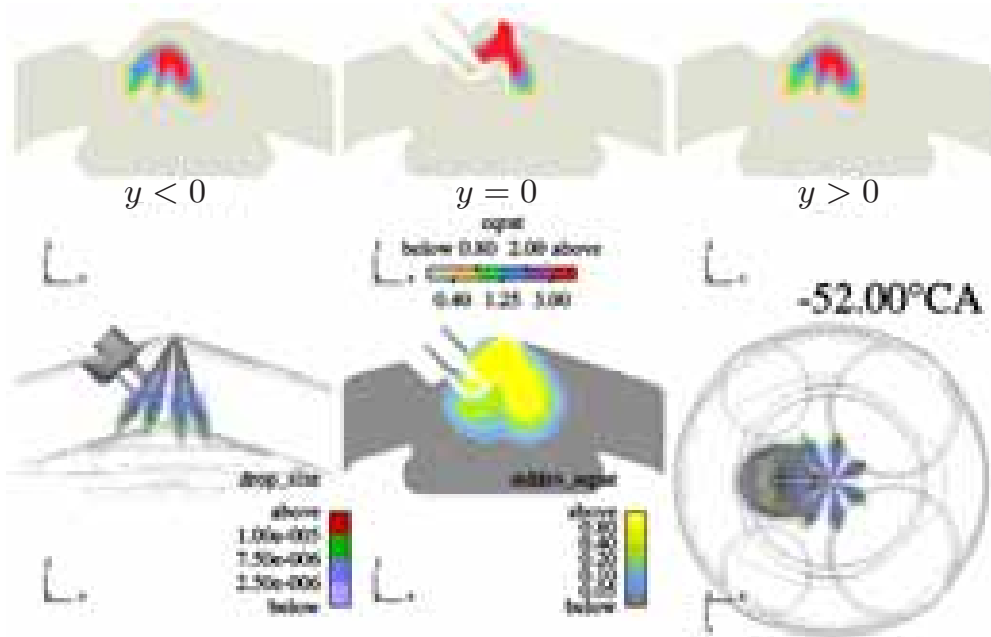
In figure 5.22 results from an injection-only CFD calculation for the spray and the mixture distribution are shown. The corresponding case can be found in section 5.3.3. Instead of  $\tilde{Z}$  and  $\widetilde{Z''^2}$  in the figure the equivalence ratio  $\tilde{\phi}$  and its standard deviation is depicted. The latter quantity is directly derived from  $\widetilde{Z''^2}$ . It is the square root of the equivalence ratio variance

$$\tilde{\phi}''^2 = \frac{\widetilde{Z''^2}}{(\tilde{Z} - 1)^4} \frac{(1 - Z_{\text{st}})^2}{Z_{\text{st}}^2}. \quad (5.8)$$

In the aforementioned figure it can be seen that the mixture stratification in the vicinity of the spark plug is very large since high spatial gradients of the equivalence ratio are observed which cause high variances of equivalence ratio. The rich mixture cloud passes the spark electrodes before ignition occurs in a still rich mixture.

### 5.3.2 Optically accessible engine

The base engine was also manufactured in a version for optical access of the combustion chamber through a quartz piston window, cf. fig. 5.23. Due to additional plumbing and minor changes in piston geometry for the optical access, the compression ratio of



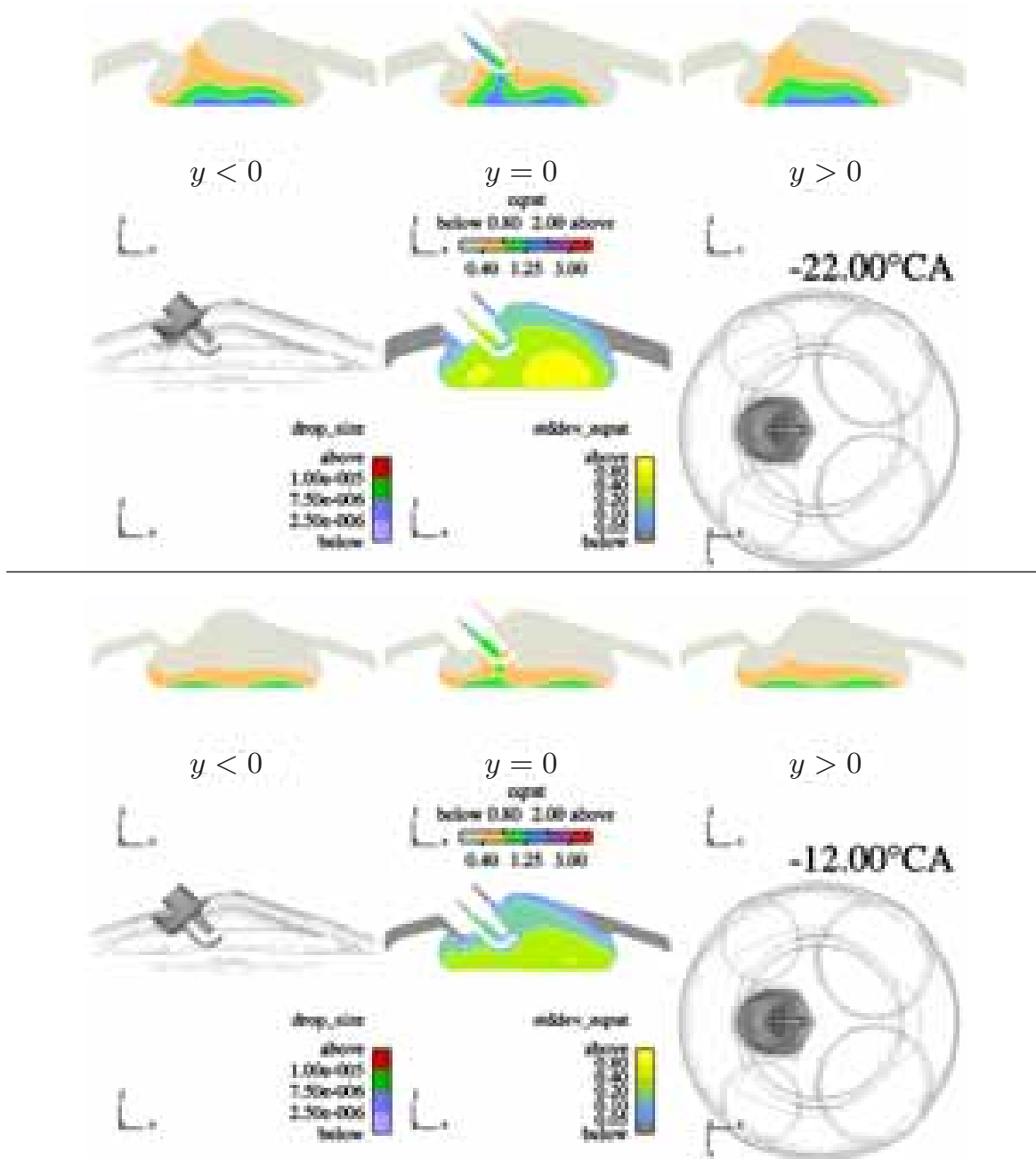


**Figure 5.22:** Spray and fuel distribution images obtained by an injection-only CFD run for the ‘3k1’ case discussed in section 5.3.3. Including the image on the previous page, five crank angles are depicted, for which the distribution of the mean equivalence ratio  $\tilde{\phi}$  on three vertical cut planes is shown. Additional images are showing the spray from different perspectives. The picture in the middle depicts the root mean square of the equivalence ratio  $\tilde{\phi}''^2$ .

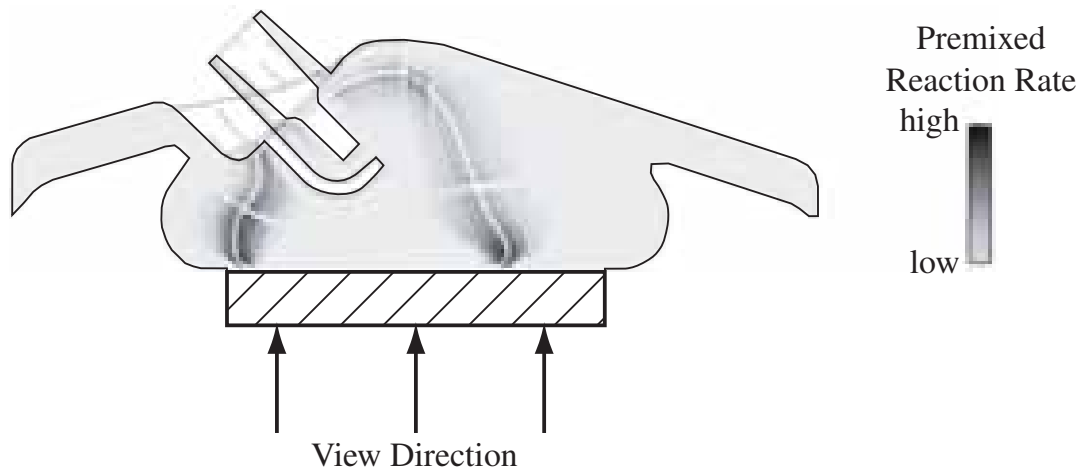


**Figure 5.23:** Schematic of optical engine access for the spatial measurement of the reaction rate. The hatched rectangle indicates the location of the quartz window in the piston. Results for an arbitrary crank position are also shown. In analogy to figure 5.13, mean flame front position and flame brush thickness are indicated by white lines. The premixed reaction rate is also depicted with color-coded intensity. A few streaks can be observed also, which are artifacts caused by post-processing.

| rpm                 | Injected mass | IMAP add.      | Injection timing (CFD) |                  | Spark timing (CFD) |                  |
|---------------------|---------------|----------------|------------------------|------------------|--------------------|------------------|
|                     |               | $N_2$          | begin                  | end              | begin              | end              |
| $[\text{min}^{-1}]$ | $[\text{mg}]$ | $[\text{kPa}]$ | $[\%]$                 | $[\text{°aTDC}]$ | $[\text{°aTDC}]$   | $[\text{°aTDC}]$ |
| 2000                | 10.0          | 95             | 0                      | -45.5            | -24.9              | -16.6            |

**Table 5.6:** Spread sheet of engine operating condition for the optically accessible engine. IMAP denotes the Intake Manifold Pressure. The injection timings given here take magnetic and mechanical injector delays into account.

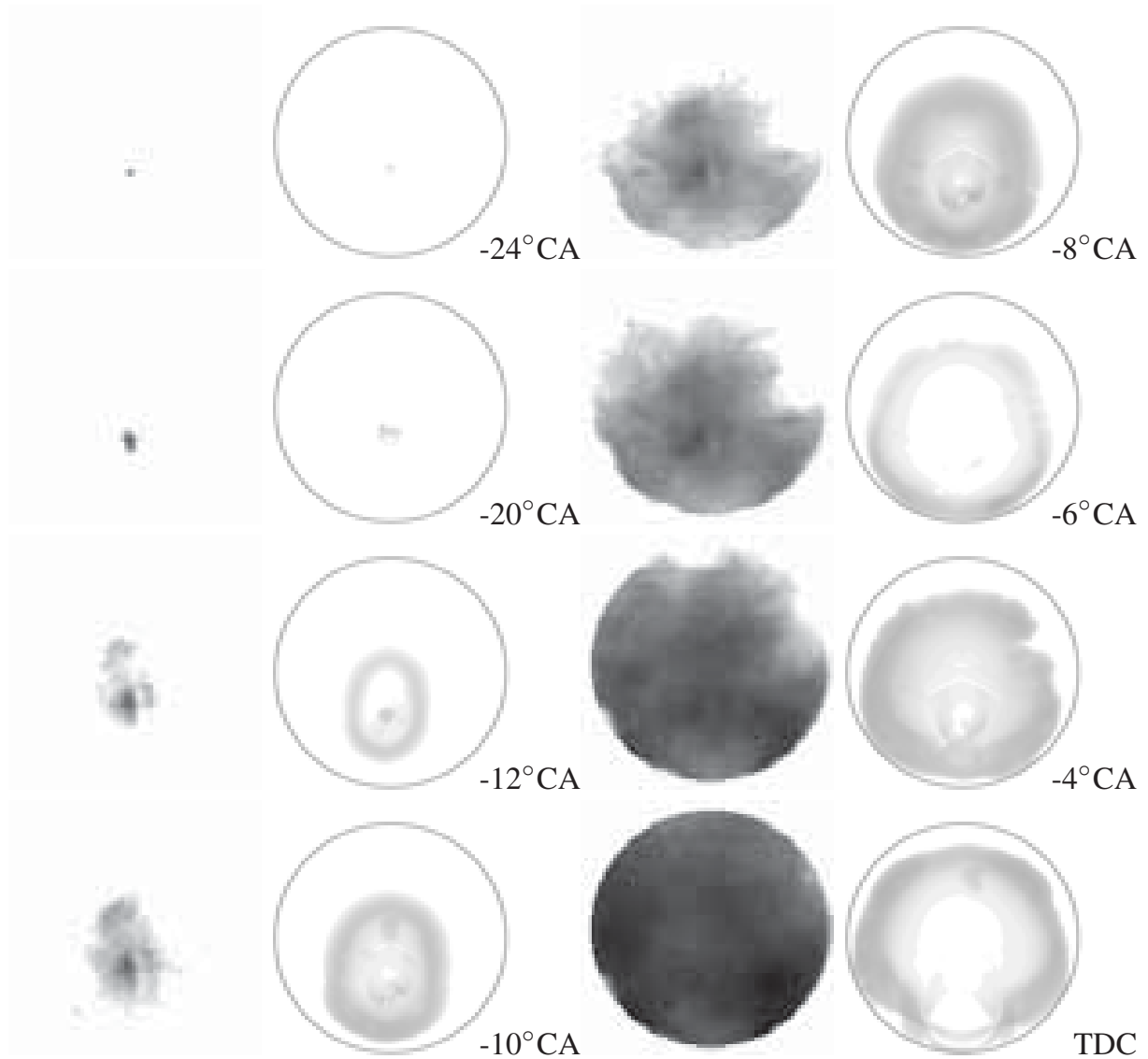


**Figure 5.24:** Qualitative comparisons between OH\* chemiluminescence images (left columns) from individual cycles and premixed reaction rates from CFD (right columns). The images from CFD are encircled to indicate the experimental view. The time series range is between 24°bTDC and TDC.



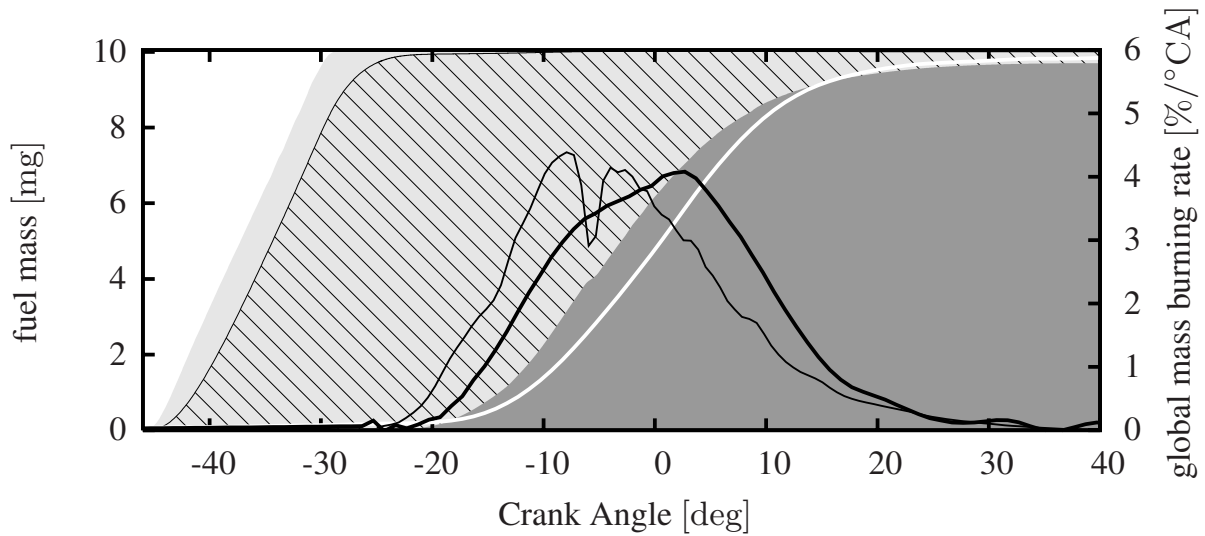


**Figure 5.25:** Experimental and CFD results for the test case performed in the optically accessible engine. On the left ordinate, injected, vaporized and burnt fuel mass are plotted. On the right ordinate, the normalized global heat release is plotted. Burnt fuel mass and global heat release rates obtained from CFD and experiments are compared to each other. Both experimental and CFD global heat release data are obtained by means of the first derivative of the burnt global fuel mass with respect to the crank angle normalized against the total heat of the injected fuel.

the optical version is slightly lower than the one for the metal engine for which the CFD model was created. The diameter of the cylindrical quartz window is  $d = 48$  mm. This means that the spatial location of combustion can only be detected in the inner cylinder and the piston bowl, but not in the squish region.

In tab. 5.6, the operating conditions for this case are given. The engine was run without dilution. This corresponds to a non-EGR case.

The experimental visualization of the combustion process was carried out for a similar engine by means of broadband flame luminosity as described by *Drake et al.* in [20]. Next to two measured wavelengths for detecting soot radiation as an indicator of diffusion burning, at 306 nm wavelength  $\text{OH}^*$  chemiluminescence emission was imaged. The  $\text{OH}^*$  emission serves as an indicator for premixed combustion. However, the authors of [20] point out the difficulty to establish a quantitative correlation between the  $\text{OH}^*$  intensity and the heat release rate due to premixed combustion. In figure 5.25, results for  $\text{OH}^*$  chemiluminescence from single-cycle experiments and premixed heat release rate from CFD are depicted for times from ignition until TDC. The CFD results are computed using the premixed volumetric reaction rate according to eqn. (4.18). The location of combustion as shown in the single-cycle experiment is sufficiently recovered by the RANS CFD.

In fig. 5.25, global results from the spray and combustion calculation are depicted for the optical engine test case. Results for the global mass burning rate due to com-

| Case | rpm                 | $a_{fr}$ | Injected      |                | EGR (exp.) | Injection timing (CFD) |                  | Spark timing (CFD) |                  |
|------|---------------------|----------|---------------|----------------|------------|------------------------|------------------|--------------------|------------------|
|      |                     |          | mass          | IMAP           |            | begin                  | end              | begin              | end              |
|      | $[\text{min}^{-1}]$ | $[-]$    | $[\text{mg}]$ | $[\text{kPa}]$ | $[\%]$     | $[\text{°aTDC}]$       | $[\text{°aTDC}]$ | $[\text{°aTDC}]$   | $[\text{°aTDC}]$ |
| 2k1  | 2000                | 25.7     | 8.53          | 95             | 43.8       | -49.25                 | -37.90           | -35.0              | 4.0              |
| 3k1  | 3000                | 45.3     | 5.58          | 90             | 33.7       | -60.85                 | -46.85           | -43.0              | 15.5             |
| 3k2  | 3000                | 22.3     | 11.78         | 95             | 32.4       | -60.71                 | -39.85           | -35.0              | 23.5             |

**Table 5.7:** Spread sheet of investigated engine operating points. IMAP denotes the Intake Manifold Pressure,  $a_{fr}$  the global air/fuel ratio (2.22). The external EGR dilution level given here refers to the definition of experimentally measured EGR for non-stoichiometric air/fuel ratios. It is different to the EGR definition in the CFD calculation. The injection timings given here already take into account magnetic and mechanical injector delays.

bustion are from the experimental investigations and from CFD are compared to each other. It can be seen that combustion predicted by CFD is slightly faster than for the experiment in the beginning. The global fuel mass burning rate is the sum of fuel consumption due to premixed and non-premixed combustion. Non-premixed combustion is approximated by an infinitely fast chemistry assumption. However, non-premixed combustion, which is also referred to as diffusion burning, is assumed to have only a small contribution to total burning [20].

### 5.3.3 Variation of engine speed and injected fuel mass

The following series of operating points was carried out in a metal engine. Here, both engine speed and injected fuel mass were varied. In table 5.7 the operating points are specified. Due to the ignition system, the spark duration was identical for all cases (3.25 ms), which results in the time windows given in the table. The initial spark kernel radius is  $r_{ign} = 1$  mm. Note that the injection and ignition data given here refer to specifications for the CFD calculation and not to the experimental parameters, because mechanical and magnetic opening and closing delay times of the injector are taken into consideration in the table data. The EGR composition used in the CFD calculation is assumed to be the product of stoichiometric mixture, regardless of the actual air/fuel ratio that exists at the operating point. In the experiment, in contrast, EGR is equal to the exhaust gas composition that is produced by the conditions of the operating point.

#### Criterion for successful ignition

The criterion for successful ignition conditions developed in section 5.2.3 is applied to the stratified cases. The condition (5.7) was developed for homogeneous mixtures, where variations of the laminar burning velocity and the flame thickness were not assumed. In the following we will discuss extensions of (5.7) for the stratified cases

that take mixture fraction fluctuations into account. This is accomplished by substituting the expression  $s_L \widetilde{\Sigma}_t$  in (5.7) by a term similar to (3.140), thereby considering the probability  $\widetilde{P}(Z)$  of finding a specific mixture fraction value:

$$r_{k,t,\text{crit}} = 2c_\kappa \hat{k}_{\text{spk}}^{1/2} \left[ \int_0^1 s_L(Z) \widetilde{\Sigma}_t(Z) \widetilde{P}(Z) dZ \right]^{-1}. \quad (5.9)$$

The pdf  $\widetilde{P}(Z)$  will be evaluated by the same approach as outlined in chapter 3.5.7, in which the beta-pdf using  $\widetilde{Z}$  and  $\widetilde{Z}''^2$  is assumed. This is accomplished by considering a spherical control volume with the size of the initial spark kernel and by averaging local quantities over this control volume. A “spark-global” (i.e. one value over the entire control volume) mixture fraction  $\widetilde{Z}_{\text{gl}}$  and a resolved variance  $\widetilde{Z}''^2_{\text{res}}$  can be obtained from the local  $\widetilde{Z}$  field. From the local  $\widetilde{Z}''^2$  field, an average  $\widetilde{Z}''^2_{\text{lok,av}}$  can be computed.

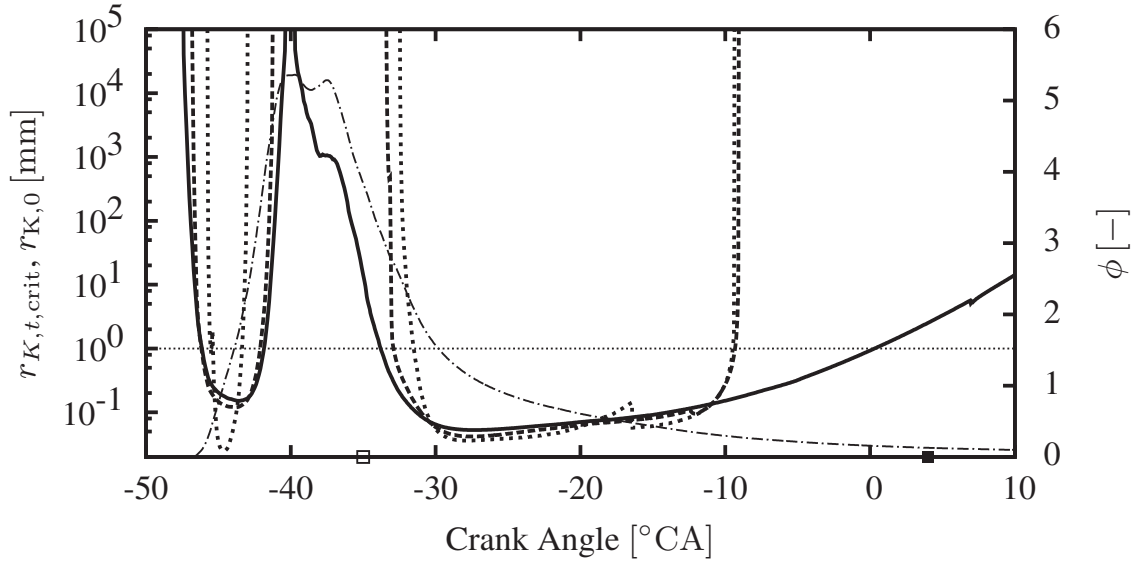
The turbulent ignition criterion  $r_{K,t,\text{crit}}$  is evaluated in the following employing three different approaches for the assumption of the mixture fraction pdf within the spark volume for the injection-only cases without ignition. The results using each of the three assumptions are compared with each other. The injection and ignition timings were experimentally determined such that the engine ran most stably for the chosen engine speed and injection parameters. Therefore we assume that the ignition timings determined from the experiments lead to successful ignition and can therefore be compared to the numerical findings.

All three approaches assume the mean mixture fraction distribution in the whole control volume to be  $\widetilde{Z}_{\text{gl}}$ . The first approach assumes this distribution to be homogeneous, that is  $\widetilde{Z}''^2 = 0$ . The second approach assumes the variance to be equal to the resolved variance  $\widetilde{Z}''^2_{\text{res}}$ . The third approach takes globally and locally averaged variances into account such that the total variance is assumed to be  $\widetilde{Z}''^2_{\text{res}} + \widetilde{Z}''^2_{\text{lok,av}}$ .

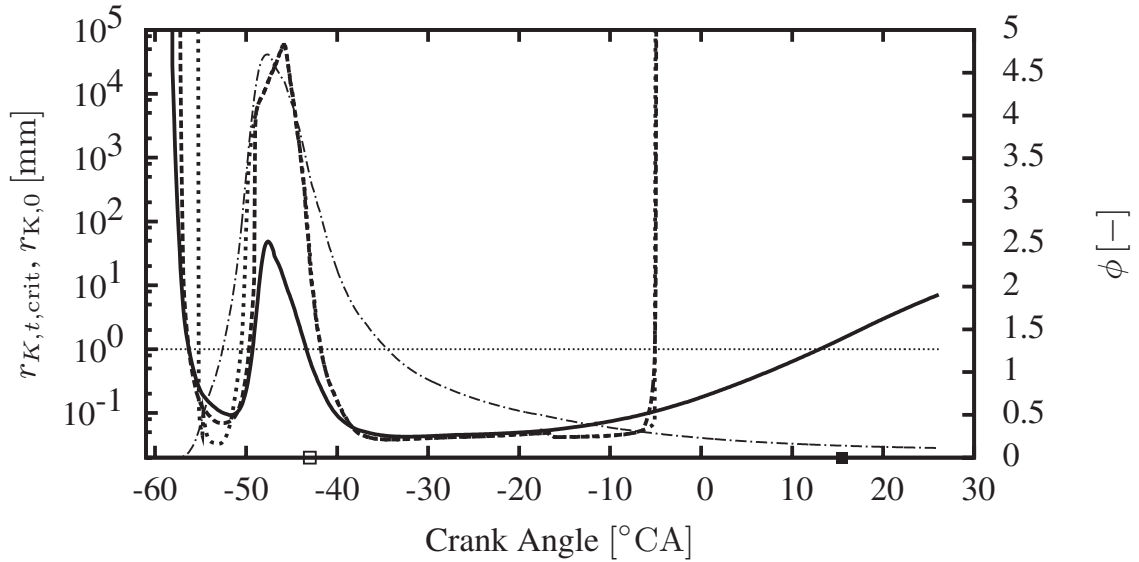
In figure 5.26, the three different approaches are plotted for several operating points. Also, the initial flame kernel radius is depicted. In order to evaluate  $r_{K,t,\text{crit}}$ , a different Schmidt number for the mean curvature term was employed. In (5.7) the constant  $c_\kappa$  was calculated using  $\text{Sc}_t = 7.0$ . With this model parameter, best agreement to the experimental ignition timings was obtained.

It can be seen that the global equivalence ratio  $\widetilde{\phi}$  increases rapidly after injection, and for a very short time period favorable ignition conditions exist according to the turbulent ignition criterion until the global mixture becomes too rich. Then, the global equivalence ratio decreases again. This can be attributed to an advanced mixing of the spray cloud with the ambient air. The second time period of favorable ignition conditions lasts until the mixture in the control volume becomes too lean to ignite. This corresponds to an increase in the value of  $r_{K,t,\text{crit}}$ . This phenomenon is also observed in fig. 5.22 in which the passing of the spray cloud by the plug is depicted.

Case: 2k1



Case: 3k1



Case: 3k2

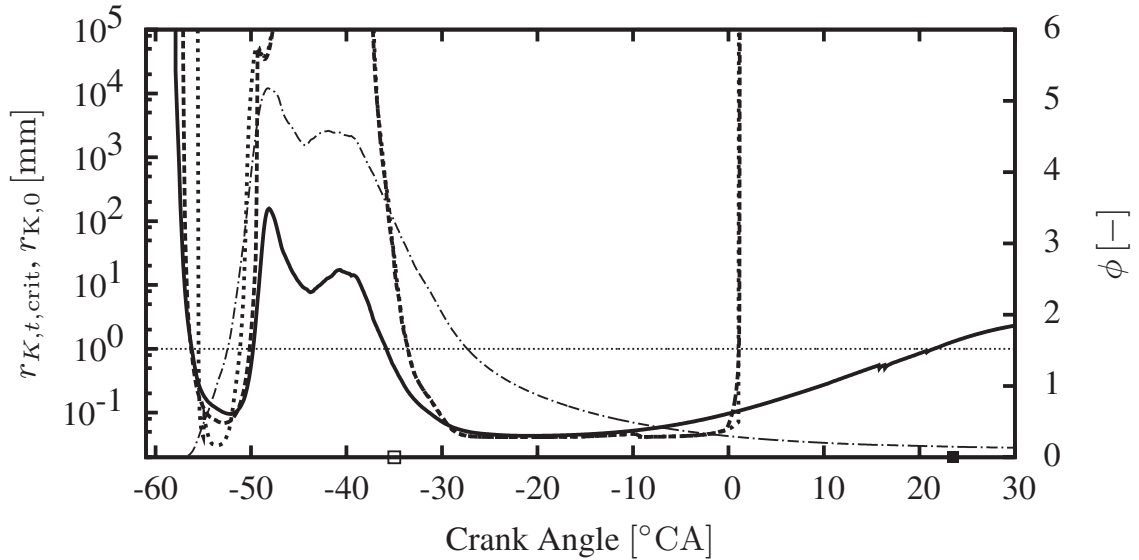
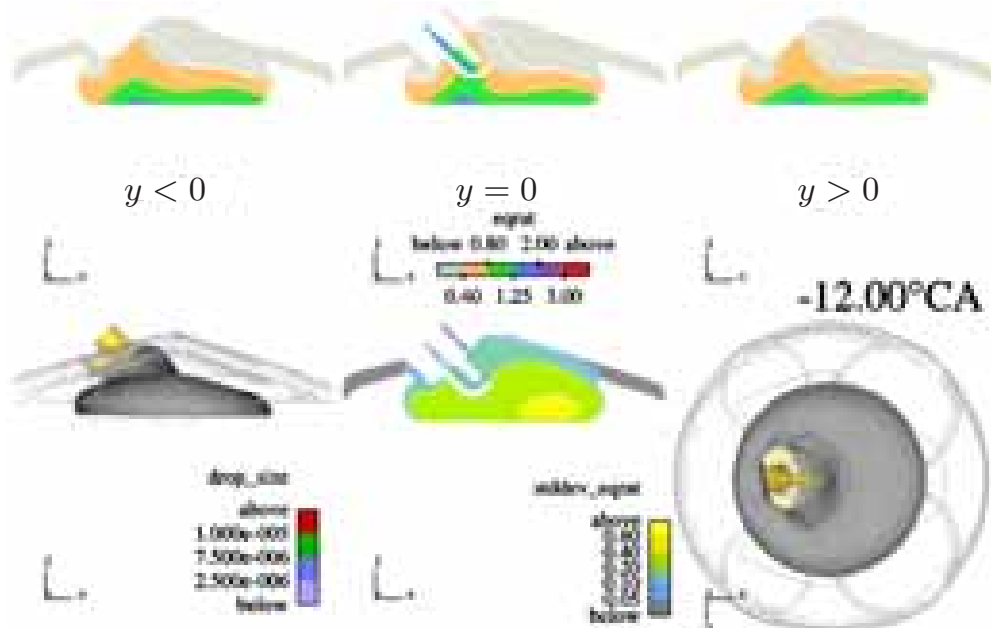
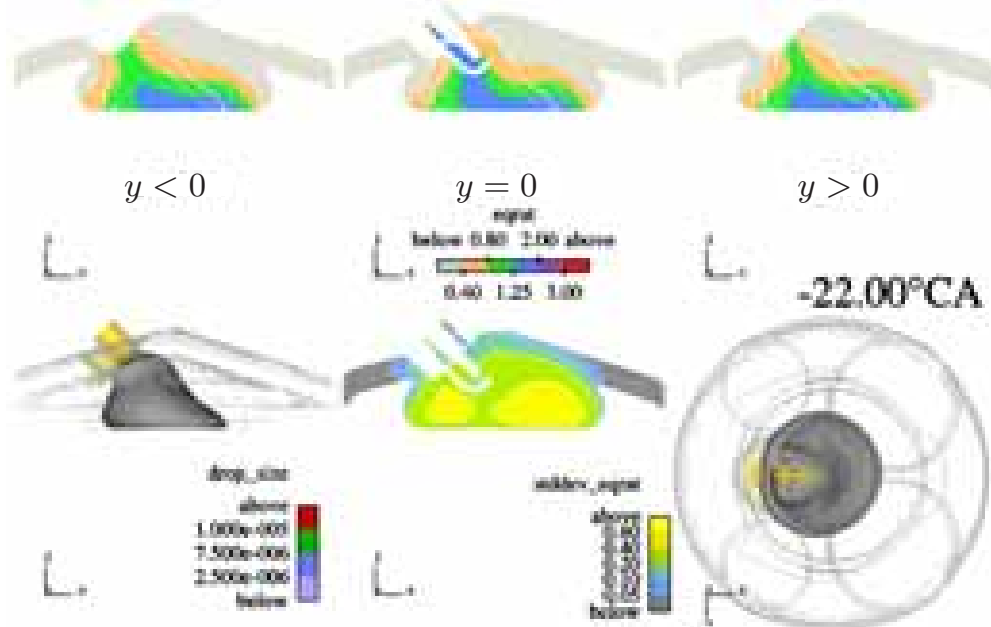
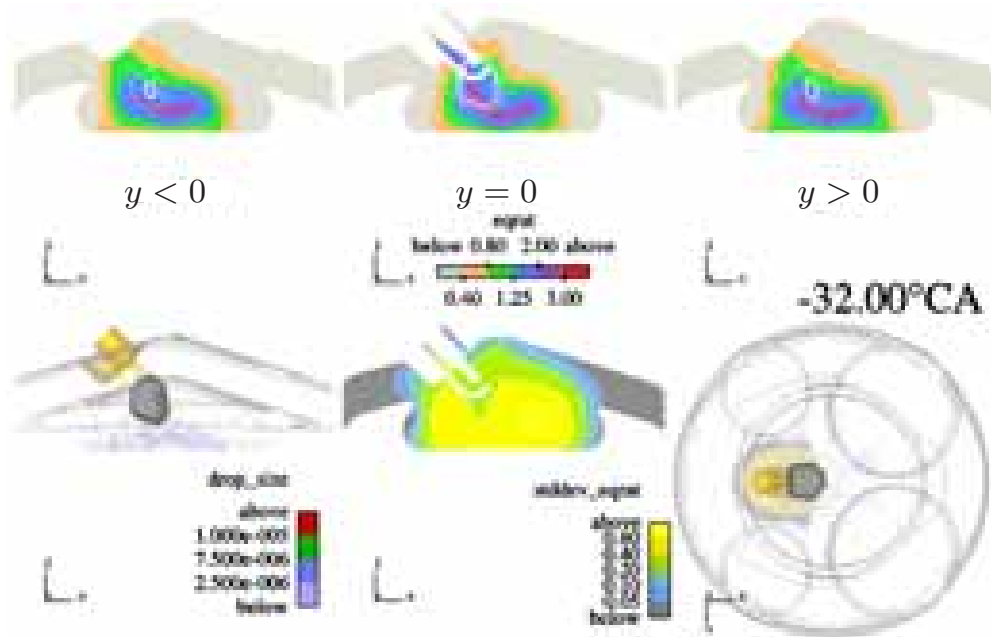


**Figure 5.26:** Plot (on previous page) of the turbulent ignition criterion  $r_{k,t,crit}$  over the crank angle evaluated for the control volume at the spark location for the injection-only case without ignition for different operation points. On the right ordinate, the average equivalence ratio of the control volume is plotted. On the abscissa, start and end of ignition timings are indicated by outlined and solid squares, respectively.

| Plot Legend |  |
|-------------|--|
| .....       | $r_{ign}$  |
| .....       | $r_{K,t,crit}$ , homogeneous                       |
| —           | $r_{K,t,crit}$ , resolved and local $\tilde{P}(Z)$ |
| -----       | $r_{K,t,crit}$ , resolved $\tilde{P}(Z)$           |
| - - - - -   | $\tilde{\phi}$ global                              |

It is also significant that the different assumptions for the mixture fraction variance yield different results for very rich and very lean mean mixtures. For approximately stoichiometric mixtures, predictions of  $r_{K,t,crit}$  using the different assumptions for the mixture fraction distribution are similar. One could expect that favorable ignition conditions are more frequently predicted, if the evaluation of  $r_{K,t,crit}$  is only based on a global homogeneous mixture, rather than by assuming both global and local mixture fraction variation. In fact, the opposite is the case. For in average very rich and very lean mixtures the inclusion of  $\widetilde{Z''^2}_{gl}$  and  $\widetilde{Z''^2}_{lok,av}$  lead to a mixture fraction pdf  $\tilde{P}(Z)$  that includes stoichiometric mixtures which enhance combustion. On the other hand, for mean stoichiometric mixtures a minor decrease in  $r_{K,t,crit}$  is observed if the mixture fraction pdf using the full variance  $\widetilde{Z''^2}_{gl} + \widetilde{Z''^2}_{lok,av}$  is considered. A comparison of the criterion  $r_{K,t,crit} \leq r_{ign}$  for the CFD calculation with the timings used in the experiments shows that favorable ignition timings are correctly predicted for all operating points. They exhibit only a minor deviation if the full variance  $\widetilde{Z''^2}_{gl} + \widetilde{Z''^2}_{lok,av}$  is used. This does not only apply to the beginning of spark ignition, but also to its end. We can conclude therefore that the application of the  $\widetilde{Z''^2}$  transport equation (3.138) is important for the correct prediction of stratified premixed combustion, leading to an improvement of the numerical results shortly after spray injection. For the operating points investigated here, a decrease in predicted ignition propensity due to the inclusion of the full mixture fraction variance  $\widetilde{Z''^2}_{gl} + \widetilde{Z''^2}_{lok,av}$  was not observed. Additionally, the liquid volume fraction of the fuel spray was not considered.

It appears to be likely that an increase in mixture fraction variance leads to an increase in COV. The latter coefficient, however, depends on the whole combustion process and not on ignition only. For this reason, a correlation between mixture fraction variance in the control volume during ignition and the experimentally measured COV of the investigated operating points was not established.



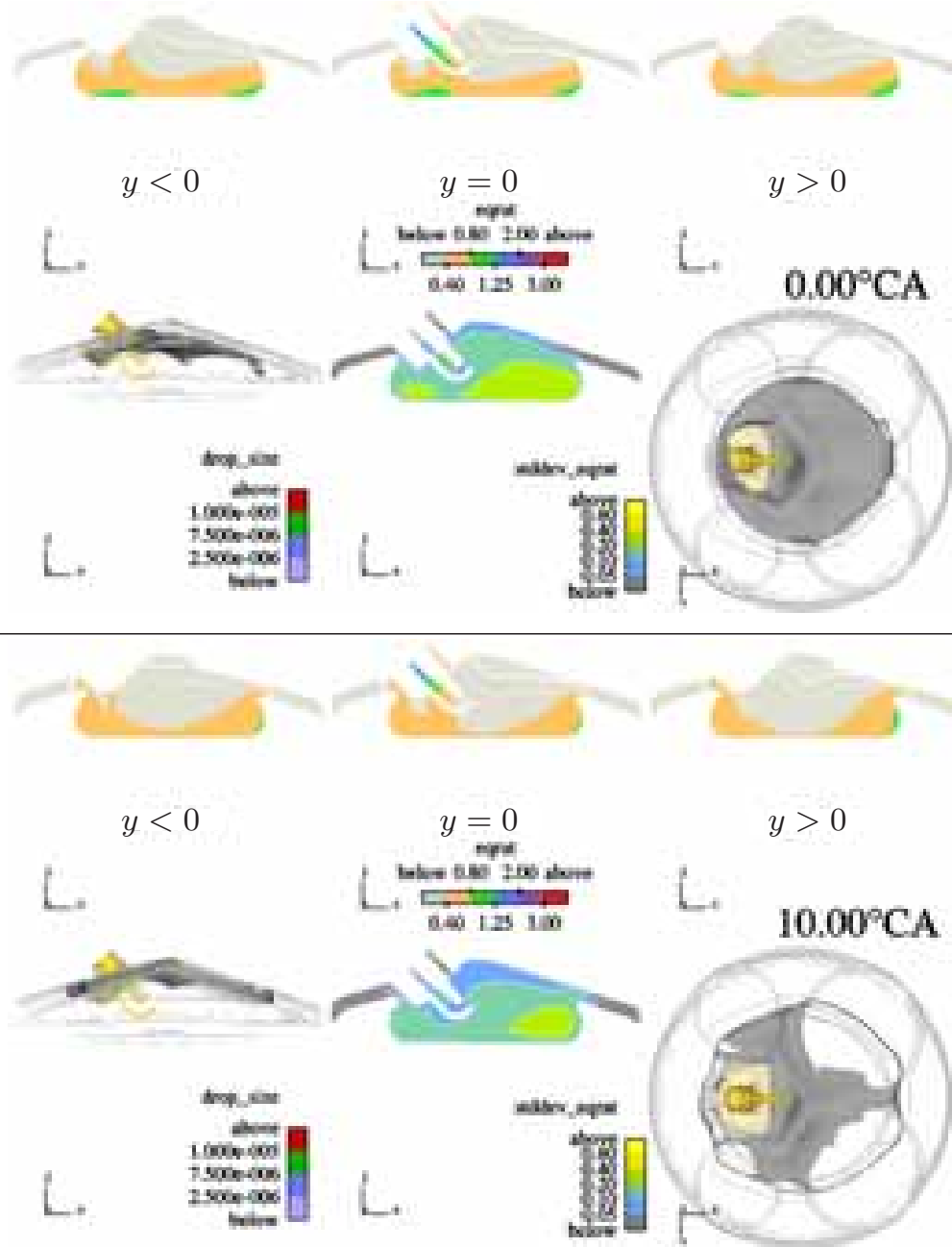


**Figure 5.27:** Caption for plots on this and previous page. CFD results are depicted for case ‘3k1’ for five different crank angles including combustion. The images are in accordance with the plots in fig. 5.22. It is important to note that the equivalence ratio plotted is directly derived from the mixture fraction  $\tilde{Z}$  which is insensitive to fuel consumption due to combustion. On the upper row the mean flame front and the flame brush thickness are additionally indicated by white lines for each crank angle. On the lower row, the left and right images depict the mean flame front surface in grey color.

### Combustion validation

In this sub-section, the cases are discussed including combustion. Here, the interaction between the turbulent flow and the spray injection including fuel vaporization and mixture stratification leads to the predicted propagation of the flame and the predicted mass burning rate. In contrast to homogeneous combustion, another physical sub-model, the model for spray transport and vaporization, has therefore significant influence on the combustion results.

In analogy to the ignition criterion investigation above the turbulent Schmidt number appearing in the mean curvature term of the  $\tilde{G}$  equation (3.106) was increased, see also eqn. (3.108). The ignition kernel radius is equal to the radius employed in the homogeneous cases.  $f_D$  is a model coefficient of the order of unity.

In figure 5.27, a visualization of the flame propagation for the 3k1 case is depicted. Only images until TDC are shown for brevity. Immediately after combustion, mixture stratification is significant and leads to a non-negligible  $\widetilde{Z''^2}$  field, in the plot indicated as standard deviation of equivalence ratio. With increasing crank angles,  $\widetilde{\phi''^2}^{1/2}$  quickly decreases. As can be seen from the figure, at TDC the standard deviation of equivalence ratio has dropped to insignificant values, especially in those regions, where flame propagation prevails. A comparison with fig. 5.22 for  $-32^\circ\text{CA}$  and  $-22^\circ\text{CA}$  shows that the mixture fraction field is not significantly disturbed by the advancing flame front.

For the combustion calculation in fig. 5.27 it can be seen at  $-22^\circ\text{CA}$  that flame propagation is strongly dependent on the fuel distribution. For example, flame propagation is noticeably reduced in regions with very lean mixtures. The highest flame propagation rate, however, is not found for stoichiometric mixtures, but for rich mixtures with a mean equivalence ratio range of  $1.25 \leq \tilde{\phi} \leq 2.00$ . At the same time, in these regions also high mixture fraction variances are found. This observation is in line with the remarks made in chapter 3.5.7: For increasing values of  $\widetilde{Z''^2}$  the maximum of the turbulent burning velocity shifts to richer fuel/oxidizer mixtures. Due to the mixture stratification in this case and the almost vertical spray angle, most portions of the injected fuel evaporate and remain in the piston bowl. Combustion in the squish region therefore is widely suppressed.

Now, results for all three investigated cases are discussed. In figure 5.28, averaged experimental and simulated cylinder pressure histories are plotted. The over-all agreement is good except for the case '2k1' in which the simulated maximum pressure does not reach the experimentally observed, although initially the pressure is overpredicted. In figure 5.29, global mass balances and mass burning rates are depicted. From simulation, the amounts of injected fuel mass, vaporized fuel mass, and burnt fuel mass are plotted. As for the experiments, the amount of burnt fuel is determined from the pressure history employing a two-zone model with a heat transfer model according to Woschni's correlation [44, 111]. In both simulation and experiment, the global mass burning rates are obtained as the normalized derivative of the burnt fuel mass with re-



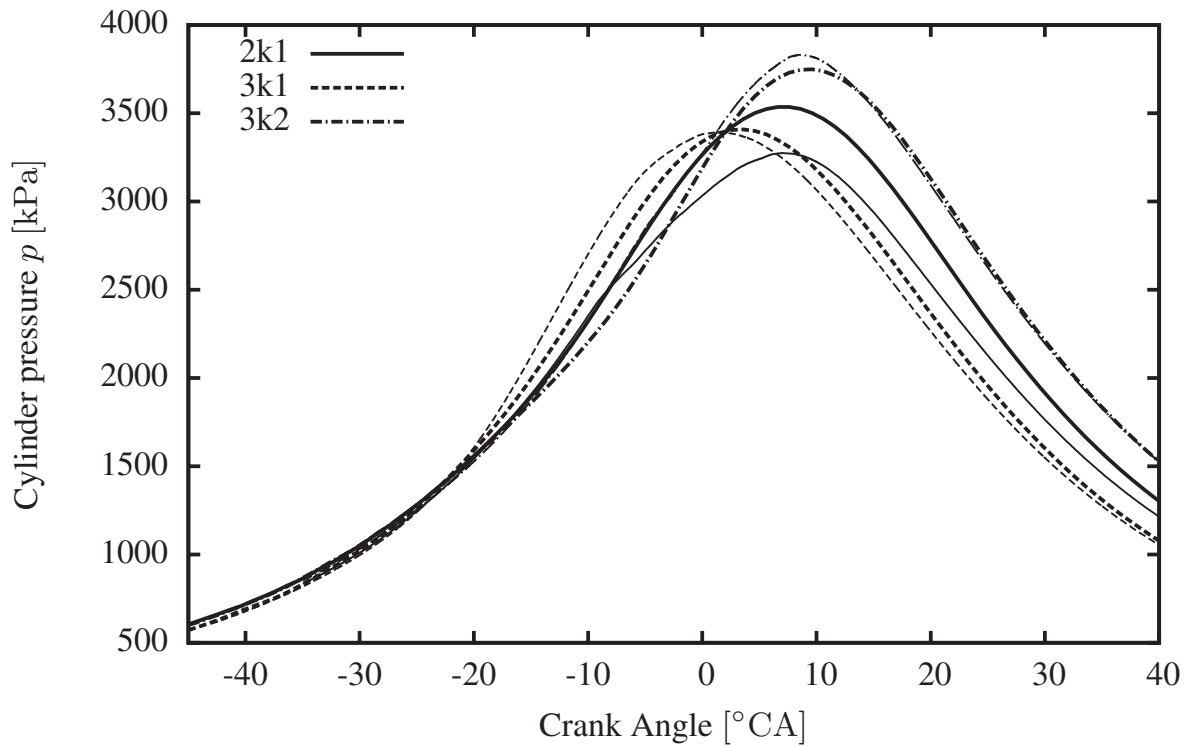


**Figure 5.28:** Cylinder pressure comparisons between experiments (thick lines) and simulations (thin lines) for the cases in section 5.3.3

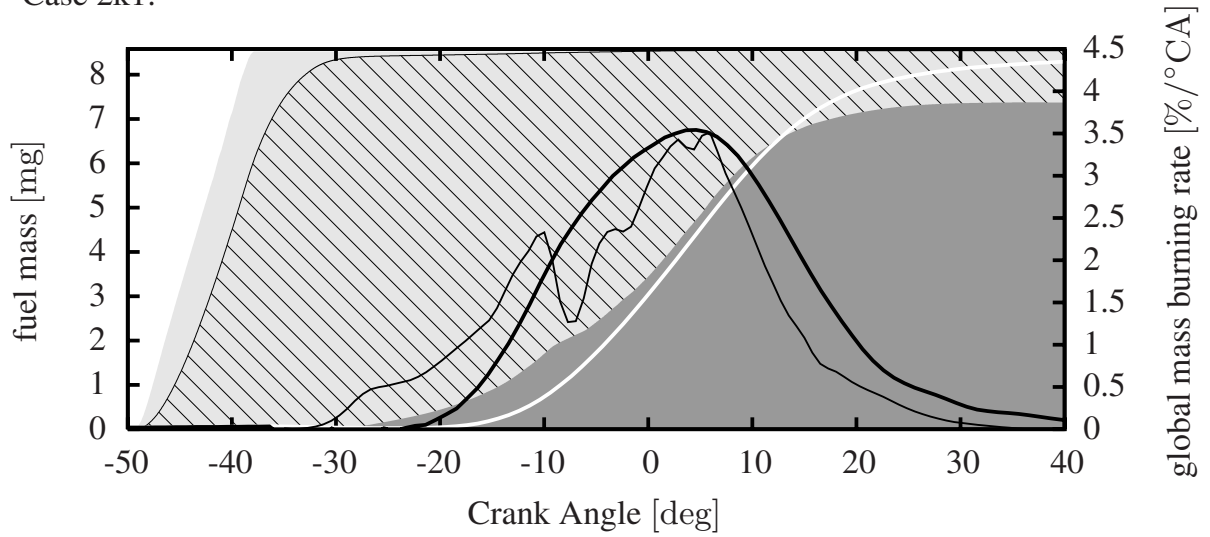
spect to crank angle. The derivative is normalized with respect to the totally injected mass.

The comparison of injected to vaporized fuel mass from CFD shows that the totally injected fuel is almost completely vaporized at the time of ignition, that is, a direct interaction between the spray droplet modeling and the combustion modeling is not required for this problem. The comparison between the results of burnt fuel mass from CFD and experiment confirms the results from the pressure curves. Best agreement is obtained for case ‘3k2’. For this case, the simulated combustion efficiency is 94%, which is close to the experiments (95%). On the other hand, for case ‘3k1’ less fuel is burnt in the simulation than in the experiment (94.5% vs. 98%). For case ‘2k1’, the results are 86% vs. 97%.

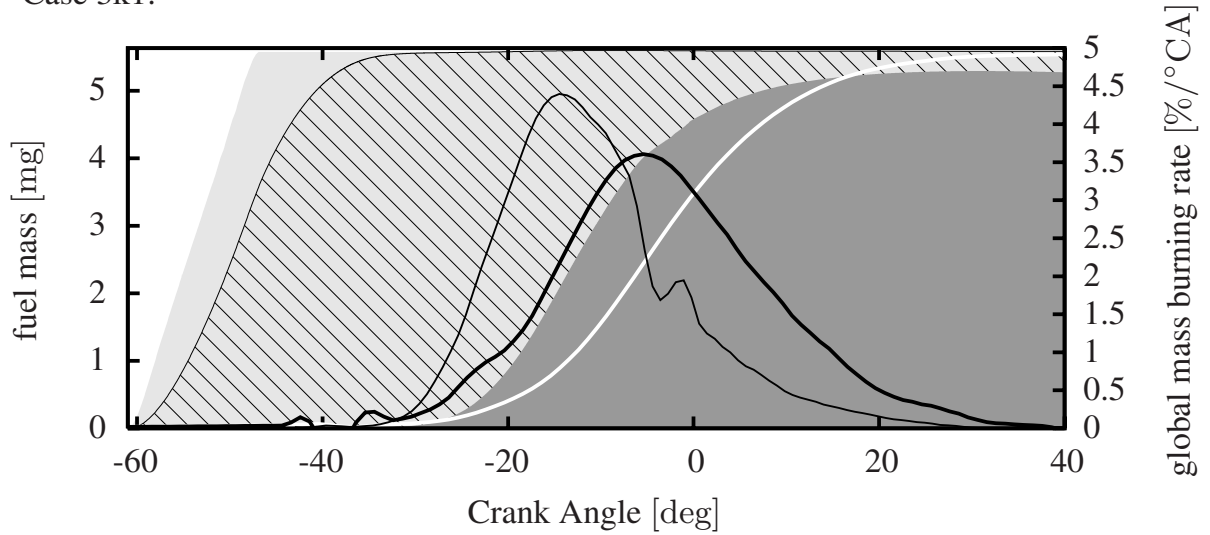
## 5.4 Discussion

Focus of the validations is on the prediction of the turbulent burning velocity and – especially in SI engines – on the global heat release rate over crank angle. In section 5.1, different approaches for the algebraic  $\tilde{\sigma}_t$ -equation (4.7) and the global curvature term in the kinematic  $\tilde{G}$ -equation, (3.106) are discussed and applied to a cylindrical vessel case. Appropriate models are chosen as a result from this test case. With regards to the  $\tilde{\sigma}_t$ -equation chosen, two different choices for the model parameter  $q$  are discussed.

Case 2k1:



Case 3k1:



Case 3k2:

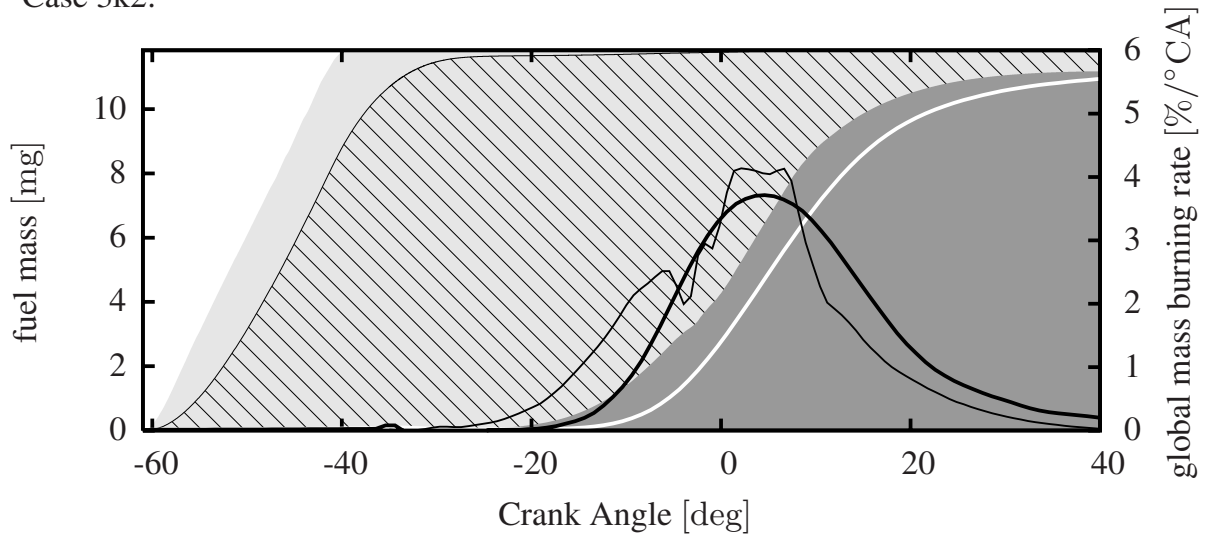


**Figure 5.29:** Comparison of experimental and CFD results for the cases discussed in section 5.3.3. The plot legend can be found in fig. 5.25.

For homogeneous and stratified charge, the choice  $q = 2/3$  appears to be appropriate and is used for all engine calculations.

Besides the effects of development and curvature of the mean turbulent flame, two constants are important to be verified. The model constant  $b_1 = 2.0$  in the expression  $s_T = b_1 v'$  has been found by many experimental researchers and has also been validated in DNS calculations for moderate intense turbulence [106]. Therefore no modifications of this constant are proposed for fully developed flames in the limit of large Damköhler numbers.

In order to correctly predict the bending effect according to expression (3.45), information from the laminar flamelet and from turbulent interaction is required. Apart from the quantification of the laminar burning velocity  $s_L$ , also a correct measure of the flame diffusivity  $D_0$  for the laminar flamelet is essential. In chapter 3.1.2, the calculation of  $D_0$  is discussed. The conclusion drawn in that section is that  $D_0$  varies depending on the reference position taken inside the reaction zone. Therefore, a certain inaccuracy lies in the data from the laminar flamelet. With regards to turbulent interaction and using a fixed Schmidt number in the expression for  $D_t$ , (3.94),  $b_3$  needs to be quantified. In this work  $b_3$  is set to 1.0. In view of eqn. (4.7), the correction factor  $f_D$  does not only account for the corrections to the laminar flame diffusivity in the approximative expression, but also for modifications to  $b_3$ . A decrease of  $f_D$  by a factor of 4 yields an increase of  $b_3$  by a factor of 2.

As for the cylindrical vessel experiment presented in section 5.1, the correction factor is found to be close to unity. Thus we can conclude that the constant  $b_3 = 1.0$  from literature is in line with the reported experimental conditions. However, in the homogeneous engine calculations presented in section 5.2, the factor  $f_D$  was decreased by almost an order of magnitude. This cannot be sufficiently explained by possible differences between the laminar flame diffusivity of the real flamelet and its approximation. This fact implies instead that the coefficient  $b_3$  requires additional readjustment. One may therefore conclude that there exist conditions in which the bending effect has lower importance, indicated by a coefficient  $b_3$  greater than unity. Such conditions may occur for engine configurations where higher order hydrocarbon fuels at high unburnt temperatures (above approx. 600 K) and elevated pressures are combusted.

For the homogeneous charge cases, the interaction between the combustion process and the linear turbulence model, describing the flow in the engine geometry was discussed. Here, also the unburnt flow region and the advancing flame front have a mutual influence which is caused by turbulence. It is shown that for the turbulence prediction at late stages of the cycle, not all questions regarding the accuracy of the results could be answered. The underprediction of the mass burning rate as soon as the flame front enters into the squish region may be due to the turbulence model that is unable to capture the effects of the complex flow structure there. In order to reduce the effects of turbulence modeling on the combustion results, we must primarily consider the results of initial flame propagation.

With regards to the stratified cases, the interaction of the spray with the combustion model was shown. Analysis of injection-only cases with respect to ignition propensity

yielded good agreement with the experimental ignition timings if both the resolved and modeled mixture fraction fluctuations were considered. On the other hand, turbulent curvature effects on the mean flame front were found to have a weaker influence for the stratified combustion cases than for the homogeneous cases.

## Chapter 6

# Conclusions

In this work, the theory of premixed and partially premixed turbulent combustion modeling was presented, reviewed and applied to Spark Ignition engine simulation. The combustion model used was the  $G$ -equation concept based on the Level Set approach by Peters [70, 71] with extension to spark ignition modeling and unsteady flame behavior.

The model predicts the turbulent burning velocity taking four effects into account. The first effect is the Damköhler-number dependent bending effect that distinguishes between premixed combustion in large and small scale turbulence. Secondly, effects of turbulent mass fluxes due to global curvature of the mean turbulent flame front are taken into account. The third mechanism is due to unsteady flame development. This mechanism was formulated such that it consistently models the transition from a laminar to a fully developed turbulent flame by additionally taking the ratio of the turbulent flame brush thickness to the corresponding length scale of the turbulent flow into account. Additionally, a numerical procedure suited for describing spark ignition was developed. It allows for using the same physical model in both spark ignition and flame propagation phase. At last, the fourth mechanism that influences the turbulent burning velocity is caused by the instationary fluctuation of the air/fuel mixture ratio.

While the first and the last mechanism already were reported previously in the literature [13, 71], the second and third have been formulated in this work. Additionally, all these four mechanisms were integrated into one generalized model.

The model presented in this work was finally tested and validated using combustion cases in a closed cylindrical vessel with constant volume and in a Spark Ignition engine with homogeneous charge and charge stratification due to direct injection. For the homogeneous charge case, a variation of different levels of nitrogen dilution was successfully predicted. Also, a case of unsuccessful ignition was correctly predicted. The consideration of the direct injection cases with mixture stratification also gave good agreement between experiment and simulation with respect to the ignition timing window. The combustion simulations for the injected cases were in weaker agreement

with the experiments than the homogeneous cases. This can be explained with the more complex interaction (f. ex. spray) of physical sub-models involved than in homogeneous combustion. However, we can conclude that the  $G$ -equation concept for turbulent premixed combustion based on the Level Set Method is a suitable approach in order to predict premixed combustion phenomena in SI engines, both in homogeneous charge and stratified charge.

In order to improve the model performance, further work on the formulation is proposed. The physical sub-models for global flame curvature and unsteady flame development were derived by a heuristic approach and then applied to simulate complex experimental setups in which the above mentioned effects cannot be separated from each other. Although the approaches for these sub-models employed predict combustion with satisfying accuracy investigations to find a unique set of modeling constants are proposed. This applies primarily to the coefficient  $b_3$  in the algebraic  $\tilde{\sigma}_t$ -equation and the  $Sc_t$  number for the curvature term of the  $\tilde{G}$ -equation. It is therefore proposed carry out investigations by which the influence of the effects can be assessed separately from each other. For example, this can be accomplished by DNS of turbulent flame kernel development and the transition of planar laminar flames into turbulent flames.

The focus of future premixed turbulent combustion model development will likely be on the coupling of the  $G$ -equation concept with the Large Eddy Simulation (LES) approach [41] for turbulent flows, where turbulent motion of numerically resolvable structures is directly simulated and sub-grid structures are modeled. The LES approach promises to overcome modeling deficiencies that the RANS model has, for example – as discussed in this work – in predicting late cycle turbulence. Furthermore, the combination of these two approaches promises to provide solutions to questions about the cyclic variability of engine combustion, for instance, an aspect that is of great interest. Both LES and  $G$ -equation concepts have been previously combined [22], however with less modeling effort for premixed combustion. Since the RANS approach of the  $G$ -equation which has been further developed in this work requires more modeling effort than present LES models, these insights may also be used for LES/ $G$ -equation approaches in future.

## Appendix A

# The premixed turbulent reaction rate

In this appendix an attempt is made to derive a transport equation for the progress variable  $\tilde{c}$  from the Level Set flamelet parameters  $\tilde{G}$  and  $\widetilde{G''^2}$ . As a result, an expression for the volumetric reaction rate  $\dot{\tilde{\omega}}_G$  is obtained.

At first, we write eqn. (3.106) valid for the mean flame front position as

$$\frac{D\tilde{G}}{Dt} = -D'_t \tilde{\kappa} |\nabla \tilde{G}| + \frac{(\widetilde{\rho s_T})}{\langle \rho \rangle} |\nabla \tilde{G}|. \quad (\text{A.1})$$

Additionally, we will use the variance equation (3.98). In order simplify terms, the substantial derivative  $D/Dt$  is used for both equations to collect the temporal change and the convective terms.

In chapter 3.5.6, we have already assumed a functional relationship between the probability of finding burnt gas  $\tilde{P}_b$ ,  $\tilde{G}$ , and  $\widetilde{G''^2}$ . This relationship will not directly be used, except that we stipulate that the mean and the variance of the flame front position can be reduced to a non-dimensional coordinate  $\xi$ . Also, we equate  $\tilde{P}_b$  with the progress variable:

$$\tilde{c} = \tilde{P}_b = 1 - \tilde{I}_u = f\left(\frac{\tilde{G}}{\sqrt{\widetilde{G''^2}}}\right) = f(\xi). \quad (\text{A.2})$$

Using the following expressions for the derivatives of  $\tilde{c}$

$$\frac{\partial \tilde{c}}{\partial \tilde{G}} = \frac{\partial \tilde{c}}{\partial \xi} \frac{\partial \xi}{\partial \tilde{G}} = \frac{\partial \tilde{c}}{\partial \xi} \frac{1}{\sqrt{\widetilde{G''^2}}} \quad (\text{A.3})$$

$$\frac{\partial \tilde{c}}{\partial \widetilde{G''^2}} = \frac{\partial \tilde{c}}{\partial \xi} \frac{\partial \xi}{\partial \widetilde{G''^2}} = -\frac{\partial \tilde{c}}{\partial \xi} \frac{1}{2} \frac{\tilde{G}}{\widetilde{G''^2}^{3/2}} = -\frac{1}{2} \frac{\tilde{G}}{\widetilde{G''^2}} \frac{\partial \tilde{c}}{\partial \tilde{G}} \quad (\text{A.4})$$

and the chain rule of differentiation the transport equation reads:

$$\begin{aligned} \frac{D\tilde{c}}{Dt} &= \frac{\partial\tilde{c}}{\partial\tilde{G}} \frac{D\tilde{G}}{Dt} + \frac{\partial\tilde{c}}{\partial\widetilde{G''^2}} \frac{D\widetilde{G''^2}}{Dt} \\ &= \left\{ -D'_t\tilde{\kappa}|\nabla\tilde{G}| + \frac{\widetilde{(\rho s_T)}}{\langle\rho\rangle} |\nabla\tilde{G}| - \frac{1}{2} \frac{\tilde{G}}{\widetilde{G''^2}} \frac{D\widetilde{G''^2}}{Dt} \right\} \frac{\partial\tilde{c}}{\partial\tilde{G}}. \end{aligned} \quad (\text{A.5})$$

Here, no terms other than contribution due to premixed reaction and global curvature are identified. In analogy to *Peters* [71] we assume a convective-reactive balance for the progress variable apart from the global curvature effects and write after using the chain rule of differentiation

$$\frac{D\tilde{c}}{Dt} = -\text{sign}\left(\frac{\partial\tilde{c}}{\partial\tilde{G}}\right) D'_t\tilde{\kappa}|\nabla\tilde{c}| + \dot{\tilde{\omega}}_G \quad \text{with} \quad (\text{A.6})$$

$$\dot{\tilde{\omega}}_G = \left\{ \frac{\widetilde{(\rho s_T)}}{\langle\rho\rangle} |\nabla\tilde{G}| - \frac{1}{2} \frac{\tilde{G}}{\widetilde{G''^2}} \frac{D\widetilde{G''^2}}{Dt} \right\} \frac{\partial\tilde{c}}{\partial\tilde{G}}. \quad (\text{A.7})$$

Consequently, for  $\tilde{I}_u$  (see chapter 4.3.2), the transport equation reads:

$$\frac{D\tilde{I}_u}{Dt} = -\text{sign}\left(\frac{\partial\tilde{I}_u}{\partial\tilde{G}}\right) D'_t\tilde{\kappa}|\nabla\tilde{I}_u| - \dot{\tilde{\omega}}_G. \quad (\text{A.8})$$

For a fully developed turbulent flame the substantial derivative of  $\widetilde{G''^2}$  is negligibly small. Then, we can simplify the expression for the premixed reaction rate to

$$\dot{\tilde{\omega}}_G \approx \frac{\widetilde{(\rho s_T)}}{\langle\rho\rangle} |\nabla\tilde{G}| \frac{\partial\tilde{c}}{\partial\tilde{G}} = \text{sign}\left(\frac{\partial\tilde{c}}{\partial\tilde{G}}\right) \frac{\widetilde{(\rho s_T)}}{\langle\rho\rangle} |\nabla\tilde{c}| = -\text{sign}\left(\frac{\partial\tilde{I}_u}{\partial\tilde{G}}\right) \frac{\widetilde{(\rho s_T)}}{\langle\rho\rangle} |\nabla\tilde{I}_u|. \quad (\text{A.9})$$



## Appendix B

# Level Sets methods on unstructured grids

### B.1 Level Set Numerics

#### B.1.1 Introduction

Level Set methods can be used to describe the position of interfaces in 3D space and their evolution in time. The basis is a scalar field, here denoted by the quantity  $G$ . As regards to the premixed combustion modeling, this scalar  $G$  may refer to the instantaneous flame front position as well as to the averaged mean flame front position  $\tilde{G}$ . Therefore, in this section the tilde is omitted completely but the methods presented here are valid both for the instantaneous and the averaged  $G$ .

Interfaces are located where  $G = G_0$  (and  $G_0 \equiv 0$ ). Outside of this interface  $G$  represents the signed distance between the point in space where  $G$  is defined and the closest point of the interface. Two issues are important when employing Level Set Methods:

- Development of a method in order to advect the interface according to the underlying physical model.
- Maintaining the distance information outside of the interface.

At the interface position  $G = G_0$  we define the following PDE for the advection of the front.

$$\frac{dG}{dt} + F |\nabla G| = 0 \quad (\text{B.1})$$

The scalar  $F$  denotes the normal velocity of the interface. Non-orthogonal velocity components do not need to be considered.

*Per se* the scalar field of  $G$  is not defined for  $G \neq G_0$ . However, in the context of premixed turbulent combustion it is helpful to give  $G$  a useful meaning everywhere

else. In order to accomplish that, outside of the front we impose a distance constraint by

$$|\nabla G| = 1. \quad (\text{B.2})$$

The sign of  $G$  gives the information on which side of the interface the point is located.

### B.1.2 Characteristics of the $G$ -equation

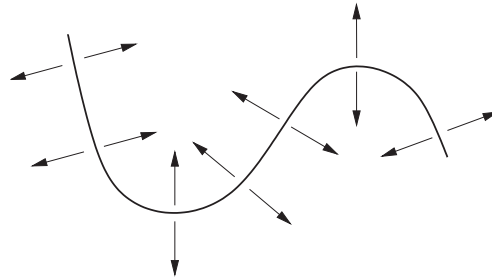


**Figure B.1:** Characteristics of the  $G$ -equation with a given interface position. Arrows indicate the information transport.

The characteristics of the  $G$ -equation are related to the propagation of information due to the distance constraint (B.2). The interface  $G = G_0$  imposes an inner boundary condition on the field. The information propagation is normal to the iso- $G$  surface, where the normal is defined as

$$\vec{n} \equiv -\frac{\nabla G}{|\nabla G|}. \quad (\text{B.3})$$

In general, the definition of the sign is arbitrary. Due to the information transport away from the front, this implies that the value of  $G$  at a certain point is only determined by points closer to the interface. Some conclusion for the correct and most efficient numerics can be drawn from this fact. Upwind differencing should be used from the direction of the interface. It is most efficient to start the calculation from the interface and let it propagate from there into the whole domain.

In [97] and [98], a PDE dependent on an artificial time scale  $\tau$

$$\frac{dG}{d\tau} = \text{sign}(G_{\tau=0})(1 - |\nabla G|) \quad (\text{B.4})$$

with an adapted sign function  $\text{sign}(G)$  is solved until a steady state solution is reached. When the solution in respect to the iteration in  $\tau$  has converged, the distance constraint (B.2) is obtained. This procedure is called *reinitialization*.  $|\nabla G|$  is calculated employing upwind differencing. This method can be realized in parallelized environments in a straight forward way, but it does not take the location of the interface position into account. This method therefore lacks efficiency since many subcycles for the artificial

time loop might be required for obtaining a steady state solution. Another disadvantage is that it requires an initial  $G$  field that represents sufficiently accurate a distance field.

Another method by *Sethian* [88] is called “Fast Marching Method”. This method enables a fast reinitialization procedure and updates  $|G|$  according to the distance from the interface thus calculating farthest points last.

## B.2 Defining an Extension Velocity

If the kinematics of the interface at a point  $\vec{x}_0$  are known,  $F$  can be determined to:

$$F = -\frac{d\vec{x}_0}{dt} \cdot \vec{n} . \quad (\text{B.5})$$

*Adalsteinsson* [2] has proposed to extend  $F$  and thereby eqn. (B.1) from the interface position to the whole computational domain:

$$\frac{dG}{dt} + F_{\text{ext}} |\nabla G| = 0 . \quad (\text{B.6})$$

$F_{\text{ext}}$  is the so-called extension velocity valid in the whole computational domain. At the interface,  $F \equiv F_{\text{ext}}$  as inner boundary condition. It is clear that in order to correctly use eqn. (B.6),  $F_{\text{ext}}$  has to be suitably defined. For the special case  $|\nabla G| = 1$  it is apparent that the following equation is suitable:

$$\nabla F_{\text{ext}} \cdot \nabla G = 0 \quad (\text{B.7})$$

That means that in principle  $F_{\text{ext}} = \text{const.}$  along the direction of  $\vec{n}$ . A signed function  $G$  remains a distance function if eqn. (B.7). This is illustrated as follows:

$$\begin{aligned} \frac{d|\nabla G|^2}{dt} &= \frac{d}{dt} (\nabla G \cdot \nabla G) = 2\nabla G \cdot \frac{d}{dt} \nabla G \\ &= \underbrace{-2\nabla G \cdot \nabla F_{\text{ext}}}_{\text{eqn. (B.7)}} |\nabla G| - 2\nabla G \cdot \nabla \underbrace{|\nabla G|}_{\stackrel{!}{=} 1}} F_{\text{ext}} = 0. \end{aligned} \quad (\text{B.8})$$

Since eqn. (B.7) features the same characteristics as eqn. (B.6), it can be solved either by an artificial time dependent PDE [66]

$$\frac{dF_{\text{ext}}}{d\tau} + \text{sign}(G) \frac{\nabla G}{|\nabla G|} \cdot \nabla F_{\text{ext}} = 0 \quad (\text{B.9})$$

or by an appropriate Fast Marching Method. The latter will be discussed below for unstructured meshes.

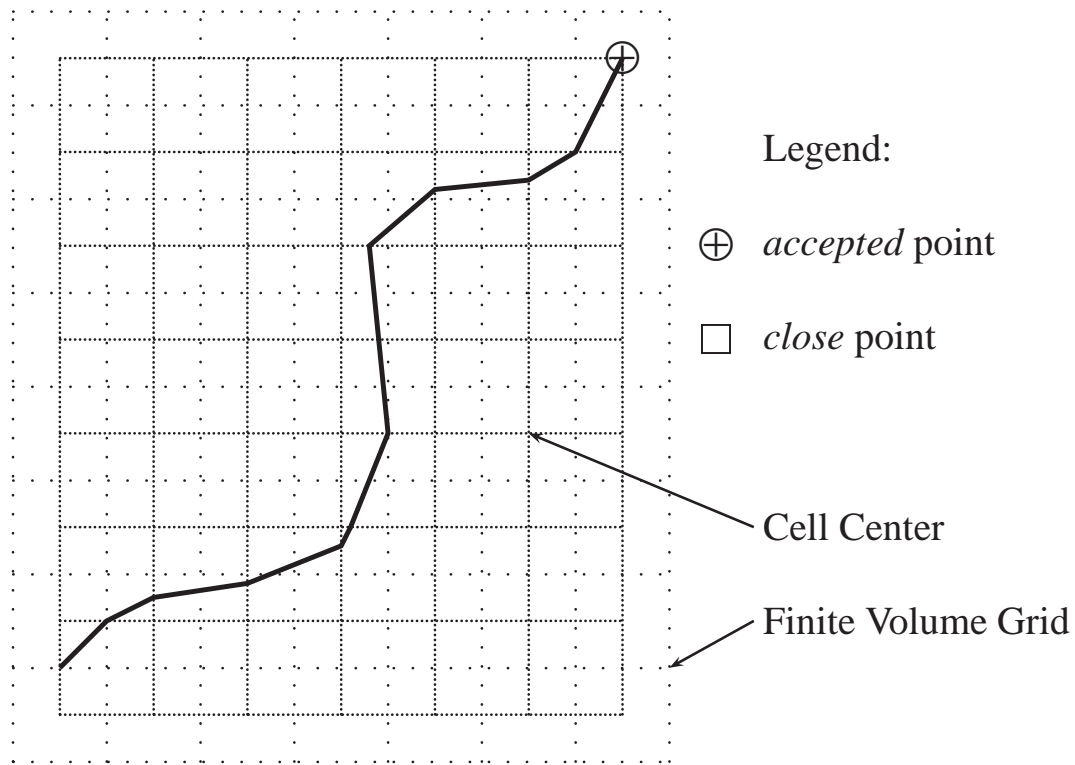


**Figure B.2:** Begin of the Fast Marching Algorithm: points on the interface are tagged as *accepted* immediately.

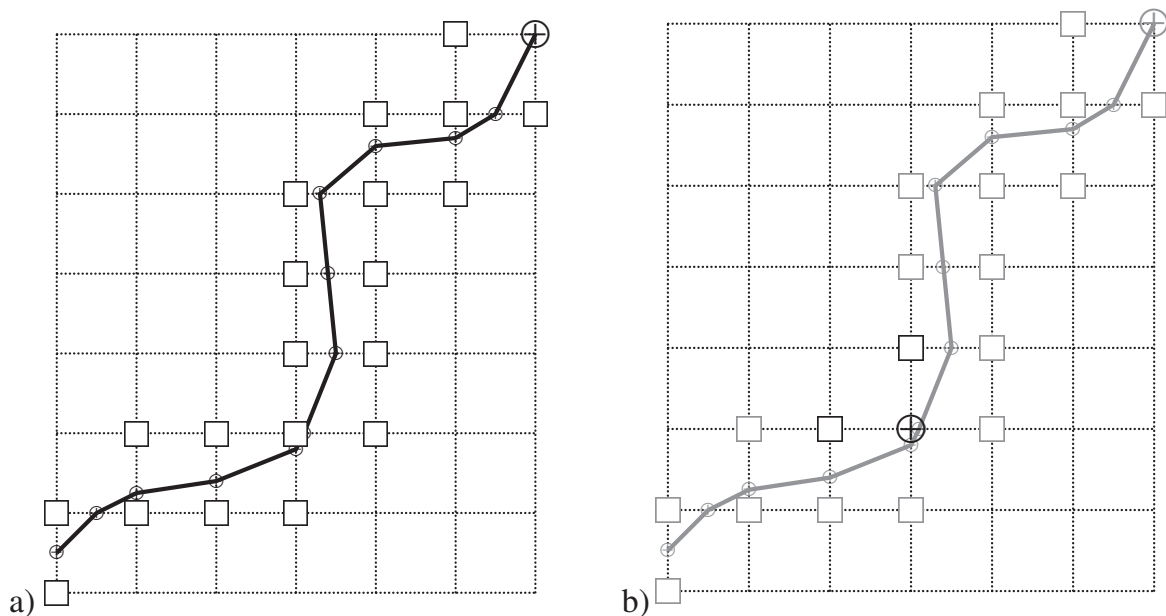


**Figure B.3:** Image a) depicts the first determination of *close points* neighboring the interface. The intersections between the interface and the grid can also be considered as *accepted* help points. In b) one step has been performed where the values for the points to be updated are colored in black. The closest point is moved into the *accepted* set. Unchanged points are colored in grey.

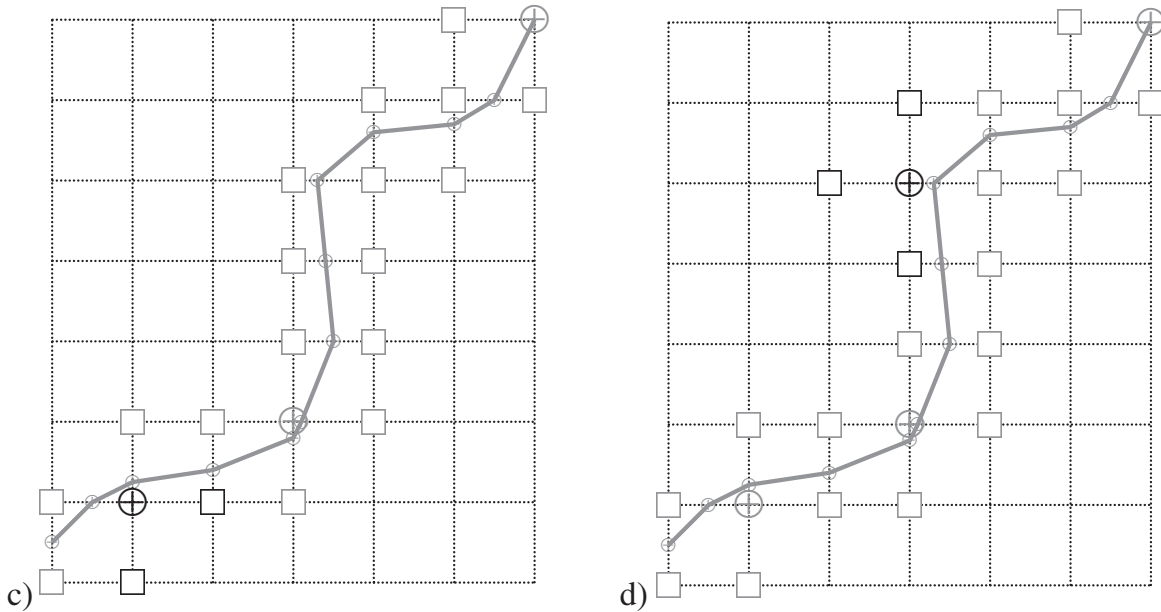


Figure B.4: Two more steps of the update procedure.

### B.3 The Fast Marching Method

The intention of this section is to give an overview of the Fast Marching Method by Sethian [88, 89]. Additional information can be found in those references.

As a prerequisite, information about the location of the interface is needed. From a numerical point of view, this would be a discretized scalar field  $\mathcal{G}$  that partitions the domain into the two groups  $\mathcal{G} > G_0$  and  $\mathcal{G} < G_0$  and allows for the determination of the  $G = G_0$  surface by means of interpolation between two sign opposing neighbors with respect to  $\mathcal{G}$ . It is not required that  $\mathcal{G}$  satisfies the constraint (B.2). By means of the Fast Marching Method one can generate a Level Set field of  $G$  obeying the distance constraint eqn. (B.2) from such a field  $\mathcal{G}$ .

In the following section the update procedure of the Fast Marching Method thus leading to a reinitialized  $G^{\text{tmp}}$ -field is described.

1. At the beginning of the Fast Marching Procedure all points that are exactly on the interface (i.e.  $G = G_0$ ) will be identified. Since no update is required for these points  $G^{\text{tmp}}$  will be assigned to be *accepted*. Points with this status are finally determined in terms of their distance value. It is clear that  $G^{\text{tmp}} = G_0$  for points on the interface. The other cells will be tagged as *far* and the  $G^{\text{tmp}}$ -field of these cells will be initialized with a very large signed distance value thus indicating on which side in the domain they are located.
2. The next step is to identify those points where a preliminary value of  $G^{\text{tmp}}$  can be computed. Such points will be collected in the set of *close* points. They must have neighbors that are either *accepted* or have the opposite sign, which means

that the interface is crossed in between. Using either the  $G^{\text{tmp}}$  distance information of the neighbors on the same side of the interface or the direct interface information, what ever is available, a preliminary value of  $G^{\text{tmp}}$  is computed for these cells. They are tagged as *close* and put into the set of *close* points.

3. All points in the *close* set will be sorted according to their value  $|G^{\text{tmp}}|$ , starting with the lowest value of  $|G^{\text{tmp}}|$ . The point with the lowest value of  $|G^{\text{tmp}}|$  will not be updated anymore because no new information from points closer to the interface is available. It will be taken out of this set and tagged as *accepted*.
4. The neighbors of this point that taken out of the set must be double checked in terms of  $G^{\text{tmp}}$ , and tagged as *close* unless this is already the case. For each of these points their neighbors closer to the interface are chosen in order recompute  $G^{\text{tmp}}$  accounting for eqn. (B.2). The points checked can be divided into two groups: The first group is already in the *close* set and their value of  $G^{\text{tmp}}$  either remains unchanged or the value of  $|G^{\text{tmp}}|$  is smaller now. In the latter case the set of *close* points must be resorted. The second group contains points of the *far* set. The value of  $G^{\text{tmp}}$  must be updated for the first time here. The points are tagged as *close* and put into the set of *close* points. Again, the set of *close* points needs to be resorted.
5. The procedure is repeated starting with step # 3 until the domain is completely resolved and all points are in the *accepted* set.

This update procedure ensures that the closest points in the domain are computed first, farrest points last.

## B.4 Discretisation on an unstructured grid

While the other field quantities and scalars are solved using an implicit Finite Volume method, the  $G$ -equation is solved by an explicit method based on finite differences. The points where the  $G$ -equation is stored in the implementation used here are located on the cell centers of the finite volume mesh. This is due to the fact that the  $G$ -equation (B.1) is a transport equation of a length scale field while the other field variables are related to the mass density or to the mass contained in a control volume of the flow field. Hence the connectivity of the finite volume mesh based on hexahedra needs to be transformed into a tetrahedral finite difference mesh with  $G$  defined at the mesh nodes.

Consider  $p$  to be a certain point in space at which the  $G$  equation has to be discretized. The value of  $G_p$  at  $p$  has to be determined considering (B.2). In order to discretize the gradient operator by an upwind formulation, only neighbors  $i_k$  of  $p$  closer to the  $G_0$  interface than  $p$  must be taken. Since the  $\nabla G$  vector is not curved in the domain, a spatial discretisation of first order is sufficient. Hence only up to three neighbors of  $p$  can be used for discretizing the gradient in 3D space. One constraint of choosing possible neighbor candidates is that calculating  $G_p$ ,  $|G_p|$  is minimized. If



**Figure B.5:** Constructed Finite Difference grid around  $p$  and its neighbors in 2D (left side) with triangles and in 3D (right side) consisting of tetrahedras.

only one neighbor is available,  $G_p$  can geometrically determined in a straight forward way. If there are two or more neighbors, it is advantageous to square the equation (B.2) and calculate the geometrically reasonable solution of the quadratic equation

$$(\nabla G)^2 = 1 . \quad (\text{B.10})$$

Once  $G_p$  is obtained,  $F_{\text{ext},p}$  must be solved for by  $\nabla G \cdot \nabla F_{\text{ext}} = 0$ , where the same neighbors as for calculating  $G_p$  have to be employed for discretizing  $\nabla G$  and  $\nabla F_{\text{ext}}$ .

As pointed out above, up to three neighbors of  $p$  can be used for discretizing the gradient  $\nabla G$ . Even in a 3D problem, there exist situations, where two or even only one neighbor can be employed for discretization. The occurrence of these situations will be explained below.

During the update procedure of  $G_p$  it is likely that  $p$  has less than three neighbors that are closer to the interface than  $p$  itself. Each set of suitable nodes for discretization must belong to the same tetrahedron of the finite difference grid (see fig. B.5).

Each choice of possible neighbors results in a value  $G_p$  and gradient  $\nabla G$ . Then, the gradient of  $G$  at  $p$  needs to be checked for validity. If two neighbor candidates are chosen,  $\nabla G$  must be directed as coming from the triangle that is formed by the two neighbors and it must be coplanar to the triangle in order to be valid. This is depicted in figure B.6. If three neighbor candidates are chosen,  $\nabla G$  must be oriented from within the tetrahedron formed for validity, see figure B.7.

## B.5 Temporal integration

The discretization of eqn. (B.1), or eqn. (B.6) respectively, leads to an explicit first-order method for the advection in time:

$$G^{n+1} = G^n - \Delta t F_{\text{ext}}^n \quad (\text{B.11})$$

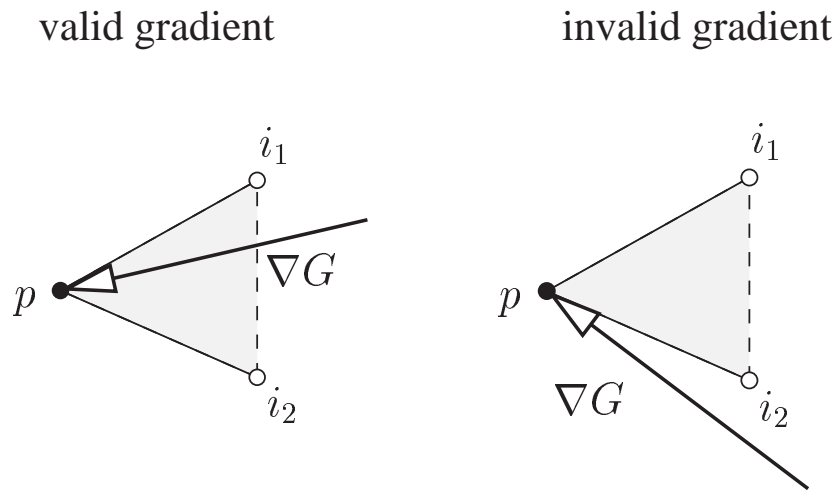


**Figure B.6:** Valid and invalid gradient in 2D.

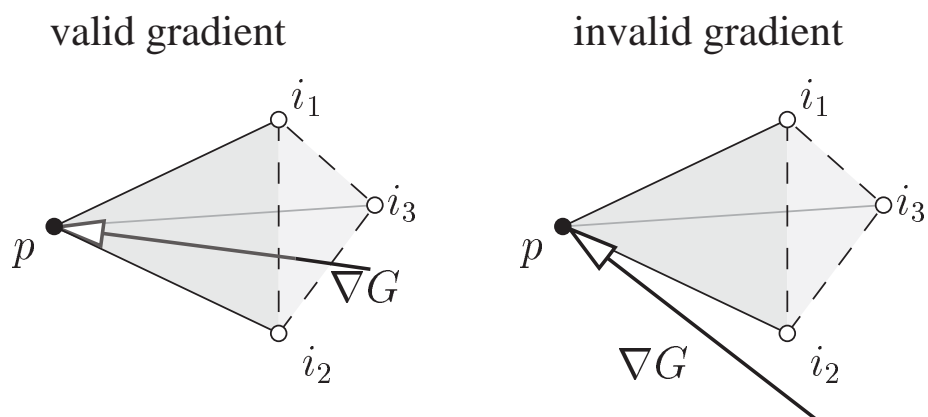


**Figure B.7:** Valid and invalid gradient in 3D.



An extension of this approach to second order accuracy in time reads:

$$\begin{aligned} G^{(n+1)'} &= G^n - \Delta t F_{\text{ext}}^n \\ G^{n+1} &= G^n - \frac{\Delta t}{2} \left( F_{\text{ext}}^n + F_{\text{ext}}^{(n+1)'} \right) \end{aligned} \quad (\text{B.12})$$

For each time level, where  $F_{\text{ext}}$  is determined, also a reinitialized field of  $G$ ,  $G^{\text{tmp}}$  is calculated simultaneously. In order to maintain stability, the field of  $G^n$  at the old time level can be replaced by the reinitialized field  $G^{n,\text{tmp}}$  after a predefined number of time steps. In this case, eqn. B.12 transforms into:

$$\begin{aligned} G^{(n+1)'} &= G^{n,\text{tmp}} - \Delta t F_{\text{ext}}^n \\ G^{n+1} &= G^{n,\text{tmp}} - \frac{\Delta t}{2} \left( F_{\text{ext}}^n + F_{\text{ext}}^{(n+1)'} \right) \end{aligned} \quad (\text{B.13})$$



## Appendix C

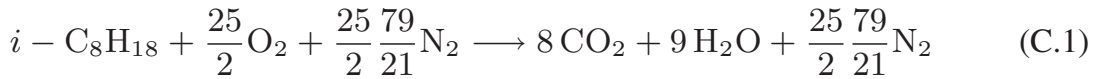
# Laminar Burning Velocity approximation

The approximation for the laminar burning velocity of iso-octane is valid for a wide range of unburnt conditions:

| Sign             | Description         | validity    |
|------------------|---------------------|-------------|
| $p$              | pressure            | 1...50 bar  |
| $T_u$            | unburnt temperature | 300...800 K |
| $\phi$           | equivalence ratio   | 0.5...2.0   |
| $Y_{\text{EGR}}$ | EGR mass fraction   | 0.0...0.3   |

The limits given are to be understood as limits for high accuracy while the approximation for the burning velocities are also reasonable a much wider parameter range, however with lower accuracy.

The EGR species composition is assumed to consist of the products of the global reaction step with air as oxidizer stream



under stoichiometric conditions. While eqn. (2.20) is assumed for the definition for the mixture fraction  $Z$ , the definition of the inert EGR mass fraction  $Y_{\text{EGR}}$  reads:

$$Y_{\text{EGR}} = \frac{\dot{m}_{\text{EGR}}}{\dot{m}_{\text{fuel}} + \dot{m}_{\text{air}} + \dot{m}_{\text{EGR}}}. \quad (\text{C.2})$$

For determining  $s_L$ , the following information is needed: the pressure  $p$ , the unburnt temperature  $T_u$ , the reduced mixture fraction  $Z^*$  and the mass fraction of exhaust gas  $Y_{\text{EGR}}$ . The reduced mixture fraction  $Z^*$  denotes the reduced mass fraction of fuel atoms in a gas mixture excluding EGR:

$$Z^* = \frac{Z}{1 - Y_{\text{EGR}}} \quad (\text{C.3})$$

where  $Z$  is the mixture fraction of the fuel.  $Z^*$  can be linked directly with the equivalence ratio by

$$Z^* = \frac{1}{\frac{1 - Z_{st}^*}{\phi Z_{st}^*} + 1}. \quad (\text{C.4})$$

The starting point for developing an approximation expression for lean and rich mixtures is the approach presented in [62]. The expression (12) for  $s_L$  in this reference was derived by asymptotic analysis in [73] for lean and stoichiometric flames. The expression here for  $s_L$  is based on [62]. By exchanging the unburnt fuel mass fraction  $Y_{F,u}$  by a ‘‘reactive mass fraction’’  $Y_{\text{react}}$ , the following approximative relationship is obtained:

$$s_L = A(T^0) Y_{\text{react}}^m \left( \frac{T_u}{T^0} \right)^r \left( \frac{T_b - T^0}{T_b - T_u} \right)^n. \quad (\text{C.5})$$

with

$$A(T^0) = F \exp \left( -\frac{G}{T^0} \right) \quad (\text{C.6})$$

and

$$Y_{\text{react}}(Z^*, Y_{\text{EGR}}) = \left( \frac{Z^*}{1.1 Z_{st}^*} \right)^{n_a} \left( \frac{1 - Z^*}{1 - 1.1 Z_{st}^*} \right)^{[(1.1 Z_{st}^*)^{-1} - 1] n_a} (1 - Y_{\text{EGR}})^{n_{\text{EGR}}}. \quad (\text{C.7})$$

The frequency factor  $A(T^0)$  is dependent on the inner layer temperature  $T^0$  adjusted for fitting  $s_L$ . Since the laminar burning velocity reaches its maximum at  $\phi \approx 1.1$ ,  $Y_{\text{react}}$  has been scaled such that it reaches its maximum also in the vicinity of this equivalence ratio. This behavior is also verified in experimental and numerical investigations.

$$T^0 = T_u S_1(Z^*) + \frac{E_i S_2(Z^*)}{\ln \frac{B_i}{p}} \quad (\text{C.8})$$

$$T_b = T_u (S_4(Z^*)(1 - Y_{\text{EGR}}) + Y_{\text{EGR}}) + (1 - Y_{\text{EGR}}) S_3(Z^*) \quad (\text{C.9})$$

$S_1$  to  $S_4$  are splines valid in the mixture fraction space  $Z^* \in [0..1]$  defined by knot points as given in table C.1. The remaining constants for fitting  $s_L$  are given in table C.1.

| $Z^*$   | $S_1$       | $S_2$       | $S_3$ [K]  | $S_4$       |
|---------|-------------|-------------|------------|-------------|
| 0.0     | 1.0         | 0.0         | 0.0        | 1.0         |
|         | $S_1'' = 0$ | $S_2'' = 0$ | $S_3' = 0$ | $S_4'' = 0$ |
| 0.025   | 0.28        | 0.814       | 1103.8     | 0.824       |
| 0.05    | 0.0         | 0.993       | 1879.5     | 0.708       |
| 0.06211 | 0.0         | 1.0         | 2206.6     | 0.610       |
| 0.07    | 0.0         | 0.989       | 2097.8     | 0.710       |
| 0.08    | 0.0         | 0.996       | 1950.2     | 0.716       |
| 0.1     | 0.0         | 1.023       | 1340.4     | 0.677       |
| 0.12    | 0.0         | 1.030       | 1651.0     | 0.460       |
| 0.15    | 0.0         | 0.985       | 1340.5     | 0.627       |
| 0.18    | 0.05        | 0.513       | 1297.2     | 0.422       |
| 0.2     | 0.1         | 0.939       | 1267.9     | 0.356       |
| 1.0     | 1.0         | 0.0         | 0.0        | 1.0         |
|         | $S_1' = 0$  | $S_2'' = 0$ | $S_3' = 0$ | $S_4'' = 0$ |

**Table C.1:** Spline knot points for splines  $S_1$  to  $S_4$  for fitting  $s_L$ .

|            |                                  |
|------------|----------------------------------|
| $Z_{st}^*$ | 0.062113                         |
| $E_i$      | 72017.8671 K                     |
| $B_i$      | $0.296729694 \times 10^{23}$ bar |
| $m$        | 1.5                              |
| $r$        | 0.985                            |
| $n$        | 2.439                            |
| $F$        | 0.2679 cm/s                      |
| $G$        | -11376.6362 K                    |
| $n_{EGR}$  | 0.8507                           |
| $n_a$      | 0.5                              |

**Table C.2:** Additional constants for the  $s_L$  fit.

Fit for the diffusivity  $D$ :

$$D = C_{D0} \left[ S_5(Z^*) (1 - Y_{\text{EGR}})^{C_{DE}} + 1.0 \right] \left( \frac{p}{1 \text{ bar}} \right)^{-C_{Dp}} \left( \frac{T_u}{1 \text{ K}} \right)^{C_{DT}} \quad (\text{C.10})$$

Constants:

|          |   |
|----------|---|
| $C_{Dp}$ | 1.047                                     |
| $C_{DT}$ | 1.462                                     |
| $C_{DE}$ | 1.876                                     |
| $C_{D0}$ | $0.12414 \times 10^{-5} \text{ (cm m)/s}$ |

Knot points for the Spline  $S_5$ :

| $Z^*$   | $S_5$       |
|---------|-------------|
| 0.0     | 0.0         |
|         | $S'_5 = 0$  |
| 0.05    | 1.105       |
| 0.06211 | 1.418       |
| 0.07    | 1.335       |
| 0.08    | 1.079       |
| 0.1     | 0.688       |
| 0.12    | 0.680       |
| 0.15    | 0.360       |
| 0.18    | 0.139       |
| 0.4     | 0.0         |
|         | $S''_5 = 0$ |

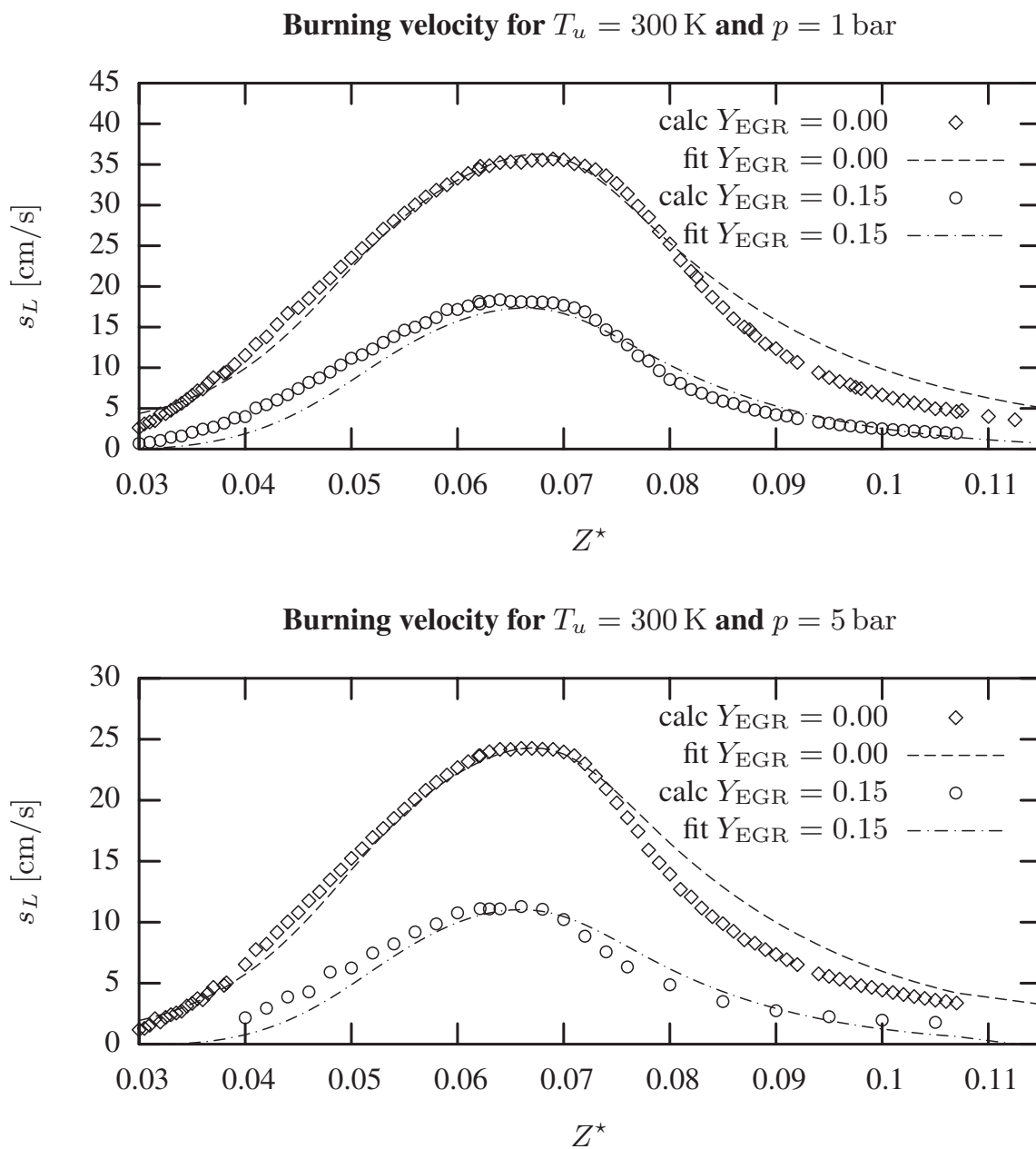


**Figure C.1:** Comparison of burning velocities obtained using the 1D DNS code `FlameMaster` [76] and the approximation for iso-octane over mixture fraction space for a fixed unburnt temperature and two different pressures with different EGR levels.

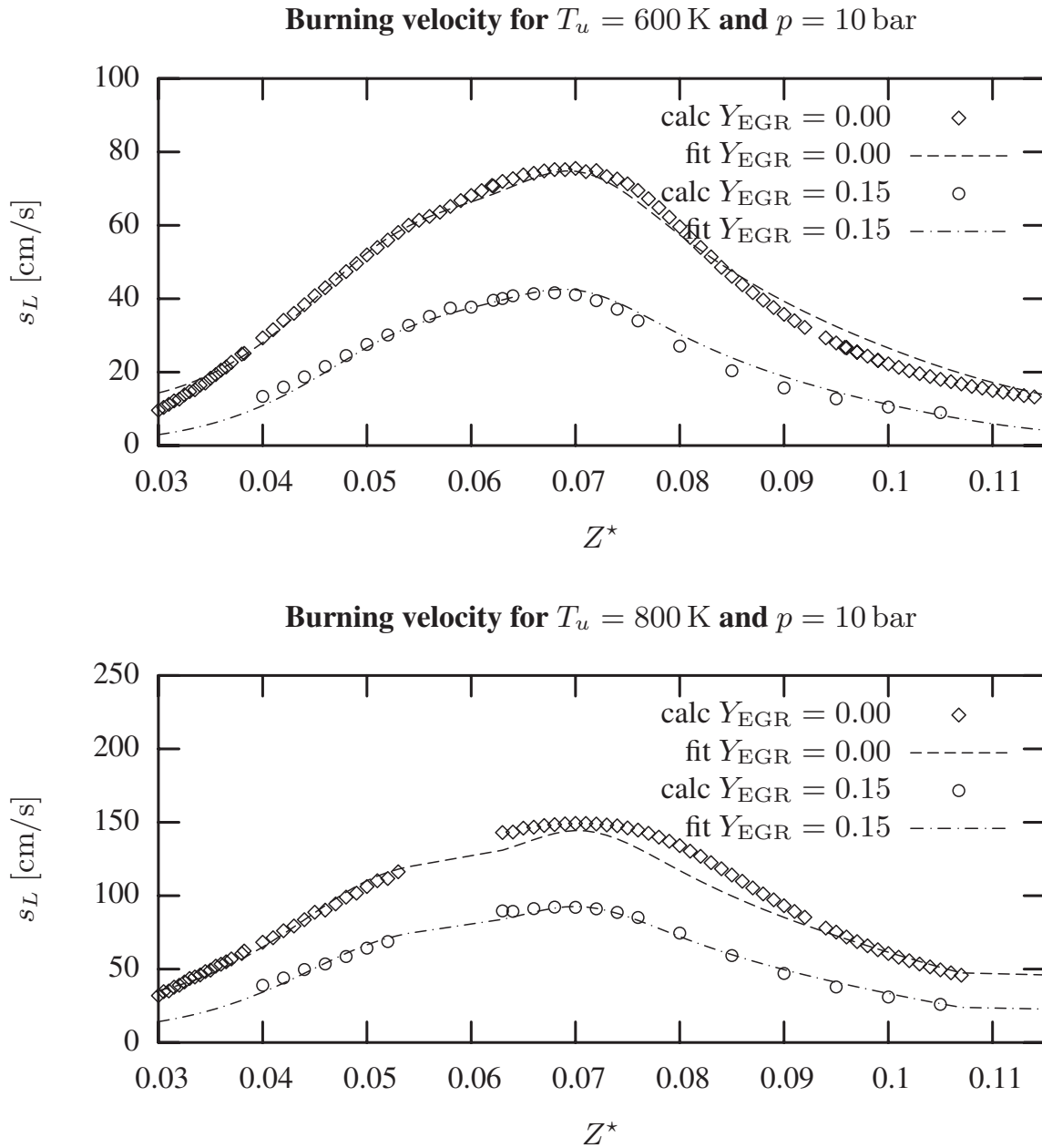


**Figure C.2:** Analog to previous figure, but with different pressure and unburnt temperatures



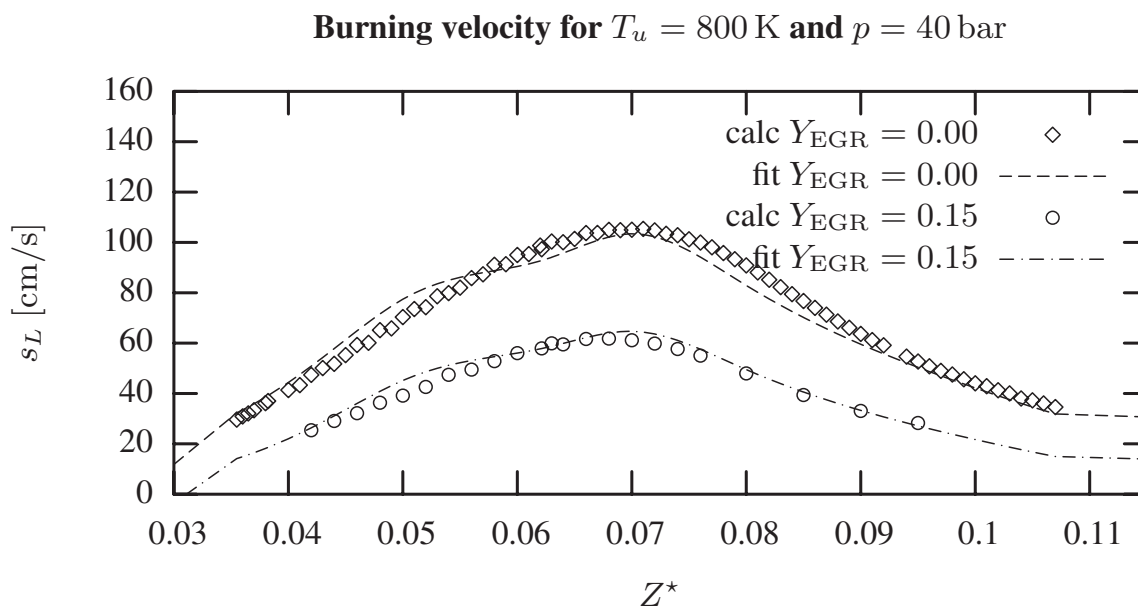


**Figure C.3:** Analog to figures C.2, but with another unburnt temperature and pressure.

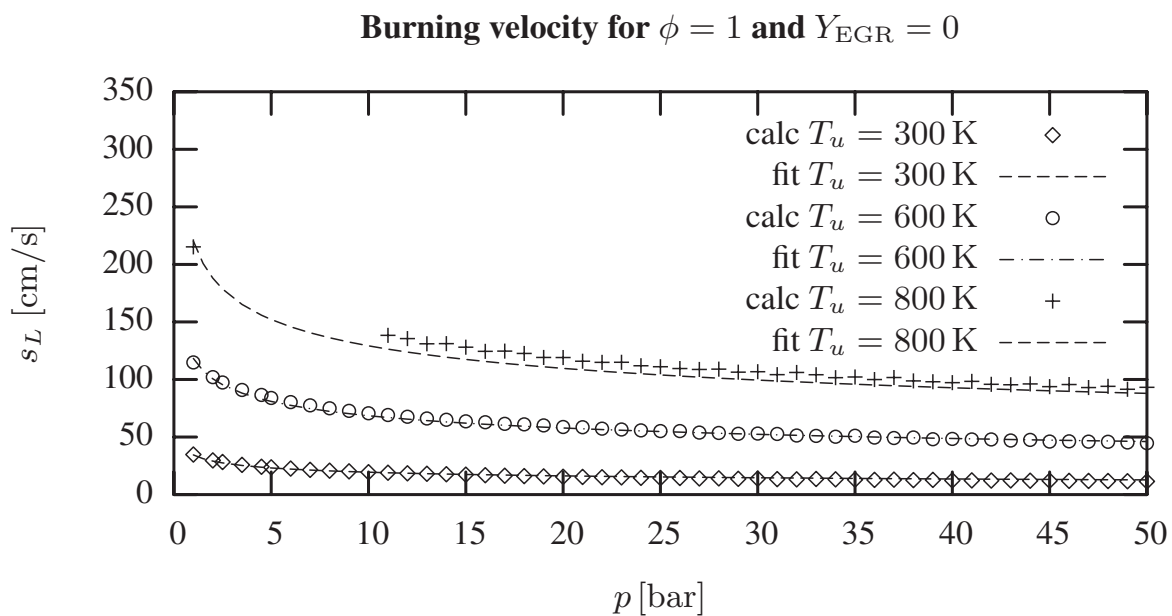


**Figure C.4:** Comparison of burning velocities between 1D-DNS calculations and approximation at stoichiometric mixture over pressure for different unburnt temperatures.



## Appendix D

# Turbulence prediction in the engine squish

In this appendix, the behavior of the turbulent kinetic energy and the turbulent dissipation in a specified location within the squish region for engine case I presented in chapter 5.2 are discussed.

Here we will compare the production term  $\mathcal{P}$ , eqn. (2.54), without the density for different crank angle positions in radial direction. The modified production term reads then:

$$\mathcal{P} = - \langle u_i'' u_j'' \rangle \frac{\partial \tilde{u}_j}{\partial x_i} = \mathcal{P}_1 + \mathcal{P}_2 + \mathcal{P}_3 . \quad (\text{D.1})$$

In order to assess different effects better, the production term is split into three components. The linear Boussinesq approach (2.60) leads to the terms

$$\mathcal{P}_1 = \frac{\mu_t}{\langle \rho \rangle} \left( \frac{\partial \tilde{u}_i}{\partial x_j} + \frac{\partial \tilde{u}_j}{\partial x_i} \right) \frac{\partial \tilde{u}_j}{\partial x_i} \quad (\text{D.2})$$

and

$$\mathcal{P}_2 = -\frac{2}{3} \frac{\mu_t}{\langle \rho \rangle} \left( \nabla \cdot \tilde{\vec{u}} \right)^2 . \quad (\text{D.3})$$

$\mathcal{P}_1$  is the contribution due to shear to the deviatoric components of the Reynolds stress tensor. In  $\mathcal{P}_2$ , the corrections due to global compressibility and variable density flows are collected. The third component,

$$\mathcal{P}_3 = -\frac{2}{3} k \nabla \cdot \tilde{\vec{u}} , \quad (\text{D.4})$$

is due to the isotropic contributions of the Reynolds stress tensor. This term also appears in the unclosed equation for  $k$ , see eg. [83, 107].

Now, the mean velocity components, the distribution of  $k$  and  $\varepsilon$ , and the three components of the turbulent production term for the  $k$  equation are investigated for the homogeneous engine case I discussed in chapter 5.2.

In figs. D.1-D.3 results are displayed from CFD on a line in the squish in the  $y, z$  plane for several crank angle positions before and after TDC, as indicated in the first figure. In the range between  $-20^\circ\text{CA}$  and  $10^\circ\text{CA}$ , the turbulent kinetic energy decreases. This can be explained by the fact that on the extracted line, the net rate of turbulent production  $\mathcal{P} - \varepsilon$  becomes negative at about  $-10^\circ\text{CA}$ . Therefore, the contributing components need to be further investigated.

It is evident that the correction of the mean shear tensor due to compressibility to turbulent production  $\mathcal{P}_2$  is negligibly small and will not be discussed any further. The leading order terms are therefore  $\mathcal{P}_1$ ,  $\mathcal{P}_3$ , and  $\varepsilon$ . In the linear turbulence model, the isotropic contribution to the turbulent production  $\mathcal{P}_3$  is positive and dominant against the deviatoric contribution  $\mathcal{P}_1$  for increasing pressure in non-reacting flow regions. For decreasing pressure and flow regions subjected to heat release,  $\mathcal{P}_3$  is negative. Provided that the calculation of the mean flow and  $k$  is sufficiently accurate, this term is exact and does not require any further modeling.  $\mathcal{P}_1$  decreases with a progressing crank angle position. Turbulent dissipation  $\varepsilon$  is approximately constant except for large radii close to the cylinder walls where it strongly increases.

With regards to the mean flow pattern, three main phenomena can be identified. The first is due to the swirl from the intake procedure which is present in the squish for low piston positions. For higher piston positions, this swirl is superimposed by the other patterns. The second phenomenon is the pressure increase and decrease which force the flow in and out of the squish region, respectively. The last phenomenon is due to the moving piston which causes the gas to be displaced as well. The result is a complex flow pattern in which the velocity vectors frequently change their direction. In fig. D.1 it can be seen that additionally a tumble in radial direction exists in the squish. At TDC, this tumble does not exist anymore.

*Miles et al.* [61] have compared the turbulent flow in a DI Diesel engine at late crank angles with linear RANS turbulence model calculations. It was found that the CFD results sufficiently calculated the main flow patterns, but poorly predicted the Reynolds stresses around TDC, especially in those regions, in which flow from the squish into the piston bowl can be observed. The reason for this discrepancy was argued to be due to the modeling of turbulent production for which the linear  $k, \varepsilon$  model takes only shear of the mean flow into account, but no rotation. In a later work [60], the same authors investigated the influence of swirl on the accuracy of Reynolds stress prediction. They found that with the linear  $k, \varepsilon$  model, the accuracy decreases with increasing swirl ratio. The inability of the linear model to predict turbulence in rotational flows is well known [11].

Further, there are uncertainties in  $\varepsilon$ , which is difficult to be measured directly and for which to the knowledge of the author no comparisons to experiments are available for engine applications in the literature. In the postulated model equation (2.58) for the turbulent dissipation the leading order terms in turbulent production containing the

divergence of the mean flow can be summarized as

$$\left(-\frac{2}{3}C_{\varepsilon 1} + C_{\varepsilon 3}\right) \varepsilon \left(\nabla \cdot \tilde{\mathbf{u}}\right) . \quad (\text{D.5})$$

Analogous to the equation for  $k$ , these terms have great influence on the production of turbulent dissipation. The factor  $C_{\varepsilon 3}$ , as discussed in chapter 2.4, is empirical. A parameter study in which  $C_{\varepsilon 3} = 0$ , however, did not lead to a significant change of the results.

The decrease of turbulent kinetic energy in the squish region which is predicted by the CFD calculations cannot be validated by experimental investigations since no data are available for this specific engine geometry. As discussed above, however, it is likely that the CFD calculations underpredict the Reynolds stresses in the squish, a phenomenon that has already been reported. If this is the case, the underprediction may be due to the contribution of mean shear to production in the  $k$  equation. Error contributions due to the  $\varepsilon$  model cannot be excluded either.

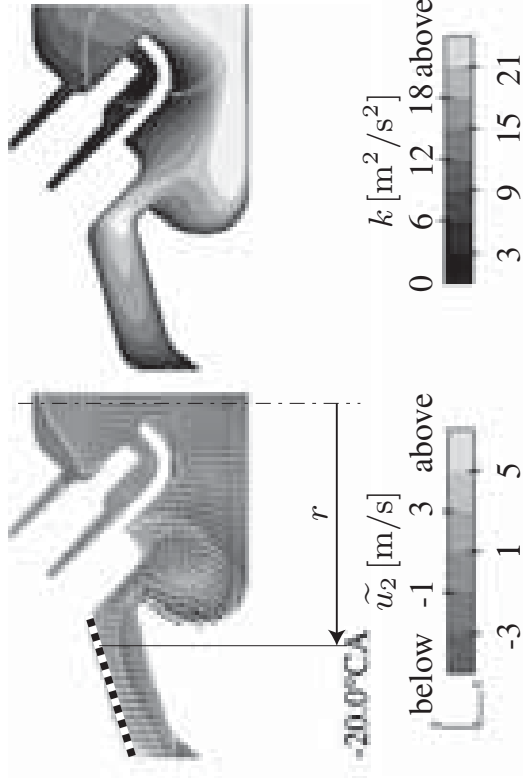
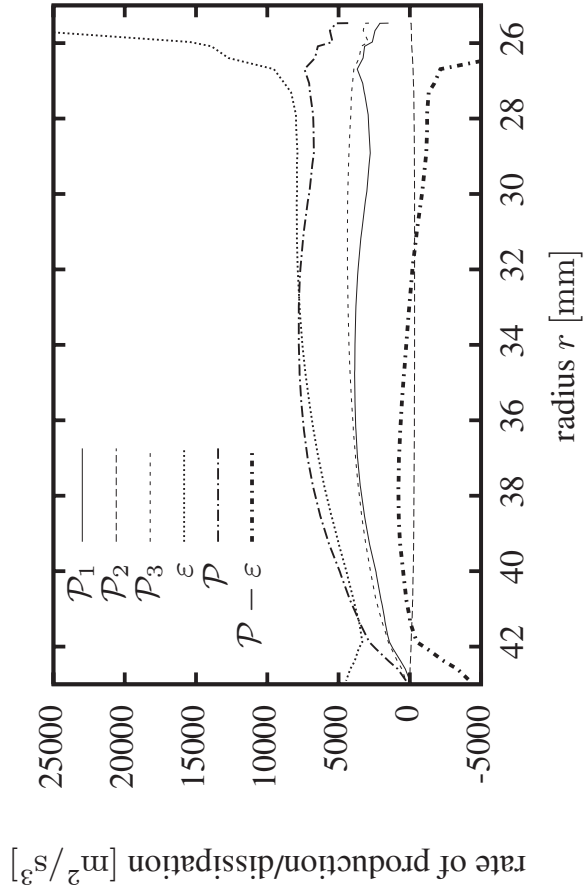


**Figure D.1:** Vertical cut through the engine in the  $x, z$  plane at  $y = 0$ . The left plot shows the velocity components in the  $x, z$  plane as vectors and the velocity in  $y$  direction (identical to the radial component) as color coded field. The middle plot shows the distribution of the turbulent kinetic energy in color coding. Additionally, the mean flame front is indicated as a light grey line. In the right diagram, turbulent energy rates of production and dissipation and the global balance  $\mathcal{P} - \varepsilon$  are depicted. The location of the line containing the data is indicated as a black and white dashed line in the left plot.

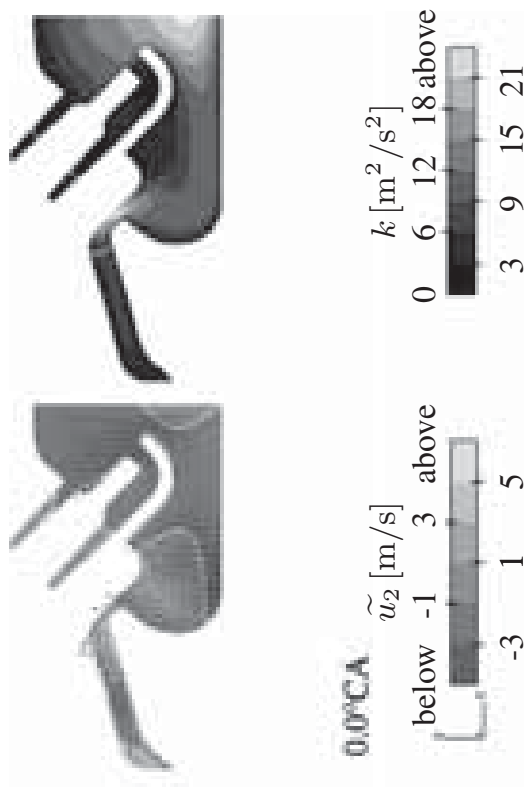
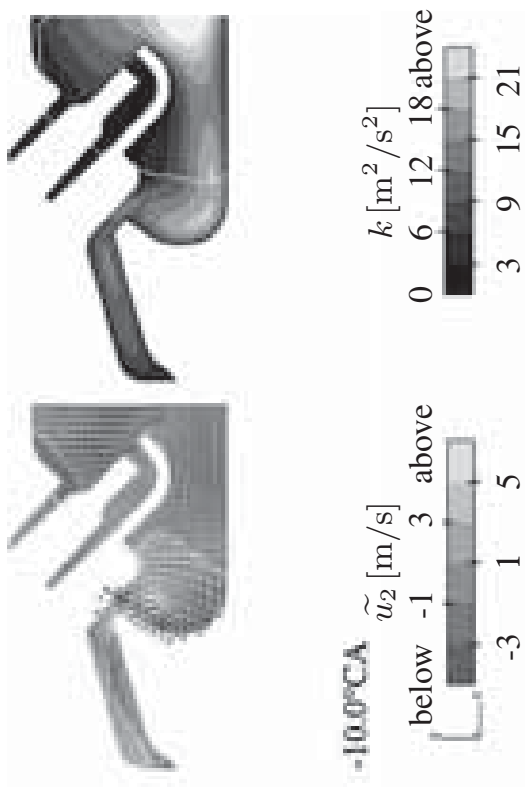
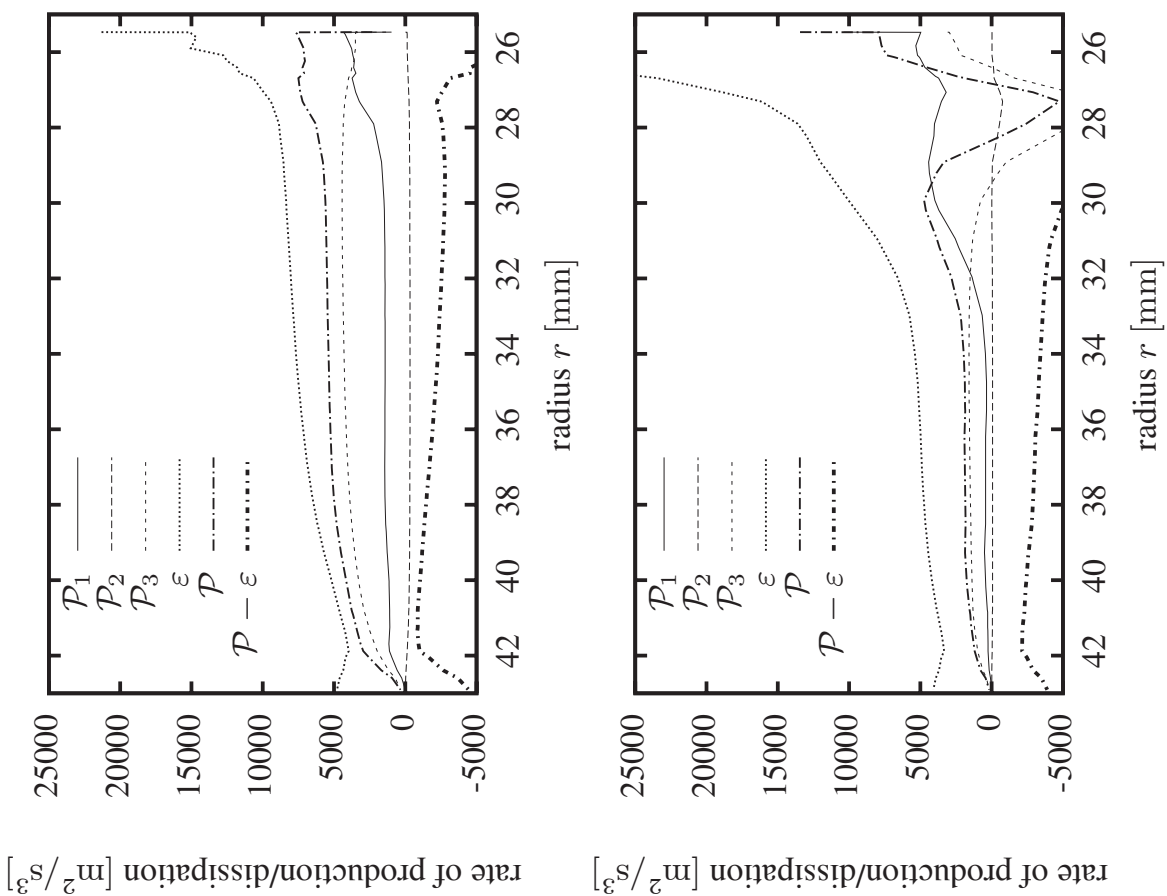


Figure D.2: Same as fig. D.1, but for  $-10^\circ\text{CA}$  and TDC.

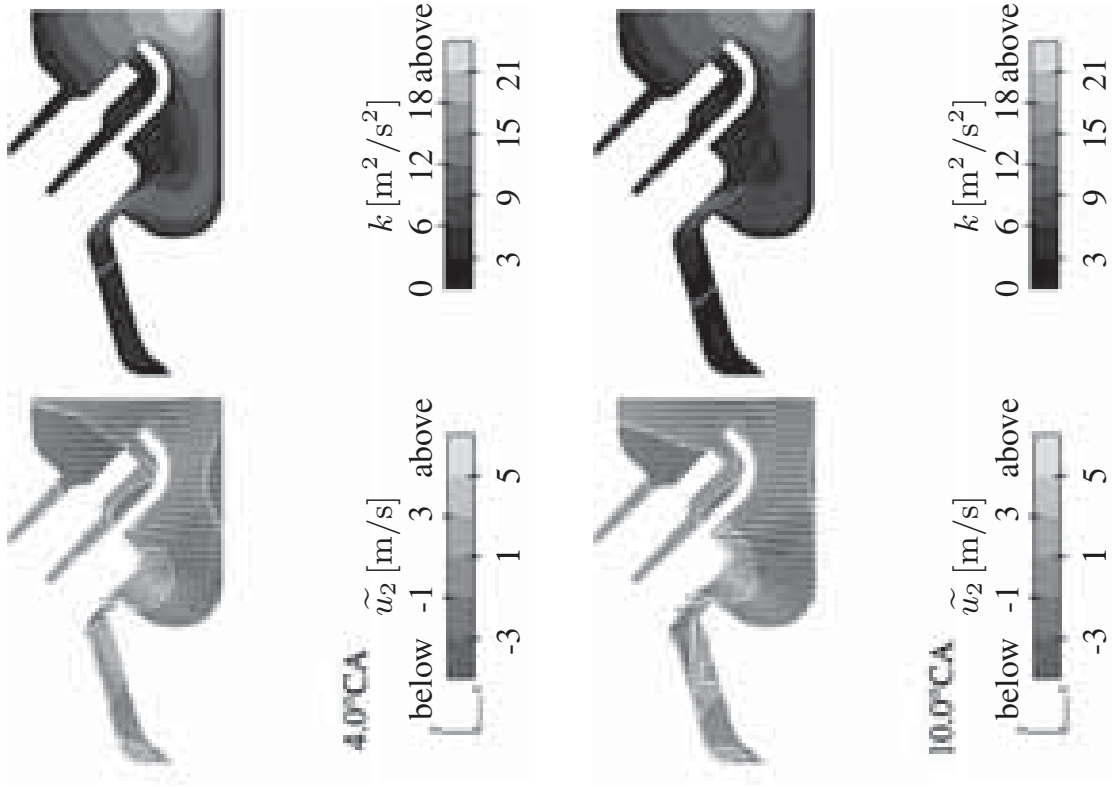
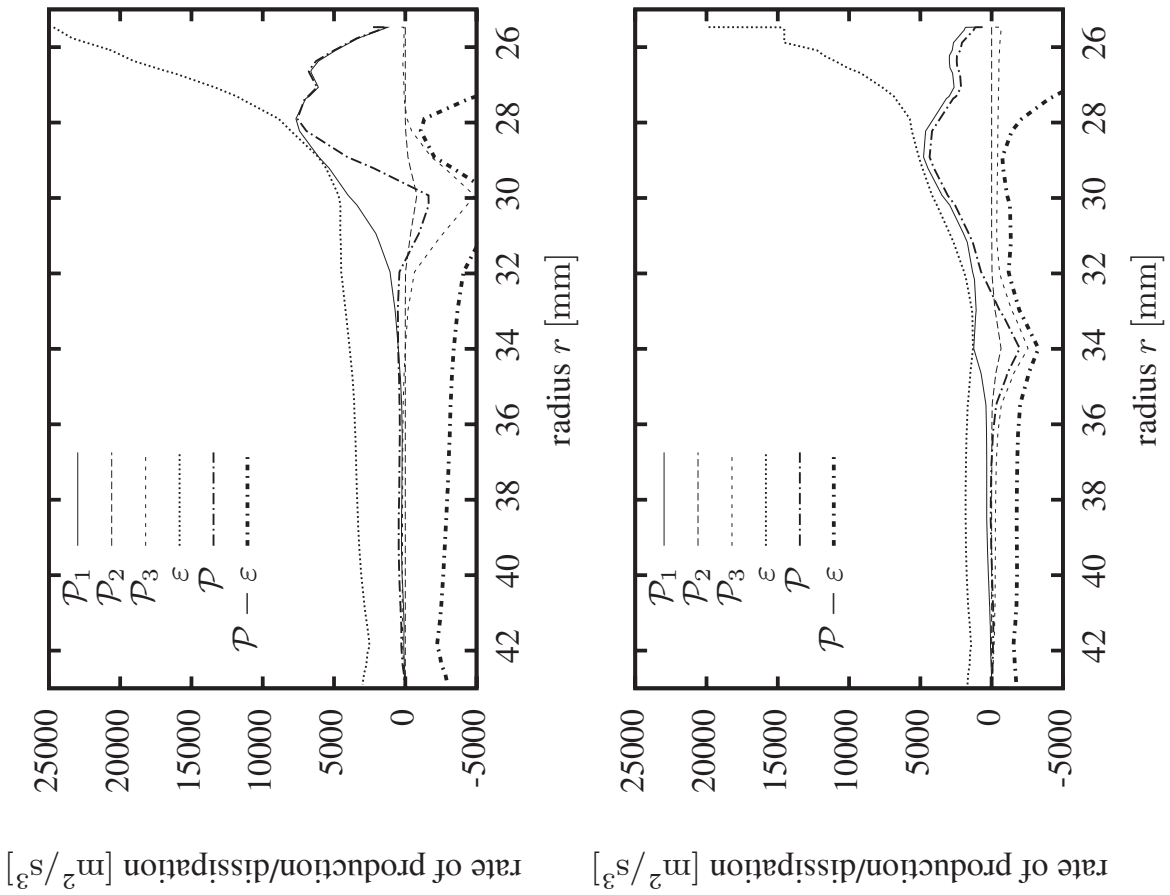


Figure D.3: Same as fig. D.1, but for 4° CA and 10° CA.



# Bibliography

- [1] R. G. Abdel-Gayed and D. Bradley. A two-eddy theory of premixed turbulent flame propagation. *Phil. Trans. of the Royal Soc. of London A*, 301(1457):1–25, 1981.
- [2] D. Adalsteinsson and J. A. Sethian. The fast construction of extension velocities in level set methods. *Journal of Computational Physics*, 148:2–22, 1999.
- [3] L. Andreassi, S. Cordiner, and V. Rocco. Modelling the early stage of spark ignition engine combustion using the KIVA-3V code incorporating an ignition model. *Int. Journ. Engine Res.*, 4(3):179–192, 2003.
- [4] D. R. Ballal and A. H. Lefebvre. The influence of flow parameters on minimum ignition energy and quenching distance. *Fifteenth Symposium (International) on Combustion*, pages 1473–1481, 1974.
- [5] J. Betten. *Finite Elemente für Ingenieure*, volume 1. Springer Verlag, 1997.
- [6] L. Boltzmann. Weitere Studien über das Wärmegleichgewicht unter Gas-molekülen. *Sitzungsberichte Kaiserl. Akad. der Wissenschaften*, 66(2):275–370, 1872.
- [7] K. Boulouchos, T. Steiner, and P. Dimopoulos. Investigation of flame speed models for the flame growth period during premixed engine combustion. *SAE Technical Paper Series*, no. 940476, 1994.
- [8] J. Boussinesq. Essai sur la théorie des eaux courantes. *Mem. pres. Acad. Sci.*, XXIII(1):46, 1877.
- [9] K. N. C. Bray. Studies of the turbulent burning velocity. *Proc. Roy. Soc. Lond.*, A 431:315–335, 1990.
- [10] K. N. C. Bray, P. A. Libby, and J. B. Moss. Flamelet crossing frequencies and mean reaction rates in premixed turbulent combustion. *Comb. Sci. Tech.*, 41:143–172, 1984.

- [11] D. E. Burgess and P. J. O'Rourke. Modeling turbulence in flows with a strong rotational component. Technical Report LA-12552-MS, Los Alamos National Laboratory, Nov 1993.
- [12] S. Chapman and T. G. Cowling. *The Mathematical Theory of Non-uniform Gases*. Cambridge University Press, 3rd edition, 1991.
- [13] M. Chen. *Simulation of Flame Stabilization of Lifted Turbulent Jet Diffusion Flames*. Dissertation, RWTH Aachen University, 2000.
- [14] P. Clavin. Dynamic behaviour of premixed flame fronts in laminar and turbulent. *Prog. Energ. Comb. Sci.*, 11:1–59, 1985.
- [15] T. J. Craft, B. E. Launder, and K. Suga. Development and application of a cubic eddy-viscosity model of turbulence. *Int. J. Heat and Fluid Flow*, 17:108–115, 1995.
- [16] G. Damköhler. Der Einfluss der Turbulenz auf die Flammengeschwindigkeit in Gasgemischen. *Zeitschr. f. Elektrochemie*, 46(11):601–626, 1940.
- [17] L. P. H. de Goey and J. H. M. Ten Thije Boonkkamp. A mass-based definition of flame stretch for flames with finite thickness. *Comb. Sci. Tech.*, 122:399–405, 1997.
- [18] J. W. Dold. Flame propagation in a nonuniform mixture: Analysis of a slowly varying triple flame. *Combust. Flame*, 76:71–88, 1989.
- [19] P. Domingo and L. Vervisch. Triple flames and partially premixed combustion in autoignition of non-premixed turbulent mixtures. *Twenty-Sixth Symposium (International) on Combustion*, pages 233–240, 1996.
- [20] M. C. Drake, T. D. Fansler, and A. M. Lippert. Stratified-charge combustion: modeling and imaging of a spray-guided direct-injection spark-ignition engine. *Proc. Combustion Inst.*, 30:2683–2691, 2005.
- [21] J. M. Duclos and O. Colin. Arc and kernel tracking ignition model for 3D spark-ignition engine calculations. *Intl. Symp. COMODIA 2001*, pages 343–350, 2001.
- [22] K. M. Düsing. *Large-Eddy Simulation turbulenter Vormischflammen*. Dissertation, TU Darmstadt, 2003.
- [23] S. H. El Tahry.  $k$ - $\varepsilon$  equation for compressible reciprocating engine flows. *AIAA Journal of Energy*, 7(4):345–353, 1983.
- [24] J. Ewald, F. Freikamp, G. Paczko, J. Weber, D. C. Haworth, and N. Peters. *GMTEC Developer's Manual*. Advanced Combustion GmbH, 2003.

- [25] L. Fan, G. Li, Z. Han, and R. D. Reitz. Modeling fuel preparation and stratified combustion in a gasoline direct injection engine. *SAE Technical Paper Series*, no. 1999-01-0175, 1999.
- [26] L. Fan and R. D. Reitz. Development of an ignition and combustion model for spark-ignition engines. *SAE Technical Paper Series*, no. 2000-01-2809, 2000.
- [27] J. H. Ferziger and H. G. Kaper. *Mathematical theory of transport processes in gases*. North-Holland, 1972.
- [28] J. H. Ferziger and M. Perić. *Computational Methods for Fluid Dynamics*. Springer, 3rd edition, 2002.
- [29] W. C. Gardiner. *Combustion Chemistry*. Springer Verlag, 1984.
- [30] J. Geiger, O. Lang, W. Salber, and K. Krebber-Hortmann. Status Quo und zukünftige Potenziale strahlgeführter Otto-DI Brennverfahren. In *Strahlgeführte Verbrennungssysteme*, pages 19–38. Menne, R., Brinkmann, B., 2005.
- [31] V. Giovangigli. *Multicomponent Flow Modeling*. Birkhäuser, 1999.
- [32] G. R. A. Groot. *Modelling of Propagating Spherical and Cylindrical Premixed Flames*. PhD thesis, Technische Universiteit Eindhoven, The Netherlands, 2003.
- [33] G. R. A. Groot and L. P. H. de Goey. A computational study on propagating spherical and cylindrical premixed flames. *Twenty-Ninth Symposium (International) on Combustion*, pages 1445–1451, 2002.
- [34] G. R. A. Groot, J. A. van Oijen, L. P. H. de Goey, K. Seshadri, and N. Peters. The effects of strain and curvature on the mass burning rate of premixed laminar flames. *Comb. Theory Modelling*, 6:675–695, 2002.
- [35] Y. Hamamoto, M. Izumi, and E. Tomita. The effect of swirl on the combustion of a homogeneous mixture in a closed vessel, 1st report, swirl and its turbulence characteristics in a combustion chamber (*in Japanese*). *Proc. of JSME*, 53(488):1395–1402, 1986.
- [36] Y. Hamamoto, M. Izumi, and E. Tomita. The effect of swirl on the combustion of a homogeneous mixture in a closed vessel, 2nd report, burning velocity and burning zone thickness of turbulent flames (*in Japanese*). *Proc. of JSME*, 53(489):1627–1634, 1986.
- [37] Y. Hamamoto, M. Izumi, and E. Tomita. The effect of swirl on the combustion of a homogeneous mixture in a closed vessel. *JSME International Journal Series II*, 31(1):140–149, 1988.

- [38] Y. Hamamoto, M. Izumi, and E. Tomita. Turbulent premixed flames in a closed vessel studied through analysis of flame photographs. *JSME International Journal Series II*, 32(3):443–448, 1989.
- [39] Y. Hamamoto, M. Izumi, and E. Tomita. Effects of swirl and air-fuel ratio on premixed combustion in a closed vessel. *JSME International Journal Series II*, 33(2):370–376, 1990.
- [40] C. Hasse, M. Bollig, N. Peters, and H. A. Dwyer. Quenching of laminar iso-octane flames at cold walls. *Combust. Flame*, 122:117–129, 2000.
- [41] D. C. Haworth and K. Jansen. Large-eddy simulation on unstructured deforming meshes: towards reciprocating IC engines. *Comp. Fluids*, 29:493–524, 2000.
- [42] M. Herrmann. *Numerical Simulation of Premixed Turbulent Combustion Based on a Level Set Flamelet Model*. Dissertation, RWTH Aachen University, 2001.
- [43] R. Herweg and R. Maly. A fundamental model for flame kernel formation in S. I. engines. *SAE Technical Paper Series*, no. 922243, 1992.
- [44] J. B. Heywood. *Internal Combustion Engine Fundamentals*. McGraw Hill, 1988.
- [45] R. I. Issa, A.D. Gosman, and A. P. Watkins. Solution of the implicitly discretised fluid flow equations by operator splitting. *J. Comp. Phys.*, 62:66–82, 1986.
- [46] W. P. Jones and P. Musonge. Closure of the reynolds stress and scalar flux equations. *Phys. Fluids*, 31(12):3589–3604, December 1988.
- [47] N. Kawahara, E. Tomita, S. Yoshiyama, A. Nishiyama, and Y. Hamamoto. Effects of swirl turbulent flow field and inhomogeneous concentration field on combustion of fuel-air mixture in a constant volume vessel. *5th Intl. Symp. CO-MODIA 2001*, pages 219–225, 2001.
- [48] P. Keller-Sornig. *Berechnung der turbulenten Flammenausbreitung bei der otomotorischen Verbrennung mit einem Flamelet-Modell*. Dissertation, RWTH Aachen University, 1996.
- [49] A. N. Kolmogorov. The equations of turbulent motion in an incompressible fluid. *Izvestia Acad. Sci. USSR; Phys.*, 6:56–58, 1942. *in Russian*.
- [50] B. E. Launder and D. B. Spalding. The numerical computation of turbulent flows. *Computer Methods in Applied Mechanics and Engineering*, 3:269–289, 1974.

- [51] G. A. Lavoie. Correlations of combustion data for S. I. engine calculations – laminar flame speed, quench distance and global reaction rates. *SAE Trans.*, 87(no. 780229):1015ff, 1987.
- [52] T. W. Lee and S. J. Lee. Direct comparison of turbulent burning velocity and flame surface properties in turbulent premixed flames. *Combust. Flame*, 132:492–502, 2003.
- [53] A. H. Lefebvre. *Atomization and Sprays*. Taylor & Francis, 1989.
- [54] M. T. Lim, R. W. Anderson, and V. S. Arpaci. Prediction of spark kernel development in constant volume combustion. *Combust. Flame*, 69:303–316, 1987.
- [55] A. M. Lippert, T. D. Fansler, and M. C. Drake. High-speed imaging and CFD modeling of sprays and combustion in a spray-guided spark ignition direct injection engine. In *6th Int. Symp. on Internal Combustion Diagnostics*, Baden-Baden, Germany, June 15–16 2004.
- [56] A. M. Lippert and R. D. Reitz. Modeling of multicomponent fuels using continuous distributions with application to droplet evaporation and sprays. *SAE Technical Paper Series*, no. 972882, 1997.
- [57] J. Maaß, B. Leyh, and H. Tschöke. Computersimulation der Gemischbildung für Hochdruck-Benzindirekteinspritzung (HD-BDE). *12. Aachener Kolloquium Fahrzeug- und Motorentechnik*, pages 327–352, 2003.
- [58] R. Maly and M. Vogel. Initiation and propagation of flame fronts in lean  $\text{CH}_4$ -air mixtures by the three modes of the ignition spark. *Seventeenth Symposium (International) on Combustion*, pages 821–831, 1978.
- [59] M. Matalon and B. J. Matkovsky. Flames at gasdynamic discontinuities. *J. Fluid Mech.*, 124:239–259, 1982.
- [60] P. C. Miles, D. Choi, M. Megerle, B. Rempelewert, R. D. Reitz, M.-C. D. Lai, and V. Sick. The influence of swirl ratio on turbulent flow structure in a motored HSDI Diesel engine - a combined experimental and numerical study. *SAE Technical Paper Series*, no. 2004-01-1678, 2004.
- [61] P. C. Miles, M. Megerle, J. Hammer, Z. Nagel, R. D. Reitz, and V. Sick. Late-cycle turbulence generation in swirl-supported, direct-injection Diesel engines. *SAE Technical Paper Series*, no. 2002-01-0891, 2002.
- [62] U. C. Müller, M. Bollig, and N. Peters. Approximations for burning velocities and markstein numbers for lean hydrocarbon and methanol flames. *Combust. Flame*, 108:349–356, 1997.

- [63] M. Oberlack, H. Wenzel, and N. Peters. On symmetries, invariant solutions and averaging of the  $G$ -equation for premixed combustion. *Combust. Theory Modelling*, pages 363–383, 2001.
- [64] Y. H. Pao. Structure of turbulent velocity and scalar fields at large wavenumbers. *Phys. Fluids*, 8(6):1063–1075, 1965.
- [65] S. V. Patankar. *Numerical Heat Transfer and Fluid Flow*. McGraw Hill, 1980.
- [66] D. Peng, B. Merriman, S. Osher, H. Zhao, and M. Kang. A PDE-based fast local level set method. *Journal of Computational Physics*, 155:410–38, 1999.
- [67] N. Peters. Numerical and asymptotic analysis of systematically reduced reaction schemes for hydrocarbon flames. In R. Glowinski, B. Larrouturou, and R. Temam, editors, *Numerical Simulation of Combustion Phenomena, Lecture Notes in Physics*, volume 241, pages 90–109. Springer Verlag, 1985.
- [68] N. Peters. *Fifteen Lectures on Laminar and Turbulent Combustion*. Ercof-tac Summer School, September 14-28 1992. Institut für Technische Mechanik, RWTH Aachen, 1992.
- [69] N. Peters. A spectral closure for premixed turbulent combustion in the flamelet regime. *J. Fluid Mech.*, 242:611–629, 1992.
- [70] N. Peters. The turbulent burning velocity for large scale and small scale turbulence. *J. Fluid Mech.*, 384:107–132, 1999.
- [71] N. Peters. *Turbulent Combustion*. Cambridge University Press, 2000.
- [72] N. Peters, P. Terhoeven, J. H. Chen, and T. Echekki. Statistics of flame displacement speeds from computations of 2-D unsteady methane-air flames. *Twenty-Seventh Symposium (International) on Combustion*, 27:833–839, 1998.
- [73] N. Peters and F. A. Williams. The asymptotic structure of stoichiometric methane-air flames. *Combust. Flame*, 68:185–207, 1987.
- [74] S. Pischinger and J. B. Heywood. A study of flame development and engine performance with breakdown ignition systems in a visualization engine. *SAE Technical Paper Series*, no. 880518, 1988.
- [75] S. Pischinger and J. B. Heywood. How heat losses to the spark plug electrodes affect flame kernel development in an SI-engine. *SAE Technical Paper Series*, no. 900021, 1990.
- [76] H. Pitsch. *FlameMaster: A C++ Computer Program for 0D Combustion and 1D Laminar Flame Calculations*. URL: <http://www.stanford.edu/~hpitsch/FlameMaster.html>, 1998.

- [77] H. Pitsch and N. Peters. A consistent flamelet formulation for non-premixed combustion considering differential diffusion effects. *Combust. Flame*, 114(1):26–40, 1998.
- [78] T. Poinso and D. Veynante. *Theoretical and Numerical Combustion*. Edwards, 2001.
- [79] T. Poinso, D. Veynante, and S. Candel. Quenching processes and premixed turbulent combustion diagrams. *J. Fluid Mech.*, 228:561–606, 1991.
- [80] S. B. Pope. A more general effective-viscosity hypothesis. *J. Fluid Mech.*, 72(2):331–340, 1975.
- [81] S. B. Pope. *Turbulent Flows*. Cambridge University Press, 2000.
- [82] L. Prandtl. Über ein neues Formelsystem für die ausgebildete Turbulenz. *Nachr. Akad. Wiss. Göttingen Math-Phys. Kl*, pages 6–19, 1945.
- [83] J. C. Rotta. *Turbulente Strömungen*. Teubner, 1972.
- [84] R. Rubinstein and J. M. Barton. Non-linear Reynolds stress models and the Renormalization Group. *Phys. Fluids A*, 2(8):1472–1476, 1990.
- [85] K. Seshadri, X. S. Bai, and H. Pitsch. Asymptotic structure of rich methane-air flames. *Combust. Flame*, 127:2265–2277, 2002.
- [86] K. Seshadri, X. S. Bai, H. Pitsch, and N. Peters. Asymptotic analysis of the structure of moderately rich methane-air flames. *Combust. Flame*, 113:589–602, 1998.
- [87] K. Seshadri, M. Bollig, and N. Peters. Numerical and asymptotic studies of the structure of stoichiometric and lean premixed heptane flames. *Combust. Flame*, 108:518–536, 1997.
- [88] J. A. Sethian. *Level Set Methods – Evolving Interfaces in Geometry, Fluid Mechanics Computer Vision, and Materials Science*. Cambridge University Press, 1996.
- [89] J. A. Sethian. Fast marching methods. *SIAM Review*, 41(2):199–235, 1999.
- [90] I. G. Shepherd and R. K. Cheng. The burning rate of premixed flames in moderate and intense turbulence. *Combust. Flame*, 127:2066–2075, 2001.
- [91] T.-H. Shih, J. Zhu, and J. L. Lumley. A realizable Reynolds stress algebraic equation model. *NASA Technical Memorandum*, No. 105993:1–34, 1993.
- [92] W. A. Sirignano. *Fluid Dynamics and Transport of Droplets and Sprays*. Cambridge University Press, 1999.

- [93] M. D. Smooke and V. Giovangigli. Formulation of the premixed and non-premixed test problems. In M. D. Smooke, editor, *Reduced Kinetic Mechanisms and Asymptotic Approximations for Methane-Air Flames*, volume 384 of *Lecture Notes in Physics*, pages 1–28. Springer-Verlag, 1990.
- [94] D. B. Spalding. Mixing and chemical reaction in steady confined turbulent flames. *Thirteenth Symposium (International) on Combustion*, pages 649–657, 1971.
- [95] D. B. Spalding. Development of the eddy-break-up model of turbulent combustion. *Sixteenth Symposium (International) on Combustion*, pages 1657–1663, 1976.
- [96] U. Spicher, U. Heidenreich, and A. Nauwerck. Stand der Technik strahlgeführter Verbrennungssysteme. In *Strahlgeführte Verbrennungssysteme*, pages 1–18. Menne, R., Brinkmann, B., 2005.
- [97] M. Sussman. An efficient, interface preserving level set re-distancing algorithm and its application to interfacial incompressible fluid flow. *SIAM Journal of Scientific Computing*, 20(4):1165–91, 1999.
- [98] M. Sussman, P. Smereka, and S. Osher. A level set approach for computing solutions to incompressible two-phase flow. *Journal of Computational Physics*, 94:146–59, 1994.
- [99] Z. Tan, S. C. Kong, and R. D. Reitz. Modeling premixed and direct injection SI engine combustion using the  $G$ -equation model. *SAE Technical Paper Series*, no. 2003-01-1843, 2003.
- [100] Z. Tan and R. D. Reitz. Development of  $G$ -Equation combustion model for direct injection SI engine simulations. In *13th Int. Multidim. Engine Modeling User's Group Meeting*, Detroit, MI, March 2 2003.
- [101] Z. Tan and R. D. Reitz. Modeling ignition and combustion in spark-ignition engines using a level set method. *SAE Technical Paper Series*, no. 2003-01-0722, 2003.
- [102] H. Tennekes and J. L. Lumley. *A First Course in Turbulence*. MIT Press, Cambridge, MA, 1972.
- [103] E. Tomita. personal communication, 2004.
- [104] S. Wallin and A. V. Johansson. An explicit algebraic Reynolds stress model for incompressible and compressible turbulent flows. *J. Fluid Mech.*, 403:89–132, 2000.



- [105] H. Wenzel. Turbulent premixed combustion in the laminar flamelet and the thin reaction zones regime. *Annual Research Briefs*, pages 237–252, 1997.
- [106] H. Wenzel. *Direkte numerische Simulation der Ausbreitung einer Flammenfront in einem homogenen Turbulenzfeld*. Dissertation, RWTH Aachen University, 2000.
- [107] D. C. Wilcox. *Turbulence Modeling for CFD*. DCW Industries, 1993.
- [108] W. Willems. *Numerische Simulation turbulenter Scherströmungen mit einem Zwei-Skalen Turbulenzmodell*. Dissertation, RWTH Aachen University, 1996.
- [109] F. A. Williams. A review of some theoretical considerations of turbulent flame structure. Technical Report CP-164, AGARD, 1975.
- [110] F. A. Williams. Turbulent combustion. In J. Buckmaster, editor, *The Mathematics of Combustion*, pages 97–131. SIAM, Philadelphia, 1985.
- [111] G. Woschni. Universally applicable equation for the instantaneous heat transfer coefficient in the internal combustion engine. *SAE Technical Paper Series*, no. 670931, 1967.
- [112] J. B. Zeldowitsch and D. A. Frank-Kamenetzki. A theory of thermal propagation of flame. *Acta Physicochimica URSS*, 9(2):341–350, 1938.
- [113] F. Zhao, D. L. Harrington, and M.-C. D. Lai. *Automotive Gasoline Direct-Injection Engines*. SAE, 2002.



# Author's Index

- Abdel-Gayed, R. G. 36, 53  
Adalsteinsson, D. 125  
Anderson, R. W. 85  
Andreassi, L. 64  
Arpaci, V. S. 85
- Bai, X. S. 26  
Ballal, D. R. 61  
Barton, J. M. 17  
Betten, J. 74  
Bollig, M. 26, 54, 80, 82, 92, 134  
Boltzmann, L. 6  
Boulouchos, K. 62, 64  
Boussinesq, J. 17  
Bradley, D. 36, 53  
Bray, K. N. C. 13, 39, 40, 53  
Burgess, D. E. 142
- Candel, S. 35  
Chapman, S. 5  
Chen, J. H. 29  
Chen, M. 2, 59, 119  
Cheng, R. K. 43  
Choi, D. 142  
Clavin, P. 28  
Colin, O. 62  
Cordiner, S. 64  
Cowling, T. G. 5  
Craft, T. J. 17
- Damköhler, G. 35, 53  
de Goey, L. P. H. 29  
Dimopoulos, P. 62, 64  
Dold, J. W. 58  
Domingo, P. 58  
Drake, M. C. 91, 101, 107, 108  
Duclos, J. M. 62  
Düsing, K. M. 120  
Dwyer, H. A. 54
- Echekki, T. 29  
El Tahry, S. H. 16  
Ewald, J. 14, 67
- Fan, L. 62  
Fansler, T. D. 91, 101, 107, 108  
Ferziger, J. H. 5, 14, 67  
Frank-Kamenetzki, D. A. 24  
Freikamp, F. 14, 67
- Gardiner, W. C. 8  
Geiger, J. 101  
Giovangigli, V. 5, 27  
Gosman, A.D. 14, 69  
Groot, G. R. A. 26, 29
- Hamamoto, Y. 3, 79, 80  
Hammer, J. 142  
Han, Z. 62  
Harrington, D. L. 101  
Hasse, C. 54

- Haworth, D. C. 14, 67, 120  
 Heidenreich, U. 101  
 Herrmann, M. 2, 48, 57  
 Herweg, R. 61, 63  
 Heywood, J. B. 61, 64, 114  
  
 Issa, R. I. 14, 69  
 Izumi, M. 3, 79  
  
 Jansen, K. 120  
 Johansson, A. V. 17  
 Jones, W. P. 47  
  
 Kang, M. 125  
 Kaper, H. G. 5  
 Kawahara, N. 79, 80  
 Keller-Sornig, P. 52  
 Kolmogorov, A. N. 16  
 Kong, S. C. 3, 62  
 Krebber-Hortmann, K. 101  
  
 Lai, M.-C. D. 101, 142  
 Lang, O. 101  
 Launder, B. E. 16, 17  
 Lavoie, G. A. 88  
 Lee, S. J. 44  
 Lee, T. W. 44  
 Lefebvre, A. H. 61, 102  
 Leyh, B. 101  
 Li, G. 62  
 Libby, P. A. 39  
 Lim, M. T. 85  
 Lippert, A. M. 91, 101, 102, 107, 108  
 Lumley, J. L. 17, 47  
  
 Maaß, J. 101  
 Maly, R. 61, 63  
 Matalon, M. 28  
 Matkovsky, B. J. 28  
 Megerle, M. 142  
 Merriman, B. 125  
 Miles, P. C. 142  
 Moss, J. B. 39  
  
 Müller, U. C. 80, 82, 92, 134  
 Musonge, P. 47  
  
 Nagel, Z. 142  
 Nauwerck, A. 101  
 Nishiyama, A. 79, 80  
  
 Oberlack, M. 41–44, 48  
 O'Rourke, P. J. 142  
 Osher, S. 124, 125  
  
 Paczko, G. 14, 67  
 Pao, Y. H. 12  
 Patankar, S. V. 14, 69  
 Peng, D. 125  
 Perić, M. 14, 67  
 Peters, N. 2, 14, 20, 24–26, 29, 33, 37,  
 41–44, 47–50, 52–54, 57, 59, 67, 72,  
 80, 82, 85, 92, 119, 122, 134  
 Pischinger, S. 61  
 Pitsch, H. 24, 26, 59, 137  
 Poinot, T. 35, 40  
 Pope, S. B. 11, 12, 17, 38  
 Prandtl, L. 16  
  
 Reitz, R. D. 3, 62, 63, 102, 142  
 Rempelewert, B. 142  
 Rocco, V. 64  
 Rotta, J. C. 16, 141  
 Rubinstein, R. 17  
  
 Salber, W. 101  
 Seshadri, K. 26, 29  
 Sethian, J. A. 125, 127  
 Shepherd, I. G. 43  
 Shih, T.-H. 17  
 Sick, V. 142  
 Sirignano, W. A. 102  
 Smereka, P. 124  
 Smooke, M. D. 27  
 Spalding, D. B. 16, 38  
 Spicher, U. 101  
 Steiner, T. 62, 64

- Suga, K. 17  
Sussman, M. 124
- Tan, Z. 3, 62, 63  
Ten Thije Boonkkamp, J. H. M. 29  
Tennekes, H. 47  
Terhoeven, P. 29  
Tomita, E. 3, 79, 80, 88  
Tschöke, H. 101
- van Oijen, J. A. 29  
Vervisch, L. 58  
Veynante, D. 35, 40  
Vogel, M. 61
- Wallin, S. 17  
Watkins, A. P. 14, 69  
Weber, J. 14, 67  
Wenzel, H. 36, 41–44, 48, 53, 117  
Wilcox, D. C. 15, 141  
Willems, W. 65  
Williams, F. A. 2, 25, 29, 31, 134  
Woschni, G. 114
- Yoshiyama, S. 79, 80
- Zeldowitsch, J. B. 24  
Zhao, F. 101  
Zhao, H. 125  
Zhu, J. 17



# Nomenclature

In these lists, the meanings of symbols is explained as they are used throughout the thesis. Occasionally, symbols have divergent meanings from this nomenclature. Then, the corresponding meaning directly is given in the context. Additionally, rarely used symbols are not included.

## Acronyms

|         |  |
|---------|--|
| aTDC    | after Top Dead Center                        |
| bTDC    | before Top Dead Center                       |
| CA      | Crank Angle                                  |
| CFD     | Computational Fluid Dynamics                 |
| COV     | Coefficient Of Variability                   |
| DI      | Direct Injection                             |
| DNS     | Direct Numerical Simulation                  |
| EGR     | Exhaust Gas Recirculation                    |
| IMAP    | Intake Manifold Pressure                     |
| ODE     | ordinary differential equation               |
| pdf     | probability density function                 |
| RANS    | Reynolds Averaged Navier-Stokes              |
| AG-SIDI | Air-Guided Spark-Ignition Direct-Injection   |
| SG-SIDI | Spray-Guided Spark-Ignition Direct-Injection |
| SIDI    | Spark-Ignition Direct-Injection              |
| SI      | Spark Ignition                               |
| SMR     | Sauter Mean Radius                           |
| TDC     | Top Dead Center                              |
| WG-SIDI | Wall-Guided Spark-Ignition Direct-Injection  |

## Greek Letters

|               |  |
|---------------|--|
| $\alpha$      | species index                                |
| $\chi$        | scalar dissipation rate                      |
| $\varepsilon$ | dissipation of turbulent kinetic energy      |
| $\eta$        | Kolmogorov length scale, see equation (2.42) |
| $\kappa$      | flame curvature, see equation (3.14)         |

|                        |   |
|------------------------|---|
| $\kappa$               | von-Kármán constant                               |
| $\lambda$              | normalized air/fuel ratio, see equation (2.23)    |
| $\lambda$              | thermal conductivity                              |
| $\mu_t$                | turbulent viscosity                               |
| $\dot{\omega}$         | reaction rate                                     |
| $\overline{\Omega}$    | rate of rotation tensor, see equation (2.5)       |
| $\phi$                 | equivalence ratio, see equation (2.25)            |
| $\widetilde{\phi'^2}$  | variance of equivalence ratio, see equation (5.8) |
| $\rho$                 | density   |
| $\Sigma$               | flame surface density                             |
| $\sigma$               | instantaneous flame surface area ratio            |
| $\widetilde{\sigma}_t$ | turbulent flame surface area ratio                |

### Roman Letters

|                          |   |
|--------------------------|---|
| $a_{fr}$                 | air/fuel ratio, see equation (2.24)   |
| $a_{i,j}$                | normalized anisotropic turbulent stress tensor                                  |
| $\widetilde{A}$          | area of mean flame front, see equation (3.33)                                   |
| $c$                      | progress variable parameter, see equation (3.50)                                |
| $D_0$                    | flame diffusivity, see equation (3.8)   |
| $Da$                     | turbulent Damköhler number, see equation (3.41)                                 |
| $D_{\mathcal{L}}$        | Markstein diffusivity, see equation (3.16)                                      |
| $D_t$                    | turbulent diffusivity   |
| $D'_t$                   | turbulent diffusivity based on the mixing length approach, see equation (3.108) |
| $f_b$                    | volumetric probability/fraction of finding burnt gas                            |
| $f_D$                    | flame diffusivity factor, see equation (5.1)                                    |
| $G$                      | Level Set field variable  |
| $G_0$                    | Level Set interface position  |
| $\widetilde{G}$          | Level Set field describing mean flame front position                            |
| $\widetilde{G'^2}$       | variance of the Level Set field, see equation (3.85)                            |
| $\widetilde{G'^2}_{alg}$ | algebraic variance of the Level Set field, see equation (3.99)                  |
| $h$                      | enthalpy  |
| $K$                      | flame stretch rate  |
| $k$                      | turbulent kinetic energy  |
| $Ka$                     | turbulent Karlovitz number, see equation (3.38)                                 |
| $Ka_l$                   | laminar Karlovitz number, see equation (3.21)                                   |
| $\ell$                   | integral length scale, see equation (2.44)                                      |
| $\mathcal{L}$            | Markstein length, see equation (3.16)   |
| $L$                      | turbulent scale, see equation (2.39)  |
| $\ell_\delta$            | reaction zone thickness   |
| $\ell_f$                 | laminar flame thickness, see equation (3.8)                                     |
| $\ell_{f,t}$             | turbulent flame brush thickness, see equation (3.84)                            |



|                           |   |
|---------------------------|---|
| $\ell_{f,t,alg}$          | algebraic turbulent flame brush thickness, see equation (3.100)             |
| $\ell_G$                  | Gibson scale, see equation (3.37)   |
| $\mathcal{M}$             | Markstein number  |
| $\vec{n}$                 | flame front normal vector, see equation (3.28)                              |
| $\ell_m$                  | mixing length   |
| $\mathcal{P}$             | turbulent production due to mean velocity gradients                         |
| $p$                       | pressure  |
| $\tilde{P}_b$             | mass averaged probability / mass fraction of burnt gas, see equation (3.70) |
| $Pr_t$                    | turbulent Prandtl number  |
| $q$                       | model parameter in equation (3.114)   |
| $\mathcal{R}$             | ideal gas constant  |
| $Re$                      | Reynolds number, see equation (3.36)  |
| $\overline{\overline{S}}$ | modified rate-of-strain tensor, see equation (2.6)                          |
| $S$                       | strain rate   |
| $Sc_t$                    | turbulent Schmidt number  |
| $s_L$                     | laminar burning velocity  |
| $s_L^0$                   | unstretched laminar burning velocity, see equation (3.1)                    |
| $s_T$                     | turbulent burning velocity  |
| $T$                       | temperature   |
| $t$                       | time  |
| $T_0$                     | inner layer temperature   |
| $T_{ad}$                  | adiabatic flame temperature   |
| $T_u$                     | unburnt temperature   |
| $\vec{u}$                 | fluid velocity vector   |
| $\vec{u}'$                | velocity fluctuation  |
| $\langle U \rangle$       | averaged random variable $U$  |
| $\tilde{U}$               | Favre averaged random variable $U$  |
| $v'$                      | turbulence intensity  |
| $W$                       | molecular weight of the gas mixture   |
| $x_0$                     | normal coordinate position in the inner layer                               |
| $\dot{x}_b$               | normalized heat release, page 83  |
| $\vec{x}_f$               | flame front position vector, see equation (3.26)                            |
| $x_n$                     | premixed normal flamelet coordinate   |
| $Y$                       | species mass fraction   |
| $y$                       | wall distance   |
| $Z$                       | mixture fraction, see equation (2.20)                                       |
| $\tilde{Z}$               | Favre averaged mixture fraction, see equation (3.137)                       |
| $Z_{st}$                  | stoichiometric mixture fraction   |



# Lebenslauf (Curriculum Vitae)

## Persönliche Daten

|               |                        |
|---------------|------------------------|
| Name          | Jens Ewald             |
| Geburtsdatum  | 16. Mai 1973 in Rheydt |
| Familienstand | ledig                  |

## Schulbildung

|                 |   |
|-----------------|---|
| 08/1979-06/1983 | Gemeinschaftsgrundschule Rheindahlen in Mönchengladbach |
| 08/1983-06/1992 | Gymnasium Rheindahlen in Mönchengladbach                |
| 06/1992         | Abschluss: Abitur                                       |

## Wehrdienst

|                 |   |
|-----------------|---|
| 04/1993-03/1994 | Luftfahrzeugwartungsmechaniker in Nörvenich |
|-----------------|---|

## Hochschulausbildung

|                 |  |
|-----------------|--|
| 10/1992-03/1999 | Maschinenbaustudium an der RWTH Aachen, Vertieferrichtung: Energietechnik/Wärmetechnik |
| 08/1997-06/1998 | DAAD Stipendiat an der University of California at Davis, USA                          |
| 03/1999         | Abschluss: Diplom  |

## Berufliche Tätigkeit

|                 |   |
|-----------------|---|
| 06/2001-09/2001 | General Motors Research, Development and Planning in Warren, Michigan, USA  |
| seit 03/1999    | Wissenschaftlicher Mitarbeiter am Institut für Technische Mechanik der RWTH Aachen (seit 08/2005 Institut für Technische Verbrennung) |





